SCIENCE & TECHNOLOGY JOURNAL (STJ)

ISSN:2321-3388

VOLUME 12 NUMBER 2

June 2024

Published by
Mizoram University

Science & Technology Journal (STJ)

Volume 12 Number 2 June 2024

ISSN: 2321-3388

Published by: Mizoram University, Aizawl – 796004, India

Editor-in-Chief (at the time of publication): Prof. Diwakar Tiwari

Digitally archived and updated by: Prof. Surya Kant Mehta

About the Journal

The Science & Technology Journal (STJ) is an open-access, peer-reviewed multidisciplinary journal published by Mizoram University. It disseminates original research and technological developments that advance knowledge in science, engineering, and allied disciplines.

Copyright & Licensing

© The Authors (2024). Authors retain copyright of their respective works. All articles are published under the Creative Commons Attribution 4.0 International License (CC BY 4.0), permitting unrestricted use, distribution, and reproduction in any medium, provided the original author(s) and source are properly credited.

License: https://creativecommons.org/licenses/by/4.0/

Reproduction and Archiving Policy

All published content of STJ is permanently preserved through the PKP Preservation Network (PKP PN) — a member of the Keepers Registry — and additionally deposited in the Internet Archive for long-term public access. Reproduction or redistribution of STJ content is permitted under the same CC BY 4.0 license, provided that the work is properly attributed and cited as originally published in STJ.

DOI and Citation Information

Each article is assigned a DOI under the Crossref prefix 10.22232/stj. Example format: doi.org/10.22232/stj.v12i2.xxxx. Please cite articles with their full DOI and publication details.

Contact

Editorial Office
Science & Technology Journal (STJ)
Mizoram University, Aizawl – 796004, India
Email: editor@stjmzu.org
Website: https://stjmzu.org

Science & Technology Journal

Volume 12, Number 2 — June 2024

Editorial

From the Editor: Unearthing the Deep — The Discovery of *Iridogorgia chewbacca* and the Spirit of Scientific Exploration
Surya Kant Mehta

Research Articles

Tailored Synthesis of Silver Nanoparticles using Polyphenolic and Flavonoid-rich Leaf Extract of Dryopteris cristata L. and Insights into its Antioxidant Potency
Biswajyoti Hazarika, Md. Juned K. Ahmed

Synthesis, Characterization, Photoluminescence and Photocatalytic Properties of Pr(III) Doped CdMoO4 Phosphors
N. Mohondas Singh, K. Lalchhandama, Fidelia Lalrindiki, Brojendro Singh Shagolsem

Pure CoS and Different Concentrations of Fe/Nd Co-Doped CoS Nanoparticles: Photoluminescence and Photocatalytic Studies

Assessing Soil Pollution: An Investigation into Heavy Metal Contaminations in Roadside Soil in Aizawl, Northeast India
Gospel Lallawmzuali, Angom Sarjubala Devi, Thanhmingliana

A Novel Method to Translate a Physical Watershed into Matrix Form for Run-off Estimation
Panchalika Dutta, Sundararajan Muniyan

3D Analysis of Wave Propagation in Generalized Magneto Thermoelastic Medium

Special Projective Semi-symmetric Connection on Kenmotsu Manifolds
K.C. Biakkim, M. Saroja Devi

Generalized H-almost Ricci Soliton in Almost Kenmotsu Manifold
Robert Sumlalsanga, J. P. Singh, M. Sundararajan

Velocity and Energy Distribution at Corrugated Interface of Monoclinic Medium
Lalvohbika Jongte, Lianngenga Rengsi, Lalhriattira Fanai

Functional Efficiency Quality of Indian Software Industry: A Computational Approach
Sajal Kanti Das, Jamal Hussain

Distance Estimation of Bok globule CB69
R.S. Paul, H.S. Das

Ab initio Study of Halide Double Perovskite Cs,NaAIX (X=Br,I) for Optoelectronics and Cs2NaAIX (X=Br,I) Thermoelectric Materials

Teda H. Lalrinmawii, Laihnuna, Z. Pachuau, Joel Lalbiakkimaa, G.C. Lalremruata

Celestial Harmony: Exploring the Analogy of Greek, Indian, South East Asian and Mizo Astronomy
T. Malsawmtluanga

Patient Satisfaction with Nursing Care: A Comparative Study on Communication and Psychological Support given by the Nurse in Medical and Orthopedic Ward
M. Lalhlimpuii, A.K. Trivedi, G. Konwar

Shadowed and Redundant Rules Removal in the Cloud Firewall Policy: A Modified Tree Rule Firewall Approach
Dhwani Hakani, Palvinder Singh Mann

Artificial Intelligence Techniques for Rainfall Prediction in Mizoram
Abul Kashim Md Fujail, Jarita Das

Refinements of Generalized Jacobi Method: A Higher-Order Approach
Urboshi Hazarika, Samira Behera

Empowering Mizoram State Museum Applying Virtual Reality on Linked Data and Smart Objects
V.D. Ambeth Kumar, Rajesh Ramasamy, Gurram Ramakrishna, R. Ramesh Prabhakaran

Citation: Science & Technology Journal, Vol. 12 No. 2 (2024): June 2024
ISSN 2319-9150 | DOI Prefix 10.22232/stj
© Authors 2024, Mizoram University
Licensed under CC BY 4.0 (https://creativecommons.org/licenses/by/4.0/)
Original publication: https://stjmzu.org/

From the Editor: Unearthing the Deep — The Discovery of Iridogorgia chewbacca and the Spirit of Scientific Exploration

Prof. S. K. Mehta
Editor-in-Chief, Science & Technology Journal (STJ)
Mizoram University, Aizawl, India

In the ever-expanding frontier of science, every discovery reminds us of how much remains unknown beneath the surface of our planet. In September 2025, marine biologists reported a remarkable new deep-sea coral species, *Iridogorgia chewbacca*, discovered in the tropical western Pacific Ocean at depths of 400–1000 m[1]. Its long, iridescent, hair-like branches inspired the name—a nod to the "Wookiee" character Chewbacca from *Star Wars*. This newly described species, together with *Iridogorgia curva*, expands our understanding of the genus *Iridogorgia* Verrill, 1883—deep-sea corals characterized by spiral axial structures and brilliant iridescence. The study by Xu, Watling, Zhan, and Xu (2025) combined morphological and molecular analyses to confirm two new species and clarify the taxonomy of ten related forms. Notably, the authors demonstrated that direction of growth (clockwise or counterclockwise) is not a reliable diagnostic trait, while *28S rDNA* sequencing provided robust phylogenetic support[1]. Beyond taxonomy, this discovery highlights the unexplored diversity of deep-sea ecosystems, often overshadowed by terrestrial research. Deep-sea corals such as *I. chewbacca* serve as living archives of environmental history—their skeletal layers preserve chemical traces of past ocean conditions. These insights are essential as we confront rapid climate and ecological change in marine environments. The *Science & Technology Journal (STJ)* has long aimed to showcase the breadth of scientific innovation and curiosity across disciplines. This issue (Vol. 12, No. 2, June 2024) continues that mission through eighteen articles spanning computational science, nanotechnology, mathematical modeling, environmental monitoring, cultural astronomy, and healthcare research. Collectively, they echo the same spirit of exploration that led to the discovery of *I. chewbacca*—a reminder that whether in the depths of the Pacific or within the microcosm of a laboratory, science thrives on the courage to look deeper. As we transition from print to digital publication, the journal remains committed to providing open access to quality research and fostering cross-disciplinary collaboration. We thank our contributors and readers for their unwavering support in sustaining this scientific dialogue.

Reference

[1] Xu, Y., Watling, L., Zhan, Z., & Xu, K. (2025). *Studies on western Pacific gorgonians (Anthozoa: Octocorallia: Chrysogorgiidae). Part 2: Unexpected diversity of the genus Iridogorgia in the tropical western Pacific with descriptions of two new species. Zootaxa*, **5689**(3), 451–486. https://doi.org/10.11646/zootaxa.5689.3.3

Science and Technology Journal Vol. 12 Issue: 2 June 2024 ISSN: 2321-3388

Tailored Synthesis of Silver Nanoparticles using Polyphenolic and Flavonoid-rich Leaf Extract of *Dryopteris cristata* L. and Insights into its Antioxidant Potency

Biswajyoti Hazarika[1] and Md. Juned K. Ahmed[2]*
[1,2]Department of Chemistry, Arunachal University of Studies,
Namsai-792103, Arunachal Pradesh, India
*E-Mail: juned.nits@gmail.com
*Corresponding Author

Abstract—Biosynthesized nanoparticles are increasingly recognized for their potential due to the biologically active secondary metabolites in plants that facilitate green synthesis and offer unique biological applications. This study presents a simple, eco-friendly and cost-effective method for the synthesis of silver nanoparticles using the aqueous leaf extract of *Dryopteris cristata* L., which serves as both a reducing and capping agent. Characterization through UV-visible spectroscopy (UV-Vis.), Fourier transform infrared spectroscopy (FT-IR), X-ray diffraction (XRD), scanning electron microscopy with energy-dispersive X-ray analysis (SEM-EDX), and transmission electron microscopy (TEM) analyses confirmed the properties of the *Dryopteris cristata*-silver nanoparticles (Dc-AgNPs). Phytochemical analysis identified the compounds responsible for nanoparticle reduction and stabilization. Antioxidant activity was assessed using 2,2-diphenyl-1-picrylhydrazyl (DPPH) and 3-ethylbenzothiazoline-6-sulfonic acid (ABTS) assays, revealing significant antioxidant potential. These Dc-AgNPs exhibit potential for use as antioxidant, antimicrobial and antiproliferative agents, making them valuable candidate for diverse therapeutic applications.

Keywords: Phytochemicals; Green synthesis; Nanoparticles; Silver; *Dryopteris cristata* L.; Antioxidant.

INTRODUCTION

In the field of nanotechnology, the synthesis of silver nanoparticles (AgNPs) has experienced a significant escalation, drawing considerable interest from both nanotechnologists and biologists. Silver, with an annual production of approximately 500 tons, stands as one of the most extensively commercialized nanomaterials, and future projections suggest further growth (Bruna *et al*., 2021). The methods for synthesizing silver nanoparticles are diverse, spanning both physical and chemical approaches. These include sol-gel processing, chemical reduction, laser-mediated synthesis, chemical vapor deposition, hydrothermal synthesis, reverse micelle methods, microwave and ultraviolet irradiation, and photochemical reduction (Rafique *et al*., 2017; Wang *et al*., 2005; Khaydarov *et al*., 2009). Biological synthesis, utilizing plant and microbial sources, has gained particular prominence due to its environmentally friendly nature, cost-effectiveness, and reduced reliance on toxic chemicals (Tarannum *et al*., 2019). Among these methods, plant-derived extracts have shown superior efficiency in reducing silver ions and stabilizing silver nanoparticles compared to microbial sources (Tarannum *et al*., 2019). Extensive research has investigated the synthesis of silver nanoparticles using various plant materials, including

https://doi.org/10.22232/stj.2024.12.02.01

leaves, flowers, seeds, bark, roots, and fruits. Notable examples include *Ocimum sanctum* (Ramteke *et al*., 2012), *Azadirachta indica* (Tripathy *et al*., 2010), *Murraya koenigii* (Sajeshkumar *et al*., 2015), *Carica papaya* (Banala *et al*., 2015), *Moringa oleifera* (Prasad *et al*., 2011), *Coffea arabica* (Dhand *et al*., 2016), *Tanacetum vulgare* (Dubey *et al*., 2010), *Punica granatum* (Shanmugavadivu *et al*., 2014), *Vitis vinifera* (Roy *et al*., 2014), *Berberis vulgaris* (Behravan *et al*., 2019), *Citrus recticulata* (Shanmugavadivu *et al*., 2017), and *Catharanthus roseus* (Mukunthan *et al*., 2011). These plant extracts serve as reductases, converting Ag^{+} ions into elemental silver (Ag°) nanoparticles. Beyond their recognized antibacterial properties, silver nanoparticles are also pivotal in environmental pollutant remediation (Hazarika *et al*., 2024; Behravan *et al*., 2019). Despite advancements in nanobiotechnology, the specific roles of various bioactive compounds in plant extracts in the synthesis of nanoparticles remain inadequately understood. Variability in nanoparticle yield among different plant species, even when using identical protocols, underscores the need for a detailed exploration of the underlying bioactive components. Establishing standardized procedures based on these findings is crucial for ensuring consistent large-scale production, addressing a significant challenge in the current domain of biosynthesized nanoparticles (Dhand *et al*., 2016; Shanmugavadivu *et al*., 2017).

Dryopteris cristata L., known as the crested wood fern, is a member of the Dryopteridaceae family and is indigenous to wetlands across the northern hemisphere (Zuo *et al*., 2022). Its name reflects the distinctive crested appearance of its fronds, which emerge from the central axis, contributing to its notable visual appeal. In Arunachal Pradesh, India, this species is referred to as "*Pukutphet*" within the *Tai-Khamti* community. Beyond its aesthetic qualities, *Dryopteris cristata* is recognized for its potential pharmacological properties, including anti-inflammatory, antimicrobial, antioxidant, and antitumor activities (Alam *et al*., 2021; Erhirhie *et al*., 2019). While qualitative phytochemical analyses and quantitative assessments have been extensively documented for other Dryopteris species, such as *Dryopteris ramosa* (Alam *et al*., 2021), *Dryopteris juxtapostia* (Rani *et al*., 2022), *Dryopteris cochleata* (Kathirvel *et al*., 2016), and *Dryopteris filix-mas* (Femi-Adepoju *et al*., 2021), there is a notable absence of studies focused on the phytochemical profile of *Dryopteris cristata*. This gap presents a novel research opportunity. The current study aims to develop a rapid, simple, and eco-friendly method for the synthesis of silver nanoparticles (AgNPs) using the leaf extract of *Dryopteris cristata*, which is abundant in polyphenols and flavonoids. This research will identify the role of these phytochemicals in the nanoparticle synthesis process and characterize the silver nanoparticles' morphological properties using different analytic techniques. Additionally, the antioxidant activity of the synthesized silver nanoparticles will be evaluated to assess their potential applications in the biomedical field.

MATERIALS AND METHODS

Materials and Reagents

The fresh leaves of *Dryopteris cristata* L. were collected from the botanical garden of the University campus. Analytical-grade reagents used in the study, including α,α-diphenyl-β-picrylhydrazyl (DPPH), 2,2′-azino-bis(3-ethylbenzothiazoline-6-sulfonic acid) (ABTS), L-ascorbic acid, Folin-Ciocalteu reagent, catechin, sodium bicarbonate, aluminum chloride, methanol, silver nitrate and deionized water, were purchased from HiMedia Laboratories and Sigma-Aldrich, India.

Preparation of the Plant Extract

Briefly, 10 g of air-dried *Dryopteris cristata* leaves were washed thoroughly with distilled water and finely ground using a mortar and pestle. The resulting leaf powder was then immersed in 100 mL of deionized water and boiled for approximately 15 min at 60°C. After boiling, the mixture was filtered through Whatman filter paper (No. 1) and centrifuged at 5000 rpm for 10 min. The supernatant was collected and stored at 4°C for future applications.

Phytochemical Screening

Phytochemical analysis was conducted to identify the presence of various phytoconstituents in the freshly prepared *Dryopteris cristata* leaf extract, including phenols, tannins, terpenoids, steroids, flavonoids, saponins, and alkaloids. This analysis was carried out using established methodologies as described by Sofowora (1993).

Determination of Phenolic Content

The phenolic content of the *Dryopteris cristata* leaf extract was quantified using the Folin-Ciocalteu (FC) assay, with modifications based on Singleton *et al*. (1999). In this method, 150 µL of the leaf extract was combined with 1.25 mL of a tenfold diluted FC reagent. After 5 min incubation, 1.25 mL of 6% (w/v) sodium bicarbonate was added to neutralize the reaction. The mixture was then incubated in the dark for 90 min. Absorbance was measured at 760 nm, and phenolic content was determined using a gallic acid equivalent standard curve, with results expressed as mg/mL of gallic acid equivalent (GAE).

Determination of Flavonoid Content

The flavonoid content of the *Dryopteris cristata* leaf extract was quantified using a colorimetric assay, adapted from Woisky and Salatino (1998) with modifications. Specifically, 1 and 1.5 µL/mL of the leaf extract were combined with 2 mL of ethanol containing 0.1 mL of 10% aluminum chloride and 2.5 mL of distilled water. After 20 min of incubation at room temperature, the absorbance of the reaction mixture was recorded at 415 nm. The total flavonoid content was determined using a catechin equivalent standard, and results were expressed as catechin equivalents (CAE).

Biosynthesis of Silver Nanoparticles

Silver nanoparticles (AgNPs) were synthesized from *Dryopteris cristata* leaf extract using the biological method (Mohanta *et al*., 2017). In this procedure, 10% (v/v) of leaf extract was added dropwise to 45 mL of 2 mM AgNO3 solution, maintaining a 5:1 ($AgNO_3$: extract) ratio and a pH of approximately 7.2. The mixture was stirred vigorously at room temperature until a notable color change from light brown to reddish brown occurred, indicating the reduction of Ag+→Ag°. The resulting colloidal solution was allowed to stand undisturbed for 24 h at room temperature to facilitate nucleation. Following this period, the solution was centrifuged at 5000 rpm for 20 min. The precipitate was then washed with an ethanol-water mixture (3:2) and dried at 60°C for 24 h to yield the desired Dc-AgNPs. Figure 1 depicts the synthetic pathway for Dc-AgNPs, where phytochemicals in the leaf extract play a crucial role in capping and stabilizing the nanoparticles.

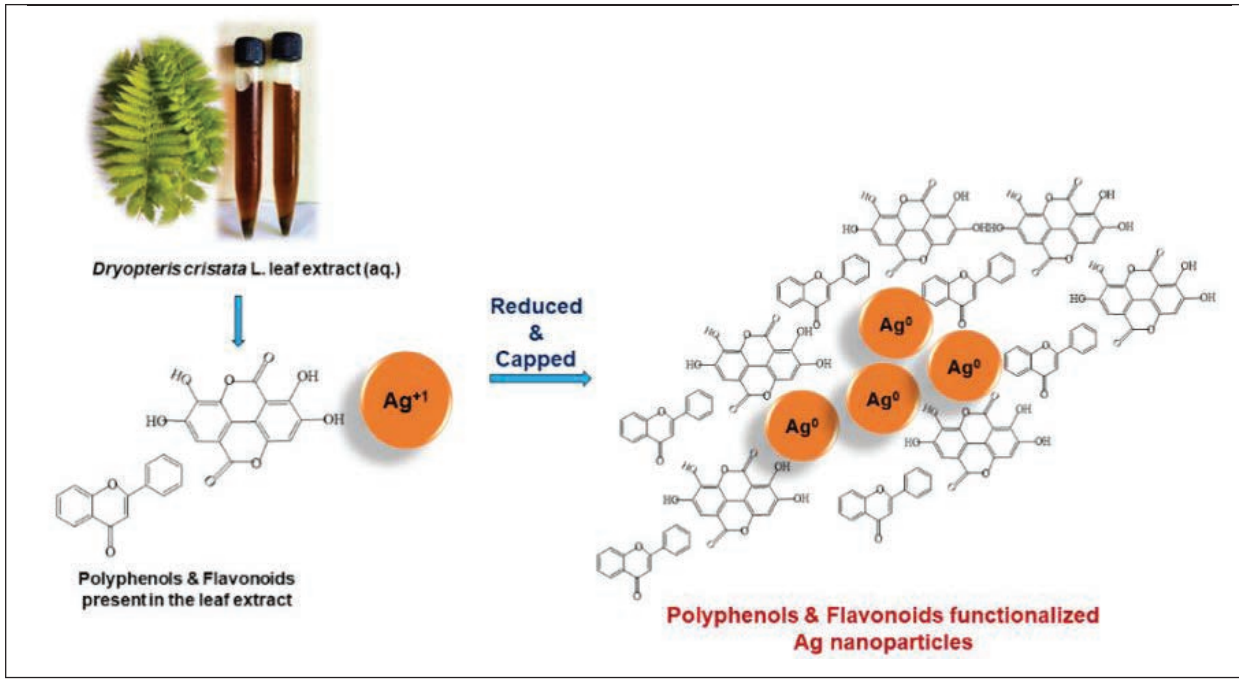

Fig. 1: Plausible Mechanism for the Formation of Dc-AgNPs by the Utilization of Dryopteris cristata L. Leaf Extract.

Antioxidant Activity

DPPH Free Radical Scavenging Assay

The antioxidant activity of the leaf extract was evaluated using the DPPH radical scavenging assay, following the protocol outlined by Sekar *et al*. (2020). Various concentrations of Dc-AgNPs, leaf extract, and ascorbic acid (30, 50, 70, 90 and 110 µg/mL) were mixed with 100 µL of 0.1 mM DPPH solution in 80% ethanol. The mixtures were incubated in darkness at room temperature for 30 min. The absorbance of the samples was measured at 517 nm using a LABTRONICS LT-291 spectrophotometer, with 80% ethanol as the blank. The percentage of DPPH radical scavenging activity was calculated using the formula:

$$DPPH\ radical\ scavenging\ ability\ (\%) = \frac{(Abs_{control} - Abs_{sample})}{Abs_{control}} \times 100$$

The IC_{50} values for the leaf extract and Dc-AgNPs were determined from the plotted graph using the equation $Y = mX + C$ and the linear regression coefficient.

ABTS Free Radical Scavenging Assay

The ABTS radical scavenging activity of various concentrations of the leaf extract and Dc-AgNPs was assessed using a standardized method (Sekar *et al*., 2020). A stock solution of ABTS was prepared by reacting 7 mM ABTS with 2.45 mM potassium persulfate, followed by incubation in darkness at room temperature for 16 h. The working solution was then prepared by diluting the stock solution with methanol to achieve an absorbance of approximately 0.80 ± 0.15 at 734 nm. For the assay, 20 µL of each concentration (30, 50, 70, 90 and 110 µg/mL) of the leaf extract and Dc-AgNPs were mixed with 100 µL of the ABTS working solution. The mixture was incubated for 30 min at room temperature. Absorbance was measured at 734 nm using a LABTRONICS LT-291 spectrophotometer, with ascorbic acid serving as the standard. The percentage of ABTS radical scavenging activity was calculated using the formula:

$$ABTS\ radical\ scavenging\ ability\ (\%) = \frac{(Abs_{control} - Abs_{sample})}{Abs_{control}} \times 100$$

RESULTS AND DISCUSSION

Phytochemical Screening

Table 1 illustrates a detailed phytochemical analysis of *Dryopteris cristata* leaf extract. The presence of various phytochemicals was confirmed through distinctive reactions, such as the development of specific colorations and precipitates. The analysis identified a diverse range of phytoconstituents in the leaf extract, including phenols, tannins, flavonoids, glycosides, steroids, terpenoids, and alkaloids. These findings highlight the complex phytochemical profile of the leaf extract.

Table 1: Phytochemical Constituents Present in *Dryopteris cristata* Leaf Extract (aq.).

Sl. No.	Phytochemical	Test performed	Observation	Inference
1	Saponins	Foam test	The emergence of a dense and persistent layer of frothy.	(+)
2	Quinones	Borntrager's test	There was no formation of red coloration upon the addition of KOH solution.	(-)
3	Terpenoids and Steroids	Salkowski test	Reddish-brown coloration is formed in the organic layer.	(+)
4	Phenols and Tannins	$FeCl_3$ test	Blue-black colored solution is formed.	(+)
5	Flavonoids	Alkaline reagent test	An intense yellow-colored solution is formed, which turns colorless upon the addition of few drops of dilute HCl.	(+)
6	Alkaloids	Wagner's test	Reddish-brown colored precipitate is formed.	(+)
(+) means presence and (-) means absence of the respective phytochemicals.				

Characterization of Dc-AgNPs

The synthesis of Dc-AgNPs was verified through UV-Vis. spectroscopy, with spectra recorded at specific intervals to monitor the progress of nanoparticle formation. Samples were withdrawn at 0 min, 5 min, 60 min, 12 h, and 24 h to track the kinetics of Dc-AgNPs synthesis. The UV-Vis. spectra exhibited a distinct bell-shaped peak, confirming nanoparticle formation, as depicted in Fig. 2(a). This peak is indicative of surface plasmon resonance (SPR), where the free electrons in the nanoparticles oscillate in response to incident light, resulting in an absorption band in the 390-420 nm range due to Mie scattering phenomena (Ouedraogo *et al*., 2022; Nayak *et al*., 2016). A broad absorption band within the 400-460 nm range was observed, characteristic of Mie scattering. Optimization of synthesis parameters was performed, including the concentration of the leaf extract, the ratio of precursor solution to leaf extract, and the concentration of the precursor solution. Fig. 2(b) illustrates the effect of varying volumes of *Dryopteris cristata* leaf extract mixed with a 2 mM precursor solution at a 1:5 ratio. Increased leaf extract volume led to a broader SPR peak and a shift in the absorption band, resulting in the selection of a 5:1 ratio of precursor solution to leaf extract as optimal. The effect of precursor concentration on Dc-AgNPs synthesis was examined, as shown in Fig. 2(c). Different concentrations of $AgNO_3$ (0.5 mM, 1 mM, and 2 mM) were evaluated while maintaining constant other parameters. Higher concentrations of $AgNO_3$ enhanced the intensity of the absorbance peak, indicating that increased precursor concentration facilitates the formation of smaller and more numerous nanoparticles. Thus, a 2 mM $AgNO_3$

solution was identified as optimal. Fig. 2(d) presents the influence of leaf extract concentration (v/v) on Dc-AgNPs synthesis. A 5% leaf extract concentration resulted in a broad SPR peak with lower intensity, while a 20% concentration produced no significant peak. Conversely, 10% leaf extract concentration yielded a prominent peak at approximately 425 nm, suggesting improved interaction between bioactive compounds and the precursor solution, leading to the formation of highly stable Dc-AgNPs. Consequently, 10% (v/v) leaf extract concentration was selected for further optimization.

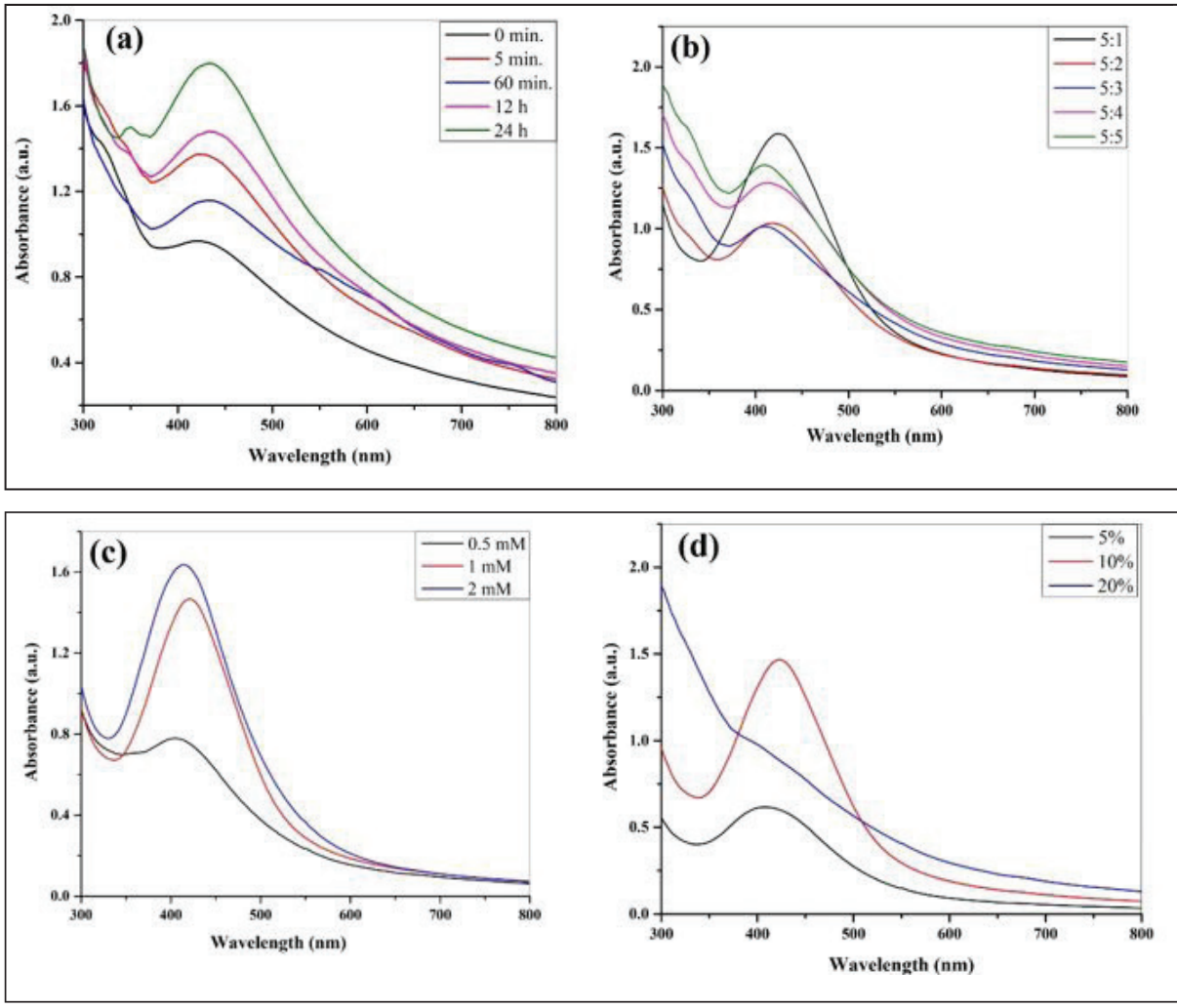

Fig. 2: UV-Vis. Analysis of Dc-AgNPs Colloidal Solution; (a) Absorbance Spectra at Different Time Intervals, (b) Effect of Leaf Extract Volumes, (c) Effect of Precursor Concentrations and (d) Effect of Leaf Extract Concentrations.

FT-IR spectroscopy was employed to characterize the secondary metabolites involved in the reduction and stabilization of Dc-AgNPs. The spectrum (Fig. 3) revealed prominent absorption bands/peaks at 3327 cm^{-1}, 1573 cm^{-1}, 1351 cm^{-1} and 1044 cm^{-1}, indicating the presence of phytoconstituents that function as capping agents. The board band at 3327 cm^{-1} corresponds to O–H stretching vibrations of phenolic compounds in the leaf extract. The peak at 1573 cm^{-1} is attributed to C-C stretching vibrations in alkenyl or aromatic rings. The peak at 1351 cm^{-1} represents O-H bending vibrations, while the peak at 1044 cm^{-1} is associated with C-O stretching in phenolic groups (Ramteke *et al*. 2012). These band/peaks are indicative of the phenolic groups in polyphenols and flavonoids present in the leaf extract, suggesting their involvement in the interaction with the biosynthesized nanoparticles.

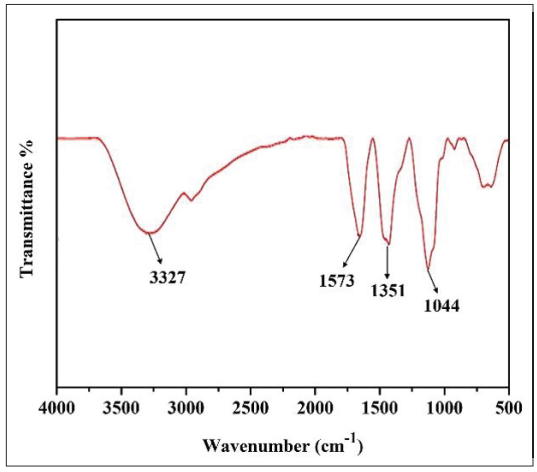

Fig. 3: FT-IR Spectrum of Dc-AgNPs.

Fig. 4 illustrates the XRD analysis of the biosynthesized Dc-AgNPs, and four distinct diffraction peaks are observed at 38.26°, 44.45°, 64.56°, and 77.48°, which correspond to the (1 1 1), (2 0 0), (2 2 0) and (3 1 1) planes, respectively, as indicated by JCPDS card No. 04-0783 (Syed *et al*., 2016). These peaks confirm the face-centered cubic (fcc) crystalline structure of the Dc-AgNPs. The observed XRD patterns are influenced by the nanoparticle size, which affects peak positions and intensities. The leaf extract's reducing agents contribute to the stabilization of Dc-AgNPs and support their crystalline formation, as extensively documented in biosynthesis studies (Meng, 2015). Using Scherrer's equation, the average crystallite size of the Dc-AgNPs was found to be 20.12 nm.

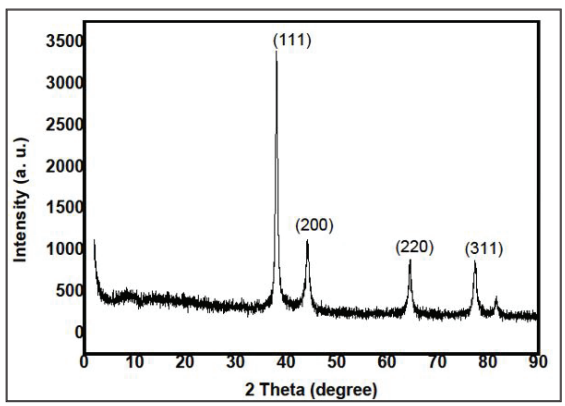

Fig. 4: XRD Pattern of Dc-AgNPs.

The morphology of Dc-AgNPs was characterized using SEM, which revealed that the nanoparticles exhibited polymorphic shapes, including irregularly granulated and ellipsoidal forms, and were highly aggregated (Fig. 5(a)). The ellipsoidal and aggregated morphology was further confirmed by the TEM image, as depicted in Fig. 5(c). The average length of the nanoparticles ranged from 20 to 45 nm (Fig. 5(a)), consistent with previous studies on silver nanoparticles synthesized from *Prosopis juliflora* (Raja et al., 2012), where the majority of nanoparticles had length between 30 and 37.5 nm, with only a small fraction exhibiting extreme values (Fig. 5(d)). Elemental analysis using EDX identified a prominent peak at 3 keV, confirming silver as the primary component (Fig. 5(b)). Additionally, the detection of carbon and oxygen peaks suggests the involvement of bioactive organic compounds from the leaf extract in the reduction and stabilization processes of Dc-AgNPs. The elemental composition of the nanoparticles was determined to be 78.35% silver, 18.91% carbon, and 2.74% oxygen.

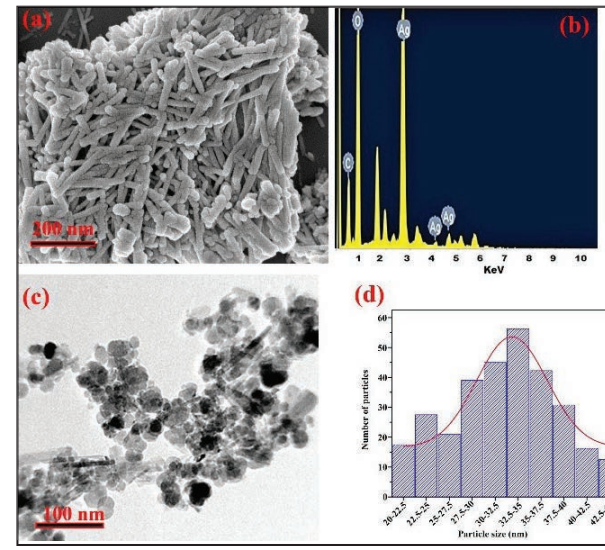

Fig. 5: Electron Micrograph Analysis of Dc-AgNPs; (a) SEM Image, (b) EDX Spectrum, (c) TEM Image and (d) Particle Size Distribution.

Estimation of Total Phenolic and Flavonoid Content in the Leaf Extract and Dc-AgNPs

The absorbance peak at 292 nm in the *Dryopteris cristata* leaf extract indicates the presence of polyphenols and flavonoids (Fig. 6(a)). Quantitative analysis revealed that the total phenolic content in the leaf extract was 46.21 ± 1.25 mg gallic acid equivalents (GAE) per 100 g, and the flavonoid content was 18.02 ± 0.13 mg catechin equivalents (CAE) per mL. In contrast, the colloidal solution of Dc-AgNPs contained 25.67 ± 2.13 mg GAE per 100 g and 10.04 ± 1.36 mg CAE per mL (Fig. 6(b)). These results indicate a higher concentration of phenolic and flavonoid compounds in the leaf extract compared to the Dc-AgNPs. The data suggest that the polyphenolic and flavonoid compounds in the

Dryopteris cristata leaf extract function as effective reducing agents, facilitating the conversion of Ag+ ions to Dc-AgNPs. This observation is consistent with findings from other plant extracts, including leaves, stems, fruits, barks, and roots, which have demonstrated potential in nanoparticle synthesis via Ag^{+} ion reduction. The leaf extract showed approximately twice the phenolic and flavonoid content compared to the resulting Dc-AgNPs. Given their known antioxidant properties, these bioactive compounds suggest that the *Dryopteris cristata* leaf extract has significant antioxidant activity. Consequently, Dc-AgNPs synthesized from *Dryopteris cristata* leaves could function as potent antioxidants with potential therapeutic applications, utilizing the leaf extract as a sustainable and cost-effective bio-reducing agent. Similar findings have been reported for *Erythrina suberosa* (Roxb.) (Mohanta *et al*., 2017) and *Tagetes erecta* L. (Nagaich *et al*., 2016), underscoring the versatility of plant-derived bio-reducing agents in nanoparticle synthesis for commercial applications.

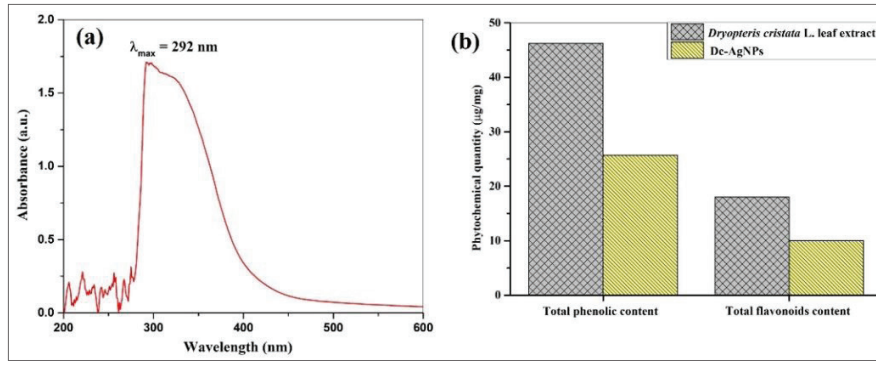

Fig. 6: Dryopteris Cristata L. aq. Leaf Extract, (a) Absorption Spectrum; (b) Total Phenolic and Flavonoid Content of the Leaf Extract and Dc-AgNPs Colloidal Stolution.

Antioxidant Activity using DPPH and ABTS Assay

The in vitro antioxidant activity of *Dryopteris cristata* leaf extract and Dc-AgNPs was evaluated using DPPH (Fig. 7(a)) and ABTS assays (Fig. 7(b)). The results demonstrated a dose-dependent increase in scavenging activity for both the leaf extract and Dc-AgNPs relative to ascorbic acid, the standard antioxidant. Notably, Dc-AgNPs exhibited superior radical scavenging efficacy, with IC50 values of 15.27 µg/mL for DPPH and 10.23 µg/mL for ABTS, compared to the leaf extract's IC50 values of 32.71 µg/mL and 22.35 µg/mL, respectively. These assays highlighted the Dc-AgNPs' ability to neutralize both neutral and cationic radicals, with the DPPH assay reflecting the nanoparticles' capacity to transfer electrons and neutralize DPPH radicals, while the ABTS assay indicated their ability to scavenge ABTS cationic radicals through both electron and hydrogen transfer mechanisms (Sekar *et al.*, 2020). These findings elucidate the multifaceted antioxidant mechanisms of Dc-AgNPs, demonstrating their effective role in neutralizing unstable radicals.

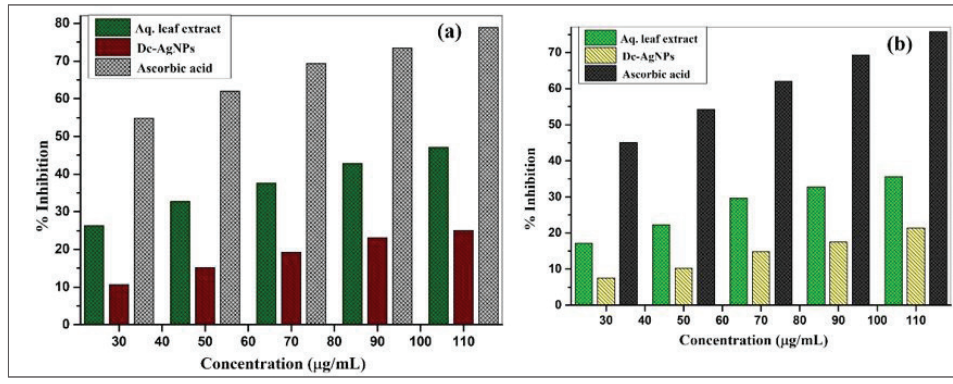

Fig. 7: Antioxidant Activity Study of Different Concentrations of Dryopteris Cristata L. aq. Leaf Extract and Dc-AgNPs; (a) DPPH Scavenging Assay and (b) ABTS Assay.

Table 2 illustrates the comparative analysis of various green synthesized AgNPs regarding their antioxidant properties, assessed through DPPH and ABTS scavenging assays. The IC50 values obtained from these assays are indicative of the antioxidant efficacy, with a lower IC50 value signifying stronger activity, as they represent a reduced concentration required to inhibit 50% of free radicals. The data shows that *Dryopteris cristata* leaf extract exhibits a lower IC_{50} value in both assays compared to *Cucumis prophetarum* (Table 2, Entry 2) and *Alnus nitida* (Table 2, Entry 1) leaf extracts, indicating its superior antioxidant potential. Similarly, Dc-AgNPs present a markedly lower IC50 value in both assays compared to other biosynthesized AgNPs (Table 2, Entries 1-5), demonstrating their enhanced antioxidant activity. This enhanced antioxidant capacity of Dc-AgNPs is attributed to the synergistic interaction between the *Dryopteris cristata* leaf extract and AgNPs, which collectively increase the efficacy of free radical neutralization. The leaf extract independently shows strong antioxidant activity, and its incorporation into AgNPs further amplifies this effect. In comparison, Bhutto *et al*. (2018) reported that AgNPs synthesized with polyphenolic compounds exhibited higher IC_{50} values, suggesting lower antioxidant activity relative to Dc-AgNPs. Similarly, Alves *et al*. (2018) observed that poly(3-aminophenyl) boronic acid-poly (vinyl alcohol) (PABA-PVA) mediated AgNPs also demonstrated higher IC_{50} values compared to Dc-AgNPs. Therefore, Dc-AgNPs exhibit significant synergistic antioxidant activity owing to the combined effect of the *Dryopteris cristata* leaf extract, underscoring their potential for use in therapeutic applications as effective antioxidants.

Table 2: Comparative Study of the Antioxidant Activity of Green Synthesized AgNPs.

Sl. No.	Sample	Method of preparation	IC_{50} value (µg/mL)	Ref.
1	*Alnus nitida* leaf extract (aq.)	Biological synthesis	37.35 (DPPH assay) 24.25 (ABTS assay)	Khuda *et al.*, 2023
	AgNPs		19.25 (DPPH assay) 16.46 (ABTS assay)	
2	*Cucumis prophetarum* leaf extract (aq.)	Biological synthesis	33.31 (DPPH assay) 50 (ABTS assay)	Hemlata *et al.*, 2020
	Cp-AgNPs		29.2 (DPPH assay) 34.5 (ABTS assay)	
3	*Reynoutria japonica* Houtt root extract (aq.)	Biological synthesis	27.80 (DPPH assay) 25.25 (ABTS assay)	Khuda *et al.*, 2022
	AgNPs		19.25 (DPPH assay) 18.88 (ABTS assay)	
4	AgNPs (*Alcaligenes faecalis* GH3 cell extract aq.)	Biological synthesis	710 (DPPH assay) 220 (ABTS assay)	Badoei-dalfard *et al.*, 2019
5	CA-AgNPs	Biological synthesis	55.66 (DPPH assay) 25.77 (ABTS assay)	Mendam *et al.*, 2023
6	*Dryopteris cristata* leaf extract (aq.)	Biological synthesis	32.71 (DPPH assay) 22.35 (ABTS assay)	Present work
	Dc-AgNPs		15.27 (DPPH assay) 10.23 (ABTS assay)	

CONCLUSION

In summary, the leaf extract of *Dryopteris cristata* was employed to synthesize Dc-AgNPs, with the extract's phytochemicals acting as both reducing and capping agents, thereby stabilizing the silver nanoparticles. FT-IR analysis further substantiated the involvement of these phytochemicals in the nanoparticle synthesis. The leaf extract is rich in polyphenols and flavonoids, which are indicative of its inherent antioxidant properties. Antioxidant assays, including DPPH and ABTS scavenging tests, demonstrated that the synthesized Dc-AgNPs exhibited

superior radical scavenging activity compared to the leaf extract, with efficacy increasing with higher concentrations. These results highlight the potential of Dc-AgNPs as effective free-radical scavengers and underscore their promise in developing potent antioxidants for addressing diseases associated with oxidative stress.

ACKNOWLEDGEMENTS

The authors are grateful to Arunachal University of Studies and the World Education Mission (WEM) for providing financial assistance in the form of Ph.D. scholarship to Biswajyoti Hazarika. Special thanks extended to CIF, IISER Kolkata, for instrumental facilities.

CONFLICTS OF INTEREST

The authors declare no conflict of interest.

REFERENCES

Alam F., Khan S.H.A., Asad M.H.H.B. (2021) Phytochemical, antimicrobial, antioxidant and enzyme inhibitory potential of medicinal plant *Dryopteris ramose* (Hope) C. Chr. *BMC Complement. Med. Ther.*, 21: 197.

Alves T.F., Chaud M.V., Grotto D., Jozala A.F., Pandit R., Rai M., Alves C. (2018) Association of silver nanoparticles and curcumin solid dispersion: antimicrobial and antioxidant properties. *Aaps Pharmscitech*., 19: 225-231.

Badoei-dalfard A., Shaban M., Karami Z. (2019) Characterization, antimicrobial, and antioxidant activities of silver nanoparticles synthesized by uricase from *Alcaligenes faecalis* GH3. *Biocatal. Agric. Biotechnol*., 20: 101257.

Banala R.R., Nagati V.B., Karnati P.R. (2015) Green synthesis and characterization of *Carica papaya* leaf extract coated silver nanoparticles through X-ray diffraction, electron microscopy and evaluation of bactericidal properties. *Saudi J. Biol. Sci*., 22: 637–644.

Behravan M., Panahi A.H., Naghizadeh A., Ziaee M., Mahdavi R., Mirzapour A. (2019) Facile green synthesis of AgNPs using *Berberis vulgaris* leaf and root aqueous extract and its antibacterial activity. *Int. J. Biol. Macromol*., 124: 148-154.

Bhutto A.A., Kalay Ş., Sherazi S.T.H., Culha M. (2018) Quantitative structure-activity relationship between antioxidant capacity of phenolic compounds and the plasmonic properties of silver nanoparticles. *Talanta*, 189:174-181.

Bruna T., Maldonado-Bravo F., Jara P., Caro N. (2021) Silver nanoparticles and their antibacterial applications. *Int. J. Mol. Sci*., 22:7202.

Dhand V., Soumya L., Bharadwaj S., Chakra S., Bhatt D., Sreedhar B. (2016) Green synthesis of AgNPs using *Coffea arabica* seed extract and its antibacterial activity. *Mater. Sci. Eng. C*., 58:36-43.

Dubey S.P., Lahtinen M., Sillanpää M. (2010) Tansy fruit mediated greener synthesis of silver and gold NPs. *Process Biochem*., 45:1065-1071.

Erhirhie E.O., Emeghebo C.N., IIodigwe E.E., Ajaghaku D.L., Umeokoli B.O., Eze P.M., Ngwoke K.G., Okoye F.B.G.C. (2019) *Dryopteris filix-mas* (L.) Schott ethanolic leaf extract and fractions exhibited profound anti-inflammatory activity. *Avicenna J. Phytomed*., 9: 396-409.

Femi-Adepoju A.G., Oluyori A.P., Fatoba P.O., Adepoju A.O. (2021) Phytochemical and antimicrobial analysis of *Dryopteris filix-mas* (L.) Schott. *Rasayan J. Chem*., 14: 616-621.

Hazarika B., Ahmed M.J.K. (2024) Green synthesis of Au-Ag@TiO2 nanocomposite for photocatalytic oxidation of substituted benzyl alcohols. *ChemistrySelect*., 9: e202400759.

Hemlata, Meena P.R., Singh A.P. Tejavath K.K. (2020) Biosynthesis of silver nanoparticles using *Cucumis prophetarum* aqueous leaf extract and their antibacterial and antiproliferative activity against cancer cell lines. *ACS Omega*, 5:5520-5528.

Kathirvel A., Sujatha V. (2016) Phytochemical studies, antioxidant activities and identification of active compounds using GC-MS of *Dryopteris cochleata* leaves. *Arabian J. Chem*., 9: S1435-S1442.

Khaydarov R.A., Khaydarov R.R., Gapurova O., Estrin Y., Scheper T. (2007) Electrochemical method for the synthesis of silver nanoparticles. *J. Nanopart. Res*., 11: 1193-1200.

Khuda F., Jamil M., Khalil A.A.K., Ullah R., Ullah N., Naureen F., Abbas M., Khan M.S., Ali S., Farooqi H.M.U., Ahn M.-J. (2022) Assessment of antioxidant and cytotoxic potential of silver nanoparticles synthesized from root extract of *Reynoutria japonica* Houtt. *Arab. J. Chem*., 15: 104327.

Khuda F., Gul M., Khalil A.A.K., Ali S., Ullah N., Khan M.S., Nazir S., Khan S.I., Büyüker S.M., Almawash S., Shafique M., Shah S.A. (2023) Biosynthesized silver nanoparticles using *Alnus nitida* leaf extract as a potential antioxidant and anticancer agent. *ACS Omega*, 8: 30221-30230.

Mendam K., Naik S.J.K. (2023) Anticancer and antioxidant activities Cyphostemma auriculatum green mediated silver nanoparticles. *Mater. Today Proc*., 92: 618-625.

Meng Y. (2015) A sustainable approach to fabricating Ag nanoparticles/PVA hybrid nanofiber and its catalytic activity. *Nanomaterials*., 5:1124-1135.

Mohanta Y.K., Panda S.K., Jaybalan R., Sharma N., Bastia A.K., Mohanta T.K. (2016) Antimicrobial, antioxidant and cytotoxic activity of silver nanoparticles synthesized by leaf extract of *Erythrina suberosa* (Roxb.) *Front. Mol. Biosci*., 4:14.

Mukunthan K.S., Elumalai E.K., Patel, T.N., Murty V.R. (2011) *Catharanthus roseus*: a natural source for the synthesis of silver nanoparticles. *Asian Pac. J. Trop. Biomed*., 1: 270-274.

Nagaich U., Gulati N., Chauhan S. (2016) Antioxidant and antibacterial potential of silver nanoparticles: Biogenic synthesis utilizing apple extract. *J. Pharm*., 7141523 Nayak D.,

Ashe S., Raute P.R., Kumari M., Nayak B. (2016) Bark extract mediated green synthesis of silver nanoparticles: Evaluation of antimicrobial activity and antiproliferative response against osteosarcoma. *Mater. Sci*. Eng., 58:44-52.

Ouedraogo T.L., Zongo S., Sougoti M., Kam S.Z., Bado F., Koulidiati J., Bere A. (2022) Green synthesis and characterization of silver nanoparticles using *Combretum micranthum* leaves extract as bio-reductor. *Asian J. Nanosci. Mater*., 5:174-184.

Prasad T.N.V.K.V., Elumalai E.K. (2011) Biofabrication of Ag nanoparticles using *Moringa oleifera* leaf extract and their antimicrobial activity. *Asian Pac. J. Trop. Biomed*., 1: 439-442.

Rafique M., Sadaf I., Rafique M.S., Tahir M.B. (2017) A review on green synthesis of AgNPs and their applications. *Artif. Cells, Nanomed. Biotechnol*., 45:1272-1291.

Raja K., Saravanakumar A., Vijayakumar R. (2012) Efficient synthesis of silver nanoparticles from *Prosopis juliflora* leaf extract and its antimicrobial activity using sewage. *Spectrochim*. *Acta A: Mol. Biomol. spectrosc*., 97:490-494.

Ramteke C., Chakrabarti T., Sarangi B.K., Pandey R. A. (2012) Synthesis of silver NPs from the aqueous extract of leaves of *Ocimum sanctum* for enhanced antibacterial activity. *J. Chem*., 2013: 278925.

Rani A., Uzair M., Ali S., Qamar M., Ahmad N., Abbas M.W., Esatbeyoglu T. (2022) *Dryopteris juxtapostia* root and shoot: Determination of phytochemicals; antioxidant, anti-inflammatory, and hepatoprotective effects; and toxicity assessment. *Antioxidants (Basel)*., 11: 1670.

Roy K., Biswas S., Banerjee P.C. (2014) Green synthesis of silver nanoparticles by using grape (*Vitis vinifera*) fruit extract: Characterization of the particles and study of antibacterial activity. *Res. J. Pharm. Biol. Chem. Sci*., 4: 1271.

Sekar R.K., Sridhar A., Perumalsamy B., Manikandan D.B., Ramasamy T. (2020) In vitro antipathogenicity and cytotoxicity effect of silver nanoparticles fabricated by onion (*Allium cepa* L.) peel extract. *BioNanoSci*.,10:235-248.

Sajeshkumar N.K., Vazhacharickal P.J., Mathew J.J., Sebastin A. (2015) Synthesis of silver NPs from curry leaf (*Murraya koenigii*) extract and its antibacterial activity. *CIBTech J. Pharm. Sci*., 4: 12-25.

Shanmugavadivu M., Kuppusamy S., Ranjithkumar R. (2014) Synthesis of pomegranate peel extract mediated silver nanoparticles and its antibacterial activity. *Am. J. Adv. Drug Delivery*., 2:174-182.

Shanmugavadivu M., Kuppusamy S. (2017) Green synthesis of AgNPs using *Citrus reticulata* fruit peel aqueous extract and their antibacterial activity. *Int. J. Adv. Res*., 5:700-708.

Singleton V.L., Orthofer R., Lamuela-Raventos R.M. (1999) Analysis of total phenols and other oxidation substrates and antioxidants by means of Folin-Ciocalteu reagent. *Methods Enzymol*., 299:152-178.

Sofowora A. (1993) *Phytochemical screening of medicinal plants and traditional medicine in Africa*. 2nd Ed., Spectrum Books Ltd., Nigeria.

Syed B., Nagendra Prasad M.N., Dhananjaya B.L., Mohan K.K., Yallappa S., Satish S. (2016) Synthesis of silver nanoparticles by endosymbiont *Pseudomonas fluorescens* CA 417 and their bactericidal activity. *Enzyme Microb. Technol*., 95:128-136.

Tarannum N., Divya, Gautam Y.K. (2019) Facile green synthesis and applications of silver nanoparticles: A state-of-the-art review. *RSC Adv*., 9:34926-34948.

Tripathy A., Raichur A.M., Chandrasekaran N., Prathna T.C., Mukherjee A. (2010) Process variables in biomimetic synthesis of silver nanoparticles by aqueous extract of *Azadirachta indica* (Neem) leaves. *J. Nanoparticle Res*.,12: 237-246.

Wang H., Qiao X., Chen J., Ding S. (2005) Preparation of AgNPs by chemical reduction method. *Colloids Surf*., A, 256:111-115.

Woisky R.G., Salantino A. (1998) Analysis of propolis: Some parameters and procedures for chemical quality control. *J. Apic. Res*., 37:99-105.

Zuo Z.-Y., Zhao T., Du X.-Y., Xiong Y., Lu J.-M., Li D.-Z. (2022) A revision of *Dryopteris* sect. *Diclisodon* (Dryopteridaceae) based on morphological and molecular evidence with description of a new species. *Plant Divers*., 44: 181-190.

Science and Technology Journal Vol. 12 Issue: 2 June 2024 ISSN: 2321-3388

Synthesis, Characterization, Photoluminescence and Photocatalytic Properties of Pr(III) Doped $CdMoO_4$ Phosphors

N. Mohondas Singh[1*], K. Lalchhandama[2], Fidelia Lalrindiki[3], and Brojendro Singh Shagolsem[4]
[1,2,3,4]Department of Chemistry, School of Physical Sciences,
Mizoram University, Aizawl-796004, India
*E-Mail: nmdas08@rediffmail.com
[*]Corresponding Author

Abstract—In this study, tetragonal-shaped $CdMoO_4:Pr^{3+}$ phosphors were produced using the co-precipitation approach at room temperature. The sample was characterised using various methods such as UV-visible spectroscopy, FT-IR, SEM, and XRD. XRD pattern revealed a tetragonal phase, and FT-IR spectroscopy indicated that the sample had adsorbed H_2O molecules. SEM studies showed the aggregation and development of irregular shapes in the prepared samples. Excitation spectra were obtained by setting the λ_{em} wavelength at 605 nm, which resulted in the detection of strong peaks at transitions of ($^3H_4 \rightarrow {}^3P_2$), ($^3H_4 \rightarrow {}^3P_1$), and ($^3H_4 \rightarrow {}^3P_0$) at 453 nm, 477 nm, and 495 nm respectively. Emission spectra were also obtained by exciting the Pr^{3+} ions at 468 nm, resulting in the detection of distinctive emission spectra at 561 nm and 654 nm at a transition of ($^3P_0 \rightarrow {}^3H_5$) and ($^3P_0 \rightarrow {}^3F_2$), with a degradation percentage of 95.063% successfully obtained. Using Tauc's plot, the band-gap energy was calculated, and the band-gap energy was found to be 4.415 eV, deemed suitable for photocatalytic activity. The decay curves were well-fitted using the bi-exponential equation for the prepared sample, obtaining an R^2 value of 0.977, indicating that the process follows first-order kinetics.

Keywords: $CdMoO_4$: Pr^{3+}, XRD, photocatalytic, Kinetic study, PL Spectroscopy, decay curve

INTRODUCTION

Rare earth-activated inorganic phosphors are becoming more and more common in lighting and display technologies, including cathode ray tubes, field emission displays, plasma display panels, and many other optical devices; research on these materials has increased significantly in recent years (Lin *et al.* 2014). These materials are made of a host lattice and an activator ion. The activator ion, a dopant rare earth ion, acts as an activator and emits radiation (Lin *et al*. 2016). On the other hand, the parity-forbidden f-f transitions of rare earth ions resulted in poor cross-sections and luminescence efficiency (Nedeljkovic *et al*. 2013). Therefore, it is necessary to include them in an appropriate host matrix to boost the luminescence intensity, stability, and colour purity, among other things.

Due to their outstanding thermal, chemical, hardness, and physical stability, metal molybdates with scheelite structures are considered decent hosts for luminescent materials. Due to its exceptional optical and chemical properties, the molybdate compounds $CdMoO_4$, isostructural to $CaMoO_4$, and $PbMoO_4$ are among the most intriguing. It formed a tetragonal crystal structure with a $C^{4h}{}_6$ space group and an orthorhombic unit cell as the body centre. This compound might be a promising option for a luminescent material because of its significant thermal and chemical stabilities and remarkable crystallographic anisotropy (Wang *et al.* 2013). The roughly tetrahedral symmetry of each Mo^{6+} in the tetragonal structure of $CdMoO_4$ is encircled by four equivalent oxygen sites, while

 https://doi.org/10.22232/stj.2024.12.02.02

each Cd^{2+} is coordinated to eight oxygen sites. It is well known that annealing temperature and doping ion concentrations significantly impact a phosphor's photoluminescence property. $CdMoO_4$ has been synthesised using various techniques, such as hydrothermal, reverse micelle, co-precipitation, and others. However, because it is so inexpensive, the high emission efficiency synthesis at room temperature is especially attractive. At room temperature, red luminescence $CdMoO_4:Eu^{3+}$ was synthesised by Wang and his workers (Chen *et al*. 2012).

Additionally, a report on the photoluminescence characteristics of the sonically synthesised $CdMoO_4:Ln^{3+}$ (Ln = Dy, Sm, Eu, Pr, Ho, and Er) (Gan *et al*. 2014). According to the author's expertise, no studies have been done on the impact of dopant ion concentration on the behaviour of photoluminescence of $CdMoO_4:Pr^{3+}$ and its photocatalytic activity. Therefore, the current work's main objective is to investigate the photoluminescence behaviour of $CdMoO_4$ that has been synthesised at room temperature and doped with various Pr^{3+} concentrations.

EXPERIMENTAL SECTION

Sample Preparation

$Cd(NO_3)_2{\cdot}4H_2O$(LOBACHEMIEPVT.LTD),$(NH_4)_6Mo_7O_{24}{\cdot}4H_2O$, (SDFCL), and $PrCl_3{\cdot}xH_2O$ (99.9%, Alfa-Aesar) were used in the co-precipitation method at room temperature to create the phosphors $CdMoO_4:Pr^{3+}$. Stoichiometric volumes of $Cd(NO_3)_2$ and $PrCl_3$ were dissolved in 25 millilitres of double-distilled water for this synthesis procedure. Then, drop by drop, with constant magnetic stirring, the separately produced $(NH_4)_6Mo_7O_{24}{\cdot}4H_2O$ solution was added to the aforementioned solution. Five hours of magnetic stirring were spent on the combined solution. The mixture was then refrigerated without being shaken or stirred for five days. Centrifugation was used to separate the white precipitates, which were then cleaned five times using double distilled water and acetone. The precipitates were dried for 24 hours at 70°C in an oven (Singh *et al*. 2018).

Characterization of the Sample

The UV-visible absorbance spectrum and degradation studies of the sample were obtained using the UV-visible spectrophotometer EVOLUTION 220. To determine their absorption band, the prepared sample was sent to FT-IR Spectroscopy (SHIMADZU CORP - 00703). Utilising powder X-ray diffraction (XRD - BRUNKER AXS, D8 FOCUS-Powder) investigation, the phase and chemical composition of the $CdMoO_4:Pr^{3+}$ phosphor were ascertained. The photoluminescence property of the sample was evaluated using the Fluorescence Spectrophotometer (F-7000). The morphology and particle size of the samples were analysed using SEM (JOEL-JSM-6390LV).

RESULTS AND DISCUSSION

XRD Study

The $CdMoO_4$ tetragonal structure, as reported by JCPDS no. 07-0209, has cell characteristics of a = b = 5.155, c = 11.194, and V = 297.473 is shown by XRD analyses in Fig.1. The tetragonal phase of $CdMoO_4$ may be properly indexed, to every one of the observed diffraction peaks. We increase the reactant concentration, $[Cd^{2+}]=[MoO_4^{2-}]$ = 0.02 M to $[Cd^{2+}] = [MoO_4^{2-}]$ = 0.14 M, throughout this time to track the impact of reactant concentration on size and morphology. The highest intensity of the 2θ Degree of 29.217 corresponds to the (112) body centred of the tetragonal system of $CdMoO_4$, while the lowest intensity, having (332) planes lies at 2θ of 80.918. Fig. 1 demonstrates that the majority of the as-obtained products are large-scale microspheres, suggesting that a high yield may be achieved under the chosen reaction conditions. We observed that the product can maintain its spherical form with a change in reactant concentration. By careful inspection, it can be seen that the reactant concentration significantly influences the monodispersity and homogeneity of $CdMoO_4$ microspheres. Fine morphology is not favoured by reactant concentrations that are either too high or too low. To synthesise, it is crucial to select an ideal situation ($[Cd^{2+}] = [MoO_4^{2-}]$ = 0.10 M). $CdMoO_4$ has a limited size distribution, perfect spherical form, and less aggregating (Singh *et al*. 2018).

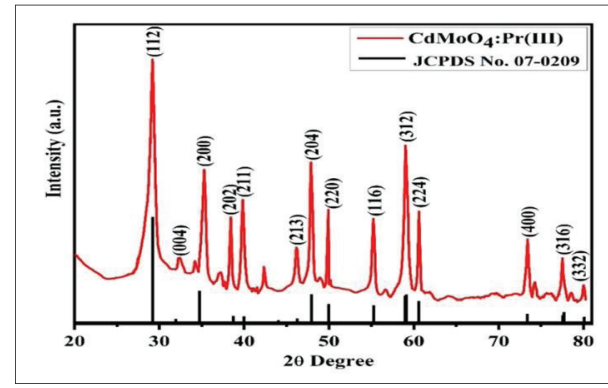

Fig. 1: XRD Patterns of $CdMoO_4:Pr^{3+}$.

FT-IR and SEM Study

The $CdMoO_4$ sample was subjected to FT-IR spectroscopy, as shown in Fig. 2. There are observations of the bands at 455.20, 540.07, 817.82, 833.25, 1491, and 2487cm^{-1}. Mo-O and Cd-O bending vibration has been implicated due to the absorption band at 455.20 and 540.07 cm^{-1}. O-Mo-O lengths of the MoO_4 tetrahedron are associated with a prominent absorption band at 817.82 and 833.25 cm^{-1}. This suggests that the as-prepared particles have formed the crystalline $CdMoO_4$ phase. The absorption band identifies the CO_2 on the sample's surface with a centre at 2487 cm^{-1}. The water-bending vibration of O-H deposited on the samples' surface is responsible for the absorption band at 1491 cm^{-1}. Since the samples were created in aqueous solutions, absorbed water molecules will inevitability end up on the surface of the particles (Wang *et al*. 2013).

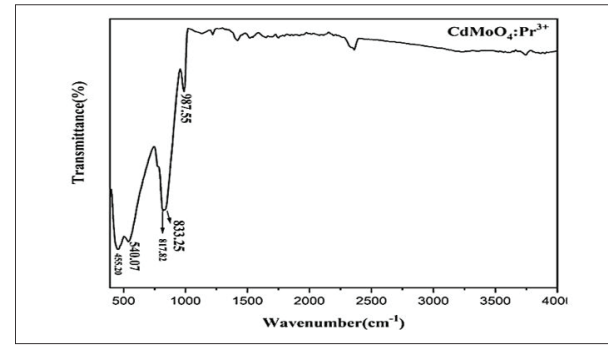

Fig. 2: FT-IR Spectra of $CdMoO_4:Pr^{3+}$.

Small particles are made up of several irregular nanoparticles (NPs), according to a high-magnification SEM image. We discovered that the sources of Mo and Cd are essential for developing the microsphere structures. The average particle size was calculated and found to be 70.5 nm (Varela *et al.* 2011).

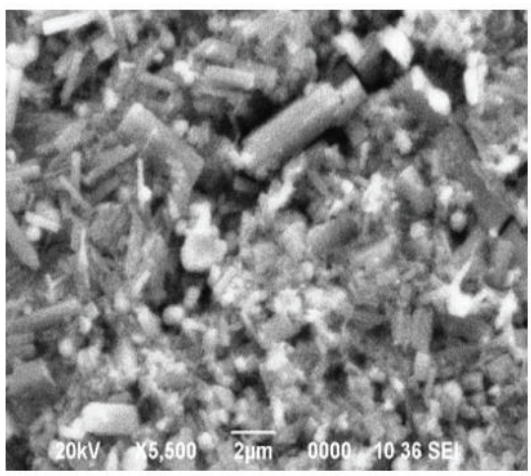

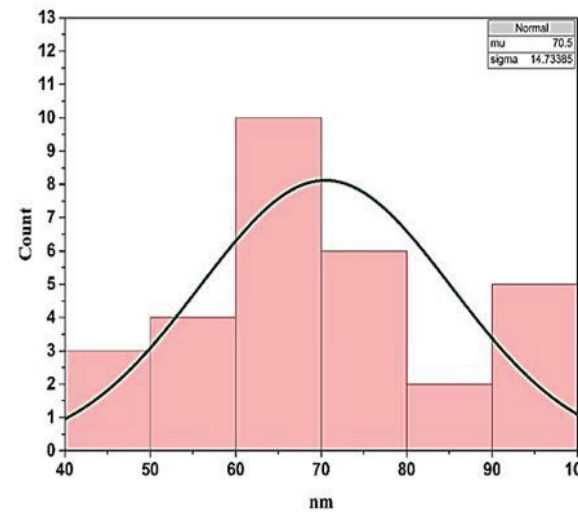

Fig. 3: SEM Image of $CdMoO_4:Pr^{3+}$ an Average Particle Size (70.5 nm).

Optical Property Study

The sample absorption peak was speculated to be around 209.860 nm, within a wavelength range of 190 to 280 nm, due to O-Mo charge transfer transitions (CTT) of MoO_4^{2-} groups. The spectral profile was steep, indicating that the band-gap transition rather than the transition from the impurity level was responsible for the absorption (Wang *et al*. 2014). The band-gap was determined for $CdMoO_4:Pr^{3+}$ using Tauc's plot, and the semiconductor's band-gap energy may be derived by using the following equation:

$$\alpha h\nu = A(h\nu - Eg)^n$$

The energy intercept plot of $(\alpha h\nu)^2(eVcm^{-1})^2$ versus energy is plotted which yields the E_g for a direct transition. By this method, the band gap energy for the $CdWO_4:Pr^{3+}$ sample is found to be 4.415 eV (Wang *et al*. 2014).

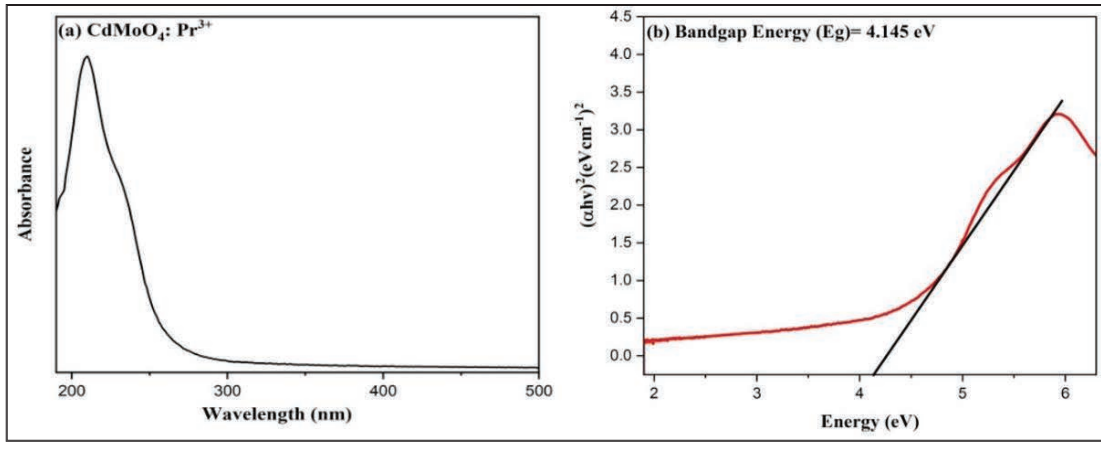

Fig. 4: (a) UV Spectra of $CdMoO_4:Pr^{3+}$; (b) Bandgap Energy Value of $CdMoO_4:Pr^{3+}$.

PL Study

At room temperature, the $CdMoO_4:Pr^{3+}$ phosphor's excitation and emission spectra are displayed in Figures 5a and 5b. The excitation spectra measured at 605 nm have a broadband that can be identified, with a maximum of 322 nm. This band originates from the charge transfer bands (CTB) between the molybdate core atom and oxygen ligands inside MoO_4^{2-} groups. Some of the sharp lines, as shown in Fig. 5a, have long wavelengths: 453 nm ($^3H_4 \rightarrow {}^3P_2$), 477 nm ($^3H_4 \rightarrow {}^3P_1$), and 495 nm ($^3H_4 \rightarrow {}^3P_0$), respectively. These lines are located between 400 and 500 nm in wavelength [33]. Zhang and colleagues have shown that excitation into the MoO_4^{2-} group at 322 nm produces the characteristic emission spectra of the Pr^{3+} ions at 561 nm ($^3P_0 \rightarrow {}^3H_5$) and 654 nm ($^3P_0 \rightarrow {}^3F_2$) (Sun *et al.* 2011).

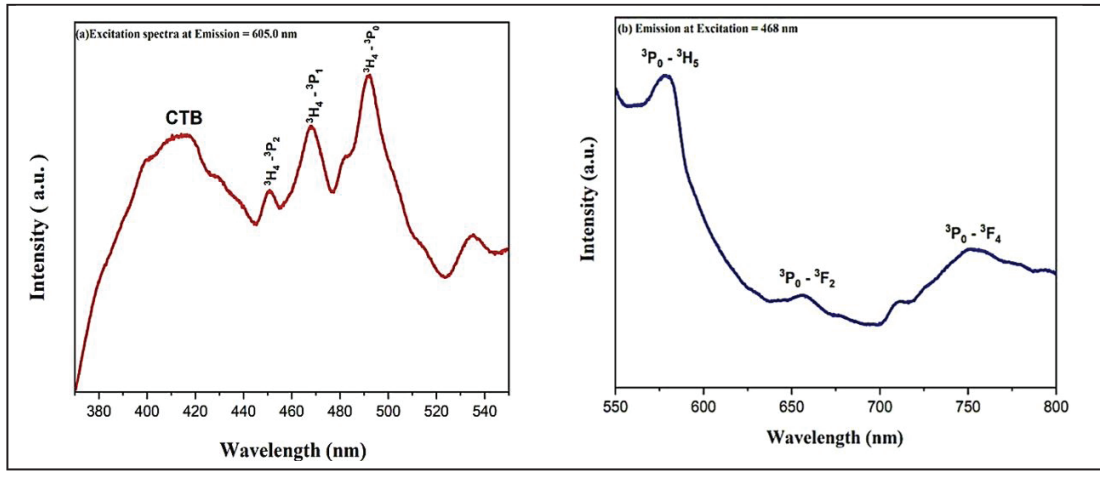

Fig. 5: (a) PL Spectra of Pr^{3+} Doped $CdMoO_4$ λ_{em}=605 nm; (b) PL Spectra of Pr^{3+} Doped $CdMoO_4$ λ_{ex}=468 nm.

CIE Analysis

For photoluminescence applications, a phosphor's CIE colour coordinates are crucial. Based on the emission spectra data seen when stimulated at 335 nm, Fig. 6 displays the CIE chromaticity diagram for samples of $CdMoO_4:Pr^{3+}$(5 at. %) that have been synthesised and stored at room temperature. The predicted colour coordinates (x, y) for the $CdMoO_4:Pr^{3+}$(5 at. %) samples as produced and at room temperature are determined to be (0.255, 0.212), respectively. From this plot, it can be seen that all samples are displayed in the bluish-purple colour area, and the inset

in this image depicts the emission colour seen upon UV light excitation at 468 nm (Nongmaithem *et al*. 2014).

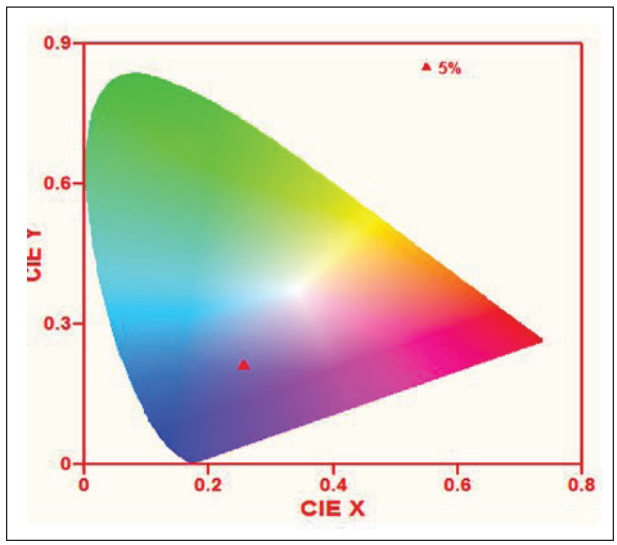

Fig. 6: CIE Chromaticity Diagram for as Prepared Sample of $CdMoO_4:Pr^{3+}$(5 at. %).

Lifetime Study

At room temperature, the produced samples of $CdMoO_4:Pr^{3+}$(5 at. %) measured with the excitation fixed at 468 nm exhibit decay curves depicted in Fig. 7, displaying the typical bi-exponential fitting for the same sample. The samples' fit (R^2) qualities for the concentrations was 0.97773 respectively, and the estimated average lifetimes is 5.08835, respectively. The bi-exponential equation can be used to fit all decay curves effectively:

$$I = I_1 \exp(-t/T_1) + I_2 \exp(-t/T_2)$$

where I_1 and I_2 stand for intensities at time '0' and 't,' and 1 and 2 are the times at which they would decay, respectively. An activator's bi-exponential decay pattern suggests the existence of Pr^{3+} in two separate sites and is frequently linked to the transmission of excitation energy from the donor. A particle with a spherical form has two sites: an inner core and a surface site. Because the impurities and surface flaws on the sample's surface may serve as pathways for non-radiative relaxation, the Pr^{3+} at surface sites should have a shorter projected lifetime. In contrast, the Pr^{3+} at inner core sites should have a longer predicted lifetime (Singh *et al*. 2020). Using the formula shown below, one can determine the average lifetime:

$$\tau_{ave} = I_1 T^2_1 + I_2 T^2_2 / I_1 T_1 + I_2 T_2$$

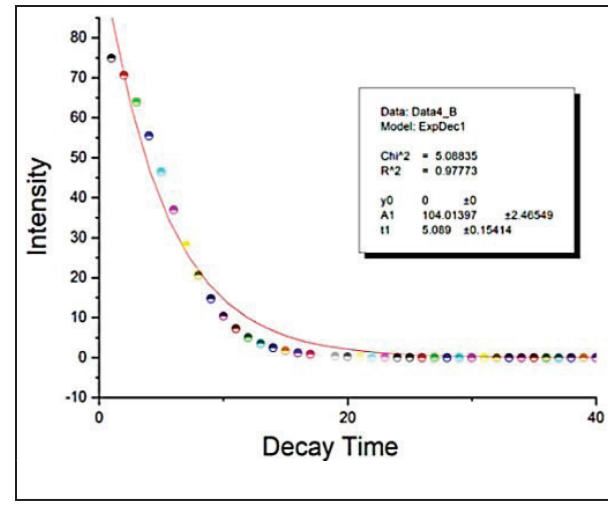

Fig. 7: Photoluminescence Decay Curve of $CdMoO_4:Pr^{3+}$.

PHOTOCATALYTIC STUDY

Methyl Red was used as the target pollutant to evaluate the photocatalytic activity of the produced materials under 50-watt LED Philips Stellar irradiation. Under 50-watt LED Philips Stellar irradiation, Fig. 8 illustrates the degradation efficiency of methyl red using $CdMoO_4$ photocatalysts produced in distilled water, respectively. Without the catalyst, photo-induced dye self-degradation was essentially non-existent. However, when the catalyst was present, a notable deterioration was seen (Singh *et al*. 2020). This finding suggests that $CdMoO_4$ may work well as a visible light active photocatalyst to degrade methyl red dye. After 150 minutes of exposure to a 50-watt LED Philips Stellar, the $CdMoO_4$ photocatalyst that was prepared was able to degrade 95.063% of the Methyl Red dye, while the $CdMoO_4$ photocatalyst that was prepared with water only degraded 73.244% of the dye in 60 minutes. Because of their short band-gap energy, $CdMoO_4$ photocatalysts are readily photoexcited by 50-watt LED Philips Stellar irradiation. When exposed to sunlight, an electron in the valence band is stimulated to the conduction band, creating an electron-hole pair and a hole in the valence band. O_2 was adsorbed from water molecules by the electron in the conduction band of the $CdMoO_4$ photocatalyst, creating $O^{2-\cdot}$. Conversely, the valence band hole forms $OH\cdot$ through interactions with adsorbed water molecules. Methyl Red dye breaks down into carbon dioxide and water under the influence of $O^{2-\cdot}$ and $OH^{\cdot}$. This discovery concludes that the catalyst's photocatalytic activity is significantly influenced by the solvents utilised in the synthesis.

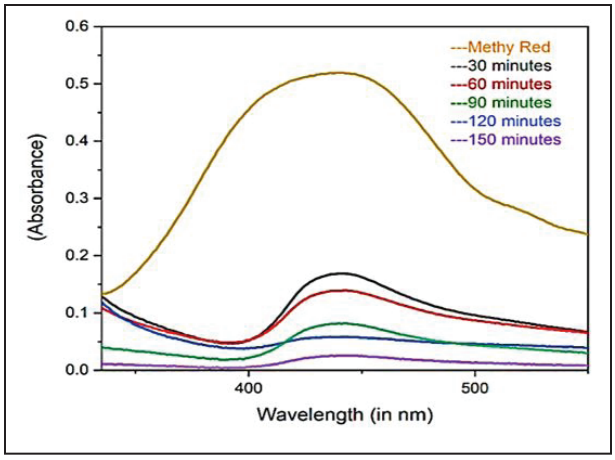

Fig. 8: Degradation of $CdMoO_4:Pr^{3+}$.

KINETIC STUDY

The kinetics of Methyl Red degradation under 50-watt Philips Stellar LED illumination was addressed. The graphs between ln [C_t] vs time (Fig. 9) was plot using the equation:

$$\ln(C_o/C_t)=k_t$$

showed first-order kinetics having an R^2 value of 0.977, where C_t stand for Methyl Red's initial and time-at-time concentrations, respectively (Singh *et al*. 2020).

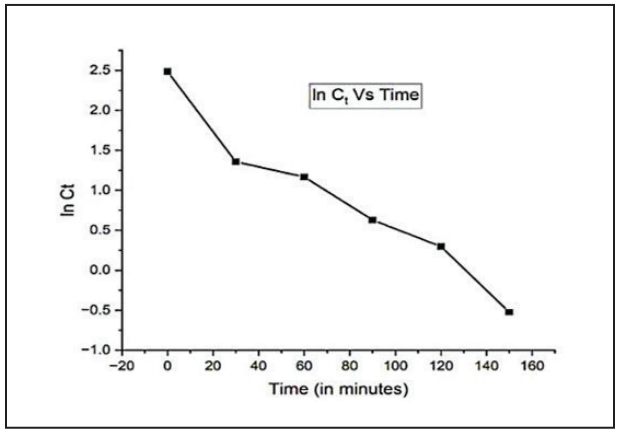

Fig. 9: Kinetic Rate of Degradation of Methyl Red Using Prepared $CdMoO_4:Pr^{3+}$.

CONCLUSION

$CdMoO_4:Pr^{3+}$, the host of the rare-earth-doped luminous nanoparticle we obtained, was successfully doped. Cell parameters (JCPDS no. 07-0209) are a = b = 5.155, c = 11.194, and V = 297.473; our as-prepared sample is a tetragonal structure of $CdMoO_4$ with a bluish-purple hue in the CIE diagram, as is evident from the data acquired from the absorption spectra, the Fourier transform infrared area, the XRD diagram, and luminescence spectroscopy. The image of the sample is also examined with the scanning electron microscope (SEM), where we can see its morphology, but it is not well portrayed due to agglomeration.

For photocatalytic degradation, methyl red was added to the synthesis of $CdMoO_4:Pr^{3+}$ and was degraded under Philip LED light at 30, 60, 90, 120 and 150 min intervals of time. The degradation decreases with increases in time, and the photocatalytic efficiency of $CdWO_4$ was calculated using the formula: Degradation efficiency% = $[C_0\text{-}C_t]/C_0 \times 100$ and obtained about 95.063%, a remarkably high efficiency. The bi-exponential equation can be used to fit the decay curves with good accuracy for our prepared sample obtaining a R^2 value of 0.977, indicating that the process will follow first-order kinetics.

ACKNOWLEDGEMENT

The authors express their gratitude to the Department of Chemistry, School of Physical Sciences, DST-Funding, Mizoram University, Aizawl, Mizoram, for providing the advanced instrumentation equipment necessary to meet our requirements.

REFERENCES

Gai S., Li C., Yang P., & Lin J. (2014). Recent Progress in Rare Earth Micro/Nanocrystals: Soft Chemical Synthesis, Luminescent Properties, and Biomedical Applications. *Chemical Reviews,* 114(4), 2343–2389. https://doi.org/10.1021/cr4001594

Wang D., Fan J., Shang M., Li K., Zhang Y., Lian H., & Lin J. (2016). Pechini-type sol-gel synthesis and multicolour-tunable emission properties of $GdY(MoO_4)_3:RE^{3+}$ (RE=Eu, Dy, Sm, Tb) phosphors. *Optical Materials, 51*, 162–170. https://doi.org/10.1016/j.optmat.2015.11.029

Vranješ M., Kuljanin-Jakovljević J., Ahrenkiel S. P., Zeković I., Mitrić M., Šaponjić Z., & Nedeljković J. M. (2013). Sm^{3+} doped TiO_2 nanoparticles synthesized from nanotubular precursors—Luminescent and structural properties. *Journal of Luminescence, 143*, 453–458. https://doi.org/10.1016/j.jlumin.2013.05.022

Lin J., Zeng Z., & Wang Q. (2013). $CdMoO_4:Eu^{3+}$ micro-sized luminescent particle synthesis and photocatalytic performance. *Inorganica Chimica Acta, 408*, 59–63. https://doi.org/10.1016/j.ica.2013.08.023

Wang W. S., Zhen L., Xu C. Y., Shao W. Z., & Chen Z. L. (2012). Eu^{3+}-doped $CdMoO_4$ red phosphor synthesized through an aqueous solution route at room temperature. *Journal of Alloys and Compounds*, *529*, 17–20. https://doi.org/10.1016/j.jallcom.2012.03.058

Zhang J., Zhang N., Zou L., & Gan S. (2014). Formation mechanism and optical properties of $CdMoO_4$ and $CdMoO_4:Ln^{3+}$ (Ln = Pr, Sm, Eu, Dy, Ho and Er) microspheres synthesized via a facile sonochemical route. *RSC Advances*, *4*(72), 38455–38465. https://doi.org/10.1039/C4RA05038J

Singh N. P., Singh N. R., & Singh N. M. (2018). Synthesis of $CdMoO_4:Sm^{3+}$ phosphors at room temperature and investigation of photoluminescence properties. *Optik*, *156*, 365–373. https://doi.org/10.1016/j.ijleo.2017.11.045

Longo V. M., Cavalcante L. S., Paris E. C., Sczancoski J. C., Pizani P. S., Li M. S., Andrés J., Longo E., & Varela J. A. (2011). Hierarchical Assembly of $CaMoO_4$ Nano-Octahedrons and Their Photoluminescence Properties. The *Journal of Physical Chemistry C*, *115*(13), 5207–5219. https://doi.org/10.1021/jp1082328

Liu X., Lv L., Huang S., Su Y., & Wang X. (2014). Microwave-assisted synthesis and luminescence properties of $Cd(1-x)Eu(x)MoO_4$ red phosphor. *Journal of Nanoscience and Nanotechnology*, *14*(5), 3618–3622. https://doi.org/10.1166/jnn.2014.7992

Yang X., Zhou Y., Yu X., Demir H. V., & Sun X. W. (2011). Bifunctional highly fluorescent hollow porous microspheres made of $BaMoO_4:Pr^{3+}$ nanocrystals via a template-free synthesis. *Journal of Materials Chemistry*, *21*(25), 9009–9013. https://doi.org/10.1039/C1JM10458F

Sharma K., Singh D. T., & Nongmaithem R. (2014). Low-temperature synthesis, characterization and tunable optical properties of Eu^{3+}, Tb^{3+} doped $CaMoO_4$ nanoparticles. *Journal of Alloys and Compounds*, *602*, 275–280. https://doi.org/10.1016/j.jallcom.2014.02.186

Singh N. P., Singh N. R., Devi Y. R., Singh Sh B., Singh Th. D., Singh N. R., & Singh N. M. (2020). Effects of annealing temperature on structural and luminescence properties of $CdMoO_4:Dy^{3+}$ phosphor synthesized at room temperature by co-precipitation method. *Solid State Sciences, 102*, 106172. https://doi.org/10.1016/j.solidstatesciences.2020.106172

Naorem R. S., Singh N. P., & Singh N. M. (2020). Photoluminescence studies of Ce^{3+} ion-doped $BiPO_4$ phosphor and its photocatalytic activity. *International Journal of Applied Ceramic Technology*, *17*(6), 2744–2751. https://doi.org/10.1111/ijac.13600

Singh N. M., Naorem R. S., Lalthlamuanpuii H., Lalhmingmawia, & Borgohain, D. (2020). Kinetic study for the interaction of Nd(III) with creatine in different organic solvents using 4f-4f transition spectra as a probe. *Journal of the Indian Chemical Society*, *97*(11b), 2385–2390.

Science and Technology Journal Vol. 12 Issue: 2 June 2024 ISSN: 2321-3388

Pure CoS and Different Concentrations of Fe/Nd Co-Doped CoS Nanoparticles: Photoluminescence and Photocatalytic Studies

N. Mohondas Singh[1*], Daphilabianghun Nonglang[2], Fidelia Lalrindiki[3], and Lallianmawii[4]
[1,2,3,4]Department of Chemistry, School of Physical Sciences, Mizoram University, Aizawl-796004, India
*E-Mail: nmdas08@rediffmail.com
*Corresponding Author

Abstract—This research utilized the co-precipitation method to produce pure CoS, and Fe/Nd co-doped CoS nanoparticle with different concentrations at room temperature. The samples were characterized using UV-visible spectroscopy, FT-IR, SEM, and XRD. XRD pattern showed a cubic structure, and the Debye-Scherrer technique revealed an average particle size of 8 nm and 13 nm for 3 at.% and 5 at.% of Fe/Nd co-doped CoS. FT-IR spectroscopy identified the functional groups present and chemical bonding and the adsorption of H_2O molecules in the samples. In the prepared samples, SEM investigations revealed aggregation and the emergence of irregular forms. The excitation spectra set at 300-500 nm range with λ_{em} of 300 nm detected two broad peaks at 350 and 400 nm and a sharp peak at 470 nm. On the other hand, the emission spectrum recorded in the 400-650 nm range with λ_{ex} of 400 nm showed broad emission peaks at 420 nm, 450 nm, and 480 nm. Tauc's plot revealed that the optical bad-gap of pure and co-doped CoS nanoparticles ranged from 3.19 eV to 3.81 eV, suitable for photocatalytic activity. The testing revealed that the photocatalytic degradation of methyl red dye proved to be significantly more efficient in alkaline mediums, demonstrating clear pH dependence. Furthermore, the kinetic study for the degradation of the samples yielded R^2 values of 0.976, 0.996, and 0.991, indicating that the process followed first-order kinetics.

Keywords: Cobalt Sulphide, co-doped, XRD, photocatalytic, photoluminescence, Kinetic study.

INTRODUCTION

The method of photochemical conversion and solar energy storage using photocatalytic technology is efficient (Xu *et al.* 2020). Investigating new photocatalyst materials and their reaction processes has been emphasised over the past 20 years (Rehman *et al*., 2020). Numerous papers have studied a variety of photocatalysts, including metal-free (Mullins *et al*. 2020), metal oxides (Julkapli *et al.* 2020), metal sulphides (Wang *et al.* 2021), metal phosphides (Zhan *et al.* 2018), and metal selenides (Niasari *et al.* 2021) closely. Nevertheless, most single-component photocatalysts have demonstrated unexceptional photocatalytic performance because of the photogenerated charge carrier's quick recombination, insufficient active site, and restricted spectrum absorption.

Due to low availability, abundant resources, strong stability, and catalytic solid action, transition metal cocatalysts have recently attracted much attention in photocatalysis. Due to its ample catalytic sites, noble-metal-free cobalt sulphide (Co_xS_y) has received the most attention for replacing the noble metal cocatalyst (Jin *et al.* 2021). The CoS/Ag_2WO_4 photocatalyst was created using a simple chemical precipitation approach reported by Kokilavani *et al.*, and the composites exhibit outstanding photocatalytic degradation

 https://doi.org/10.22232/stj.2024.12.02.03

and antibacterial activity (Khan *et al.* 2021). Cobalt sulphides with various phase forms and morphologies were produced using various methods, including hydrothermal/ solvothermal synthesis, spray pyrolysis, thermal breakdown, high-temperature solid phase processes, and cobalt oxide sulfuration. The preparation method significantly impacts the powder's characteristics, including particle dimensions, form, surface area, degree of crystallinity, and crystal structure, significantly impacting the material's catalytic performance.

However, the chemical co-precipitation method was employed in this work as it is a suitable approach for manufacturing large quantities of target material at a reasonable cost in light of large-scale production. The photocatalytic activity of the prepared sample was evaluated successfully in this research using an organic dye of methyl red. The co-doped and doped samples have several effects on the pure sample of CoS, which has been reported using the photoluminescence activity in this work

EXPERIMENTAL SECTION

Sample Preparation

For a pure CoS, a stoichiometric amount of $CoCl_2.6H_2O$ (1 mol) and NaS (1 mol) was taken, and solutions were made using distilled water separately. NaS solution was added to the cobalt solution drop by drop until the black precipitate appeared. It was stirred in for 1 hour, then heat was given at 70°C and kept overnight. For various atomic percentages (at.%) of dopants Fe and Nd, different percentage amounts of $FeCl_3$ and $NdCl_3$ were added to the Cobalt solution, following the same procedure. The $FeCl_3$ and $NdCl_3$ solutions were prepared with specific concentrations to achieve the desired doping levels. The precipitate was then dried in a hot air oven for 12 hours at 70°C to dry it. It was then washed four times with distilled water and finally with acetone.

Characterization of the Sample

The UV-visible absorbance spectrum and degradation studies of the sample were obtained using the UV-visible spectrophotometer EVOLUTION 220. The prepared sample was sent to FT-IR Spectroscopy (SHIMADZU CORP - 00703) to determine its absorption band. Utilising powder X-ray diffraction (XRD-BRUNKER AXS, D8 FOCUS-Powder) investigation, the phase and chemical composition of the CoS doped Fe and Nd nanoparticles were ascertained. The photoluminescence property of the sample was evaluated using the Fluorescence Spectrophotometer (F-7000). The morphology and particle size of the samples were analysed using SEM (JOEL-JSM-6390LV).

RESULTS AND DISCUSSION

XRD Study

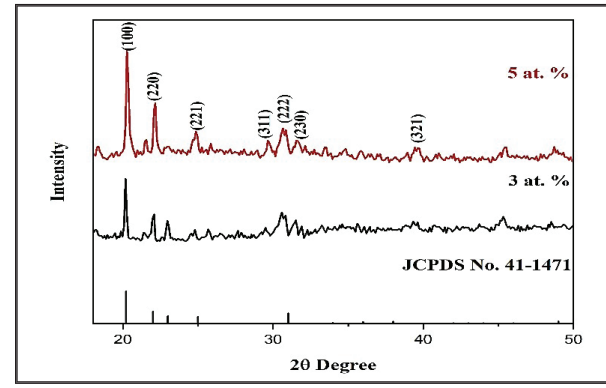

Fig. 1: Powder XRD Pattern for Fe/Nd Co-doped CoS Nanoparticles with JCPDS 41-1471 as Standard for CoS.

The X-ray diffraction (XRD) pattern of the CoS nanoparticles co-doped with 5 and 3 at.% of Fe and Nd is shown in Fig. 1. The observed peaks in the spectra show a cubic structure according to JCPDS card no. 41-1471 (Gao *et al.* 2017). The indexed diffraction peaks are assigned to (100), (220), (221), (311), (222), (230) and (321). The peaks do not show a noticeable shift after increasing Fe/Nd doping concentration, and no new phases are connected to Fe or Nd. This implies that both components have been successfully doped into the CoS structure. The average crystalline size is 3 at.% and 5 at.% Fe/Nd co-doped CoS nanoparticles were calculated using the Debye-Scherrer relation (Aghamaliyev *et al.* 2018).

$$D = 0.9\lambda / \beta \cos\theta$$

where β is the full width at half maximum (FWHM) of the peaks at diffracting angle θ, D is the crystallite diameter, and λ is the X-ray photon wavelength. The average particle size calculated is found to be 8 and 13 nm.

FTIR and Sem Study

The FTIR spectra of pure CoS and (1, 3, 5, 7, 9 and 11 at.%) Fe/Nd co-doped CoS are shown in Fig. 2. As seen in the figure, pure and doped CoS samples show similar absorption peaks at 3307, 1628, 1419, 1081, 769 and 598 cm^{-1}. The broad absorption peak at about 3307 cm^{-1} corresponds to the O-H stretching, and 1628 cm^{-1} corresponds to the O-H bending vibrations of H_2O.

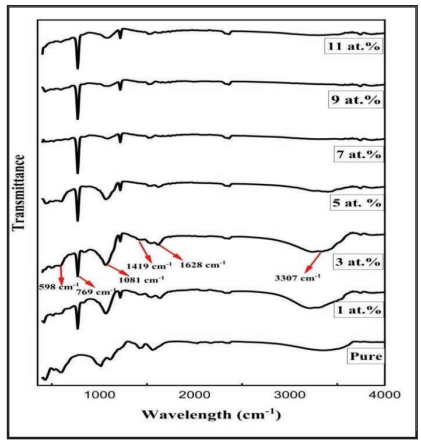

Fig. 2: FTIR Spectrum of Pure CoS and (1, 3, 5, 7, 9 and 11 at.%) Fe/Nd Co-doped CoS Nanoparticle.

The weak peak at 1419 cm^{-1} and 1081 cm^{-1} is assigned to the C-O-H deformation vibration and C-O stretching or bending vibration of sulfonated groups. In addition, the intense peak located at 769 cm^{-1} is a typical peak for the polysulfide bond group and the stretching vibration modes of Co-S. Finally, the absorption peak at 598 cm^{-1} is assigned to the stretching vibration between Co and S (Hosseinpour *et al*. 2018). As a consequence, as shown by the data above, no other phases associated with dopants were found, demonstrating the incredible purity of the samples.

Scanning Elelctron Microscopy (SEM)

Fig. 3a and b are the SEM images of the synthesized (3 and 5 at.%) Fe/Nd co-doped CoS. Small particles of various sizes in agglomerated forms were observed in both the images. The electron micrograph (Fig. 3c & d) is used to determine the average particle size, which is found to be 73.16 nm for 3 at.% and 50.18 nm for 5 at.% Fe/Nd co-doped CoS nanoparticles.

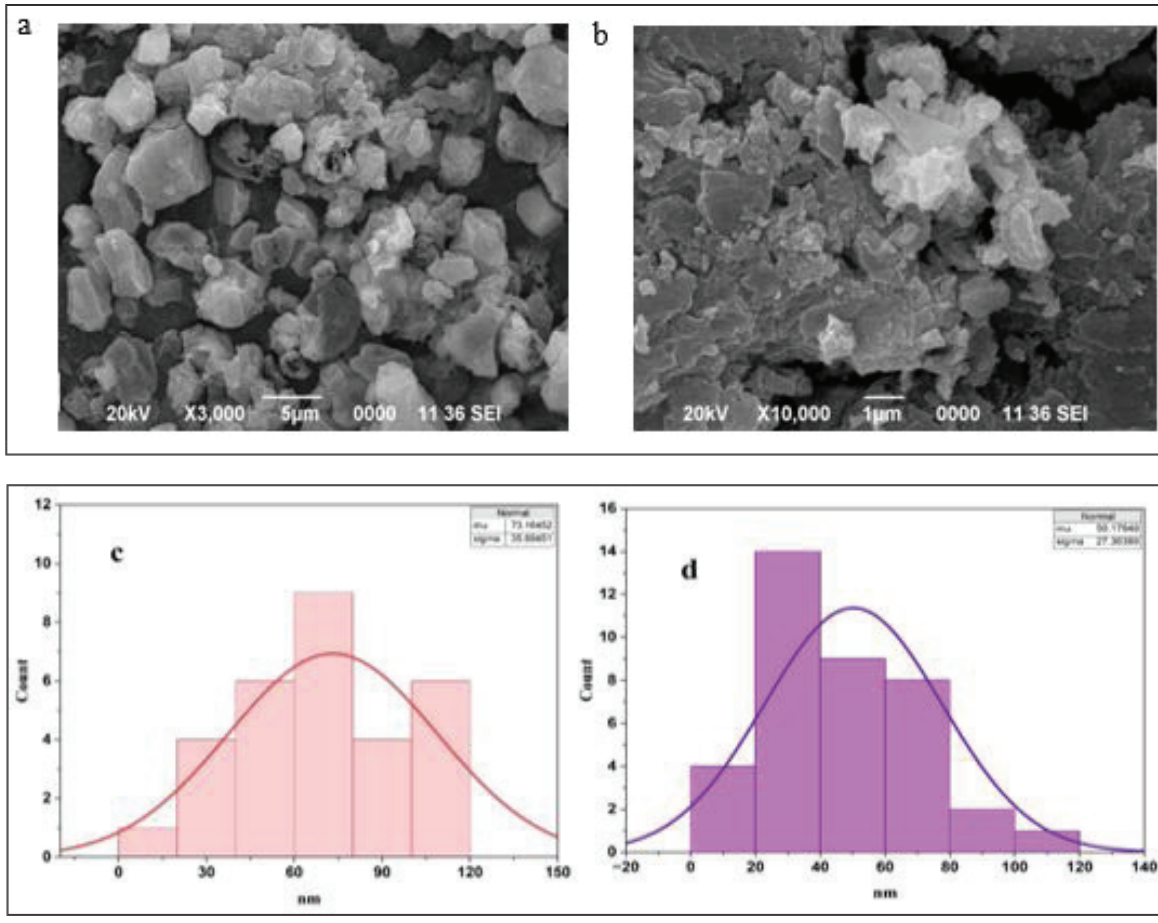

Fig. 3: (a, b) SEM Images and (c, d) Size Distribution Graphs for Average Size of (3 and 5 at.%) Fe/Nd Co-doped CoS Nanoparticles.

Photoluminescence Study

The photoluminescence studies of pure and (1, 3, 5, 7, 9 and 11 at.%) Fe/Nd co-doped CoS nanoparticles were studied for electron emission and excitation at room temperature. The excitation spectrum is observed in the 300-500 nm range at an emission wavelength of 300 nm. It displays two broad peaks in Fig. 4(a) at 350 nm and 400 nm and a strong peak at 470 nm, which agrees with the literature (Hosseinpour *et al.* 2018). The blue and violet emission peaks at 400 and 470 nm may be due to Co vacancy and S interstitial-related defects.

In Fig. 4(b), the emission spectrum is configured in the 400-650 nm range with a λ_{ex} of 400 nm. Prominent violet emission peaks at 420 nm and 450 nm are consistently observed across all the samples, accompanied by a faint blue emission peak at 480 nm.

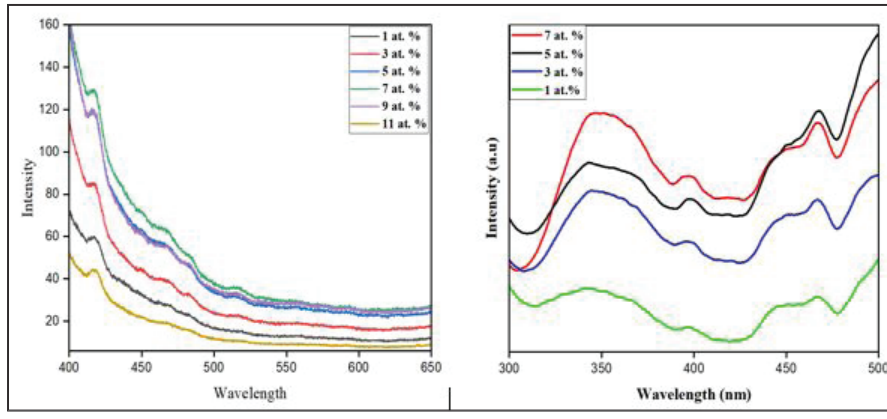

Fig. 4: (a) Photoluminescence of Pure and Different Percentages of (1, 3, 5, 7, 9 and 11 at.%) Fe/Nd Co-doped CoS Nanoparticles Using an Emission Wavelength of 300 nm and (b) Photoluminescence of Pure and Different Percentages of (1, 3, 5 and 7 at.%) Fe/Nd Co-doped CoS Nanoparticles using an Excitation Wavelength of 400nm.

CIE Analysis

Fig. 5 illustrates the CIE chromaticity diagram for the samples in their prepared state for pure and (3 and 5 at.%) Fe/Nd co-doped CoS calculated using the emission spectrum data observed when stimulated at 470 nm. For the samples that were created, the determined colour coordinates (x, y) are (0.236, 0.389), (0.236, 0.322), and (0.313, 0.204), respectively. This graphic shows the bluish-green region in all of the samples, and the inset shows the colour of the emission observed following UV light excitation at 470 nm (Singh *et al*. 2022).

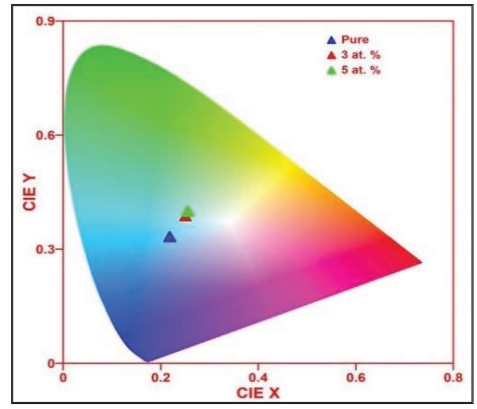

Fig. 5: CIE Chromaticity Diagram for as Prepared Pure CoS, 3 at.% Fe/Nd Co-doped CoS and 5 at.% Fe/Nd Co-doped CoS Nanaoparticles.

Lifetime Study

The decay curves were measured with the excitation fixed at 470 nm for each concentration. The curves of the measured deterioration are shown in Fig. 6. All reported decay curves fit well with the biexponential equation. The samples' fit (R^2) qualities for the concentrations above are 0.9152, 0.9573, and 0.9636, respectively, and their estimated average lifetimes are 1.21, 1.36, and 1.73 ms, respectively (Singh *et al*. 2018).

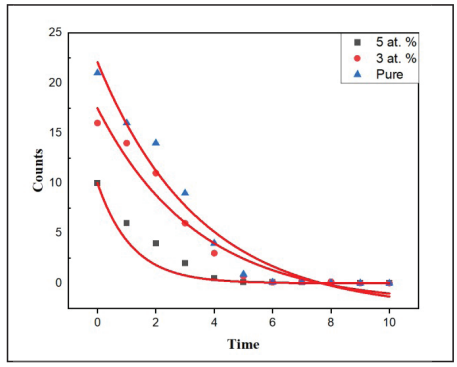

Fig. 6: Decay Curves for as Prepared Pure CoS, 3 at.%, 5 at. % Fe/Nd Co-doped CoS Samples.

Optical Properties Analysis

The optical properties after Fe and Nd have been successfully incorporated into CoS (1, 3, 5, 7, 9 and 11 at.%) were investigated using a UV-visible spectrometer as shown in Fig. 7 and were observed in the wavelength range of 200-400nm. According to the literature, the absorption peak for CoS was speculated to be around 210 nm (Sundararajan *et al*. 2021). Fig. 7a shows slight differences in the absorption spectra of pure and Fe/Nd co-doped CoS. These arise due to impurity centres, band gaps, surface roughness and oxygen deficiency. The band gap of CoS pure (3, 5, 7, 9 and 11 at.%) Fe/Nd co-doped CoS nanoparticles, as seen in Fig. 7b, were found to be 3.40eV, 3.50eV, 3.65eV, 3.50eV, 3.81eV and 3.19eV as per the Tauc's plot (energy vs $(\alpha h\nu)^2$. The equation is expressed as

$$(\alpha h\nu)^2 = K(h\nu - Eg)$$

where ν, α, h, Eg and K are the frequency, absorption coefficient, plank constant, band gap and proportionality constant, respectively (Singh *et al*. 2022).

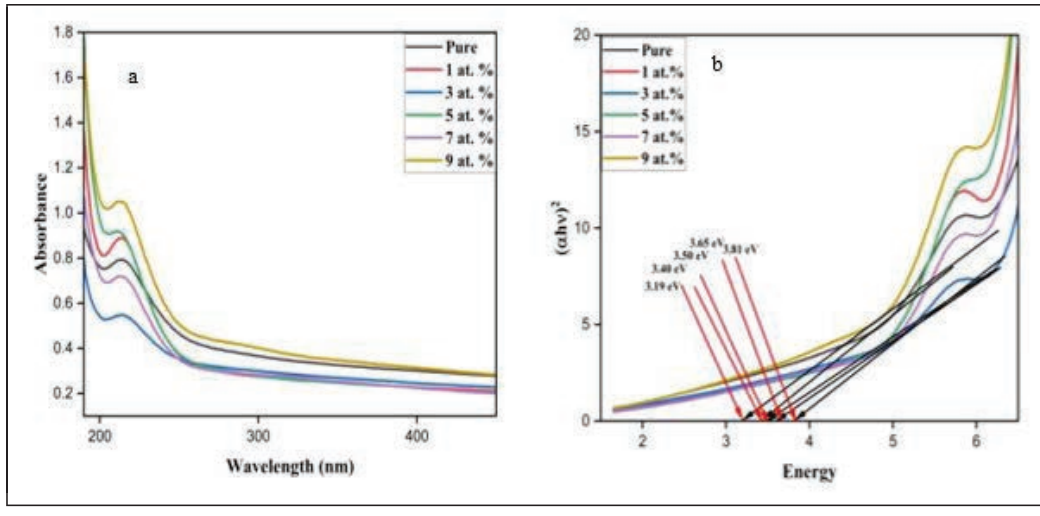

Fig. 7: UV-Visible Spectrum of (a) Pure CoS and Fe/Nd Co-doped CoS at Various Concentrations (b) Tauc Plot for Fe/Nd Co-doped CoS for the Calculation of Band Gap Energy.

Photocatalytic Activity

The degradation of dye methyl red under uv-irradiation every 30, 60, 90, 120, 150, and 180 minutes and in the presence of 7 at.% Fe/Nd co-doped CoS nanoparticles as photocatalyst is shown in Fig. 8a. This research, a novel exploration in the field, unveils the maximum absorption intensity of the dye methyl red at 436 nm, serving as a crucial reference point for studying the degradation abilities of the photocatalyst. The absorption intensity of the dye decreases as the exposure duration increases from 0-180 mins (Singh *et al*. 2020). From the degradation

spectra, we observe a rapid decline in the absorption peak when the catalyst was added to the targeted dye. The enhanced photocatalytic activity of the doping structures, attributed to the ease of electron-hole separation, surface defects, and significant light absorption, is a significant and exciting finding in the field (Cui *et al.* 2015). The doping concentration of 7 at.% might be the optimal value for achieving the best photocatalytic performance. Higher or lower doping concentrations may lead to decreased photocatalytic activity due to changes in the material's electronic structure, defects, or surface properties. Fe and Nd co-doping can introduce electron-hole pairs, enhancing photocatalytic activity. The 7 at.% concentration might balance electron-hole generation & recombination, maximizing the photocatalyst's efficiency.

Furthermore, we study the impact of pH on the degradation percentage of methyl red dye by the above photocatalyst at pH values of 7, 8, 9, and 10. As shown in Fig. 8b, the degradation efficiency is 50%, 60%, 80%, and 70% at pH 7, 8, 9, and 10, respectively. The maximum degradation efficiency is at pH 9 and again decreases at pH 10. The prepared Fe/Nd co-doped CoS under visible light irradiation is photoexcited, leading to the successful degradation of methyl red dye.

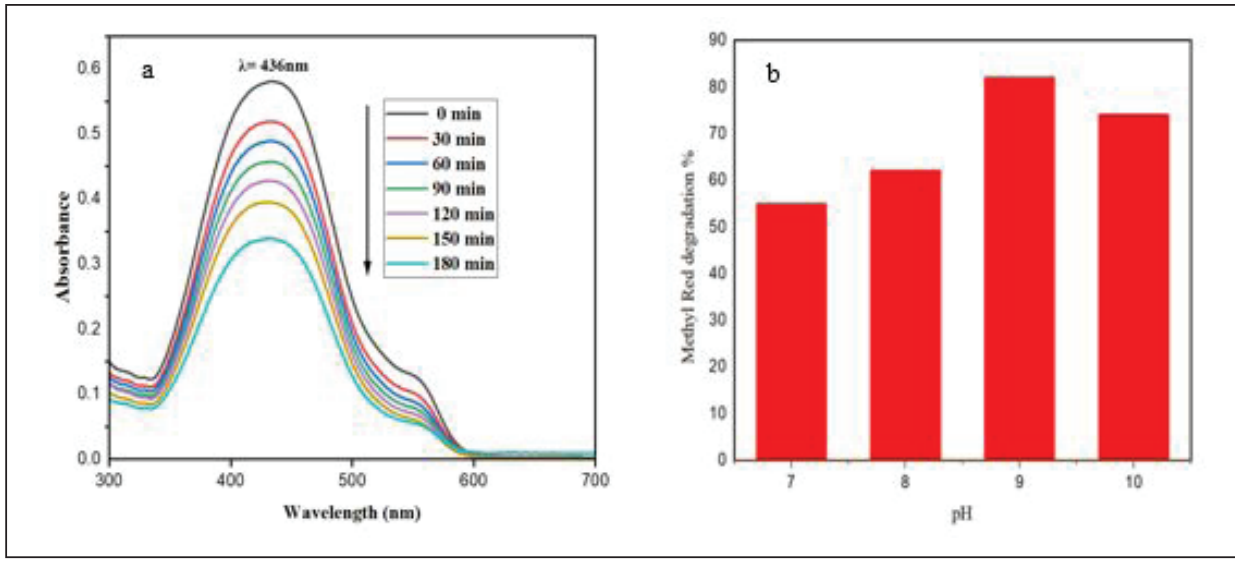

Fig. 8: (a) Time-dependent UV-Vis Absorption Spectra for MR Dye in the Presence of Fe/Nd Co-doped CoS 7 at.%. (b) Degradation Percentage of Methyl Red Dye.

Kinetic Study For Degradation

In general, first-order processes are obeyed by photodegradation of dyes if the plots of $\ln(C_0/C)$ vs time are simple lines (Modrek *et al.* 2013). The pseudo-first-order kinetic of methyl red degradation provided the following description of the photo-catalytic kinetic:

$$v = -dC/dt = -kC \text{ (or } C = C_o e\text{-}k_t) \quad (1)$$

where t is the reaction time, k is the rate constant, C_o is the initial concentration of MR, v is the reaction rate, and C is the MR dye concentration at a specific reaction time. Equation (2) can be used to express the model once equation (1) has been integrated.

$$\ln (C_o/C) = k_t \quad (2)$$

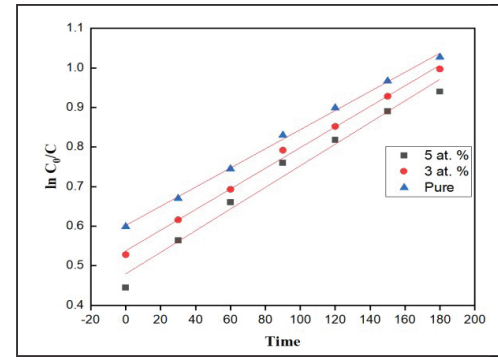

Fig. 9: Plot of Linear Transform ln [C_o/C] vs Irradiation Time in Minutes of the Kinetic Curve of Degradation of Methyl Red Using CoS as Photocatalyst.

A plot of ln (C_o\C) with time will yield a linear plot with slope k (Hein *et al*. 2107). Methylene red dye is discovered to degrade at an observed rate constant of 0.00512 min^{-1} in the presence of a catalyst, and the R^2 values were found to be 0.976, 0.996, and 0.991, respectively.

CONCLUSION

The chemical co-precipitation method was used to synthesize pure and Fe/Nd co-doped CoS nanoparticles, exhibiting a cubic structure in XRD analysis. The functional groups of the pure and doped CoS nanoparticles were visible in their FTIR spectra. Photoluminescence investigations showed an excitation spectrum range of 300-500 nm with strong peaks at 350 and 400 nm and a peak at 470 nm. The emission spectrum ranged from 400-650 nm with 420, 450, and 480 nm peaks. The UV-visible spectrum and the optical band gap of pure and Fe/Nd co-doped CoS nanoparticles from Tauc's plot were found to be in the range of 3.19eV to 3.81eV. Furthermore, the Fe/Nd co-doped CoS catalyst demonstrated higher efficiency in the photodegradation of methyl red dye than the pure sample, making it a promising option for removing organic dye contaminants from wastewater.

ACKNOWLEDGEMENT

The authors express their gratitude to the Department of Chemistry, School of Physical Sciences, DST-Funding, Mizoram University, Aizawl, Mizoram, for providing the cutting-edge instrumentation necessary to meet our specific requirements.

REFERENCES

Li, Y.H.; Tang, Z.R.; Xu, Y.J. Multifunctional graphene-based composite photocatalysts oriented by multifaced roles of graphene in photocatalysis. Chin. J. Catal. 2022;43:708–730.

Jamshaid, M.; Khan, H.M.; Nazir, M.A.; Wattoo, M.A.; Shahzad, K.; Malik, M.; Rehman, A.-U. A novel bentonite–cobalt doped bismuth ferrite nanoparticles with boosted visible light induced photodegradation of methyl orange: Synthesis, characterization and analysis of physiochemical changes. Int. J. Environ. Anal. Chem. 2022.

Rahman, M.Z.; Kibria, M.G.; Mullins, C.B. Metal-free photocatalysts for hydrogen evolution. Chem. Soc. Rev. 2020; 49: 1887–1931.

Mohd Adnan, M.A.; Phoon, B.L.; Muhd Julkapli, N. Mitigation of pollutants by chitosan/metallic oxide photocatalyst: A review. J. Clean. Prod. 2020; 261: 121190.

Wu, X.J.; Xie, S.J.; Zhang, H.K.; Zhang, Q.H.; Sels, B.F.; Wang, Y. Metal Sulfide Photocatalysts for Lignocellulose Valorization. Adv. Mater. 2021; *33*: 2007129

Ma, B.J.; Zhang, R.S.; Lin, K.Y.; Liu, H.X.; Wang, X.Y.; Liu, W.Y.; Zhan, H.J. Large-scale synthesis of noble-metal-free phosphide/CdS composite photocatalysts for enhanced H_2 evolution under visible light irradiation. Chin. J. Catal. 2018; 39: 527–533.

Sobhani, A.; Salavati Niasari, M. Transition metal selenides and diselenides: Hydrothermal fabrication, investigation of morphology, particle size and and their applications in photocatalyst. Adv. Colloid Interface Sci. 2021; 287: 102321.

Li, J.K.; Li, M.; Jin, Z.L. Rational design of a cobalt sulfide/bismuth sulfide S-scheme heterojunction for efficient photocatalytic hydrogen evolution. J. Colloid Interface Sci. 2021; 592: 237–248.

Kokilavani, S.; Syed, A.; Al-Shwaiman, H.A.; Alkhulaifi, M.M.; Almajdhi, F.N.; Elgorban, A.M.; Khan, S.S. Preparation of plasmonic CoS/Ag_2WO_4 nanocomposites: Efficient visible light driven photocatalysts and enhanced anti-microbial activity. Colloid Interface Sci. Commun. 2021; 42: 100415

J. Zhang, Y. Liu, B. Xia, C. Sun, Y. Liu, P. Liu, D. Gao, Facile one-step synthesis of phosphorus-doped CoS_2 as efficient electrocatalyst for hydrogen evolution reaction, Electrochimica Acta .2017; 259: 955-961.

M.B. Muradov, O.O. Balayeva, A.A. Azizov, A.M. Maharramov, L.R. Qahramanli, G.M. Eyvazova, Z.A. Aghamaliyev, Synthesis and characterization of cobalt sulfide nanoparticles by sonochemical method. Infrared Physics & Technology 2018; 89: 255-262.

Zahra Hosseinpour, Zahra Arefinia, Sara Hosseinpour. Cu doped cubic pyrite-type CoS ball like superstructures as heterogeneous photocatalyst. Materials Chemistry and Physics. 2018; 220: 426-432.

N. Mohondas Singh, Monica Lalnunsiami Zadeng, Fidelia Lalrindiki and Lallianmawii. Synthesis, Characterization and Photocatalytic Properties of Pr^{3+} -Doped $CdWO_4$ Using Godzilla Insecticide. Novel Aspects on Chemistry and Biochemistry. 2022; 4: 978-81-19491-04-9.

Singh NP, Singh NR, Singh NM. Synthesis of $CdMoO_4$:Sm^{3+} phosphors at room temperature and investigation on photoluminescence properties. Optik. 2018; 156: 365–373.

G. Gurumoorthy, R. Hema, M. Sundararajan. Synthesis and Characterization of Cobalt Sulfide and Cobalt-Iron Sulfide Nanoparticles from Cobalt (III) Dithiocarbamate Complexes. Annals of the Romanian Society for Cell Biology. 2021; 25(2): 2086–2090.

Naorem RS, Singh NP, Singh NM. Synthesis of SnS_2 photocatalysts and investigation of their photocatalytic activities under sun light irradiation. Advances in Materials and Processing Technologies. 2022; 8(4): 4720- 4730.

Naorem RS, Singh NP, Singh NM. Photoluminescence studies of Ce^{3+} ion-doped $BiPO_4$ phosphor and its photocatalytic activity. International Journal of Applied Ceramic Technology. 2020; 17(6): 2744–2751. DOI: https://doi.org/10.1111/ijac.13600

Chenjuan Zhou, Junjie Luo, Qinqin Chen, Yinzhi Jiang, Xiaoping Dong and Fangming Cui. Titanate nanosheets as highly efficient

non-light-driven catalysts for degradation of organic dyes. Chem. Commun. 2015; 51: 10847-10849.

H. R. Ebrahimi, M. Modrek. Photocatalytic Decomposition of Methyl Red Dye by Using Nanosized Zinc Oxide Deposited on Glass Beads in Various pH and Various Atmosphere. Journal of Chemistry.2013; 2013(5): 151034.

Vo Thi Thu Nhu, Do QuangMinh, Nguyen Ngoc Duy, Nguyen QuocHien .Photocatalytic Degradation of Azo Dye (Methyl Red) In Water under Visible Light Using AgNi/TiO2 Sythesized by γ - Irradiation Method. International Journal of Environment, Agriculture and Biotechnology (IJEAB). 2017; 2(1).

Science and Technology Journal Vol. 12 Issue: 2 June 2024 ISSN: 2321-3388

Assessing Soil Pollution: An Investigation into Heavy Metal Contaminations in Roadside Soil in Aizawl, Northeast India

Gospel Lallawmzuali[1], Angom Sarjubala Devi[2], and Thanhmingliana[3]*
[1,2] Department of Environmental Science, Mizoram University, Aizawl-796004, India
[3]Department of Chemistry, Pachhunga University College, Aizawl, Mizoram, India
*E-Mail: thantea13@gmail.com
*Corresponding Author

Abstract— The study investigates the heavy metal contamination in the roadside soils of Aizawl, located in Northeast India, where the roadside soil is vulnerable to heavy metal pollution due to vehicular traffic and human activities. A systematic analysis was conducted at twelve sampling sites throughout the city from August 2020 to July 2021, with three replicates taken at each location. Metal concentrations were measured using atomic absorption spectrophotometry after acid digestion, following the USEPA 3050B method. The heavy metals analysed include copper (Cu), nickel (Ni), lead (Pb), and zinc (Zn). The mean metal concentrations at the selected sites range from 0.46 – 0.99 for Cu, 0.25 - 0.54 for Ni, 0.29 - 0.50 for Pb, and 1.35 – 1.84 for Zn. All measured metal concentrations exceeded the local average background values (ABVs), but they generally fall within the safe limits established by the Canadian and Chinese soil quality standards for residential areas. While all contamination levels fall within the moderately contaminated category based on the geo-accumulation index (Igeo), the pollution load index (PLI) indicated moderate to high levels of contamination by Cu at site S9 (Chanmari) and by Zn at sites S1 (Kulikawn), S5 (Bazar Bungkawn), S9 (Chanmari), and S12 (Khatla). The Pearson correlation analysis revealed a moderate positive correlation between copper and zinc, indicating a common source of pollution. Effect of monsoon Pb and Zn is also observed. The findings revealed varying metal concentrations at the different sites, with variations in the different sampling periods due to the influence of urbanization, human activities, vehicular traffic, and weather.

Keywords: Contamination, anthropogenic, vehicular traffic, contamination factor, pollution load index, geo-accumulation index.

INTRODUCTION

Environmental pollution is a major concern globally, with heavy metal contamination posing a significant threat to ecosystems and human health (Wang 1998). The widespread release of heavy metals into the environment, mainly through industrial activities and transportation, has led to the degradation of soil quality (Chowdhury *et al*. 2021). Soil pollution has become a growing environmental concern in both developed and developing countries. The presence of heavy metals in soils poses a particular threat to human health and the integrity of natural ecosystems, as these contaminants can accumulate through the food chain and have detrimental effects on wildlife and the overall functioning of terrestrial environments (Dhokpande *et al*. 2024; Wan *et al*. 2024). Soil, as a major sink for the accumulation of different contaminants, such as heavy metals released through human activities, requires immediate attention (Keshavarzi *et al*. 2021).

Roadside soil and dust can be exposed to significant levels of heavy metals due to the accumulation of heavy metals in soils, which can be attributed to a range of human activities,

 https://doi.org/10.22232/stj.2024.12.02.04

including automobile emissions, industrial activities, and land use practices (Abdullahi *et al*. 2023; Huang *et al*. 2022). It has been observed that roadside soil is highly contaminated with various heavy metals, namely Cu, Ni, Pb, and Zn, which poses a significant environmental concern with potential implications for human health and ecological systems (Chen *et al*. 2022; Arora *et al*. 2023). Thus, understanding the impact of heavy metal concentration on roadside soil is crucial for implementing effective mitigation strategies and safeguarding the environment (Kaur *et al*., 2022). Many studies have been conducted to explore the spatial distribution of heavy metal pollution in roadside soils (Wang *et al*. 2017; Kaur *et al*. 2022; Ayaz *et al*. 2023; Ma *et al*. 2023).

Human activities are the main cause of heavy metal pollution (Liu *et al*. 2024). The level of heavy metal contamination of soils depends on its type, climate, human activity, and atmospheric conditions, including wind direction and speed, type of precipitation, type of terrain, and type of vegetation (Skorbiłowicz *et al*. 2021). The surface layer of roadside soil near roads with heavy traffic in urban areas is a good indicator of heavy metal pollution, and heavy metals are released through different parts of vehicles. Metals such as Cu, Pd, and Zn enter the environment through the consumption of brake pads, lubricating and industrial oils, while Ni enters through the wear of metal parts and Ni-plated accessories (Altaf *et al*. 2021; Skorbiłowicz *et al*. 2021). Moreover, heavy metal content in soils along the road is strongly related to traffic and decreases with distance from the road and traffic volume (Arslan and Gizir 2006; Duong and Lee 2011). Therefore, soil contamination caused by vehicular transport has received much scientific attention in recent years and should be monitored to preserve environmental quality and prevent degradation (Wan *et al*. 2024; Kaur *et al*. 2022).

Given the environmental and public health implications of heavy metal pollution in urban soils, it is crucial to conduct comprehensive assessments of the spatial patterns and underlying factors contributing to soil contamination, particularly in rapidly developing regions (Feng *et al*. 2024). Rapid urbanization and industrial growth have placed significant pressure on delicate ecological systems (Ma *et al*. 2023). Aizawl, the capital city of Mizoram state, Northeast India, which is situated in hilly terrains, presents a unique geographic context for understanding the spatial distribution of heavy metal pollution. In a rapidly growing city like Aizawl, there is potential for roadside environments to accumulate heavy metals from vehicular emissions, industrial activities, and other human sources. This study aims to assess the extent of heavy metal contamination in roadside soils in Aizawl, addressing the level of pollution, the effect of monsoon, and highlighting the possible factors contributing to the pollution.

MATERIALS AND METHODS

Sample Collection and Analysis

Samples were collected monthly from 12 different sites within Aizawl City from August 2020 to July 2021, with three replicates at each site, maintaining at least 10-meter spacing between the replicates. The soil samples collected also contain sediments and dust most of the time. Sampling sites were carefully chosen, avoiding the sites where ongoing buildings and road construction were nearby. The sampling was conducted during the Covid-19 pandemic when the public activities and vehicular movements were restricted due to the imposed lockdowns the Mizoram state government during these periods. Pristine soil samples were also collected from the undisturbed sites of Pachhunga University College campus and ITI Veng area, Aizawl, for comparison. Soil from each site was transferred to air-tight polythene bags and taken to the laboratory. Samples were processed for metal concentration analysis using the USEPA 3050B acid digestion method. In brief, unwanted and larger particles were removed, and drying was done at 75°C for 12 hours, followed by sieving through a 150-micron mesh. For digestion, 1 g of soil was mixed with 10 ml of 8.5 M nitric acid, heated, and again treated with nitric acid, hydrogen peroxide, and hydrochloric acid. After cooling, the samples were filtered and diluted to 100 ml with deionized water (USEPA 1996; Nnodum *et al*. 2022). All reagents were obtained from HiMedia, India. The contents of heavy metals such as Cu, Ni, Pb Zn were measured using an atomic absorption spectrophotometer (Shimadzu, AA-7000F).

Pollution Indices

The pollution load index (PLI) serves as valuable tools for establishing simple but comparative means for assessing pollution levels while the geo-accumulation index (Igeo) evaluates pollution status and quantifies the influence of human activities, and the PLI and Igeo were assessed as detailed in previous literature (Chen *et al*. 2015; Mafuyai *et al*. 2015; Kaur *et al*. 2022). The Pollution load index (PLI) for the entire sampling site was determined as the nth root of the product of the n CF, i.e., PLI = $(CF1 \times CF2 \times CF3 \times \cdots \times CFn)^{1/n}$, where CF is the ratio of the metal concentration in the sample to the metal concentration in background.

This empirical index provides a simple, comparative means for assessing the level of heavy metal pollution. The PLI is classified as either background concentration (PLI = 0), unpolluted (PLI ≤ 1), unpolluted to moderately polluted (PLI ≤ 2), moderately polluted (PLI ≤ 3), moderately to highly polluted (PLI ≤ 4), highly polluted (PLI ≤ 5), or very highly polluted (PLI > 5) to indicate the degree of contamination. Igeo is a geochemical criterion to evaluate pollution levels. It was calculated using the formula, Igeo = $\log_2 (C_n / 1.5B_n)$, where C_n is the measured concentration of metal in soils or sediments and B_n is the geochemical background value of the corresponding metal and 1.5 is a constant. The Igeo consists of 7 classes: Igeo value of < 0, practically unpolluted; > 0–1, unpolluted to moderately polluted; > 1– 2, moderately polluted; > 2–3, moderately to strongly polluted; 3–4, strongly polluted; 4–5, strongly polluted to extremely polluted > 5 extremely polluted.

RESULTS AND DISCUSSION

Mean Heavy Metal Concentrations

Table 1 shows the mean of heavy metal concentrations in roadside soil samples at different selected sites within Aizawl City during August 2020 to July 2021. Significant variations in the concentrations of Cu, Ni, Pb, and Zn are observed in different sampling periods at each site. The concentrations Zn are the highest, and the Cu concentrations are also higher than Ni and Pb in all the sites. Due to the absence of specific Indian soil guidelines, both the Canadian and the China soil guidelines for residential sites are utilized to assess the safety levels of contamination. The heavy metal concentrations are mostly higher than the average background values (ABVs), but they still fall within safe limits when compared with the soil guidelines of China and Canada (Teng *et al*. 2014; CCME 2023). The surface layer of roadside soil in urban areas is a good indicator of heavy metal pollution. It was reported that heavy metal pollution in urban areas primarily arose from anthropogenic activities, including vehicular emissions, construction activities, and improper waste disposal. Vehicles contributed significantly through emissions, tire and brake wear, and the deposition of lead and zinc from fuels and paints (Altaf *et al*. 2021; Skorbiłowicz *et al*. 2021). Additionally, improper waste management, including the disposal of electronic waste and batteries, added to heavy metal contamination in urban environments (Ali-Taleshi *et al*. 2022; Motuzova *et al*. 2014).

Table 1: Mean Metal Concentration at the Study Site in Aizawl (in ppm).

Site	Cu (ppm)	Ni (ppm)	Pb (ppm)	Zn (ppm)
S1 (Kulikawn)	0.54±0.45	0.54±0.59	0.50±0.40	1.61±0.50
S2 (Vaivakawn)	0.46±0.20	0.31±0.27	0.29±0.27	1.53±0.63
S3 (Sikulpuikawn)	0.77±0.37	0.34±0.35	0.40±0.42	1.55±0.51
S4 (Bethlehem Vengthlang)	0.71±0.51	0.38±0.24	0.49±0.37	1.49±0.56
S5 (Bazar Bungkawn)	0.92±0.76	0.25±0.14	0.36±0.39	1.65±0.62
S6 (Laipuitlang)	0.63±0.55	0.25±0.18	0.31±0.23	1.55±0.66
S7 (Temple Square)	0.94±0.96	0.31±0.31	0.49±0.52	1.58±0.58
S8 (Ramhlun)	0.64±0.46	0.34±0.30	0.44±0.46	1.55±0.58
S9 (Chanmari)	0.99±0.49	0.26±0.07	0.33±0.27	1.77±0.59
S10 (Bawngkawn)	0.65±0.34	0.35±0.24	0.36±0.36	1.60±0.67
S11 (MINECO)	0.47±0.41	0.43±0.68	0.32±0.34	1.35±0.60
S12 (Khatla)	0.61±0.27	0.37±0.33	0.43±0.52	1.84±0.76
ABVs in Aizawl	0.24	0.14	0.14	0.49
China soil guidelines	100	50	300	250
Canada soil guidelines	64	50	140	200

Assessment of Contamination Level using Pollution Indices

Pollution Load Index

The PLI was used to assess the contamination levels and the PLI value is depicted in Figure 1. The figure reveals notable fluctuations in heavy metal contamination among various sampling locations, showcasing discernible variations in the concentrations of the studied heavy metals. The site S1 displays the highest PLI for Pb (2.67). S1, S4, S10, and S11 are classified as moderately polluted, while all other sites are categorized as unpolluted to moderately polluted. The highest PLI for Zn (3.34) is observed at site S9. S1, S5, and S12 are also under moderate to highly polluted levels with respect to Zn, like site S9, and the rest are under the moderately polluted category. Site S9 demonstrates the highest, with a moderate to highly polluted PLI for Cu (3.55), while seven sites fall under the moderately polluted category. Site S1 exhibits the highest PLI for Ni with a value of 2.67, indicating a moderately polluted environment. Three sites (S4, S10, and S12) exhibit moderately polluted levels, while most of the sites (PLI 1.58 – 1.99) fall under unpolluted to moderately polluted levels. These observations imply that local activities or emissions have a notable impact on each site, contributing to heightened pollution levels (Kozáková *et al.* 2019; Comber *et al.* 2022).

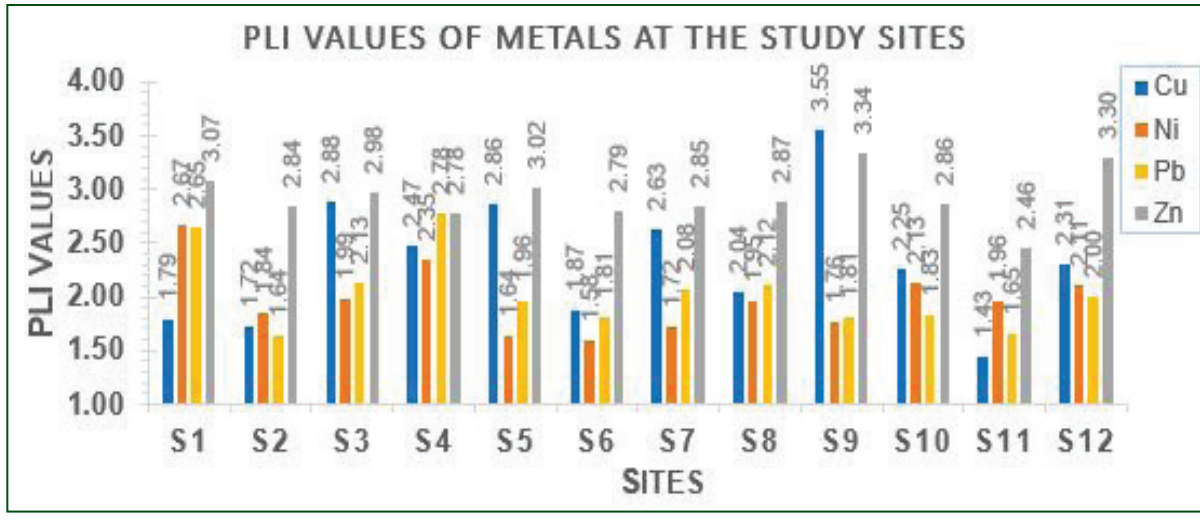

Fig. 1: PLI Values of Metals at the Study Site.

Geo-accumulation Index (Igeo)

The Igeo values calculated from the mean concentrations of metals at different months are presented in Figure 2 and it provides a comprehensive assessment of heavy metal contamination. Sites S1, S5, S7, and S9 exhibit higher Igeo values of 1.10, 1.35, 1.38, and 1.45, respectively, for Cu, indicating unpolluted to moderately polluted levels. The Igeo for Cu showed values ranging from 0.37 at S2 to 1.45 at site S9, from unpolluted to moderate pollution levels, suggesting localized pollution sources and varying degrees of anthropogenic impact at different sites (Ayaz *et al.* 2023). For Ni, Igeo values ranged from 0.26 (S5) to 1.26 (S1), indicating localized pollution sources and varying degrees of anthropogenic impact (Ali-Taleshi *et al.* 2022). The Igeo for Pb showed values ranging from 0.47 (at S2) to 1.26 (at S1), suggesting unpolluted to moderate contamination. Zn contamination was moderately high across all sites, with Igeo values ranging from 0.88 at site S11 to 1.33 at site S12. Notably, some sites displayed higher contamination at least for some of the studied heavy metals, emphasizing their vulnerability to heavy metal pollution. The Igeo values for Cu, Ni, Pb, and Zn across various sites highlight the distribution of these metals, suggesting localized sources such as human activities, vehicular traffic activities, or construction work (Kaur *et al.* 2022). Anthropogenic activities such as vehicular traffic, industrial activities, rusting and degradation of metallic structures and materials bearing these metals could affect the contamination levels (Abdullahi *et al.* 2023; Dhaliwal *et al.* 2021).

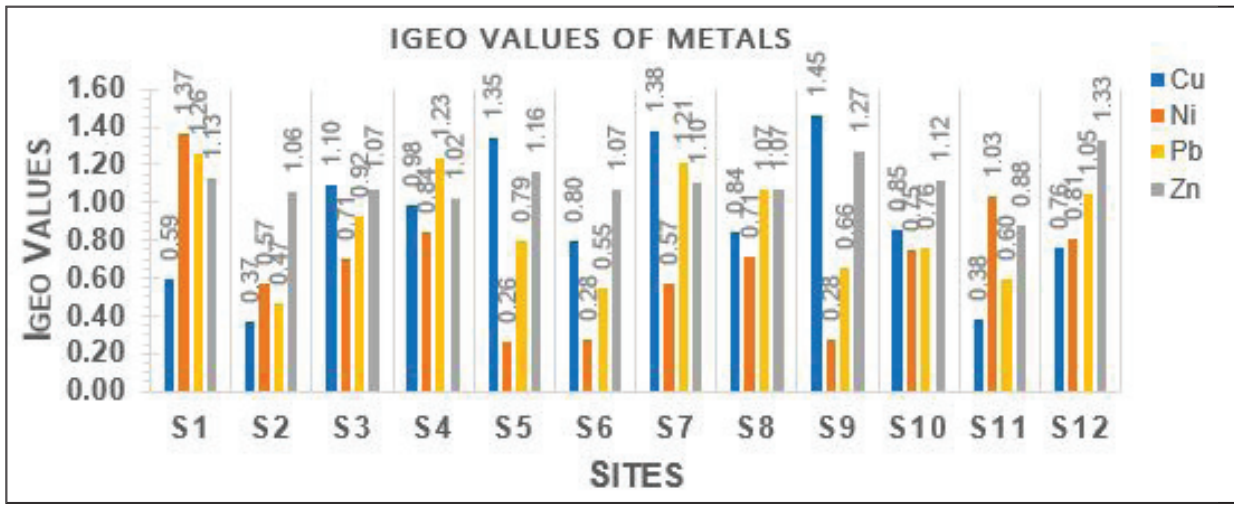

Fig. 2: Igeo Values of Metals at the Study Site.

Pearson Correlation

The Pearson correlation matrix represented in Table 2 provides insights into relationships between heavy metals, suggesting the common or distinct sources of pollution. A moderate positive correlation (0.361) between Cu and Zn suggests shared common sources like industrial activities or vehicular traffic-related pollution, as explained by Motuzova *et al*. (2014). Weak positive correlations between Ni and Zn (0.244); and Pb and Zn (0.229) indicate mixed sources, while Cu and Ni (0.122) have very weak correlations. In contrast, weak negative correlations between Cu and Pb (-0.201) and Ni and Pb (-0.224) imply different sources (Lu *et al*. 2014). These findings highlight the complex nature of factors influencing heavy metal contamination, emphasizing the need for more comprehensive source apportionment studies.

Table 2: Pearson Correlation Matrix for Metals.

Metals	Cu	Ni	Pb	Zn
Cu	1.000	0.122	-0.201	0.361
Ni	0.122	1.000	-0.224	0.244
Pb	-0.201	-0.224	1.000	0.229
Zn	0.361	0.244	0.229	1.000

Effect of Monsoon on the Variations of Heavy Metal Concentrations

The effect of monsoon on the variations of heavy metal concentrations is shown in Figure 3. The level of heavy metal contamination of soils can be affected by the atmospheric conditions, including wind direction and speed, type and level of precipitation, and the type of terrain and the soil physicochemical characteristics (Wang *et al*. 2017. Wang and Zhang 2018). The heavy metal contamination of soil can be influenced by variable factors.

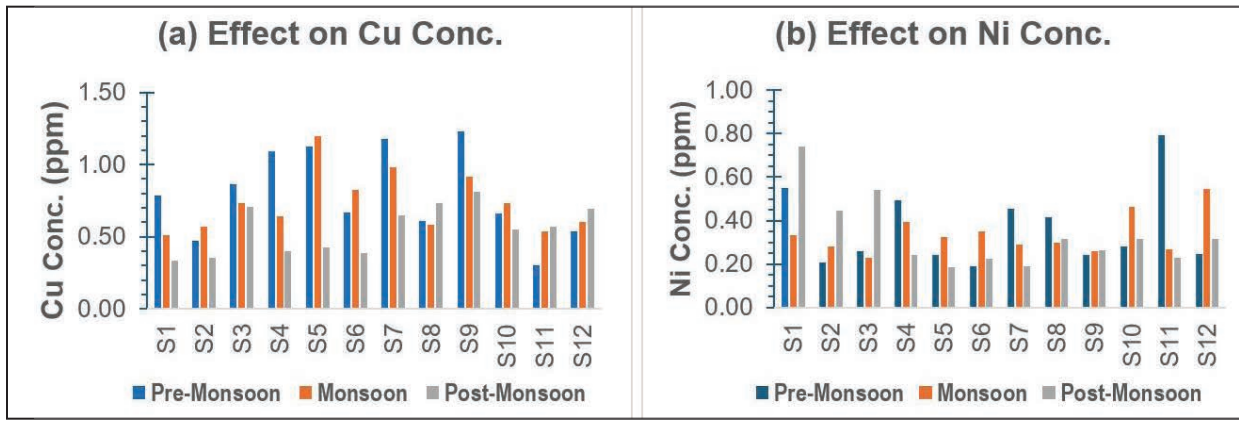

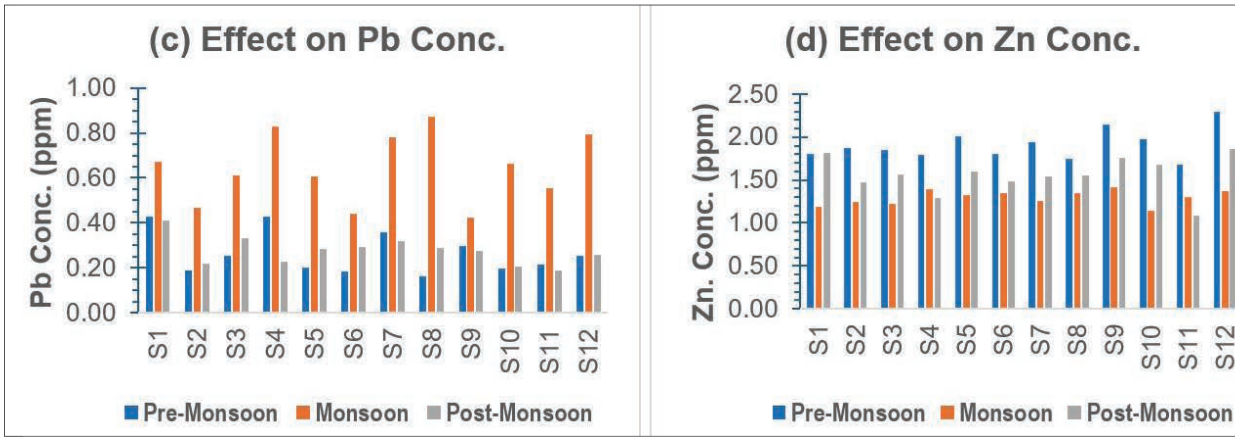

Fig. 3: Effect of Monsoon on the Variations of (a) Cu, (b) Ni, (c) Pb and (d) Zn.

It was observed from the figure that Pb concentrations reach a peak during the monsoon compared to pre-monsoon and post-monsoon, possibly due to rain washing lead-containing paints or leaching from other lead-containing materials. Previously, Schwarz (2016) reported that rain washed lead from old painted surfaces leaded into the soil and exacerbating contamination. Zn exhibited the highest concentration in pre-monsoon, with a notable decrease during the monsoon and a slight increase in post-monsoon at most of the sites. The decrease in Zn concentration during the monsoon season could be due to the dilution effect by rainfall and diminished atmospheric deposition. It was reported previously that the heavy metal contamination of the dumpsite soil samples contained lowered in which revealed higher Fe, Cr and Cd levels in pre-monsoon than in post-monsoon (Guthula *et al*. 2018). Notable effect of monsoon on the change of of concentrations of Cu and Ni was not observed. This could indicated that there could be many factors which govern the local contamination levels of these heavy metals.

CONCLUSION

This research thoroughly examined the extent of heavy metal contamination in roadside soils within Aizawl, Northeast India, focussing on the concentrations of Cu, Ni, Pb and Zn across twelve discrete sampling sites. The sampling was conducted during the Covid-19 pandemic. The public activities and vehicular movements were restricted since the Mizoram state government-imposed lockdowns during these periods. The data indicated marked spatial and temporal discrepancies in metal concentrations among the sampled sites, with Zn levels the highest, and Cu levels significantly exceeding those of Ni and Pb. The mean metal concentrations ranged from 0.46 (at S2) to 0.99 (at S9) for Cu, 0.25 (at S5) to 0.54 (at S1) for Ni, 0.29 (at S2) to 0.50 (at S1) for Pb, and 1.35 (at S11) to 1.84 (at S12) for Zn. Although the concentrations of heavy metals were observed to be elevated relative to the average background levels in the vicinity, they were generally found to be within acceptable limits when assessed against the soil quality standards established by Canada and China. Site S9 demonstrates the highest, with a moderate to highly polluted PLI value for Cu (3.55), while the sites S1, S5, S9 and S12 showed 3.07, 3.02, 3.34 and 3.34 for Zn respectively. The highest Igeo values for Cu, Ni, Pb, Zn observed are 1.45, 1.37, 1.26, 1.33 respectively and all these falls within the moderately contaminated category. Furthermore, the Pearson correlation analysis elucidated a moderate positive correlation (0.361) between Cu and Zn which suggests shared common sources like industrial activities or vehicular traffic-related pollution. The study noted decrease in Zn concentrations during the monsoon season likely because of dilution effects from rainfall. The increase in Pb levels during the monsoon could be due to rain-induced runoff from lead-based paints and lead containing materials. This seasonal variability indicates the dynamic characteristics of heavy metal pollution in Aizawl. The results highlight the widespread occurrence of heavy metal contamination, primarily resulting from anthropogenic activities such as vehicular emissions, industrial operations, and localized activities. The study underscores the necessity for ongoing monitoring and systematic evaluation of soil contamination to protect the environment and public health.

REFERENCES

Abdullahi N, Igwe EC, Dandago MA, Sani A, & Umar NB (2023) A review of heavy metals accumulation and control in active agricultural soil. Turk J Food Agri Sci 5(1): 7–18. https://doi.org/10.53663/turjfas.1247846

Ali-Taleshi MS, Feiznia S, Masiol M (2022) Seasonal and spatial variations of atmospheric depositions-bound elements over Tehran megacity, Iran: Pollution levels, PMF-based source apportionment and risks assessment. Urban Climate 42: 101113. https://doi.org/10.1016/j.uclim.2022.101113

Altaf R, Altaf S, Hussain M, Shah, RU, Ullah R, Ullah MI, Rauf A, Ansari MJ, Alharbi SA, Alfarraj S, Datta R (2021) Heavy metal accumulation by roadside vegetation and implications for pollution control. [retracted in: PLoS One. 2022 Aug 17;17(8): e0272410. doi: 10.1371/journal.pone.0272410]. PLoS One. 16(5):e0249147. doi:10.1371/journal.pone.0249147

Arora V, Bithel N, Singh, R (2023) A Study on Heavy Metal Sources and Pollution: Challenge to Biological and Ecosystem. Bull Pure App Sci - Bot 42(1): 44–49. https://doi.org/10.48165/bpas.2023.42B.1.7

Arslan, H, Gizir AM (2006) Heavy-metal content of roadside soil in Mersin, Turkey. Fresenius Environ. Bull. 2006, 15, 15–20

Ayaz H, Nawaz R, Nasim I, Irshad MA, Irfan A, Khurshid IK, Okla MK, Wondmie GF, Ahmed Z, Bourhia M (2023) Comprehensive human health risk assessment of heavy metal contamination in urban soils: insights from selected metropolitan zones. Front Environ Sci. 11. https://doi.org/10.3389/fenvs.2023.1260317

CCME. Canadian Council of Ministers of the Environment Guidelines; 2023 [Cited 2023 December 03]. https://ccme.ca/en/current-activities/canadian-environmental-quality-guidelines

Chen H, Teng Y, Lu S, Wang Y, Wang J (2015) Contamination features and health risk of soil heavy metals in China. Sci Total Environ 512–513: 143–153. doi: 10.1016/j.scitotenv.2015.01.025

Chen H, Zhan C, Liu S, Zhang J, Liu H, Liu Z, Liu T, Liu X, Xiao W (2022) Pollution Characteristics and Human Health Risk Assessment of Heavy Metals in Street Dust from a Typical Industrial Zone in Wuhan City, Central China. Inter J Environ Res Public Health. 19(17):10970. https://doi.org/10.3390/ijerph191710970

Chowdhury A, Naz A, Sharma D (2021) Geochemistry, Extent of Pollution, and Ecological Impact of Heavy Metal Pollutants in Soil. In: Geochemistry: Concepts and applications. Scrivener Publishing, Boston, pp. 73-91. https://doi.org/10.1002/9781119710134.ch5

Comber S, Deviller G, Wilson I, Peters A, Merrington G, Borrelli P, & Baken S (2022) Sources of copper into the European aquatic environment. Integrated Environmental Assessment and Management. 19(4): 1031–1047. https://doi.org/10.1002/ieam.4700

Dhaliwal SS, Setia R, Kumar V, Ghosh T, Taneja S, Singh R, Ansari J, Kukal SS, Pateriya B (2021) Assessment of seasonal variations and human health risks due to heavy metals in water, soils and food crops using multi-indices approach. Environ Earth Sci 80(11): 1–11. doi:10.1007/s12665-021-09686-4

Dhokpande R, Deshmukh SM, Khandekar A, Sankhe A (2024) A review outlook on methods for removal of heavy metal ions from wastewater. Sep Purif Technol 350, 127868. https://doi.org/10.1016/j.seppur.2024.127868

Duong TT, Lee BK (2011) Determining contamination level of heavy metals in road dust from busy traffic areas with different characteristics. J Environ Manage 92(3): 554-562. doi:10.1016/j.jenvman.2010.09.010

Feng Z, Chen W, Meng Y, Lu H, Shi X, Zhang J (2024) Spatial variability and source analysis of soil heavy metals: A case study of the key planting area of special agricultural products in Cangxi County, China. PLoS ONE 19(5): e0303387. https://doi.org/10.1371/journal.pone.0303387

Guthula SP, Chaitanya Injeti C, Peddineni PR (2018) Seasonal Heavy Metal Variations in Soil of an Active Municipal Solid Waste Dumpsite IOSR J Environ Sci Toxicol Food Tech 12(1): 85-92 DOI: 10.9790/2402-1201018592

Huang C, Zhang L, Jiuling Meng J, Yu Y, Qi J, Shen P, Li X, Ding P, Chen M, Hu G (2022) Characteristics, source apportionment and health risk assessment of heavy metals in urban road dust of the Pearl River Delta, South China. Ecotoxic Environ Safety 236: 113490. https://doi.org/10.1016/j.ecoenv.2022.113490

Kaur J, Bhat SA, Singh N, Bhatti SS, Kaur V, Katnoria JK (2022) Assessment of the Heavy Metal Contamination of Roadside Soils Alongside Buddha Nullah, Ludhiana, (Punjab) India. Int J Environ Res Pub Health 19(3): 1596. doi: 10.3390/IJERPH19031596

Keshavarzi A, Kumar V, Ertunc G, Brevik EC (2021) Ecological risk assessment and source apportionment of heavy metals contamination: An appraisal based on the Tellus soil survey. Environ Geochem Healthy. 43: 2121–2142. doi: 10.1007/s10653-020-00787-w

Kozáková J, Pokorná P, Vodicka P, Ondráčková L, Ondráček J, Křůmal K, Mikuška P, Hovorka J, Moravec P, Schwarz J (2019) The influence of local emissions and regional air pollution transport on a European air pollution hot spot. Environ Sci Pollut Res Int 26(2): 1675–1692. doi: 10.1007/s11356-018-3670-y

Liu J, Chen Y, Shang Y, Li H, Ma Q, Gao F (2024) Contamination Characteristics and Source Apportionment of Heavy Metal in the Topsoil of a Small Watershed in South Taihang. Land 13(7): 1068. https://doi.org/10.3390/land13071068

Lu X, Wang L, Li LY, Lei K, Huang J, & Zhai Y (2014) Contamination assessment of mercury and arsenic in roadway dust from Baoji, China. Atmos Environ 88: 106-113. https://doi.org/10.1016/j.atmosenv.2014.01.053

Ma H, Mi M, Wang C, Wu X, Zhen Z (2023) The Concentrations, Sources, Ecological, and Human Health Risk Assessment of Heavy Metals in Roadside Soils of Six Cities in Shanxi Province, China. Environ Toxicol Chem 42(7): 1485-1500. https://doi.org/10.1002/etc.5641

Mafuyai GM, Kamoh NM, Kangpe NS, Ayuba SM, Eneji IS (2015) Heavy Metals Contamination in Roadside Dust along Major Traffic Roads in Jos Metropolitan Area, Nigeria. J Environ Earth sci5(5): 48-57

Motuzova GV, Minkina TM, Karpova EA, Barsova NU, Mandzhieva SS (2014) Soil contamination with heavy metals as a potential and real risk to the environment. J Geochem Explor 144: 241-246. https://doi.org/10.1016/j.gexplo.2014.01.026

Nnodum CF, Yusuf KA, Wusu, AD (2022) A comparison of two digestion methods and heavy metals determination in sediments**.** Phy Sci Rev 8(11): 4233-4251. https://doi.org/10.1515/psr-2021-0194

Schwarz K (2016) Modeling to Predict High Pb Areas, Springer, Dordrecht, p. 135-145. doi: 10.1007/978-94-017-7456-7_11

Skorbiłowicz M, Skorbiłowicz E, Rogowska W (2021) Heavy Metal Concentrations in Roadside Soils on the Białystok-Budzisko Route in Northeastern Poland. Minerals 11(11):1290. https://doi.org/10.3390/min11111290

Teng Y, Wu J, Lu S, Wang Y, Jiao X, Song L (2014) Soil and soil environmental quality monitoring in China: A review. Environ Inter 69: 177-199. https://doi.org/10.1016/j.envint.2014.04.014

USEPA. United States Environmental Protection Agency (USEPA) Method 3050B: Acid Digestion of Sediments, Sludges, and Soils. Washington DC; 1996. [Cited 2020 February 15] https://www.epa.gov/sites/default/files/2015-06/documents/epa-3050b.pdf

Wan Y, Liu J, Zhuang Z, Wang Q, Li H (2024) Heavy Metals in Agricultural Soils: Sources, Influencing Factors, and Remediation Strategies. Toxics 12(1): 63. https://doi.org/10.3390/toxics12010063

Wang H, Nie L, Xu Y, Yan L (2017) The Effect of Highway on Heavy Metal Accumulation in Soil in Turfy Swamps, Northeastern China. Water Air Soil Pollut 228: 292. https://doi.org/10.1007/s11270-017-3486-2

Wang M, Zhang H (2018) Accumulation of Heavy Metals in Roadside Soil in Urban Area and the Related Impacting Factors. Int J Environ Res Public Health 15(6):1064. doi: 10.3390/ijerph15061064

Wang X (1998) Kriging and heavy metal pollution assessment in wastewater irrigated agricultural soil of Beijing's eastern farming regions. J Environ Sci Health 33(6), 1057-1073. https://doi.org/10.1080/10934529809376776

Science and Technology Journal Vol. 12 Issue: 2 June 2024 ISSN: 2321-3388

A Novel Method to Translate a Physical Watershed into Matrix Form for Run-off Estimation

Panchalika Dutta[1] and Sundararajan Muniyan[2]*
[1,2]Department of Mathematics and Computer Science,
Mizoram University, Aizawl-796004, India
*Email: dmsrajan.mzu@gmail.com
*Corresponding Author

Abstract—This article presents innovative notions of translating a micro-watershed into a unique matrix using a graphical represenation of a tree graph in graph theory assigning the order of the streams to the array of each node. It addresses new concepts of basic constituent, base and characteristic matrices of a micro-watershed. The main objective behind translating a watershed into a matrix is to develop a sediment transport model concerning different attributes of drainage system and topographical area of each micro-watershed in a river basin to predict water flow and quantify sedimentation to the reservoir through simulation. These innovations promise to advance our understanding of watershed dynamics and provide us a future scope to develop a sediment prediction which is crucial for water resource management and environmental planning. This study focuses on estimating the water flow from the contributing watersheds of the Barakar River Basin. A mathematical modeling and computer simulation of run-off from contributory topographical areas has been carried out to simulate water flow incorporating the stream order, contributory area, run-off and rainfall as matrices using the graph theory based algorithm. Key input parameters such as land use, land cover changes, soil properties, and topographical features are derived from the satellite images processed from Remote sensing techniques to incorporate their influence on water flow dynamics. The findings provide valuable insights into the hydrological behaviour of the watersheds that leads to forecast and control the flood and also aids to devise sustainable water resource management strategies in Barakar River Basin as well as water conservation and management in Maithan reservoir.

Keywords: watershed matrix**,** graph theory**,** sediment transport, easy data handling and memory management, run-off estimation

INTRODUCTION

Hossain (2015) studied and highlighted that water plays a crucial role in religious rituals. However, its distribution across the globe varies seasonally and by location. Throughout history, dams and reservoirs have been pivotal in collecting and managing water to support civilizations, as highlighted by Dwivedi *et al*. (2010). India, for instance, relies heavily on its 4500 large reservoirs and numerous smaller ones, storing water from the monsoon season to sustain non-monsoon periods. Siltation poses a significant challenge, with studies showing a loss of live storage capacity in many reservoirs, estimated at 214.2 million cubic meters annually (CWC, 2009) that costs upto a substantial loss of approximately Rs. 5.53 crores daily. Sedimentation threatens river ecosystems globally, with research indicating a decreasing flow trend in 50% of major rivers due to sediment accumulation (Walling & Fang, 2003). Globally, reservoirs are experiencing an annual sedimentation rate of about 31 cubic kilometers, potentially halving their storage capacity by 2100 (Sumi & Hirose, 2009). To mitigate these challenges, innovative approaches using geomorphological

 https://doi.org/10.22232/stj.2024.12.02.05

data and river flow simulation models are being developed to predict sediment deposition, manage reservoir capacity, and optimize downstream water discharge.

MATERIALS AND METHODS

Study Area

The chosen research area is the Maithon Reservoir, offering advantages such as hydroelectric power generation with a 60 MW capacity from three 20 MW units located underground on the left bank, supplying water to Dhanbad district, and serving as a popular tourist destination.

Some Innovations

Understanding basic geomorphological concepts of a river basin is crucial before developing a reservoir model. A micro-watershed, the fundamental unit, is defined as an area bounded by natural boundaries where runoff drains through a common outlet. Watersheds are unions of micro-watersheds, and river basins are unions of watersheds, represented using graph theory and matrix algebra principles.

Basic Constituent of a Drainage System

Exploring innovative concepts for drainage system representation involves understanding geomorphological features within micro-watersheds. Nodes collect runoff, and edges channel it, combining local sources into significant tributaries. Initial designs focus on main models, later integrating point sources using statistical methods from geomorphological studies. Connectors gather runoff where stretches meet, while receivers mark downstream terminations, forming a structured tree graph with collectors and transporters in the drainage system as shown in Fig.1

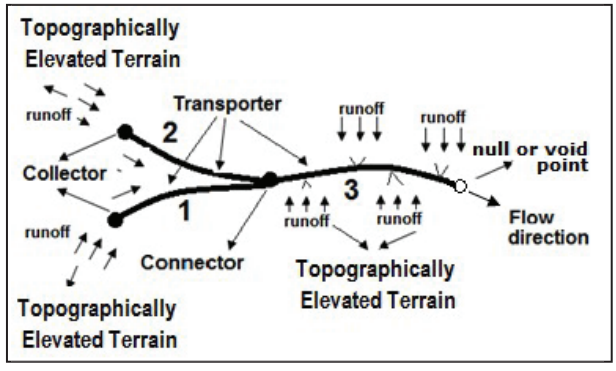

Fig. 1: An Illustrative Drainage System Showing Three Basic Constituents.

The Barakar River basin is mapped using GIS and Remote Sensing, and algorithmically coded to convert it into matrix form, involving detailed observation of each river section (Fig 2).

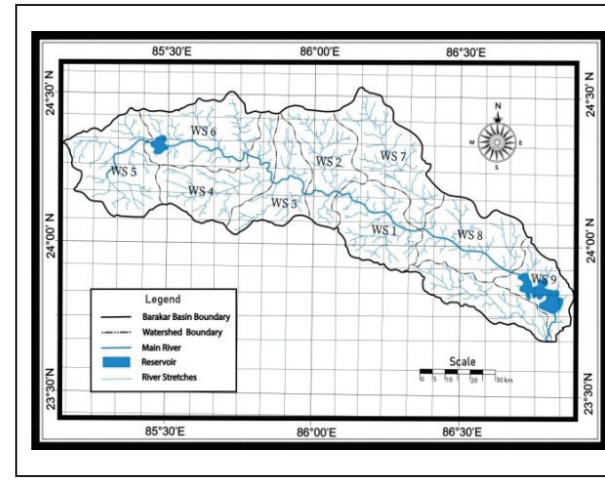

Fig. 2: Delineated Map of the Barakar River Basin.

ESTIMATION OF RUN-OFF USING ALGORITHM

An algorithm for converting a micro-watershed into a matrix is as mentioned below. The watersheds shown in Fig.2 are individually transformed into the order matrices by following the steps as follow:

1. Name nodes of stretch order 1 from the left side of the main river near the final outlet, moving clockwise as $A_{1,1}$, $A_{1,2}$, $A_{1,3}$, ..., $A_{n,r}$, where the first subscript denotes stretch order and the second denotes serial number or micro-watershed order in clockwise direction.
2. Repeat for stretch order 2 nodes as $A_{2,p}$, where $n \le p \le 1$ and p is the serial number of the first water flow contributor clockwise from stretch order 1, as shown in Fig. 2.
3. Continue similarly for stretch order 3 nodes as $A_{3,q}$, where $n \le q \le 1$ and q is the serial number of the first water flow contributor clockwise from stretch order 1, as depicted in Fig. 4, repeating until naming the last node of maximum order n as $A_{n,r}$.
4. The value of the element Ai,j is defined for the node whose latitude and longitudes is (x,y,z) and the order is *j* as follows:

$$A_{i,j}=\begin{cases}(x,y,z,i) & \text{if node P exists corresponding to the value j}\\ 0 & \text{otherwise}\end{cases}$$

The ordered 4-tuple (x, y, z, i) is necessary only during the computation of various measures involved in the reservoir modeling. This order matrix, derived from the micro-watershed, serves as a base matrix, with other attribute matrices derived from it for comprehensive drainage system representation. The Barakar River basin is mapped into 9 watersheds, further divided into micro-watersheds for individual order matrix conversion. The study utilizes five-year average rainfall data (2016-2020) from Dhanbad, Giridih, Hazaribagh, and Koderma districts, provided by JSAC, Jharkhand. Runoff calculation involves **Total Run-off (TR) = Contributory Area (CA) × Rainfall (R)**, adjusted for infiltration and evaporation at approximately 30% in the basin, determining the Final Estimated Quantity of Run-off (Q) into the river basin as **Q = TR – Infiltration rate (%) × TR.**

RESULTS

The order matrices of the micro-watersheds that fall under the watershed WS1 as shown in Fig.2 are illusttrated below:

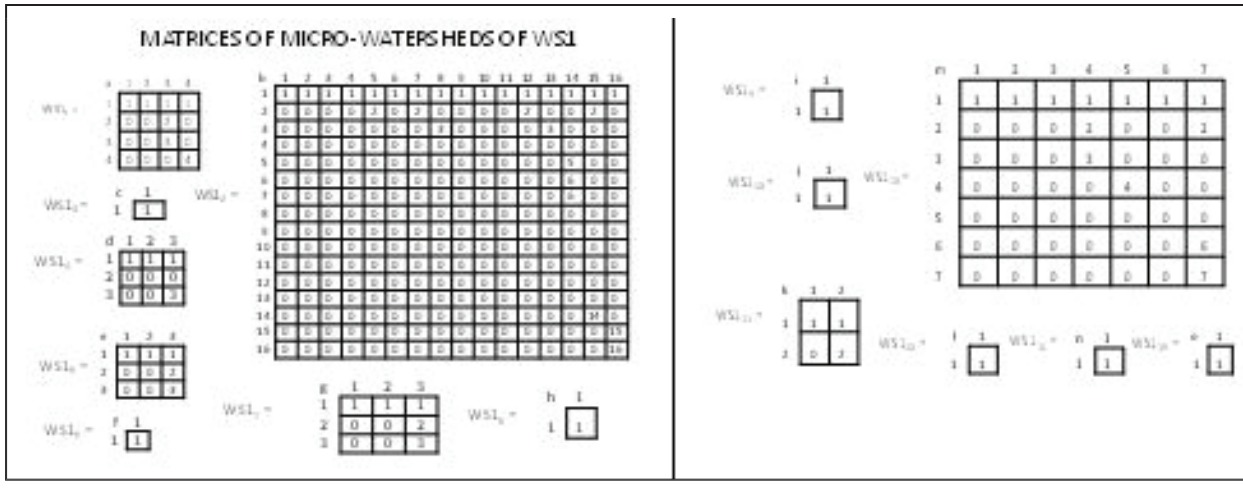

Fig. 3: Representation of 15 Micro Watersheds of WS1 into 15 Order Matrices.

All nine watersheds are transformed into matrix form to derive characteristic matrices based on contributory area, slope, elevation, stretch length, and rainfall, with Table 1 detailing run-off quantity (Q) from WS1 with infiltration deduction. Also, we have shown below the graph of the total run-off from all watersheds as shown in Fig. 4

Table 1: Represents Quantity of Run-off from WS1 into the Barakar River Basin.

Month	Total Rainfall Monthwise in Millimetre	Total Quantity of Run-off in Cubic Metre
Jan	6.96	3054223.81
Feb	10.18	4467241.147
Mar	18.4	8074384.784
Apr	30.46	13366617.42
May	62.6	27470461.28
Jun	130.96	57468556.05
Jul	305.88	134227870.5
Aug	239.86	105256626.9
Sep	236.52	103790950.5
Oct	64.4	28260346.74
Nov	21	9215330.46
Dec	6.76	2966458.758
Total	**1133.98**	**497619068.3**

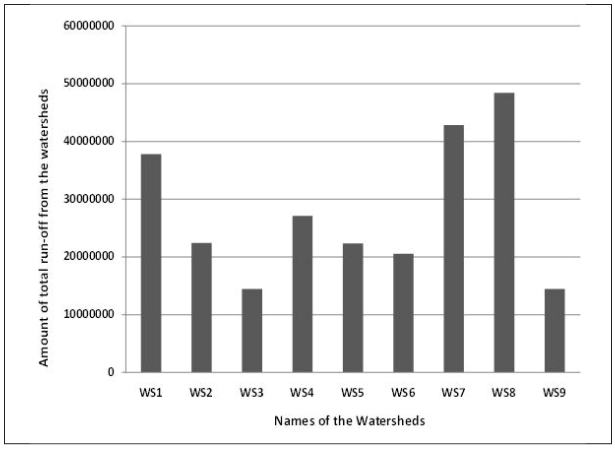

Fig. 4: Graph of the Total Contribution of Run-off by the Nine Watersheds (WS1 to WS9) into the River Basin.

DISCUSSIONS

During the rainy months of June, July, and August, increased rainfall in watersheds leads to higher runoff into the reservoir. Factors such as slope, elevation, and velocity affect runoff; higher slopes typically result in greater velocities and increased runoff. It's crucial to compute and store flow rates for each micro-watershed stretch in matrix form to predict sediment settlement in river beds and particles flushed into the reservoir. Flow rate is calculated as:

Flow rate = Stream Velocity × Contributory Area.

CONCLUSION

Our approach integrates micro-watershed nodes with various river attributes, optimizing water flow predictions and flood control. The algorithm enhances data handling efficiency and computational speed, crucial for accurate sediment and runoff predictions across diverse landscapes. Integrating infiltration rates into runoff calculations ensures precise reservoir sediment forecasts, crucial for water management strategies.

REFERENCES

CWC (2009). Central Water Commission-Annual Report 2008-09, New Delhi.

Dwivedi, V.K., Gupta, S.K, Pandey, S.N. (2010). A Study of Environmental Impact Due to Construction and Operation of Dam, National Conference on Eco-friendly Manufacturing for Sustainable Development, Nov 19-21, 2010, Paper no. 31, GLA University, Mathura, U.P. India.

Hossain, M.Z. (2015). Water: The most precious resource of our life, Global Journal of Advanced Research, Vol-2, Issue-9 PP. 1436-1445.

Sumi, T. & Hirose, T. (2009) Accumulation of sediment in reservoirs, Water storage, transport and distribution, UNESCO-IHE andEOLSS Publishers Co. Ltd., Paris, France, 224–252.

Walling, D. & Fang, D. (2003) Recent trends in the suspended sediment loads of the world's rivers, Global Planet change, 39:111–126.

Science and Technology Journal Vol. 12 Issue: 2 June 2024 ISSN: 2321-3388

3D Analysis of Wave Propagation in Generalized Magneto Thermoelastic Medium

S. Boruah[1]* and S.S. Singh[2]
[1,2]Department of Mathematics & Computer Science
Mizoram University, Aizawl-796004, India
E-Mail: *boruahshr@gmail.com, saratcha32@yahoo.co.uk

Abstract—The paper investigates the three dimensional problem of wave propagation in generalized magneto thermoelastic medium. The eigenvalue approach is adopted to solve the vector matrix differential equation which represents the equation of motion for the generalized thermoelastic materials. Components of displacements and temperature field are analyzed theoretically and computed numerically with the help of appropriate boundary conditions. The effect of magnetic and relaxation time on the propagation of waves are critically examined.

Keywords: Generalized magneto thermoelastic material; eigenvalue; Heaviside function; Phase velocity; wavenumber.

INTRODUCTION

The theory of thermoelasticity has many applications in various fields. Biot (1956) investigated the first paradox relating to the decoupling of deformation field of an elastic metarial with the temperature field. The contradiction of the infinite speed of the thermal wave was solved by Lord and Shulman (1967) in their generalized thermoelastic theory. Dhaiwal and Sherief (1980) derived the variation principle and uniqueness theorem for the generalized anisotropic thermoelastic material. Several authors, such as Puri (1973), Paria (1966) and Ezzat and Youssef (2005) contributed to the development of generalized thermoelastic theory. Youssef (2005) studied the generalized thermoelasticity of an infinite body with a cylindrical cavity and variable material properties. Wang and Dai (2004) introduced a theoretical method to analyse the magnetothermoelastic responses and perturbation of the magnetic field in the orthotropic thermoelastic cylinder subjected to thermal shock.

Zorammuana and Singh (2016) investigated the problem of elastic wave at a plane free boundary of thermoelastic saturated porous half-space and obtained the amplitude and energy ratios of the reflected waves. Abbas (2012) discussed the transient phenomena in the magneto-thermoelastic model in the context of the Lord and Shulman theory in a perfectly conducting medium. Some interesting problems of wave and vibration can be seen in (Abbas, 2013; Abbas *et al*., 2012; Abbas and Othman, 2012 and Dhaliwal *et al*., 1980).

The analysis of three dimensional thermoelastic problem has been found relatively less attention due to complicated form of the solution. Here, in this paper, we obtain the components of displacement theoretically and numerically using eigenvalue approaches for the generalized magneto thermoelastic medium. The equation of motion for such medium are derived using Maxwell's equations and modified Ohm's law. The numerical results are plotted to see the effects of thermal relaxation time and magnetic field.

https://doi.org/10.22232/stj.2024.12.02.06

Table 1: Nomenclature.

Symbols		Symbols	
λ, μ	Lamé constants	ρ	density
C_e	specific heat	t	time
T	absolute temperature	T_0	reference temperature
e_{ij}	strain tensor	**u**	displacement vector
k_0	thermal conductivity	**J**	current density vector
μ_0	magnetic permeability	σ_{ij}	stress tensor
τ	relaxation time	e	cubical dilatation
α_T	linear thermal expansion	**H**	magnetic intensity
H_0	initial magnetic field	**D**	electric displacement
E	induced electric field	**h**	induced magnetic field
σ_0	electric conductivity	**B**	magnetic inductance vector
δ_{ij}	Kronecker's delta	γ	$(3\lambda + 2\mu)\alpha_T$
c_1	$\sqrt{\mu/\rho}$	c_2	$\sqrt{\mu_0 H_0^2/\rho}$
c_3	$\sqrt{(\mu+\lambda)/\rho}$	c_4	$\sqrt{\gamma/\rho}$

BASIC EQUATIONS

The equation of motion in the absence of body force and heat source for linearly homogeneous magneto thermoelastic materials are

$$\sigma_{ij,j} + (\mathbf{J} \times \mathbf{B})_i = \rho \ddot{u}_i \tag{1}$$

The Maxwell's equations for homogeneous, thermally and electrically conducting elastic solid are given by

$$\text{curl}\,\mathbf{H} = \mathbf{J},\ \text{curl}\,\mathbf{E} = -\frac{\partial \boldsymbol{B}}{\partial t},\quad \text{div}\,\mathbf{B} = 0,\quad \mathbf{B} = \mu_0 \mathbf{H}. \tag{2}$$

The modified Ohm's law for finite conductivity is

$$\mathbf{J} = \sigma\left[\mathbf{E} + \left(\frac{\partial \mathbf{u}}{\partial t} \times \mathbf{B}\right)\right]. \tag{3}$$

If $\mathbf{H} = (H_x, H_y, 0)$, $\mathbf{E} = (E_x, E_y, 0)$ and $\mathbf{u}$ = (u, v, w) in Eqs.(2) and (3), we get

$$-\mu_0 \frac{\partial H_x}{\partial t} = \frac{\partial E_z}{\partial y} - \frac{\partial E_y}{\partial z},\quad \mu_0 \frac{\partial H_y}{\partial t} = \frac{\partial E_z}{\partial x} - \frac{\partial E_x}{\partial z}, \tag{4}$$

where

$$E_x = \frac{-1}{\sigma}\frac{\partial H_y}{\partial z} + \mu_0 H_y \frac{\partial w}{\partial t},\quad E_y = \frac{1}{\sigma}\frac{\partial H_x}{\partial z} - H_x \mu_0 \frac{\partial w}{\partial t},$$

$$E_z = \frac{1}{\sigma}\frac{\partial H_y}{\partial x} - \frac{1}{\sigma}\frac{\partial H_x}{\partial y} + \mu_0 H_x \frac{\partial v}{\partial t} - \mu_0 H_y \frac{\partial u}{\partial t} - \mu_0 \frac{\partial H_y}{\partial t}.$$

Thus, the components of **J** are given by

$$J_x = \sigma\left(E_x - \mu_0 H_y \frac{\partial w}{\partial t}\right),\quad J_y = \sigma\left(E_y + \mu_0 H_x \frac{\partial w}{\partial t}\right),$$

$$J_z = \sigma\left(\mu_0 H_y \frac{\partial u}{\partial t} - \mu_0 H_x \frac{\partial v}{\partial t} + E_z\right).$$

Equation(4) is linearized by inserting $H_x = H_0 + h_x$ and $H_y = H_0 + h_y$ so that H_x and H_y denote change in the basic magnetic field, H_0 along the x and y directions respectively. These changes can be obtained using Eq.(4) as

$$h_x = -H_0\left(\frac{\partial v}{\partial y} - \frac{\partial u}{\partial y} + \frac{\partial w}{\partial z}\right),\quad h_y = -H_0\left(\frac{\partial u}{\partial x} - \frac{\partial v}{\partial x} + \frac{\partial w}{\partial z}\right). \tag{5}$$

The constitutive relations of generalized thermoelastic solid are given by

$$\sigma_{ij} = 2\mu e_{ij} + \lambda e \delta_{ij} - \gamma \delta_{ij}\psi,\qquad \bar{\sigma}_{ij} = H_i h_j + H_j h_j - (\mathbf{H}.\mathbf{h})\delta_{ij}, \tag{6}$$

where,

$$e_{ij} = \frac{1}{2}(u_{i,j} + u_{j,i}), \quad e = \frac{\partial u}{\partial x} + \frac{\partial v}{\partial y} + \frac{\partial w}{\partial z}, \quad \psi = T - T_0.$$

The stress tensors are given by

$$\sigma_{xx} = (\lambda + \mu)\frac{\partial u}{\partial x} + \lambda\frac{\partial v}{\partial y} + \lambda\frac{\partial w}{\partial z} - \gamma\psi,$$

$$\sigma_{yy} = \lambda\frac{\partial u}{\partial x} + (\lambda + \mu)\frac{\partial v}{\partial y} + \lambda\frac{\partial w}{\partial z} - \gamma\psi,$$

$$\sigma_{zx} = \mu(\frac{\partial u}{\partial z} + \frac{\partial w}{\partial x}), \quad \sigma_{zz} = \lambda\frac{\partial u}{\partial x} + \lambda\frac{\partial v}{\partial y} + (\lambda + \mu)\frac{\partial w}{\partial z} - \gamma\psi,$$

$$\sigma_{yx} = \mu\left(\frac{\partial u}{\partial y} + \frac{\partial v}{\partial x}\right), \quad \sigma_{zy} = \mu\left(\frac{\partial w}{\partial y} + \frac{\partial v}{\partial z}\right).$$

Thus, the equations of motion for homogeneous magneto thermoelastic materials are derived using Eqs.(1) and (6) as

$$(c_3^2 - c_2^2)u_{xx} + (c_1^2 + c_2^2)u_{yy} + c_1^2 u_{zz} + c_2^2(v_{xx} - v_{yy}) + c_3^2 v_{yx}$$

$$(c_3^2 - c_2^2)w_{xz} - c_2^2 w_{zy} - c_4^2\psi_x = u_{tt}, \quad v \tag{7}$$

$$c_2^2(u_{xx} - u_{yy}) + (c_1^2 - c_2^2)v_{xx} + (c_2^2 + c_3^2)v_{yy} + c_3^2 u_{xy} + c_1^2 v_{zz}$$

$$(c_2^2 + c_3^2)w_{yz} - c_4^2\psi_y = v_{tt}, \tag{8}$$

$$c_1^2(w_{xx} + w_{yy}) + (c_3^2 + 2c_2^2)w_{zz} + (c_2^2 + c_3^2)u_{xz}$$

$$-c_2^2 u_{yz} + (c_2^2 + c_3^2)v_{yz} - c_4^2\psi_z = w_{tt} \tag{9}$$

$$k_0\psi_{ii} = (\psi_{,t} + \tau\psi_{,tt}) + \gamma T_0(e_{,t} + \tau e_{,tt}). \tag{10}$$

THREE DIMENSIONAL SOLUTION

We assume that the solutions of Eqs.(7)-(10) take the following form

$$\{u, v, w, \psi\}(x, y, z, t) = \{\bar{u}, \bar{v}, \bar{w}, \bar{\psi}\}(z)e^{\iota(\alpha x + \beta y - \omega t)}, \tag{11}$$

where α, β are wave numbers along x and y directions respectively and ω is angular frequency.

Using Eq.(11) into the equations of motions (7)-(10), we have the following set of equations

$$\frac{d\vec{V}}{dz} = A\vec{V}, \tag{12}$$

where

$$\vec{V} = \left[\bar{u}, \bar{v}, \bar{w}, \bar{\psi}, \frac{d\bar{u}}{dz}, \frac{d\bar{v}}{dz}, \frac{d\bar{w}}{dz}, \frac{d\bar{\psi}}{dz}\right]^T,$$

$$A = \begin{bmatrix} 0 & 0 & 0 & 0 & 1 & 0 & 0 & 0 \\ 0 & 0 & 0 & 0 & 0 & 1 & 0 & 0 \\ 0 & 0 & 0 & 0 & 0 & 0 & 1 & 0 \\ 0 & 0 & 0 & 0 & 0 & 0 & 0 & 1 \\ a_{51} & a_{52} & 0 & a_{54} & 0 & 0 & a_{57} & 0 \\ a_{61} & a_{62} & 0 & a_{64} & 0 & 0 & a_{67} & 0 \\ 0 & 0 & a_{73} & 0 & a_{75} & a_{76} & 0 & a_{78} \\ a_{81} & a_{82} & 0 & a_{84} & 0 & 0 & a_{87} & 0 \end{bmatrix}.$$

$$a_{51} = (c_{31}^2 - c_{21}^2)\alpha^2 + (1 + c_{21}^2)\beta^2 - k_1^2,$$

$$a_{52} = c_{21}^2(\alpha^2 - \beta^2) + c_{31}^2\alpha\beta,$$

$$a_{57} = \iota\{\beta c_{21}^2 - (c_{31}^2 - c_{21}^2)\alpha\},$$

$$a_{61} = \alpha\beta c_{31}^2 - (\beta^2 - \alpha^2)c_{21}^2, \; a_{64} = \iota\beta c_{41}^2,$$

$$a_{87} = \frac{T_0\omega(1 - \tau\omega\iota)c_{41}^2}{c_{51}^2}, \; a_{67} = -\iota\beta(c_{21}^2 + c_{31}^2$$

$$a_{73} = \frac{\alpha^2 + \beta^2 - k_1^2}{c_{31}^2 + 2c_{21}^2}, \; a_{75} = \iota\frac{c_{21}^2(\beta - \alpha) - \alpha c_{31}^2}{c_{31}^2 + 2c_{21}^2},$$

$$a_{76} = \frac{-\iota\beta(c_{21}^2 + c_{31}^2)}{c_{31}^2 + 2c_{21}^2}, \quad a_{78} = \frac{c_{41}^2}{c_{31}^2 + 2c_{21}^2},$$

$$a_{81} = \frac{T_0\omega\alpha c_{41}^2(1 - \iota\tau\omega)}{c_{51}^2}, \; a_{82} = \frac{T_0\omega\beta c_{41}^2(1 - \iota\tau\omega)}{c_{51}^2},$$

$$a_{54} = \iota\alpha c_{41}^2,$$

$$a_{62} = -k_1^2 + \beta^2(c_{31}^2 + c_{21}^2) - \alpha^2(c_{21}^2 - 1),$$

$$a_{84} = (\alpha^2 + \beta^2) - \iota\frac{c_{e1}(1 - \iota\tau\omega)\omega}{c_{51}^2}.$$

EIGENVAUE OF MATRIX DIFFERENTIAL EQUATION

We use eigenvalue approach to solve the differential equation (10). The characteristic equation of matrix, A is given by

$$-B_1\lambda^6 + B_2\lambda^4 - B_3\lambda^2 + B_4 = 0, \tag{13}$$

where

$$B_1 = a_{51} + a_{61} + a_{73} + a_{84} + a_{57}a_{75} + a_{67}a_{76},$$

$$B_2 = a_{51}a_{62} - a_{52}a_{61} + a_{51}a_{73} + a_{62}a_{73} + a_{51}a_{84} - a_{54}a_{81} + a_{62}a_{84} - a_{82}a_{64} + a_{73}a_{84} - a_{54}a_{87}a_{75} + a_{51}a_{67}a_{76} - a_{52}a_{67}a_{75} + a_{87}a_{67}a_{75} + a_{87}a_{62}a_{78} + a_{57}a_{75}a_{84} - a_{57}a_{78}a_{81} + a_{67}a_{76}a_{84} - a_{78}a_{82}a_{67},$$

$$B_3 = -a_{52}a_{61}a_{73} + a_{51}a_{62}a_{73} + a_{51}a_{62}a_{84} - a_{51}a_{62}a_{84} - a_{51}a_{64}a_{82} - a_{52}a_{61}a_{84} + a_{52}a_{64}a_{81} + a_{54}a_{61}a_{82} + a_{51}a_{73}a_{84} - a_{54}a_{73}a_{81} + a_{62}a_{73}a_{84} - a_{64}a_{73}a_{82} - a_{57}a_{61}a_{76}a_{84} + a_{57}a_{62}a_{75}a_{84} - a_{57}a_{64}a_{75}a_{82} + a_{57}a_{64}a_{76}a_{81} + a_{51}a_{67}a_{76}a_{84} - a_{52}a_{67}a_{75}a_{84} + a_{54}a_{67}a_{75}a_{82} - a_{54}a_{67}a_{76}a_{81} + a_{57}a_{61}a_{78}a_{82} - a_{57}a_{62}a_{78}a_{81} - a_{51}a_{67}a_{78}a_{82} + a_{52}a_{67}a_{78}a_{81} - a_{51}a_{87}a_{64}a_{76} + a_{52}a_{87}a_{64}a_{75} + a_{87}a_{54}a_{61}a_{75} - a_{87}a_{54}a_{62}a_{75} + a_{51}a_{87}a_{62}a_{78} - a_{52}a_{87}a_{61}a_{78},$$

$$B_4 = a_{51}a_{62}a_{73}a_{84} - a_{51}a_{64}a_{73}a_{82} - a_{52}a_{61}a_{73}a_{84} + a_{52}a_{64}a_{73}a_{81} + a_{54}a_{61}a_{73}a_{82} - a_{54}a_{62}a_{73}a_{81}.$$

The roots of characteristic equation, $\pm\lambda_1$, $\pm\lambda_2$, $\pm\lambda_3$ and $\pm\lambda_4$ are eigenvalue of matrix *A*. Thus, the full form of displacement components and temperature field in three dimensions are given by

$$(u, v, w, \psi) = \sum_{n=1}^{4}(1, b_n, d_n, f_n)\, A_n e^{\iota(\alpha x+\beta y-\omega t)} e^{-\lambda_n z} \quad (14)$$

where b_n, d_n and f_n are coupling constants and their expression are given below

$$b_n = \frac{S_n}{Q_n}, \quad d_n = \frac{R_n}{Q_n}, \quad f_n = \frac{P_n}{Q_n},$$

$$P_n = (c_{51}^2 a_{81} E_n - c_{51}^2 a_{67} a_{82} \lambda_n^2)(a_{67} D_n \lambda_n - a_{52} q_3)$$

$$-(\lambda_n c_{51}^2 q_3 a_{81} - q_4 \lambda_n a_{67})\,(P_{12} a_{67} \lambda_n^2 + E_n a_{52}),$$

$$Q_n = -\lambda_n\{(a_{54} a_{67} \lambda_n + c_{41}^2 a_{52})(E_n c_{51}^2 a_{81} - c_{51}^2 a_{82} \lambda_n^2 a_{67})$$

$$+ (c_{51}^2 a_{81} - F_n a_{67})(P_{12} a_{67} \lambda_n^2 + E_n a_{52})\},$$

$$R_n = \frac{1}{a_0}\{P_n \lambda_n(-c_{41}^2 a_{52} + a_{54} a_{67}) + Q_n(a_{67} D_n \lambda_n + a_{52} \lambda_n q_3)\},$$

$$a_0 = P_{12} a_{67} + E_n a_{52},$$

$$S_n = \frac{1}{a_{52}}\{P_{12} \lambda_n R_n - a_{54} P_n - D_n Q_n\},$$

$$E_n = g_3 + (c_{31}^2 + 2c_{21}^2)\lambda_n - \iota(c_{21}^2 + c_{31}^2)\alpha\lambda_n,$$

$$q_3 = -\iota\beta c_{21}^2,$$

$$D_n = a_{51} + \lambda_n(\lambda_n - \iota c_{21}\beta),\ P_{12} = \iota\alpha(c_{21}^2 - c_{31}^2),$$

$$g_3 = k_1^2 - (\alpha^2 + \beta^2),\ q_4 = T_0 \omega\alpha c_{41}^2.$$

BOUNDARY CONDITIONS

The boundary surface at z = 0 is subjected to a time dependent thermal shock and the conditions are given by

$$\psi(x, y, 0, t) = F(t)H(a - |x|)(b - |y|), \quad (15)$$

$$\sigma_{zz}(x, y, 0, t) + \bar{\sigma}_{zz}(x, y, 0, t) = 0\,, \quad (16)$$

$$\sigma_{yz}(x, y, 0, t) + \bar{\sigma}_{yz}(x, y, 0, t) = 0, \quad (17)$$

$$\sigma_{xz}(x, y, 0, t) + \bar{\sigma}_{xz}(x, y, 0, t) = 0, \quad (18)$$

where H denotes Heaviside's function and $F(t) = \theta_0 e^{-\delta t}$ taking θ_0 as a constant.

Inserting the values of σ_{ij}, $\bar{\sigma}_{ij}$ and ψ into Eqs.(13)-(16), we get the following matrix equation

$$bA = c,$$

where

$$b_{1i} = f_i,\ b_{2i} = \iota\lambda(\alpha + b_i\beta) - (\lambda + 1)d_i\lambda_i - \gamma\psi$$

$$+ H_0^2\{(b_i - 1)\iota(\beta - \alpha) - 2d_i\lambda_1\},$$

$$b_{3i} = d_i\iota\beta - \lambda_i b_i,\ b_{4i} = -\lambda_i + d_i\iota\alpha,$$

$$c = \left[\theta_0 e^{(-(d+\omega)t+\iota(\alpha x+\beta y))}, 0, 0, 0\right]^T, A = [A_1, A_2, A_3, A_4]^T$$

Table 2: Values of the Parameters.

Parameters	Values	Units	Parameters	Values	Units
k_0	386	$NK^{-1}s^{-1}$	α_t	1.78×10^{-5}	K^{-1}
C_e	383.1	$m^2K^{-1}s^{-2}$	ρ	8954	Kgm^{-3}
μ	3.86×10^{10}	Nm^{-2}	λ	7.76×10^{10}	$Nm^{-1}s{-}1$
μ_0	$4\pi \times 10^{-7}$	Nms^2C^{-2}	H_0	10^3	$Cm^{-1}s^{-1}$
τ	0.02		T_0	293	K
θ_0	10		δ	0.1	
x	1		y	2	
α	1.2		β	1.4	
t	1				

NUMERICAL DISCUSSION

We have developed a Matlab program for (u, v, w, ψ) and stress components. The effect of H_0 and τ on the propagation of waves have been examined. The following relevant values of parameters for the generalized thermoelastic solid are considered Ezzat and Youssef (2005) in Table 2.

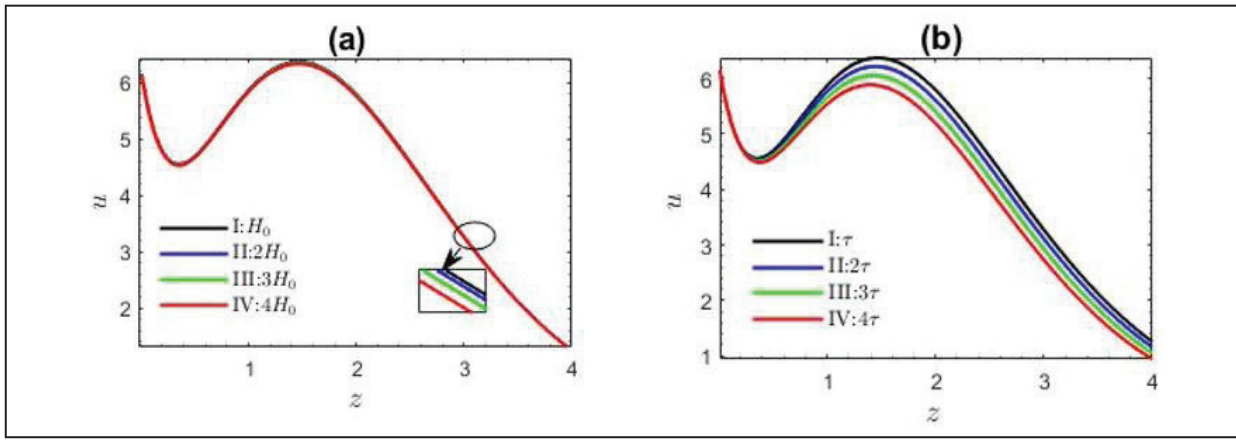

Fig. 1: Variation of *u* for Different Values of (a) H_0 and (b) τ.

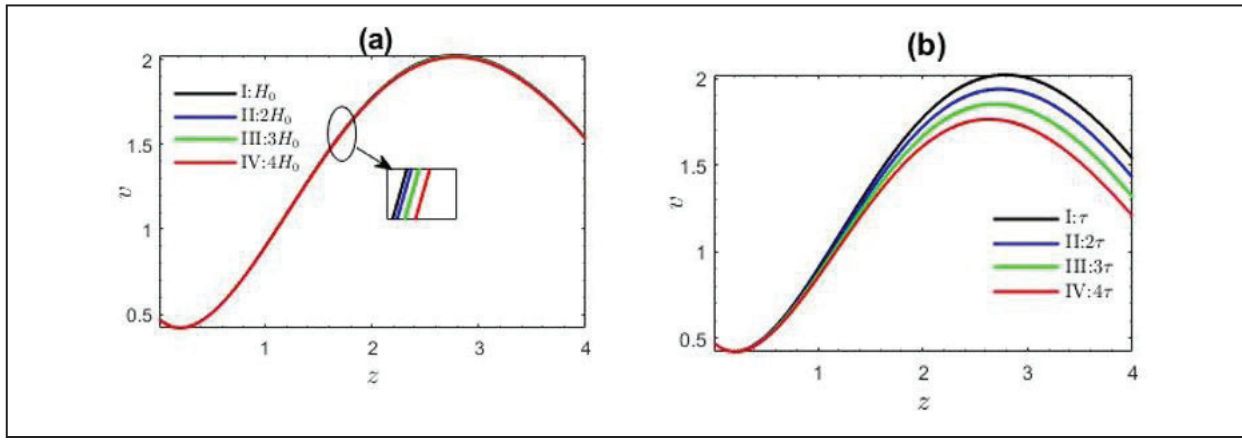

Fig. 2: Variation of ν for Different Values of (a) H_0 and (b) τ.

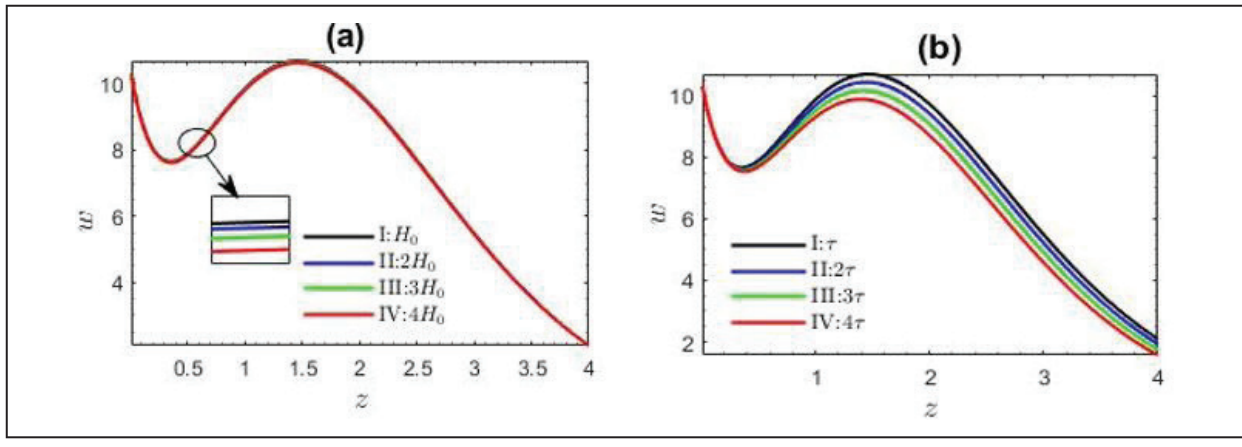

Fig. 3: Variation of *w* for Different Values of (a) H_0 and (b) τ.

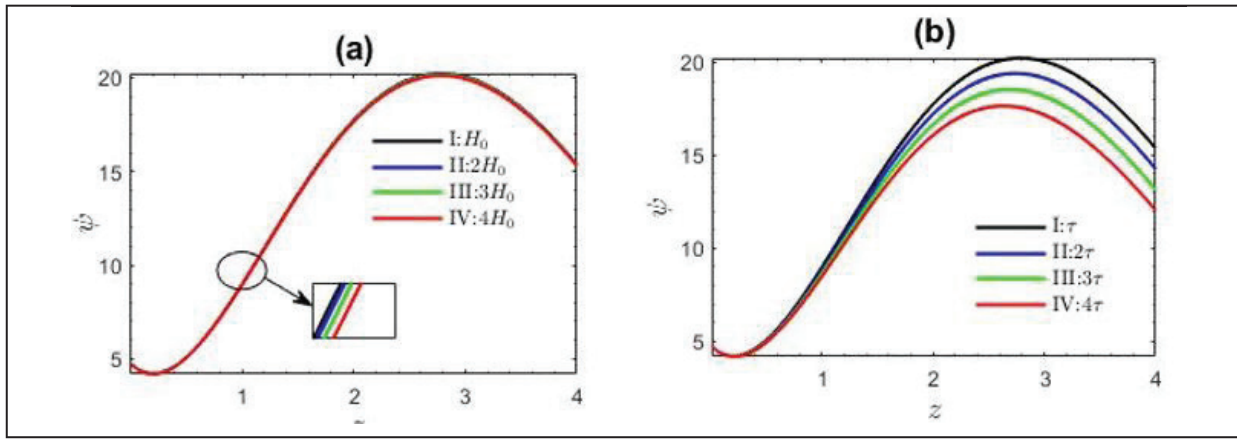

Fig. 4: Variation of ψ for Different Values of (a) H_0 and (b) τ.

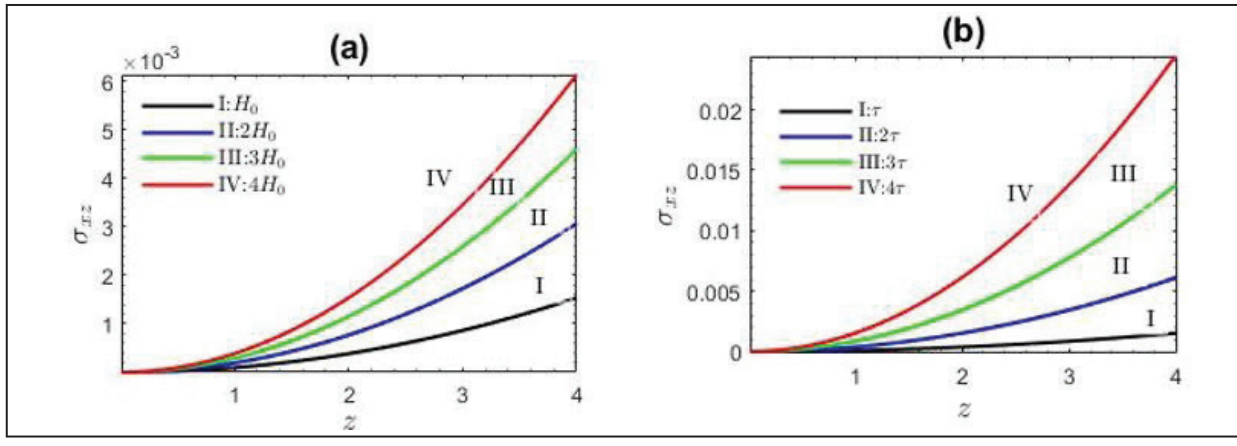

Fig. 5: Variation of σ_{xz} for Different Values of (a) H_0 and (b) τ.

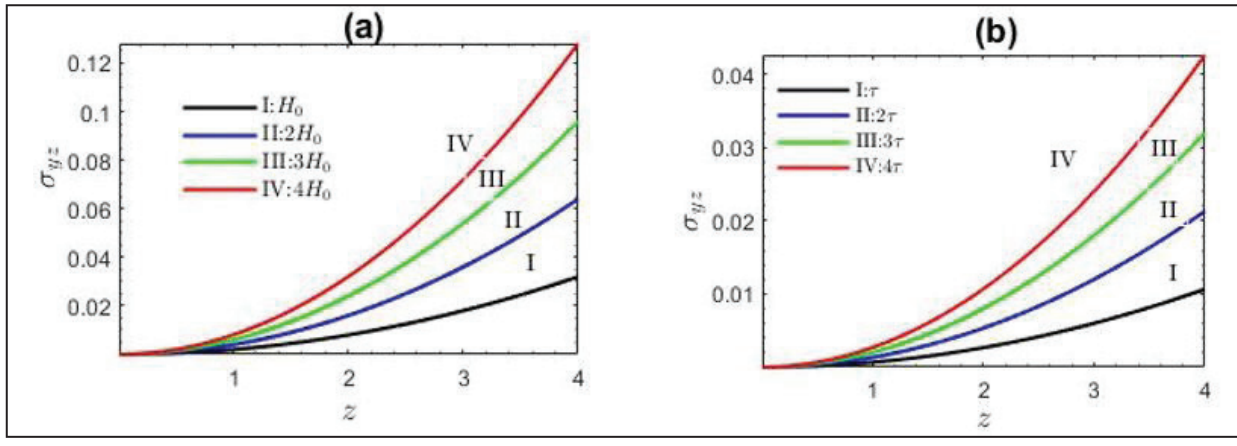

Fig. 6: Variation of σ_{yz} of Different Values of (a) H_0 and (b) τ.

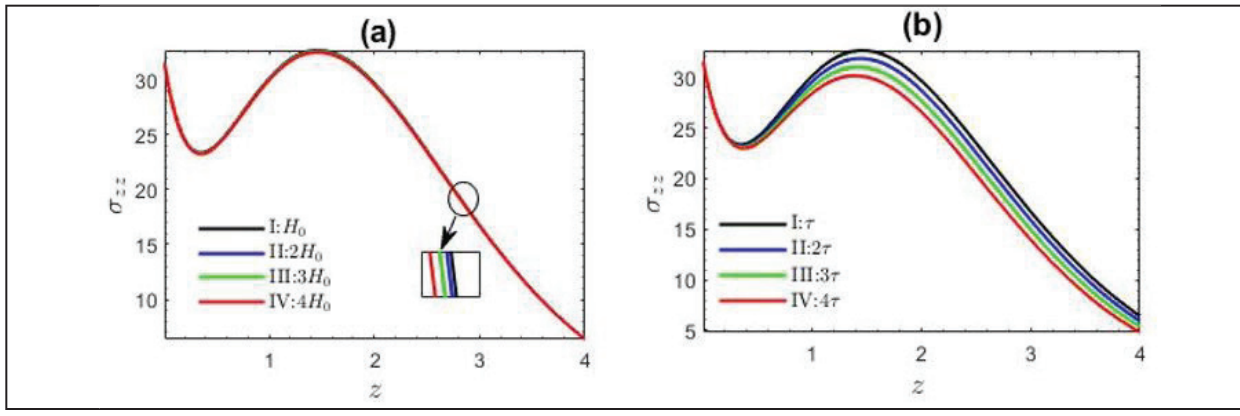

Fig. 7: Variation of σ_{zz} of Different Values of (a) H_0 and (b) τ.

Figures 1 to 4 represent the variation of the displacement components and temperature field with z for different values of H_0 and τ. We have seen a very interesting and beautiful effects of initial magnetic field and relaxation time on u, v, w. In Figure 1, the displacement component u begins from certain point which decreases with the enhancement of z upto z = 0.29 and then it increases and decreases with the increase of z. We have seen the effect of H_0 is smaller than τ. It is also clearly observed that the values of u decrease with the increase of H_0 and τ. Figure 2 shows that values of v increase upto z = 2.67 and then decrease with the increase of z. It is observed that the values of v decrease with the increase of H_0 and τ. Figure 3 shows similar nature of w with u. The variation of ψ with are shown in Figure 4 which is similar with the nature of v. The variation of σ_{xz} and σ_{xz} with z are shown in Figures 5 and 6 respectively. It is observed that both these tensors increase with the increase of z at different values of H_0 and τ. The values of these tensors increase with the increase of H_0 and τ. Similar natures of $\sigma_{zz}$with are observed in Figure 7. Thus, we have seen that all the effects of H_0 and τ to the displacement and stress are very small near origin.

CONCLUSION

We have analyzed the 3D problem of wave propagation in generalized magneto thermoelastic medium. The effects of H_0 and τ on displacement, stress tensors and temperature field are depicted graphically. We can conclude the following points:

(i) The effect τ on the displacement and stress is very small near origin. The effect of H_0 on the components of displacement and temperature field is also very small

(ii) The values of σ_{xz} and σ_{yz} increase with the increase of z.

(iii) The values of σ_{xz} and σ_{yz} increase with the increase of and H_0 and τ.

(iv) Similar natures are observed for u, w and σ_{zz}.

(v) Similar natures are observed for v and ψ.

REFERENCES

Abbas IA (2012) Generalized magneto-thermoelastic interaction in a fiber-reinforced anisotropic hollow cylinder. Int. J. Thermophys. 33: 567-579.

Abbas IA (2013) A GN model for thermoelastic interaction in an unbounded fiber-reinforced anisotropic medium with a circular hole. Appl. Math. Lett. 26(2): 232-239.

Abbas IA, Kumar R, Chawla V (2012) Response of thermal source in a transversely isotropic thermoelastic half-space with mass diffusion by using a finite element method. Chin. Phys. B. 21(8): 084601.

Abbas IA, Othman MI (2012) Plane waves in generalized thermo-microstretch elastic solid with thermal relaxation using finite element method. Int. J. Thermophys. 33: 2407-2423.

Biot MA (1956) Thermoelasticity and irreversible thermodynamics. J. Appl. Phys. 27(3): 240-253.

Dhaliwal RS, Sherief HH (1980) Generalized thermoelasticity for anisotropic media. Q. Appl. Math. 38(1): 1-8.

Ezzat MA, Youssef HM (2005) Generalized magneto-thermoelasticity in a perfectly conducting medium. Int. J. Solids Struct. 42(24-25): 6319-6334.

Lord HW, Shulman Y (1967) A generalized dynamical theory of thermoelasticity. J. Mech. Physics. 15(5): 299-309.

Paria G (1966) Magneto-elasticity and magneto-thermoelasticity. Adv. Appl. Mech. 10: 73-112. Puri P (1973) Plane waves in generalized thermoelasticity. Int. J. Engng. 11(7): 735-744.

Wang X, Dai HL (2004) Magnetothermodynamic stress and perturbation of magnetic field vector in an orthotropic thermoelastic cylinder. Int. J. Eng. Sci. 42(5-6): 539-556.

Zorammuana C, Singh S (2016) Elastic waves in thermoelastic saturated porous medium. Meccanica 51(3): 593-609.

Science and Technology Journal Vol. 12 Issue: 2 June 2024 ISSN: 2321-3388

Special Projective Semi-symmetric Connection on Kenmotsu Manifolds

K.C. Biakkim[1] and M. Saroja Devi[2]
[1,2]Department of Mathematics and Computer Science
Mizoram University, Aizawl-796004, India
E-Mail: [2*]devi_saroja@rediffmail.com
[*]Corresponding Author

Abstract—The aim of the present paper is to study the properties of Kenmotsu manifolds admitting a special projective semi-symmetric connection. We have discovered that if a Kenmotsu manifold of n dimension ($n > 2$), is Ricci flat with respect to special projective semi-symmetric connection whose 1-form η is a recurrent, then the manifold is a certain class of quasi-Einstein manifold. Finally, we show that Weyl projective curvature tensor with respect to special projective semi-symmetric connection is cyclic on the Kenmotsu manifold.

Keywords: Special projective semi-symmetric connection, Kenmotsu manifold, Weyl projective curvature, Tensor.
Mathematics Subject Classification (2020): 53C15; 53C05; 53D15

INTRODUCTION

It is intriguing to examine the properties and invariants of the semi-symmetric metric connection. Friedmann and Schouten (1924) first introduced the idea of semi-symmetric connection. Bartolotti (1930) investigated a geometrical significance for a such connection. Yano (1970) initiated the systematic investigation of a Riemannian manifold with semi-symmetric connection. Further, various geometers had studied semi-symmetric connections in various directions, including Chaubey and Ojha (2012) and Singh *et al*. (2021). Zhao and Song (2001) re-examined and defined a type of semi-symmetric connection on Riemannian manifold which has the same geodesic curves as Riemannian connection D and this new connection is projectively equivalent to D. This is known as projective semi-symmetric connection and it has been further developed by Zhao (2008), Pal *et al*. (2015) and other researchers.

The paper is presented as follows: After introduction, section 2 is devoted to preliminaries. Section 3 provides a brief description of the projectively semi-symmetric connection on the Kenmotsu manifold. Furthermore, in section 4, we have shown that Weyl projective curvature tensor with respect to the special projective semi-symmetric connection is cyclic.

PRELIMINARIES

An n-dimensional Riemannian manifold (M_n, g) of class C^∞ with a 1-form η, the associated vector field ξ and a (1, 1) tensor field ϕ satisfying

$$\phi^2 V_1 + V_1 = \eta(V_1)\xi \tag{2.1}$$

is called an almost contvact manifold and the system (ϕ, ξ, η) is called an almost contact structure to M_n (Mishra, 1984). If the associated Riemannian metric g in M_n satisfy

$$g(\phi V_1, \phi V_2) = g(V_1, V_2) - \eta(V_1)\eta(V_2) \tag{2.2}$$

for any arbitrary vector fields V_1, V_2 in M_n, then (M_n, g) is said to be an almost contact metric manifold. Putting ξ for V_1 in (2.2) and using (2.1), we obtain

$$g(\xi, V_2) = \eta(V_2). \tag{2.3}$$

Also $'F(V_1, \xi) = g(\phi V_1, \xi) = \eta(\phi V_1) = 0$ (2.4)

https://doi.org/10.22232/stj.2024.12.02.07

gives $'F(V_1, V_2)+'F(V_1, V_2) = 0$ (2.5)

If moreover,

$$(D_{V_1}\phi)(V_2) = g(\phi V_1, V_2)\xi - \eta(V_2)\phi V_2, \quad (2.6)$$

$$D_{V_1}\xi = V_1 - \eta(V_1)\xi \quad (2.7)$$

hold in (M_n, g), where D being the Riemannian connection of g, then (M_n, g) is called a Kenmotsu manifold (Kenmotsu, 1972).

The following relations also hold in a Kenmotsu manifold:

$$K(V_1,V_2)\xi = \eta(V_1)V_2 - \eta(V_2)V_1, \quad (2.8)$$

$$K(\xi, V_1)V_2 = \eta(V_2) - g(V_1, V_2)\xi, \quad (2.9)$$

$$S(V_1, \xi) = -2n\eta(V_1), \quad (2.10)$$

$$S(V_1, V_2) = g(QV_1, V_2), \; Q\xi = -2n\xi, \quad (2.11)$$

$$(D_{V_1}\eta)(V_2) = g(V_1, V_2) - \eta(V_1)\eta(V_2), \quad (2.12)$$

for arbitrary vector fields $V_1, V_2, V_3 \in T(M_n)$ where S is Ricci tensor and K is the Riemannian curvature tensor with D.

PROJECTIVE SEMI-SYMMETRIC CONNECTION

A linear connection (Yano, 1970) is defined as a semi-symmetric connection $\widetilde{D}$ on an n–dimensional Kenmotsu manifold (M_n, g), if its torsion tensor T with respect to $\widetilde{D}$ is given by

$$T(V_1, V_2) = \widetilde{D}_{V_1}V_2 - \widetilde{D}_{V_2}V_1 - [V_1, V_2] \quad (3.1)$$

which can also represent as

$$T(V_1, V_2) = A(V_2)V_1 - A(V_1)V_2. \quad (3.2)$$

where A is a 1- form associated with a vector field ρ, i.e.,

$$A(V_1) = g(V_1, \rho). \quad (3.3)$$

And this connection $\widetilde{D}$ is a metric connection since it satisfies

$$(\widetilde{D}_{V_1}g)(V_2, V_3) = 0. \quad (3.4)$$

$\widetilde{D}$ is said to be a connection projectively equivalent to D if the geodesic with respect to $\widetilde{D}$ are always consistent with those of the connection D on a Riemannian manifold. A semi-symmetric connection which is also projectively equivalent to D, is termed as projective semi-symmetric connection [Zhao and Song, 2001].

Let us consider a projective semi-symmetric connection $\widetilde{D}$ introduced by Zhao and Song (2001) as

$$\tilde{D}_{V_1}V_2 = D_{V_1}V_2 + \Psi(V_2)V_1 + \Psi(V_1)V_2 + \Phi(V_2)V_1 - \Phi(V_1)V_2, \quad (3.5)$$

for any vector fields V_1, V_2, where the 1-form ψ and Φ are given below:

$$\Psi(V_1) = \frac{n-1}{2(n+1)}A(V_1) \text{ and } \Phi(V_1) = \frac{1}{2}A(V_1). \quad (3.6)$$

Equations (3.5) and (3.6) give

$$(\widetilde{D}_{V_1}g)(V_2, V_3) = \frac{1}{n+1}\begin{bmatrix}2A(V_1)g(V_2, V_3) - nA(V_2)g(V_1, V_3)\\ -nA(V_3)g(V_1, V_2)\end{bmatrix}. \quad (3.7)$$

It shows that the connection $\widetilde{D}$ given in (3.5) is a metric one. The relations between the curvature tensors $\widetilde{K}$ and K with respect to the projective semi-symmetric connection $\widetilde{D}$ and the Riemannian connection D respectively are given as [Zhao and Song, 2001]

$$\begin{aligned}\widetilde{K}(V_1,V_2)V_3 = {} & K(V_1,V_2)V_3 + \alpha(V_1,V_3)V_2 \\ & - \alpha(V_2,V_3)V_1 + \beta(V_1,V_2)V_3,\end{aligned} \quad (3.8)$$

where α and β are the tensors of type (0, 2) given by the following relations

$$\begin{aligned}\alpha(V_1,V_2) = {} & \Psi'(V_1,V_2) + \Phi'(V_2,V_1) \\ & - \Psi(V_1)\Phi(V_2) - \Psi(V_2)\Phi(V_1)\end{aligned} \quad (3.9)$$

and

$$\begin{aligned}\beta(V_1,V_2) = {} & \Psi'(V_1,V_2) - \Psi'(V_2,V_1) + \Phi'(V_2,V_1) \\ & - \Phi'(V_1,V_2).\end{aligned} \quad (3.10)$$

The tensors ψ' and Φ' of type (0, 2) are defined by the following two relations:

$$\Psi'(V_1,V_2) = (D_{V_1}\Psi)(V_2) - \Psi(V_1)\Psi(V_2) \quad (3.11)$$

and

$$\Phi'(V_1,V_2) = (D_{V_1}\Phi)(V_2) - \Phi(V_1)\Phi(V_2). \quad (3.12)$$

A relation between the Ricci tensors of the Kenmotsu manifold with respect to the connections $\widetilde{D}$ and D is obtained by contracting the equation (3.8) over the vector field V_1, is obtained as

$$\tilde{S}(V_2,V_3) = S(V_2,V_3) + \beta(V_2,V_3) - (n-1)\alpha(V_2,V_3). \quad (3.13)$$

Putting $V_2 = V_3 = e_i$ in the above equation, where $\{e_i, 1 \le i \le n\}$, be an orthonormal basis of the tangent space at each point of Kenmotsu manifold and taking summation over i, we get

$$\tilde{r} = r + b - (n-1)a \quad (3.14)$$

where $\tilde{r} = \sum_{i=1}^{n} \tilde{S}(e_i e_i)$, $b = \sum_{i=1}^{n} \beta(e_i e_i)$ and $a = \sum_{i=1}^{n} \alpha(e_i e_i)$.

We identify the 1-form A of the connection $\widetilde{D}$ with the 1-form of the Kenmotsu manifold in order to expand the outview of the projective semi-symmetric connection $\widetilde{D}$ on

the manifold. According to the concept of equality between A and η from Equations (3.5) and (3.6), we can write

$$\widetilde{D}_{V_1}V_2 = D_{V_1}V_2 + \tfrac{1}{2}(c+1)\eta(V_2)V_1 + \tfrac{1}{2}(c-1)\eta(V_1)V_2, \quad (3.15)$$

where, $c = \frac{n-1}{n+1}$

Now, it can be seen that

$$\left(\widetilde{D}_{V_1}\eta\right)(V_2) = \left(D_{V_1}\eta\right)(V_2) - c\eta(V_1)\eta(V_2). \quad (3.16)$$

Using the relation $\left(D_{V_1}\eta\right)(V_2) = \left(D_{V_2}\eta\right)(V_1)$, in the above equation, it gives

$$\left(\widetilde{D}_{V_1}\eta\right)(V_2) = \left(\widetilde{D}_{V_2}\eta\right)(V_1) \quad (3.17)$$

The connection $\widetilde{D}$ given by the equation (3.5) becomes special projective semi-symmetric connection [Pal *et al.*, 2015]. It can also be verified that for such a projective semi-symmetric connection, the tensor β vanishes and the tensor α is symmetric, i.e.,

$$\beta(V_1, V_2) = 0\,, \quad \alpha(V_1, V_2) = \alpha(V_2, V_1). \quad (3.18)$$

According to these, the curvature tensor, the tensor α , ricci tensor and scalar curvature given by equations (3.8), (3.9), (3.10) and (3.14) become

$$\widetilde{K}(V_1, V_2)V_3 = K(V_1, V_2)V_3 + \alpha(V_1, V_3) - \alpha(V_2, V_3)V_1, \quad (3.19)$$

$$\alpha(V_1, V_2) = \lambda\left(D_{V_1}\eta\right)(V_2) - \lambda^2\eta(V_1)\eta(V_2), \quad (3.20)$$

$$\tilde{S}(V_2, V_3) = S(V_2, V_3) - (n-1)\alpha(V_2, V_3), \quad (3.21)$$

and

$$\tilde{r} = r + b - (n-1)a, \quad (3.22)$$

where $\lambda = \frac{1}{2}(c+1)$.

Let us consider a Kenmotsu manifold of dimension-n admitting the special projective semi-symmetric connection $\widetilde{D}$ having 1-form η as a recurrent and satisfies the following relation:

$$\left(\widetilde{D}_{V_1}\eta\right)(V_2) = \eta(V_1)\eta(V_2) \quad (3.23)$$

In order of the assumption, the equation (3.20) yields

$$\alpha(V_1, V_2) = (\lambda - \lambda^2)\eta(V_1)\eta(V_2). \quad (3.24)$$

By replacing $V_2 = \xi$ in the above equation, it reduces to the following

$$\alpha(V_1, \xi) = (\lambda - \lambda^2)\eta(V_1) \quad (3.25)$$

Definition 3.1 A non-flat n-dimensional Kenmotsu manifold (M_n, g), $(n > 2)$, is said to be quasi-Einstein manifold if its Ricci tensor S of type (0, 2) is not identically zero and satisfies

$$S(V_1, V_2) = \gamma g(V_1, V_2) + \delta\eta(V_1)\eta(V_2) \;\forall\; V_1, V_2 \in T(M_n), \quad (3.26)$$

for smooth functions γ and $\delta(\neq 0)$ where η is a non-zero 1-form associated with Riemannian metric g and associated unit vector field ξ [Chaki and Maithy, 2000].

Theorem 3.1 Let (M_n, g), $(n > 2)$ be an n-dimensional Kenmotsu manifold endowed with a special projective semi-symmetric connection $\widetilde{D}$ whose 1-form η is a recurrent. If the manifold is Ricci flat with respect to $\widetilde{D}$, then it is a certain class of quasi-Einstein manifold.

Proof: Let us suppose that the Kenmotsu manifold (M_n, g), $(n>2)$ is Ricci flat with respect to the special projective semi-symmetric connection $\widetilde{D}$ whose 1-form η is a recurrent, i.e, $\tilde{S} = 0$ and therefore, taking account of equation (3.24), the equation (3.21) gives

$$S(V_2, V_3) = (\lambda - \lambda^2)(n-1)\eta(V_2)\eta(V_3) \quad (3.27)$$

which shows that the manifold is a certain class of quasi-Einstein manifold.

WEYL PROJECTIVE CURVATURE TENSOR OF KENMOTSU MANIFOLD

Theorem 4.1 An n-dimensional Kenmotsu manifold M_n admitting special projective semi-symmetric connection $\widetilde{D}$ satisfy the following relations:

1. $'\widetilde{K}(V_1, V_2, V_3, V_4) = -'\widetilde{K}(V_2, V_1, V_3, V_4)$.
2. $'\widetilde{K}(V_1, V_2, V_3, V_4) \neq '\widetilde{K}(V_1, V_2, V_4, V_3)$.
3. $'\widetilde{K}(V_1, V_2, V_3, V_4) \neq '\widetilde{K}(V_3, V_4, V_1, V_2)$.
4. $\widetilde{K}(V_1, V_2)V_3 + \widetilde{K}(V_2, V_3)V_1 + \widetilde{K}(V_3, V_1)V_2 = 0$.

Proof: Taking the inner product on both sides of equation (3.19) with respect to V_4, we get

$$'\widetilde{K}(V_1, V_2, V_3, V_4) = K(V_1, V_2, V_3, V_4) + \alpha(V_1, V_3)g(V_2, V_4) - \alpha(V_2, V_3)g(V_1, V_4),$$

for all $V_1, V_2, V_3, V_4 \in T(M_n)$

where $'\widetilde{K}(V_1, V_2, V_3, V_4) = g(\widetilde{K}(V_1, V_2)V_3, V_4)$ and $'K(V_1, V_2, V_3, V_4) = g(K(V_1, V_2)V_3, V_4)$.

In considering equation (3.19) and curvature properties of K, we can easily verify the results (i), (ii) and (iii). With the help of equation (3.19) and Bianchi's first identity, we get

$$\widetilde{K}(V_1, V_2)V_3 + \widetilde{K}(V_2, V_3)V_1 + \widetilde{K}(V_3, V_1)V_2 = 0,$$

which shows that Riemannian curvature tensor with respect to $\widetilde{D}$ satisfies the Bianchi's first identity.

Definition 4.1: The Wely projective tensor W of a Kenmotsu manifold M_n with respect to Riemannian connection D

[Mishra, 1984] is given as

$$W(V_1,V_2)V_3 = K(V_1,V_2)V_3 - \frac{1}{n-1}\{S(V_2,V_3)V_1 - S(V_1,V_3)V_2\}. \quad (4.1)$$

The Weyl projective curvature tensor $\widetilde{W}$ with respect to the projective semi-symmetric connection $\widetilde{D}$ on Kenmotsu manifold is obtained as

$$\widetilde{W}(V_1,V_2)V_3 = \widetilde{K}(V_1,V_2)V_3 - \frac{1}{n-1}\{\tilde{S}(V_2,V_3)V_1 - \tilde{S}(V_1,V_3)V_2\} \quad (4.2)$$

With the help of equation (3.19), the equation (4.2) gives

$$\begin{aligned}\widetilde{W}(V_1,V_2)V_3 &= K(V_1,V_2)V_3 + \alpha(V_1,V_3)V_2 - \alpha(V_2,V_3)V_1 \\ &\quad -\frac{1}{n-1}\{S(V_2,V_3)V_1 - (n-1)\alpha(V_2,V_3)V_1 \\ &\quad -S(V_1,V_3)V_2 + (n-1)\alpha(V_1,V_3)V_2\}. \end{aligned} \quad (4.3)$$

As a consequence of equations (3.18) and (4.1), the above equation yields

$$\widetilde{W}(V_1,V_2)V_3 = W(V_1,V_2)V_3. \quad (4.4)$$

Theorem 4.2 The Ricci tensor of special projective semi-symmetric connection of a Kenmotsu manifold vanishes if and only if $W(V_1,V_2)V_3 = \widetilde{K}(V_1,V_2)V_3$.

Proof: Suppose that

$$W(V_1,V_2)V_3 = \widetilde{K}(V_1,V_2)V_3 \quad (4.5)$$

From (4.1), we have

$$\widetilde{K}(V_1,V_2)V_3 = K(V_1,V_2)V_3 - \frac{1}{n-1}\{S(V_2,V_3)V_1 - S(V_1,V_3)V_2\}.$$

In view of the equation (3.19), the above equation takes the form

$$\{S(V_2,V_3) - (n-1)\alpha(V_2,V_3)\}V_1 = \{S(V_1,V_3) - (n-1)\alpha(V_1,V_3)\}V_2.$$

Using equation (3.21) in the above equation, we get

$$\tilde{S}(V_2,V_3)V_1 = \tilde{S}(V_1,V_3)V_2$$

which is contradiction, gives $\tilde{S}(V_2,V_3) = 0$

Conversely, suppose that $\tilde{S}(V_2,V_3) = 0$, then from the equation (3.12), we have

$$S(V_2,V_3) = (n-1)\alpha(V_2,V_3).$$

Using this in the equation (4.1), we have

$$W(V_1,V_2)V_3 = K(V_1,V_2)V_3 + \alpha(V_1,V_3)V_2 - \alpha(V_2,V_3)V_1,$$

which in view of equation (3.19) gives

$$W(V_1,V_2)V_3 = \widetilde{K}(V_1,V_2)V_3.$$

Theorem 4.3 The Wely-projective curvature tensor $\widetilde{W}$ with respect to special projective semi-symmetric connection $\widetilde{D}$ satisfies

$$\widetilde{W}(V_1,V_2)V_3 + \widetilde{W}(V_2,V_3)V_1 + \widetilde{W}(V_3,V_1)V_2 = 0. \quad (4.6)$$

Proof: Utilizing equations (4.2), (3.19), (3.21) and following Bianchi's first identity of curvature tensor K, we immediately get the result (4.6).

CONCLUSION

The main propose of this work is to study the curvature tensors equipped with special projective semi-symmetric connection on Kenmotsu manifolds. We have found that a Kenmotsu manifold of dimension n, ($n > 2$) admittimg special projective semi-symmetric connection whose 1-form is a recurrent, becomes a certain class of quasi-Einstein manifold if the manifold is Ricci flat with respect to this connection.

REFERENCES

Bartolotti E (1930) Sulla geometric della variata a connection affine. Ann.di Mat. 4(8):53- 101.

Chaki MC and Maithy RK (2000) On quasi-Einstein manifolds. Publ. Math. Debrecen, 57: 297-306.

Chaubey SK and Ojha RH (2012) On Semi-symmetric non-metric connection. Filomat 26(2): 269-275.

Friedmann A and Schouten JA (1924) Uber die Geometric der halbsymmetricshen Ubertragung, Math. Zeitschr. 21: 211-221.

Kenmotsu K (1972) A class of contact Riemannian manifold. Tohoku Math. J. 24: 93-103.

Mishra RS (1984) Structure on a differential manifold and their applications. Chandrama Prakashan, Allahabad, India.

Pal SK, Pandey MK and Singh RN (2015) On a type of Projective semi-symmetric connection. Int. J. Anal Appl. (N.S.)7(2):153-161.

Singh RN, Pandey Shravan K and Pandey Giteshwari (2021) On semi-symmetric nonmetric connection in a Cosymplectic manifold, Journal of International Academy of Physical Sciences.16(1):1-16.

Yano K (1970) On Semi-Symmetric metric connection, Rev Roumaine Math.Pures Appl. 15:1579-1586.

Zhao P (2008) Some properties of projective semi-symmetric connections. Int. Math. Forum 3(7): 341-347.

Zhao P and Song H (2001), An invariant of the projective semi-symmetric connection, Chinese Quarterly J. Math. 16(4):49-54.

Science and Technology Journal Vol. 12 Issue: 2 June 2024 ISSN: 2321-3388

Generalized ϧ-almost Ricci Soliton in Almost Kenmotsu Manifold

Robert Sumlalsanga[1,*], J.P. Singh[2], and M. Sundararajan[3]
[1,3]Department of Mathematics and Computer Science, Mizoram University, Aizawl-796004, India
[2]Department of Mathematics, Central University of South Bihar, Gaya-824236, India
*E-Mail: robertsuma23@gmail.com
*Corresponding Author

Abstract—The primary objective of this paper is to give geometric classifications for ϧ-almost Ricci soliton associated with almost Kenmotsu manifolds. Initially, we demonstrate that a complete Kenmotsu manifold with a generalized ϧ-almost Ricci structure is either η-Einstein or its soliton is steady under specific circumstances. Subsequently, it is proved that a Kenmotsu manifold $(k, \varsigma)'$, with $h' \neq 0$, it shows expansion with a generalized ϧ-almost Ricci metric.

MSC:53C15, 53C25, 53D10

Keywords: ϧ-almost, Ricci soliton, Almost Kenmotsu manifold, hyperbolic space, warped product.

INTRODUCTION

In recent years, there has been significant attention devoted to the examination of Einstein manifolds and their various extensions within academic circles. Commenced the exploration of Ricci solitons within the field of contact geometry in their research (Sinha and Sharma, 2011). Subsequently, (Tripathi, 2008), along with (Bejan and Crasmareanu, 2011) among others, conducted extensive research on Ricci solitons within contact metric manifolds.

In the later part of the 20th century, Hamilton introduced the concept of Ricci flow. To elaborate, one-parameter family is taken which has a metrics g defined on a Riemannian manifold M^d over an interval $I \subset \mathbb{R}$, where S represents the metric's Ricci tensor g, the equation governing the Ricci flow is as follows:

$$\frac{\partial}{\partial t} g = -2Sg.$$

(Hamilton, 1982) established the existence of a unique solution g to the aforementioned equation for any smooth metric g defined on a compact Riemannian manifold M^d. This solution is defined over some $[0, \in)$, where $\in > 0$, which has the condition $g(0) = g_0$.

For the scenario of complete non-compact manifolds, (Shi, 1989) demonstrated the existence of a complete solution under the stipulation that the sectional curvatures of (M^d, g) remain bounded.

As a Riemannian metric, a Ricci soliton satisfies

$$S + \frac{1}{2} L_V g - \lambda g = 0.$$

In the equation provided, The symbol L_V denotes the Lie derivative operator with respect to the vector field V. The tensor S signifies the Ricci tensor corresponding to the metric g, while λ represents a constant. It's evident that a trivial Ricci soliton corresponds to Einstein metric where V can be zero or a vector field that kills. When V is the gradient of a smooth function f, denoted as $V = df$, the soliton is termed a gradient Ricci soliton (Cao, 2010). This characterization enables certain geometers to regard the equation as the defining condition for a Ricci soliton. For further insights into Ricci flow, readers are directed to consult (Chow *et. al.*, 2006).

$$S + \nabla^2 f = \lambda g$$

where S denotes the Ricci tensor of the metric g, and λ is a constant.

https://doi.org/10.22232/stj.2024.12.02.08

(Gomes *et. al.*, 2017) introduced the concept of ɧ-almost Ricci soliton for the first time. The authors have conducted a comprehensive study on the properties and characterization of ɧ-almost Ricci solitons, contributing to the literature on this subject. The study may involve discovering new findings, refining existing theorems, or presenting alternative proofs for known results. The paper also discusses various aspects of ɧ-almost Ricci solitons, including their geometric interpretations, stability characteristics, classification outcomes, and connections to other geometric constructs. The authors also explore the potential applications of ɧ-almost Ricci solitons in mathematics and theoretical physics, highlighting their importance in understanding the geometric evolution and curvature properties of Riemannian manifolds. This research offers valuable insights into the theory of ɧ-almost Ricci solitons and their relevance in contemporary geometers. Also, in a subsequent paper (Ghosh *et. al.*, 2008) studied gradient Ricci soliton of a non-Sasakian (k, ς) - contact manifold. Inspired by these conditions, this paper investigates ɧ-almost Ricci solitons in the framework of almost Kenmotsu manifolds.

The definition of a ɧ-almost Ricci soliton, as determined by their findings, is characterized by a complete Riemannian manifold (M^d, g) furnished with a vector field $X_1 \in X_1(M)$, a soliton function $\lambda : M \to \mathbb{R}$, and a function $\mathfrak{h}: M \to \mathbb{R}$. These are all smooth and satisfy the equation as given in (Gomes et. al., 2017).

$$S + \frac{\mathfrak{h}}{2} L_V g = \lambda g$$

For ease of reference, ɧ-almost Ricci soliton is denoted as $(M^d, g, X_1, \mathfrak{h}, \lambda)$. In the scenario where λ is constant, it is simply termed an ɧ-Ricci soliton. If $L_V g = L_{\nabla u} g$ holds true for some smooth function $u : M \to \mathbb{R}$, then $(M^d, g, \nabla u, \mathfrak{h}, \lambda)$ is referred to as a gradient ɧ-almost Ricci soliton having u as the potential function. Under this condition, we can expressed equation (1.2) as:

$$S + \mathfrak{h}\nabla^2 f = \lambda g$$

the notation $\nabla^2 f$ signifies the Hessian of the function f.

The paper is structured as: After preliminaries in section 3, among other results, we establish that if an almost Kenmotsu manifold enable a gradient ɧ-almost Ricci soliton, then it is a steady Ricci soliton and the manifold admits a Einstein manifold. In this section we also establish that if a Kenmotsu manifold exhibits a non-trivial gradient ɧ-almost generalized Ricci soliton with a potential vector field is η-Einstein if it is pointwise collinear with the Reeb vector field ξ. As a consequence we obtain that if a Kenmotsu manifold features a non-trivial gradient ɧ-almost generalized Ricci soliton with vanishing potential vector field and is Einstein, which are denoted by $QX_1 = -2dX_1$ with $\lambda = -m$. In the last section Additionally, we demonstrate that if a $(k, \varsigma)'$ -almost Kenmotsu manifold that $h' \neq 0$ admits a metric of an ɧ-almost Ricci soliton with $\varphi V=0$, then the soliton is expanding provided $\lambda = \frac{4d^2}{1+d} > 0$.

PRELIMINARIES

A smooth manifold M of dimension $(2d + 1)$ is designated as an almost contact metric manifold provided it accommodates a (1, 1)-tensor field φ, a unit vector field ξ (referred to as the Reeb vector field), and a 1-form, η satisfying the following conditions:

$$\varphi^2 X_1 = -X_1 + \eta(X_1)\xi, \eta(X_1) = g(X_1, \xi) \tag{2.1}$$

for all vector fields X_1 on M. Additionally, a Riemannian metric g is considered an associated (or compatible) metric if it fulfills the condition:

$$g(\varphi X_1, \varphi X_2) = g(X_1, X_2) - \eta(X_1)\eta(X_2) \tag{2.2}$$

for all vector fields X_1, X_2 on M. The combination of an almost contact manifold $M^{2d+1}(\varphi.\ \xi,\ \eta)$ with a compatible metric g is referred to as an almost contact metric manifold (Blair, 2010).

An almost Kenmotsu manifold is characterized as an almost contact metric manifold satisfying $d\eta = 0$ and $\Phi = 2\eta \wedge \Phi$, where the fundamental 2-form Φ of the almost contact metric manifold is given by $\Phi(X_1, X_2) = g(X_1, \varphi X_2)$ for any vector fields X_1, X_2 on M (Vanhecke and Janssens, 1981). On the product $M^{2d+1} \times \mathbb{R}$ of an almost contact metric manifold M^{2d+1} and $\mathbb{R}$, an almost complex structure J is defined as:

$$J\left(X_1, f\frac{d}{dt}\right) = \left(\varphi X_1 - f\xi, \eta(X_1)\frac{d}{dt}\right)$$

where t is the coordinate of $\mathbb{R}$, f is a C^∞ function on $M^{2d+1} \times \mathbb{R}$, and X_1 is a vector field tangent to M^{2d+1}. If J is integrable, it is a normal structure in almost contact metric on the manifold M^{2d+1}. A normal almost Kenmotsu manifold is denoted as a Kenmotsu manifold (Kenmotsu, 1972). An almost Kenmotsu manifold transforms into a Kenmotsu manifold if and only if

$$(\nabla_{X_1}\varphi)X_2 = g(\varphi X_1, X_2)\xi - \eta(X_2)\varphi X_1$$

for any vector fields X_1, X_2 on M^{2d+1}. On a Kenmotsu manifold, the following conditions are satisfied (Kenmotsu, 1972):

$$\nabla_{X_1}\xi = X_1 - \eta(X_1)\xi, \tag{2.3}$$

$$R(X_1, X_2)\xi = \eta(X_1)X_2 - \eta(X_2)X_1, \tag{2.4}$$

$$Q\xi = -2d\xi \tag{2.5}$$

for any vector fields X_1, X_2 on M^{2d+1}. In this case, the (1,2) Ricci tensor S has a Ricci operator Q associated with it, where each and every vector field on M^{2d+1}, X_1, X_2 is represented by the notation $S(X_1, X_2) = g(QX_1, X_2)$. R stands for the curvature tensor of g. It has been demonstrated that a Kenmotsu manifold can be locally represented as a warped product $I \times_f N^{2d}$, where I is an open interval with coordinate t, $f = ce^t$ denotes the warping function for some positive constant c, and N^{2d} is a Kählerian manifold (Kenmotsu, 1972).

On an almost Kenmotsu manifold, the following formula holds true: (Dileo and Pastore, 2007), (Dileo and Pastore, 2009):

$$\nabla_{X_1}\xi = \varphi^2 X_1 - \varphi h X_1 \tag{2.6}$$

for any vector field X_1 on M^{2d+1}. We introduce two operators, denoted by h and l, defined as $h = \frac{1}{2}L_\xi\varphi$ and $l = R(., \xi)\xi$, respectively. These operators satisfy the conditions: $h\xi = h'\xi = 0$, $Tr.h = Tr.h' = 0$, $h\varphi = -\varphi h$ where $h' = h.\varphi$, and $Tr.$ denotes the trace operation.

NORMAL ALMOST KENMOTSU MANIFOLD

Within the current section, exploration of Kenmotsu manifolds that exhibit a generalized ℏ-almost Ricci soliton structure is done. Initially, we give various illustrations of Kenmotsu manifolds accommodating a generalized ℏ-almost Ricci metric.

Theorem 3.1 *If a gradient ℏ-almost generalized Ricci soliton is embodied by Kenmotsu metric manifold $M^{2d+1}(\phi,\xi,\eta, g)$, then it either conforms to being η-Einstein or the soliton remains steady.*

Proof. From equation (1.3), we obtain

$$\hbar\nabla_{X_1}Df = \lambda X_1 - QX_1 \tag{3.1}$$

Performing the covariant derivative of equation (3.1) with respect to an arbitrary vector field X_2, we derive:

$$\begin{aligned}\hbar\nabla_{X_2}\nabla_{X_1}Df = &-\tfrac{1}{\hbar}(\hbar X_2)(\lambda X_1 - QX_1) + (\lambda X_2)X_1 + \lambda\left(\nabla_{X_2}X_1\right)\\ &-(\nabla_{X_2}Q)X_1 - Q(\nabla_{X_2}X_1)\end{aligned} \tag{3.2}$$

Employing equations (3.1) and (3.2) in the relation

$$\hbar R(X_1, X_2)Df = \hbar\nabla_{X_1}\nabla_{X_2}Df - \hbar\nabla_{X_2}\nabla_{X_1}Df - \hbar\nabla_{[X_1,X_2]}Df$$

we derive

$$\begin{aligned}\hbar R(X_1, X_2)Df = &-\tfrac{1}{\hbar}(X_1\hbar)(\lambda X_2 - QX_1) + (\lambda X_1)X_2 - \left(\nabla_{X_1}Q\right)X_2\\ &+\tfrac{1}{\hbar}(X_2\hbar)(\lambda X_1 - QX_1) - (\lambda X_2)X_1 + (\nabla_{X_2}Q)X_1\end{aligned} \tag{3.3}$$

By taking the inner product of equation (3.3) with ξ and utilizing equation (2.5), we obtain:

$$\begin{aligned}g(\hbar R(X_1, X_2)Df, \xi) = &(X_1\lambda)\eta(X_2) - (X_2\lambda)\eta(X_1) - g\left(\left(\nabla_{X_2}Q\right)X_1, \xi\right)\\ &-g((\nabla_{X_1}Q)X_2, \xi) + \frac{1}{\hbar}(\lambda + 2d)[(X_2\hbar)\eta(X_1)\\ &-(X_1\hbar)\eta(X_2)].\end{aligned} \tag{3.4}$$

Again, taking the inner product of equation (2.4) with Df and substituting it into the equation (3.4), we get:

$$\begin{aligned}&\tfrac{1}{\hbar}(\lambda + 2d)[(X_2\hbar)(\eta(X_1) - (X_1\hbar)\eta(X_2)] - (X_2\lambda)\eta(X_1)\\ &+g\left(\left(\nabla_{X_1}Q\right)X_2, \xi\right) + (X_1\lambda)\eta(X_2) + g\left(\left(\nabla_{X_2}Q\right)\xi, X_1\right)\\ &-\eta(X_2)g(X_1, Df) + \hbar\eta(X_1)g(X_2, Df)] = 0.\end{aligned} \tag{3.5}$$

Substituting X_2 with ξ in equation (3.5) and utilizing the relation $(\nabla_\xi)X_2 = -2QX_2 - 4dX_2$ (see Lemma 2 of (Ghosh, 2019)) we have

$$[\sigma(\xi h) - h(\xi\lambda) + h^2(\xi f)]\eta(X_1) = \sigma(X_1h) - h(X_1\lambda) + h^2(X_1f) \tag{3.6}$$

where $\sigma = \lambda + 2d$. Contracting equation (3.3) along an arbitrary vector field X_1 results in

$$\hbar S(Df, X_2) = \tfrac{1}{\hbar}S(X_2, D\hbar) - 2d(X_2\lambda) + \tfrac{1}{2}(X_2r) + \tfrac{1}{\hbar}(2d\lambda - r) \tag{3.7}$$

Substituting X_2 with ξ and employing equation (2.5) in equation (3.7), we obtain:

$$-2d\hbar^2(\xi f) - (2d\sigma - (r + 2d(2d + 1))(\xi\hbar) + 2d\hbar(\xi\lambda) - \tfrac{1}{2}\hbar(\xi r) = 0. \tag{3.8}$$

Moreover, on the Kenmotsu manifold, we have $\xi r = -2(r+2d)(2d+1)$ (Lemma 2 of (Ghosh, 2019)). Using into the above equation yields:

$$2d[\sigma(\xi\hbar) - \hbar(\xi\lambda) + \hbar^2(\xi f)] = r + 2d(2d + 1)(\hbar + \xi\hbar). \tag{3.9}$$

Substituting X_2 with ξ in equation (3.3) and employing $\hbar R(X_1,\xi)X_2 = \hbar g\xi - \hbar\eta(X_2)X_1$, we get

$$\begin{aligned}\frac{1}{\hbar}[\sigma(X_1\hbar) - \hbar(X_1\lambda) + \hbar^2(X_1f)]\xi = &\hbar\eta(\xi f)X_1 - (\xi\lambda)X_1\\ &+\tfrac{1}{\hbar}(\lambda X_1)(\xi\hbar) - \left(1 + \tfrac{\xi\hbar}{\hbar}\right)QX_1 - 2dX_1.\end{aligned} \tag{3.10}$$

Combining equations (3.6), (3.9), and (3.10), we derive the following relation:

$$\begin{aligned}&2d[\hbar(\xi f)X_1 + \lambda X_1/\hbar(\xi\lambda) - (\xi\lambda)X_1 - \left(1 + \tfrac{\xi\hbar}{\hbar}\right)QX_1 - 2dX_1]\\ &= \frac{1}{\hbar}(r + 2d(2d + 1))(\hbar + \xi\hbar)\eta(X_1)\xi.\end{aligned} \tag{3.11}$$

Suppose $\mathfrak{h}$ is constant and $\xi\mathfrak{h} = 0$. Utilizing equation (3.9), we have:

$$\big(r + 2d(2d+1)\big)\eta(X_1)\xi = -\frac{2d\lambda}{\mathfrak{h}}(\xi\lambda)X_1 + \big(r + 2d(2d+1)\big)X_1 - 2dQX_1 - 4d^2X_1.$$

Let $X_1 = \xi$ and $\lambda(\xi\lambda) = 0$. If $\lambda = 0$, the soliton remains steady. If $\xi\lambda = 0$, then the manifold is η-Einstein. This brings the proof to a close.

Theorem 3.2 *A Kenmotsu manifold is η-Einstein if it has a non-trivial gradient $\mathfrak{h}$-almost generalized Ricci soliton for which the potential vector field is pointwise collinear with the Reeb vector field ξ.*

Proof. Assume V which represents a potential vector field and the Reeb vector field ξ are pointwise collinear, such that $V = F\xi$, in which the smooth function F. By performing a covariant differentiation along an arbitrary vector field X_1 of $V = F\xi$ and employing equation (2.3), we obtain:

$$\nabla_{X_1}V = (X_1F)\xi + F(-\varphi^2X_1 - \varphi\mathfrak{h}X_1). \tag{3.12}$$

Substituting equation (3.12) into equation (1.2) yields:

$$\frac{\mathfrak{h}}{2}[(X_1F)\eta(X_2) + (X_2F)\eta(X_1)] + \mathfrak{h}Fg(\mathfrak{h}'X_1, X_2) - \mathfrak{h}F\eta(X_1)\eta(X_2) + S(X_1, X_2) = (\lambda - \mathfrak{h}F)g(X_1, X_2) \tag{3.13}$$

for any vector fields X_1 and X_2.

Substituting X_1, X_2 with ξ in equation (3.13) and employing equation (2.5), we get

$$\xi F = \frac{1}{\mathfrak{h}}(\lambda + 2d).$$

Furthermore, substituting X_2 with ξ and employing the final expression in equation (3.13), we have

$$X_1F = \frac{1}{\mathfrak{h}}(\lambda + 2n)\eta(X_1). \tag{3.14}$$

Contracting equation (3.13) and inserting it into the preceding equation (3.14), we have

$$r = 2(\lambda - \mathfrak{h}F - 1). \tag{3.15}$$

As a consequence of equations (3.14) and (3.15), Equation (3.13) simplifies to the following form:

$$QX_1 = \left(\frac{r}{2d} + 1\right)X_1 - \left(\frac{r}{2d} + 2d + 1\right)\eta(X_1)\xi \tag{3.16}$$

For any vector field X_1, thereby establishing the manifold as η-Einstein.

Assume that F is constant. From equation (3.14), it follows that $\lambda = -2d$. Substituting this value into equation (3.15), we deduce a constant r. Consequently, ξr vanishes, implying $r = -2d(2d + 1)$. Replacing r and λ with their respective values into equation (3.15), we find $F = 0$, which further implies $\lambda = -2d$.

Theorem 3.3 *If a Kenmotsu manifold features a non-trivial gradient $\mathfrak{h}$-almost generalized Ricci soliton with a vanishing potential vector field, then it is Einstein, denoted by $QX_1 - 2dX_1$ with $\lambda = -m$.*

NON-NORMAL ALMOST KENMOTSU MANIFOLD

If ξ, that Reeb vector field, is contained within the generalized (k, ς)-nullity distribution, then the almost Kenmotsu manifold $M^{(2d+1)}$ is refered to as a generalized almost Kenmotsu manifold (k, ς). i.e.,

$$k[\eta(X_2)X_1 - \eta(X_1)X_2] + \varsigma[\eta(X_2)hX_1 - \eta(X_1)hX_2] = R(X_1, X_2)\xi. \tag{4.1}$$

The condition holds true for all vector fields X_1, X_2 on M, with k and ς representing smooth functions defined on M. An almost Kenmotsu manifold $M^{(2d+1)}$ is termed a generalized $(k, \varsigma)'$-almost Kenmotsu manifold if the Reeb vector field ξ is part of the generalized $(k, \varsigma)'$-nullity distribution, which is defined as:

$$k[\eta(X_2)X_1 - \eta(X_1)X_2] + \varsigma[\eta(X_2)h'X_1 - \eta(X_1)h'X_2] = R(X_1, X_2)\xi \tag{4.2}$$

this condition applies to all vector fields X_1, X_2 on M, where k, ς denote smooth functions defined on M, and $h' = h \circ \varphi$ (Dileo and Pastore, 2009). Furthermore, if both k and ς are constants in equation (4.2), then M is referred to as a $(k, \varsigma)'$-almost Kenmotsu manifold (Dileo and Pastore,2009), (Wang and Liu, 2016), (Khatri and Singh, 2023). The following relations hold on a generalized (k, ς) or $(k, \varsigma)'$-almost Kenmotsu manifold with $h \neq 0$ (equivalently, $h' \neq 0$):

$$h'^2 = (k+1)\varphi^2, \quad h^2 = (k+1)\varphi^2, \tag{4.3}$$

$$Q\xi = 2dk\xi. \tag{4.4}$$

From equation (4.3), it follows that $k \leq -1$ and $v = \pm\sqrt{(-k-1)}$, where v represents an eigenvalue corresponding to the eigenvector $X_l \in D\big(D = Ker(\eta)\big)$ of h'. The equality holds if and only if $h = 0$ (equivalently, $h' = 0$). Therefore, $h' \neq 0$ if and only if $k < -1$.

Lemma 4.1 *(Wang and Liu, 2016) Consider $M^{2d+1}(\varphi, \xi, \eta, g)$ to be a generalized $(k, \varsigma)^1$-almost Kenmotsu manifold with $h' \neq 0$. For $d > 1$, the Ricci operator Q of M can be expressed as:*

$$-2dX_1 + 2d(k+1)\eta(X_1)\xi - [\varsigma - 2(d-1)h']X_1 = QX_1$$

for any vector field X_1 on M. Additionally, if k and ς are constants and $d \geq 1$, then $\varsigma = -2$, and thus

$$QX_1 = -2dX_1 + 2d(k+1)\eta(X_1)\xi - 2dh'X_1 \tag{4.5}$$

The scalar curvature of M for any vector field X_1 on M is $2d(k-2d)$ in both cases.

Theorem 4.2 *A soliton is said to be expanding if the metric of a (k, ς)′-almost Kenmotsu manifold with $h' \neq 0$ admits a ℏ-almost Ricci soliton with $\varphi V = 0$.*

Proof. Given the hypothesis $\varphi V = 0$, applying the operator φ yields $V = \eta(V)\xi$, that is, $V = F\xi$, where the function F is smooth. Equation (1.2) is obtained by calculating the final equation's covariant derivative along any vector field X_1 and adding it:

$$S(X_1, X_2) + \frac{\hbar}{2}[(X_1F)\eta(X_2) + (X_2F)\eta(X_1)] - Fg(h'^{X_1}, X_2) - \hbar F\eta(X_1)\eta(X_2) = (\lambda - \hbar F)g(X_1, X_2). \tag{4.6}$$

Substituting X_1 with ξ in equation (4.6) yields

$$\frac{\hbar}{2}(X_2F) = \left(\lambda + 2dk - \frac{\hbar}{2}(\xi F)\right)\eta(X_2) \tag{4.7}$$

for any vector field X_1 on M. Contracting equation (4.4) and utilizing a lemma, we obtain:

$$\hbar(\xi F) = (2d+1)(\lambda - 2\hbar F) - \hbar F(k+2) - \left(1 - \frac{\hbar F}{2d}\right)(2d(k-2d)). \tag{4.8}$$

Substituting $X_2$with ξ in equation (4.7) and combining it with equation (4.8) gives $F = \frac{d(\lambda+2d)}{\hbar(3d+1)}$. By inserting equation (4.7) into equation (4.6) and utilizing it in the lemma, we derive

$$\left[\frac{d(\lambda+2+8d)}{(3d+1)}\hbar X_1 + (\lambda - 2\hbar F)\varphi X_1\right](k+1) = 0. \tag{4.9}$$

Substituting X_1 with $h'X_1$ in equation (4.9) and considering $h' \neq 0$, we obtain $\lambda = \frac{4d^2}{1+d} > 0$. This concludes the proof, establishing that the soliton is expanding.

CONCLUSION

The study investigates almost Kenmotsu manifolds with gradient ℏ-almost Ricci solitons. It concluded that if a gradient is permitted by a manifold, ℏ-almost Ricci soliton, it must be an Einstein manifold, and the Ricci soliton must be steady. The analysis also showed that a Kenmotsu manifold with a non-trivial gradient ℏ-almost generalized η-Einstein is required for a Ricci soliton with a potential vector field collinear with the Reeb vector field. Additionally, if a manifold has a non-trivial gradient ℏ-almost generalized Ricci soliton with a vanishing potential vector field, Einstein manifold, that is. The study also found that the presence of an ℏ-almost Ricci soliton with certain conditions leads to an expanding soliton. These findings contribute to our understanding of almost Kenmotsu manifolds and their associated solitons.

REFERENCES

Bejan C. L. and Crasmareanu M. (2011). "Ricci solitons in manifolds with quasi-constant curvature", *Publ. Math. Debrecen* **78(1)**, 235–243.

Blair D. E. (2010). "Riemannian geometry of contact and symplectic manifolds", 2nd *edition, Progress in Mathematics, 203, Birkh¨auser Boston, Ltd., Boston, MA*.

Cao H.-D. (2010). "Recent progress on Ricci solitons, in Recent advances in geometric analysis", *1–38, Adv. Lect. Math. (ALM), 11, Int. Press, Somerville, MA, 2010*.

Chow B., Lu P. , Ni L. (2006). "Hamilton's Ricci flow", *Graduate Studies in Mathematics* **77.**

Dileo G. and Pastore A. M. (2007). "Almost Kenmotsu manifolds and local symmetry", *Bull. Belg. Math. Soc.* **Simon Stevin 14(2)**, 343–354.

Dileo G. and Pastore A. M. (2009). "Almost Kenmotsu manifolds and nullity distributions", *J. Geom.* **93(1-2)**, 46–61.

Ghosh, A. (2019). "Ricci soliton and Ricci almost soliton within the framework of Kenmotsu manifold", *Carpathian Math. Publ.* **11(1)**, 56–69.

Ghosh, A. (2008). "Contact metric manifolds with η– parallel torsion tensor", *Ann. Glob. Anal. Geom.* **34**, 287–299.

Gomes J. N., Wang Q., Xia C. (2017). "On the ℏ-almost Ricci soliton", *J. of Geom. and Phy.* **114**, 216–222.

Hamilton R. S. (1982). "Three-manifolds with positive Ricci curvature", *J. Diff. Geom.* **17(2)**, 255–306.

Kenmotsu K. (1972). " A class of almost contact Riemannian manifolds", *Tohoku Math. J.* **24(2)**, 93–103.

Khatri M. and Singh J. P. (2023). "Generalized m-quasi-Einstein structure in almost Kenmotsu manifolds", *Bull. Korean Math. Soc.* **60**, 717–732.

Sinha B. B. and Sharma R. (2011). "On Para-A-Einstein manifolds", *Publications De L'Institut Mathematique, Nouvelle serie, tome* **34(48)**, 211–215.

Shi W. -X. (1989). "Deforming the metric on complete Riemannian manifolds", *J. Diff. Geom.* **30(1)**, 223–301.

Tripathi M. M. (2008). "Ricci solitons in contact metric manifolds", arXiv:0801, 4222v1, [math DG].

Vanhecke L. and Janssens D. (1981). "Almost contact structures and curvature tensors", *Kodai Math. J.* **4(1)**, 1–27.

Wang Y. and Liu X. (2016). "On almost Kenmotsu manifolds satisfying some nullity distributions", *Proc. Nat. Acad. Sci. India Sect. A*, **86(3)**, 347–353.

Science and Technology Journal Vol. 12 Issue: 2 June 2024 ISSN: 2321-3388

Velocity and Energy Distribution at Corrugated Interface of Monoclinic Medium

Lalvohbika Jongte[1], Lianngenga Rengsi[2], and Lalhriattira Fanai[3]
[1,2,3]Department of Mathematics and Computer Science, Mizoram University, Aizawl-796004, India
E-mail: [1]vohbikajongte@gmail.com, [2]rengsi.9@gmail.com, [3]fanailalhriattira@gmail.com
*Corresponding Author

Abstract—This paper investigates how elastic waves reflect and transmit when a plane *qSV*-wave encounters a corrugated interface between two different monoclinic elastic half-spaces. The corrugations on the interface lead to the generation of both regular and irregular reflected and transmitted waves, each traveling at distinct phase velocities. The study aims to determine the velocities and energy ratios of these waves, which are affected by various factors including the angle of incidence, the elastic constants of the materials, the properties of the interface's corrugation, and the frequency parameter. To analyse the problem, we performed computations for a specific model $x_3 = d\cos(px_2)$, obtaining the velocities and energy ratios. The paper also discusses the influence of corrugation and the frequency parameter on these quantities.

Keywords: Reflection, transmission, corrugated, monoclinic, velocity, energy ratio.

INTRODUCTION

Elastic wave propagation is utilized in various domains, including seismology and earthquake engineering, Non-Destructive Testing (NDT), medical imaging (such as ultrasonography), telecommunications, and geotechnical engineering. Elastic waves arise whenever there is a sudden stress imbalance within or on the surface of an elastic medium. Virtually any abrupt deformation or displacement within the medium triggers such waves (Lay and Wallace 1995). Among natural phenomena, earthquakes stand out as significant sources, with the analysis of the waves they propagate being pivotal in enhancing our comprehension of the earth's internal composition and the mechanisms underlying seismic events (Pujol 2003). The release of energy at the source of the earthquake and propagate through the earth generates the seismic waves which carry valuable information about the event and the subsurface. The velocity, amplitude, and energy ratios of seismic waves have profound effects on seismic wave propagation. These parameters influence wave speed, refraction, reflection, attenuation, energy transfer, damage potential, signal detection, and energy partitioning. Understanding and analysing these effects are crucial for seismology, earthquake engineering, and subsurface exploration.

Numerous scholars have undertaken research on the circumstances of reflection and refraction at corrugated interfaces, and this area of study continues to captivate their interest. Several notable findings concerning the behaviour of reflection and transmission at corrugated interfaces, as well as within monoclinic materials, have already been published. From the paper of *On the dynamical theory of gratings*, Rayleigh (1907) investigated the waves propagation on a regularly corrugated surface and he observed that the depth of the corrugations is small in comparision with the length of the waves. Rice (1951) studied the reflection of electromagnetic waves from a rough or corrugated surface, and found that the Fourier components of the surface waves whose wavelengths are much greater than that of the electromagnetic wave tends to produce attenuation through scattering, while the

 https://doi.org/10.22232/stj.2024.12.02.09

guiding action of the surface is due to the components of shorter wavelength. From the investigation of the reflection of elastic waves at the corrugated surface, Sato (1955) observed that when the wavelength of the corrugations become large, the reflected waves exhibit an increase in the number of spectral components. In the study by Abubakar (1962), the scattering of *qSV* and *qP* waves at a rough boundary surface was examined. The researcher found that the reflected waves include both specularly reflected waves and several diffracted waves, which propagate in horizontal directions, then this effect is particularly pronounced when the wavelength of the incident wave is much larger than that of the surface wave. In addition to the specularly reflected *P* and *SV* -waves, whose amplitudes are independent of the surface's curvature, there are scattered waves traveling in various directions (Abubakar 1963). By applying the Rayleigh's procedure, Asano (1960, 1961) also observed that the effect of corrugated interface on reflection is larger than that on the refraction of elastic waves. Levy and Deresiewicz (1967) expanded upon Asano's research work by examining a layered medium with irregular internal interfaces. They observed that for the case of a corrugated bottom surface, the reflection and transmission amplitudes exhibit the same qualitative features as the transmission and reflection amplitudes, respectively, due to a corrugated top surface. Paul and Campillo (1988) conducted an investigation into the influence of minor-scale irregularities on elastic wave reflections at a corrugated interface. Their findings indicated that the presence of these irregularities scarcely affects the intensity of reflected *P* waves. In monoclinic media, for plane waves propagating in arbitrary directions within the plane of symmetry, *SH* waves are transverse, while *SV* waves are not purely transverse, and *P* waves are not purely longitudinal. This implies that pure longitudinal and pure transverse waves can only propagate in specific directions (Singh 1999; Singh and Khurana 2001).

The reflection coefficient plays an important role in the study of wave propagation. It helps to understand how waves behave when encountering interfaces or boundaries between different media. The reflection coefficient quantifies the portion of an incident wave that gets reflected back upon encountering such a boundary. The transmission coefficient is employed when analyzing wave propagation in a medium with discontinuities. It characterizes the amplitude, intensity, or total power of the transmitted wave in relation to the incident wave. Nayfeh (1991) derived the expressions for the reflection and transmission coefficients in the isotropic media and examined the behaviour of these coefficients for varying angle of incidence and propagation direction angles. The reflection coefficients of *P* and *SV*-waves in a monoclinic media was derived by Chattopadhyay and Choudhury (1995), they also observed that this medium have significant effect on the reflection coefficients. When the waves propagated in a monoclinic medium, the material constants have a considerable effect on the reflection and transmission coefficients of *P* and *SV*-waves (Chattopadhyay and Saha 1996). In the study conducted by Saha *et al*. (2020), they examined the behaviour of reflection and refraction of a plane wave at the interface between two functionally graded incompressible monoclinic media. The analysis took into account on the influence of initial stress and the presence or absence of gravity in each medium. The reflection and transmission coefficients of *SH*-waves at a corrugated interface between two anisotropic and between two monoclinic elastic half spaces are investigated separately by Tomar and Kaur (2003, 2007). They found that the impact of these coefficients on transverse isotropy is greatest at normal incidence. Additionally, the reflection and transmission coefficients are significantly affected by both the surface corrugation and the elastic properties of the media. They also studied the propagation of shear waves at a corrugated interface between anisotropic elastic and visco-elastic solid half-spaces, and then found that the effect of reflection and transmission coefficients are minimum near the normal incidence and maximum near the grazing incidence (Tomar and Kaur 2007). The reflection and transmission coefficients of *qP*-waves at a corrugated interface between two different elastic half-spaces of monoclinic type are derived by Singh and Tomar (2007), and observed that the coefficients corresponding to regularly reflected and transmitted waves are found to be greater than that of the irregularly reflected and transmitted waves. In a corrugated interface between two dissimilar pre-stressed elastic half spaces, the coefficients corresponding to irregularly reflected and transmitted waves are proportional to the amplitude of the corrugated interface and are also influenced significantly by the initial stresses of the half-spaces (Singh and Tomar 2008). Yu and Dravinski (2009) investigated the plain strain model for scattering of elastic waves by a completely embedded scatterer with a rough surface. Other research papers concerning the reflection and transmission of waves at free and rigid boundaries, as well as at the corrugated nature of different medium were

published by Mciver and Urka (1995), Mandal and Das (1996), Chattopadhyay *et al.* (1996), Singh and Lalvohbika (2018), Pandit *et al.* (2017), Prasad *et al.* (2017), Hermans (2003), Lalvohbika and Singh (2019), Singh *et al.* (2020), Gupta *et al.* (2022).

This paper aims to determine the phase velocities of waves and the energy distribution related to the reflection and transmission of elastic waves when a plane *qSV*-wave encounters a corrugated interface between two different monoclinic elastic half-spaces. The velocities and energy ratios are influenced by various factors, including the angle of incidence, the materials' elastic constants, the characteristics of the interface's corrugation, and the frequency parameters. To analyze this, we computed the velocities and energy ratios for a specific model and then examined how the corrugation and frequency parameters affect these quantities.

GOVERNING EQUATION

In a homogeneous anisotropic elastic material of monoclinic type, the consecutive relations with the x_2x_3-plane are given by (Singh and Khurana 2001)

$$T_{ii} = \sum_{j=1}^{3} c_{ij}e_{jj} + 2c_{i4}e_{23}, i = 1,2,3,$$

$$T_{12} = 2(c_{55}e_{13} + c_{56}e_{12}),\ T_{13} = 2(c_{56}e_{13} + c_{66}e_{12}),\ \ T_{23} = \sum_{k=1}^{4} c_{k4}e_{kk} + 2c_{44}e_{23} \tag{1}$$

where T_{ij}, for *i, j = 1, 2, 3* are stress tensors, c_{ij}, for *i, j = 1, 2, ..., 5, 6* are elastic constants and e_{ij} is the strain tensor given by

$$2e_{ij} = u_{i,j} + u_{j,i},$$

The equation of motion without body forces are given by

$$T_{ij,j} = \rho\frac{\partial^2 u_i}{\partial t^2}, \quad (i, j = 1,2,3) \tag{2}$$

where u_i are components of displacement and ρ is density of the medium.

Now, considering two dimensional wave propagation in the x_2x_3-plane so that

$$u_1 = 0 \ \text{ and } \ u_{i,1} \equiv 0 \tag{3}$$

By using (3) and the stress tensors of (1), the equations of motion (2) may be written as

$$c_{22}\frac{\partial^2 u_2}{\partial x_2^2} + c_{44}\frac{\partial^2 u_2}{\partial x_3^2} + c_{24}\frac{\partial^2 u_3}{\partial x_2^2} + c_{34}\frac{\partial^2 u_3}{\partial x_3^2} + 2c_{24}\frac{\partial^2 u_2}{\partial x_2 x_3} + (c_{23} + c_{24})\frac{\partial^2 u_3}{\partial x_2 x_3} = \rho\frac{\partial^2 u_2}{\partial t^2}, \tag{4}$$

$$c_{24}\frac{\partial^2 u_2}{\partial x_2^2} + c_{34}\frac{\partial^2 u_2}{\partial x_3^2} + c_{44}\frac{\partial^2 u_3}{\partial x_2^2} + c_{33}\frac{\partial^2 u_3}{\partial x_3^2} + 2c_{34}\frac{\partial^2 u_3}{\partial x_2 x_3} + (c_{23} + c_{24})\frac{\partial^2 u_2}{\partial x_2 x_3} = \rho\frac{\partial^2 u_3}{\partial t^2}. \tag{5}$$

The solution of these Eqs. (4) and (5) may take in the form

$$\{u_2, u_3\} = \{\mathcal{A}d_2, \mathcal{A}d_3\}e^{ik(vt - p_2x_2 - p_3x_3)}, \tag{6}$$

where A is the amplitude, v is the phase velocity, k is the wave number, p_i is the unit propagation vector and d_i is the unit displacement vector. Using the displacement components u_2 and u_3 of (6) in (4) and (5), we have the velocity equation

$$v_{1,2} = \sqrt{\frac{\Lambda + \Theta \pm \sqrt{(\Lambda - \Theta)^2 + 4\Xi^2}}{2\rho}}, \tag{7}$$

where,

$$\Lambda = c_{22}p_2^2 + c_{44}p_3^2 + 2c_{34}p_2p_3,$$
$$\Xi = c_{24}p_2^2 + c_{34}p_3^2 + (c_{23} + c_{44})p_2p_3,$$
$$\Theta = c_{44}p_2^2 + c_{33}p_3^2 + 2c_{34}p_2p_3. \tag{8}$$

Here, v_1 and v_2 represents the phase velocity of *qP* and *qSV*-waves respectively.

SOLUTION AND FORMULATION OF THE PROBLEM

Consider the Cartesian coordinate system in x_2x_3-plane where x_1 and x_2-axis are lying horizontally, and the x_3-axis perpendicular to the x_1x_2-plane. The two dissimilar homogeneous monoclinic elastic half-spaces are denoted as $\mathcal{M} = \{(x_2, x_3) : x_2 \epsilon R, x_3 \epsilon [\xi, \infty)\}$ and $\mathcal{M}' = \{(x_2, x_3) : x_2 \epsilon R, x_3 \epsilon (-\infty, \xi)\}$. In this context, $x_3 = \xi(x_2)$ defines the separation between the two half-spaces, where $\xi(x_2)$ is a periodic function of x_2 that is independent of x_1 and has a mean value of zero. The elastic constants, stress tensors, and displacement components in medium $\mathcal{M}'$ are indicated with primes, while those in medium $\mathcal{M}$ are shown without primes. The Fourier series expansion of $\xi(x_2)$ is provided as follows

$$\xi(x_2) = \sum_{n=1}^{\infty}(\xi_n e^{inpx_2} + \xi_{-n}e^{-inpx_2}), \tag{9}$$

where $\xi_{\pm n}$ are the coefficients of series expansion of order n, p is the wave number and $\imath = \sqrt{-1}$.

Let us consider the reflection and transmission of elastic waves resulting from the incidence of a plane *qSV*-wave at the corrugated interface $x_3 = \xi(x_2)$. We assume that a plane *qSV*-wave is propagating within the half-space $\mathcal{M}$ at an angle θ_0 with a constant amplitude $\mathcal{A}_0$. Due to irregular interface, this incident wave generates both regularly and

irregularly reflected waves, as well as transmitted waves of *qSV* and *qP* types. The displacement components of reflected and transmitted waves for the half-space $\mathcal{M}$ and $\mathcal{M}'$ are given by

$$u_2 = \mathcal{A}_o e^{\mathcal{P}_0} + \mathcal{A}_1 e^{\mathcal{P}} + \mathcal{A}_2 e^{\mathcal{Q}} + \sum_{n=1}^{\infty} \{\mathcal{A}_{1n}^{\pm} e^{\mathcal{P}_n^{\pm}} + \mathcal{A}_{2n}^{\pm} e^{\mathcal{Q}_n^{\pm}}\} \quad (10)$$

$$u_3 = \mathcal{B}_o e^{\mathcal{P}_0} + \mathcal{B}_1 e^{\mathcal{P}} + \mathcal{B}_2 e^{\mathcal{Q}} + \sum_{n=1}^{\infty} \{\mathcal{B}_{1n}^{\pm} e^{\mathcal{P}_n^{\pm}} + \mathcal{B}_{2n}^{\pm} e^{\mathcal{Q}_n^{\pm}}\} \quad (11)$$

$$u_{2'} = \mathcal{A}_3 e^{\mathcal{R}} + \mathcal{A}_4 e^{\mathcal{S}} + \sum_{n=1}^{\infty} \{\mathcal{A}_{3n}^{\pm} e^{\mathcal{R}_n^{\pm}} + \mathcal{A}_{4n}^{\pm} e^{\mathcal{S}_n^{\pm}}\}, \quad (12)$$

$$u_{3'} = \mathcal{B}_3 e^{\mathcal{R}} + \mathcal{B}_4 e^{\mathcal{S}} + \sum_{n=1}^{\infty} \{\mathcal{B}_{3n}^{\pm} e^{\mathcal{R}_n^{\pm}} + \mathcal{B}_{4n}^{\pm} e^{\mathcal{S}_n^{\pm}}\}, \quad (13)$$

where $(\mathcal{A}_1, \mathcal{B}_1)$ and $(\mathcal{A}_2, \mathcal{B}_2)$, are amplitude constants of the regularly reflected *qSV* and *qP*-waves at an angle θ_1 and θ_2 respectively, $(\mathcal{A}_{1n}^{\pm}, \mathcal{B}_{1n}^{\pm})$ and $(\mathcal{A}_{2n}^{\pm}, \mathcal{B}_{2n}^{\pm})$ are amplitude constants of the irregularly reflected *qSV* and *qP*-waves at an angle $\theta_{1n}^{\pm}$ and $\theta_{2n}^{\pm}$ respectively, $(\mathcal{A}_3, \mathcal{B}_3)$ and $(\mathcal{A}_4, \mathcal{B}_4)$ are amplitude constants of the regularly transmitted *qSV* and *qP*-waves at an angle θ_3 and θ_4 respectively, $(\mathcal{A}_{3n}^{\pm}, \mathcal{B}_{3n}^{\pm})$ and $(\mathcal{A}_{4n}^{\pm}, \mathcal{B}_{4n}^{\pm})$ are amplitude constants of irregularly transmitted *qSV* and *qP*-waves at angles $\theta_{3n}^{\pm}$ and $\theta_{4n}^{\pm}$ respectively.

The expressions of $\mathcal{P}_0, \mathcal{P}, \mathcal{P}_n^{\pm}, \mathcal{Q}, \mathcal{Q}_n^{\pm}, \mathcal{R}, \mathcal{R}_n^{\pm}, \mathcal{S}, \mathcal{S}_n^{\pm}$ are given as :

$$\mathcal{P}_0 = \iota k_0(v_0 t - x_2 sin\theta_0 + x_3 cos\theta_0), \mathcal{P} = \iota k_1(v_1 t - x_2 sin\theta_1 - x_3 cos\theta_1),$$
$$\mathcal{P}_n^{\pm} = \iota k_1(v_2 t - x_2 sin\theta_{1n}^{\pm} - x_3 cos\theta_{1n}^{\pm})$$
$$\mathcal{Q} = \iota k_2(v_1 t - x_2 sin\theta_2 - x_3 cos\theta_2), \quad \mathcal{Q}_n^{\pm} = \iota k_2(v_1 t - x_2 sin\theta_{2n}^{\pm} - x_3 cos\theta_{2n}^{\pm}),$$
$$\mathcal{R} = \iota k_{1'}(v_4 t - x_2 sin\theta_3 + x_3 cos\theta_3), \quad \mathcal{R}_n^{\pm} = \iota k_{1'}(v_4 t - x_2 sin\theta_{3n}^{\pm} + x_3 cos\theta_{3n}^{\pm}),$$
$$\mathcal{S} = \iota k_{2'}(v_3 t - x_2 sin\theta_4 + x_3 cos\theta_4), \quad \mathcal{S}_n^{\pm} = \iota k_{2'}(v_3 t - x_2 sin\theta_{4n}^{\pm} + x_3 cos\theta_{4n}^{\pm}). \quad (14)$$

The amplitude constants for reflection and transmission of the incident *qSV*-waves satisfy the following relations (Singh and Khurana 2001)

$$\mathcal{A}_0 = \Pi_0 \mathcal{B}_0, \quad \mathcal{A}_i = \Pi_i \mathcal{B}_i, \quad \mathcal{A}_{in}^{\pm} = \Pi_{3i}^{\pm} \mathcal{B}_{3i}^{\pm}, \quad i = 1,2,3,4, \quad (15)$$

where,

$$\Pi_0 = \frac{\Xi_0}{\rho v_0^2 - \Lambda_0}, \quad \Pi_i = \frac{\Xi_i}{\rho v_j^2 - \Lambda_i}, \quad \Pi_{in}^{\pm} = \frac{\Xi_{in}^{\pm}}{\rho v_j^2 - \Lambda_{in}^{\pm}}, i, j = 1,2, i \neq j,$$

$$\Pi_i = \frac{\Xi_i}{\rho' v_j^2 - \Lambda_i}, \quad \Pi_{in}^{\pm} = \frac{\Xi_{in}^{\pm}}{\rho' v_j^2 - \Lambda_{in}^{\pm}}, i, j = 3,4, i \neq j.$$

From Eq. (7), the velocity of incident, reflected and transmitted waves are given by

$$v_0 = \sqrt{\frac{\Lambda_0 + \Theta_0 - \sqrt{(\Lambda_0 - \Theta_0)^2 + 4\Xi_0^2}}{2\rho}},$$

$$v_i = \sqrt{\frac{\Lambda_i + \Theta_i \pm \sqrt{(\Lambda_i - \Theta_i)^2 + 4\Xi_i^2}}{2\rho}},$$

$$v_j = \sqrt{\frac{\Lambda_j + \Theta_j \pm \sqrt{(\Lambda_j - \Theta_j)^2 + 4(\Xi_j)^2}}{2\rho'}},$$

where $i = 1,2, j = 3,4$.

Using the values of Eqs. (14) and (15) into Eqs. (10)-(13), the displacement components can be written as below

$$u_2 = [\Pi_0 \mathcal{B}_0 e^{\iota\xi K_0} + \Pi_1 \mathcal{B}_1 e^{-\iota\xi K_1} + \Pi_2 \mathcal{B}_2 e^{-\iota\xi K_2} + \sum_{n=1}^{\infty} \Pi_{1n}^{\pm} \mathcal{B}_{1n}^{\pm} e^{\mp \iota m p x_2} e^{-\iota\xi K_{1n}^{\pm}} + \sum_{n=1}^{\infty} \Pi_{2n}^{\pm} \mathcal{B}_{2n}^{\pm} e^{\mp \iota m p x_2} e^{-\iota\xi K_{2n}^{\pm}}] e^{\iota(\omega t - P_0 x_2)}, \quad (16)$$

$$u_3 = [\mathcal{B}_0 e^{\iota\xi K_0} + \mathcal{B}_1 e^{-\iota\xi K_1} + \mathcal{B}_2 e^{-\iota\xi K_2} + \sum_{n=1}^{\infty} \mathcal{B}_{1n}^{\pm} e^{\mp \iota m p x_2} e^{-\iota\xi K_{1n}^{\pm}} + \sum_{n=1}^{\infty} \mathcal{B}_{2n}^{\pm} e^{\mp \iota m p x_2} e^{-\iota\xi K_{2n}^{\pm}}] e^{\iota(\omega t - P_0 x_2)}, \quad (17)$$

$$u_2' = [\Pi_3 \mathcal{B}_3 e^{\iota\xi K_3} + \Pi_4 \mathcal{B}_4 e^{\iota\xi K_4} + \sum_{n=1}^{\infty} \Pi_{3n}^{\pm} \mathcal{B}_{3n}^{\pm} e^{\mp \iota m p x_2} e^{\iota\xi K_{3n}^{\pm}} + \sum_{n=1}^{\infty} \Pi_{4n}^{\pm} \mathcal{B}_{4n}^{\pm} e^{\mp \iota m p x_2} e^{\iota\xi K_{4n}^{\pm}}] e^{\iota(\omega t - P_0 x_2)}, \quad (18)$$

$$u_3' = [\mathcal{B}_3 e^{\iota\xi K_3} + \mathcal{B}_4 e^{\iota\xi K_4} + \sum_{n=1}^{\infty} \mathcal{B}_{3n}^{\pm} e^{\mp \iota m p x_2} e^{\iota\xi K_{3n}^{\pm}} + \sum_{n=1}^{\infty} \mathcal{B}_{4n}^{\pm} e^{\mp \iota m p x_2} e^{\iota\xi K_{4n}^{\pm}}] e^{\iota(\omega t - P_0 x_2)}, \quad (19)$$

where, $P_0 = \frac{\omega sin\theta_0}{v_0}, \quad K_0 = \frac{\omega cos\theta_0}{v_0}, \quad K_i = \frac{\omega cos\theta_i}{v_j},$

$$K_{in}^{\pm} = \frac{\omega cos\theta_{in}^{\pm}}{v_i}, \quad i, j = 1,2, \ i \neq j.$$

$$K_j = \frac{\omega cos\theta_j}{v_i}, \quad K_{jn}^{\pm} = \frac{\omega cos\theta_{jn}^{\pm}}{v_i}, \quad i, j = 3,4, \ i \neq j.$$

BOUNDARY CONDITIONS

The boundary conditions at the corrugated interface require the continuity of both displacements and tractions (including normal and shear components), as described below

$$u_2 = u_{2'}, \quad u_3 = u_{3'}, \quad (20)$$

$$T_{32} + (T_{33} - T_{22})\xi' - T_{23}\xi'^2 = T_{32}' + (T_{33}' - T_{22}')\xi' - T_{23}'\xi'^2, \quad (21)$$

$$T_{33} - 2T_{23}\xi' + T_{22}\xi'^2 = T_{33}' - 2T_{23}'\xi' + T_{22}'\xi'^2, \quad (22)$$

where ξ' is the derivatives of ξ with respect to x_2.

Considering the corrugated interface's amplitude to be extremely small, we can disregard higher powers of ξ, as

follows

$$e^{\pm\iota\xi K_0} = 1 \pm \iota\xi K_0 - 0\left(\xi^2\right),\ e^{\pm\iota\xi K_1} = 1 \pm \iota\xi K_1 - 0\left(\xi^2\right). \tag{23}$$

Using Eqs. (16)-(19) and (23), we obtain a set of equations from the above boundary conditions (20)-(22) (Singh and Lalvohbika 2018)

$$\Im\Re = \nabla \quad \text{and} \quad \Im^{\mp}\Re^{\mp} = \nabla^{\mp}, \tag{24}$$

where,

$$\Im = \begin{bmatrix} 1 & 1 & -1 & -1 \\ \Pi_1 & \Pi_2 & -\Pi_3 & -\Pi_4 \\ y_1 & y_2 & -y_3 & -y_4 \\ z_1 & z_2 & -z_3 & -z_4 \end{bmatrix},\ \Re = \begin{bmatrix} \mathcal{B}_1/\mathcal{B}_0 \\ \mathcal{B}_2/\mathcal{B}_0 \\ \mathcal{B}_3/\mathcal{B}_0 \\ \mathcal{B}_4/\mathcal{B}_0 \end{bmatrix},\ \nabla = \begin{bmatrix} -1 \\ -\Pi_0 \\ -y_0 \\ -z_0 \end{bmatrix},$$

$$\Im^{\mp} = \begin{bmatrix} 1 & 1 & -1 & -1 \\ \Pi_{1n}^{\pm} & \Pi_{2n}^{\pm} & -\Pi_{3n}^{\pm} & -\Pi_{4n}^{\pm} \\ \kappa_5^{\mp} & \kappa_6^{\mp} & -\kappa_7^{\mp} & -\kappa_8^{\mp} \\ \Phi_5^{\mp} & \Phi_6^{\mp} & -\Phi_7^{\mp} & -\Phi_8^{\mp} \end{bmatrix},\ \Re^{\mp} = \begin{bmatrix} \mathcal{B}_{1n}^{\pm}/\mathcal{B}_0 \\ \mathcal{B}_{2n}^{\pm}/\mathcal{B}_0 \\ \mathcal{B}_{3n}^{\pm}/\mathcal{B}_0 \\ \mathcal{B}_{4n}^{\pm}/\mathcal{B}_0 \end{bmatrix},\ \nabla^{\mp} = \begin{bmatrix} \zeta_1^{\mp} \\ \zeta_2^{\mp} \\ \zeta_3^{\mp} \\ \zeta_4 \mp \end{bmatrix},$$

$$y_0 = (\Pi_0 c_{24} + c_{44})P_0 - (\Pi_0 c_{44} + c_{34})K_0,$$

$$y_i = \begin{cases} (\Pi_i c_{24} + c_{44})P_0 + (\Pi_i c_{44} + c_{34})K_i, & i = 1,2 \\ (\Pi_i c'_{24} + c'_{44})P_0 - (\Pi_i c'_{44} + c'_{34})K_i, & i = 3,4 \end{cases},$$

$$\zeta_1^{\mp} = \iota\xi_{\mp n}\left[-K_0 + \sum_{i=1}^{4} K_i \frac{\mathcal{B}_i}{\mathcal{B}_0}\right],$$

$$\zeta_3^{\mp} = \iota\left[\kappa_0^{\mp} + \kappa_1^{\mp}\frac{\mathcal{B}_1}{\mathcal{B}_0} + \kappa_2^{\mp}\frac{\mathcal{B}_2}{\mathcal{B}_0} - \kappa_3^{\mp}\frac{\mathcal{B}_3}{\mathcal{B}_0} - \kappa_4^{\mp}\frac{\mathcal{B}_4}{\mathcal{B}_0}\right],$$

$$z_0 = (\Pi_0 c_{23} + c_{34})P_0 - (\Pi_0 c_{34} + c_{33})K_0,$$

$$z_i = \begin{cases} (\Pi_i c_{23} + c_{34})P_0 + (\Pi_i c_{34} + c_{33})K_i, & i = 1,2 \\ (\Pi_i c'_{24} + c'_{44})P_0 - (\Pi_i c'_{44} + c'_{34})K_i, & i = 3,4 \end{cases},$$

$$\zeta_2^{\mp} = \iota\xi_{\mp n}\left[-\Pi_0 K_0 + \sum_{i=1}^{4} \Pi_i K_i \frac{\mathcal{B}_i}{\mathcal{B}_0}\right],$$

$$\zeta_4^{\mp} = \iota\left[\Phi_0^{\mp} + \Phi_1^{\mp}\frac{\mathcal{B}_1}{\mathcal{B}_0} + \Phi_2^{\mp}\frac{\mathcal{B}_2}{\mathcal{B}_0} - \Phi_3^{\mp}\frac{\mathcal{B}_3}{\mathcal{B}_0} - \Phi_4^{\mp}\frac{\mathcal{B}_4}{\mathcal{B}_0}\right],$$

$$\kappa_0^{\mp} = [\{\mp(c_{23} - c_{22})npP_0 + c_{24}P_0K_0 \pm (c_{34} - c_{24})npK_0 - c_{44}K_0^2\}\Pi_0 \pm (c_{33} - c_{23})npK_0 - c_{34}K_0^2 \mp (c_{34} - c_{24})npP_0 + c_{44}P_0K_0]\xi_{\mp n},$$

$$\kappa_1^{\mp} = [\{\mp(c_{23} - c_{22})npP_0 - c_{24}P_0K_1 \pm (c_{34} - c_{24})npK_1 - c_{44}K_1^2\}\Pi_1 \pm (c_{33} - c_{23})npK_1 - c_{34}K_1^2 \mp (c_{34} - c_{24})npP_0 - c_{44}P_0K_1]\xi_{\mp n},$$

$$\kappa_2^{\mp} = [\{\mp(c_{23} - c_{22})npP_0 - c_{24}P_0K_2 \pm (c_{34} - c_{24})npK_2 - c_{44}K_2^2\}\Pi_2 \pm (c_{33} - c_{23})npK_2 - c_{34}K_2^2 \mp (c_{34} - c_{24})npP_0 - c_{44}P_0K_2]\xi_{\mp n},$$

$$\kappa_3^{\mp} = [\{\mp(c'_{23} - c'_{22})npP_0 + c'_{24}P_0K_3 \pm (c'_{34} - c'_{24})npK_3 - c'_{44}K_3^2\}\Pi_3 \pm (c'_{33} - c'_{23})npK_3 - c'_{34}K_3^2 \mp (c'_{34} - c'_{24})npP_0 + c'_{44}P_0K_3]\xi_{\mp n},$$

$$\kappa_4^{\mp} = [\{\mp(c'_{23} - c'_{22})npP_0 + c'_{24}P_0K_4 \pm (c'_{34} - c'_{24})npK_4 - c'_{44}K_4^2\}\Pi_4 \pm (c'_{33} - c'_{23})npK_4 - c'_{34}K_4^2 \mp (c'_{34} - c'_{24})npP_0 + c'_{44}P_0K_4]\xi_{\mp n},$$

$$\kappa_5^{\mp} = -\left[\left\{c_{44}K_{1n}^{\pm} + c_{24}\left(P_0 \pm np\right)\right\}\Pi_{1n}^{\pm} + c_{34}K_{1n}^{\pm} + c_{44}\left(P_0 \pm np\right)\right],$$

$$\kappa_6^{\mp} = -\left[\left\{c_{44}K_{2n}^{\pm} + c_{24}\left(P_0 \pm np\right)\right\}\Pi_{2n}^{\pm} + c_{34}K_{2n}^{\pm} + c_{44}\left(P_0 \pm np\right)\right],$$

$$\kappa_7^{\mp} = \left\{c'_{44}K_{3n}^{\pm} - c'_{24}\left(P_0 \pm np\right)\right\}\Pi_{3n}^{\pm} + c'_{34}K_{3n}^{\pm} - c'_{44}\left(P_0 \pm np\right),$$

$$\kappa_8^{\mp} = \left\{c'_{44}K_{4n}^{\pm} - c'_{24}\left(P_0 \pm np\right)\right\}\Pi_{4n}^{\pm} + c'_{34}K_{4n}^{\pm} - c'_{44}\left(P_0 \pm np\right),$$

$$\Phi_0^{\mp} = [\{c_{23}P_0K_0 \pm 2c_{24}npP_0 - c_{34}K_0^2 - 2c_{44}npK_0\}\Pi_0 - c_{33}K_0^2 \mp 2c_{34}npK_0 - c_{34}P_0K_0 \pm 2c_{44}npP_0]\xi_{\mp n},$$

$$\Phi_1^{\mp} = [\{-c_{23}P_0K_1 \pm 2c_{24}npP_0 - c_{34}K_1^2 \pm 2c_{44}npK_1\}\Pi_1 - c_{33}K_1^2 \mp 2c_{34}npK_1 - c_{34}P_0K_1 \pm 2c_{44}npP_0]\xi_{\mp n},$$

$$\Phi_2^{\mp} = [\{-c_{23}P_0K_2 \pm 2c_{24}npP_0 - c_{34}K_2^2 \pm 2c_{44}npK_2\}\Pi_2 - c_{33}K_2^2 \mp 2c_{34}npK_2 - c_{34}P_0K_2 \pm 2c_{44}npP_0]\xi_{\mp n},$$

$$\Phi_3^{\mp} = [\{c'_{23}P_0K_3 \pm 2c'_{24}npP_0 - c'_{34}K_3^2 \mp 2c'_{44}npK_3\}\Pi_3 - c'_{33}K_3^2 \mp 2c'_{34}npk_3 + c'_{34}P_0K_3 \pm 2c'_{44}npP_0]\xi_{\mp n},$$

$$\Phi_4^{\mp} = [\{c'_{23}P_0K_4 \pm 2c'_{24}npP_0 - c'_{34}K_4^2 \mp 2c'_{44}npK_4\}\Pi_4 - c'_{33}K_4^2 \mp 2c'_{34}npK_4 + c'_{34}P_0K_4 \pm 2c'_{44}npP_0]\xi_{\mp n},$$

$$\Phi_5^{\mp} = -\left[\left\{c_{23}\left(P_0 \pm np\right) + c_{34}K_{1n}^{\pm}\right\}\Pi_{1n}^{\pm} + c_{33}K_{1n}^{\pm} + c_{34}\left(P_0 \pm np\right)\right],$$

$$\Phi_6^{\mp} = -\left[\left\{c_{23}\left(P_0 \pm np\right) + c_{34}K_{2n}^{\pm}\right\}\Pi_{2n}^{\pm} + c_{33}K_{2n}^{\pm} + c_{34}\left(P_0 \pm np\right)\right],$$

$$\Phi_7^{\mp} = \left\{-c'_{23}\left(P_0 \pm np\right) + c'_{34}K_{3n}^{\pm}\right\}\Pi_{3n}^{\pm} + c'_{33}K_{3n}^{\pm} - c'_{34}\left(P_0 \pm np\right),$$

$$\Phi_8^{\mp} = \left\{-c'_{23}\left(P_0 \pm np\right) + c'_{34}K_{4n}^{\pm}\right\}\Pi_{4n}^{\pm} + c'_{33}K_{4n}^{\pm} - c'_{34}\left(P_0 \pm np\right).$$

The spectrum theorem (Abubakar 1963) which gives the relations between the angle of regular and irregular waves and the Snell law (Asano 1960) for obtaining the above Eq. (24) are given by

$$sin\theta_m^{\pm} - sin\theta_i = \pm\frac{np}{\omega}v_i, n = 0,1,2,\ ,i = 1,2,3,4, \tag{25}$$

and $$\frac{sin\theta_i}{v_i.\theta_i} = \frac{1}{v_a},\ i = 0,1,2,3,4 \tag{26}$$

where (+ve) and (−ve) signs on both side of (25) are corresponds to each other, v_a being the apparent velocity.

On solving Eq. (24), we get the amplitude ratios of the regularly reflected and transmitted waves and irregularly reflected and transmitted waves due to the incident wave as

$$\frac{\mathcal{B}_i}{\mathcal{B}_0}=\frac{\wedge_{\mathcal{B}_i}}{\wedge},\ \frac{\mathcal{B}_{in}^{\pm}}{\mathcal{B}_0}=\frac{\wedge_{\mathcal{B}_{in}^{\pm}}}{\wedge^{\pm}}, \tag{27}$$

where the values of $\{\wedge_{\mathcal{B}_i},\wedge_{\mathcal{B}_{in}^{\pm}}\}, i=1,2,3,4$ are obtained by replacing the first, second, third and fourth columns of $\{\wedge,\wedge^{\pm}\}$ with column matrices $\{\nabla,\nabla^{\mp}\}$ respectively.

ENERGY DISTRIBUTION

Let us consider the energy distribution between the reflected and transmitted waves as they interact with the plane interface, $x_3 = 0$. The rate of transmission of energy per unit area is given by (Achenback 1973)

$$E=<T_{23}.\dot{u}_2>+<T_{33}.\dot{u}_3>+<T_{23}^{'}.\dot{u}_2^{'}>+<T_{33}^{'}.\dot{u}_3^{'}>. \tag{28}$$

By using the displacement vectors of (16), (17), (18) and (19), and the stress tensors (1) into (28), the incident energy, the energy of reflected and transmitted *qSV* and *qP*-waves are given by

$$E_0=\omega l_0\mathcal{B}_0^2 e^{2i\xi K_0}e^{2i(\omega t-P_0 t)},$$

$$E=\omega l_i\mathcal{B}_i^2 e^{-2i\xi K_i}e^{2i(\omega t-P_0 t)}+\sum_{n=1}^{\infty}\omega l_i^{\pm}(\mathcal{B}_{in}^{\pm})^2 e^{\mp 2inpx_2}$$
$$e^{-2i\xi K_{in}^{\pm}}e^{2i(\omega t-P_0 t)},\ i=1,2,3,4 \tag{29}$$

where

$$l_0=(c_{24}\Pi_0^2+c_{44}\Pi_0+c_{23}\Pi_0+c_{34})P_0-(c_{44}\Pi_0^2+2c_{34}\Pi_0+c_{33})K_0,$$

$$l_i=\begin{cases}(c_{24}\Pi_i^2+c_{44}\Pi_i+c_{23}\Pi_i+c_{34})P_0+(c_{44}\Pi_i^2+2c_{34}\Pi_i+c_{33})K_i, & i=1,2\\ (c'_{24}\Pi_i^2+c'_{44}\Pi_i+c'_{23}\Pi_i+c'_{34})P_0-(c'_{44}\Pi_i^2+2c'_{34}\Pi_i+c'_{33})K_i, & i=3,4\end{cases}$$

$$l_i^{\pm}=\begin{cases}(c_{24}(\Pi_{in}^{\pm})^2+c_{44}\Pi_{in}^{\pm}+c_{23}\Pi_{in}^{\pm}+c_{34})(P_0\pm np)+(c_{44}(\Pi_{in}^{\pm})^2\\ +2c_{34}\Pi_{in}^{\pm}+c_{33})K_{in}^{\pm}, & i=1,2\\ (c'_{24}(\Pi_{in}^{\pm})^2+c'_{44}\Pi_{in}^{\pm}+c'_{23}\Pi_{in}^{\pm}+c'_{34})(P_0\pm np)-(c'_{44}(\Pi_{in}^{\pm})^2\\ +2c'_{34}\Pi_{in}^{\pm}+c'_{33})K_{in}^{\pm}, & i=3,4\end{cases}.$$

Now, from the above expressions of different energy, the energy ratios of regularly and irregularly reflected and transmitted waves due to the incident wave is given by

$$E_i=\left|\frac{l_i}{l_0}\right|\left|\frac{\mathcal{B}_i}{\mathcal{B}_0}\right|^2 \tag{30}$$

and $E_i^{\pm}=\left|\frac{l_i^{\pm}}{l_0}\right|\left|\frac{\mathcal{B}_{in}^{\pm}}{\mathcal{B}_0}\right|^2,\forall\ i=1,2,3,4.$ (31)

Here, $(E_i,E_i^{\pm})$ represents the energy ratios for regularly and irregularly reflected and transmitted *qSV* and *qP*-wave.

SPECIAL CASE

If the corrugated interface is represented by only one cosine term i.e. $x_3 = dcospx_2$, with *d* as the amplitude of the corrugation, then we have

$$\xi_{\pm n}=\begin{cases}0, & if\ \ n\neq 1\\ \frac{d}{2}, & if\ \ n=1\end{cases}$$

The first order approximation of the amplitude ratios for irregularly reflected and transmitted waves using these values are obtained from Eq. (27) as follows

$$r_{i1}^{\pm}=\frac{\mathcal{B}_{i1}^{\pm}}{\mathcal{B}_0},\ \ i=1,2,3,4. \tag{32}$$

In the normal incidence, θ_0 = 0°, we obtain that $cos\theta_{11}^{+}=cos\theta_{11}^{-}$ and $cos\theta_{21}^{+}=cos\theta_{21}^{-}$ due to the Eqs. (25) and (26). Hence, the amplitude ratios for the irregularly reflection and transmission waves are related as follows

$$r_{i1}^{+}=r_{i1}^{-},\ \ i=1,2,3,4.$$

These outcomes are attributed to (Asano 1960) in relation to the relevant problem.

In the grazing angle of incidence, $\theta_0=\pi/2$, the amplitude ratios are given by Eq. (32) using the modifications given in the Appendix I. Then, the energy ratios are obtained from Eq. (31) by putting n=1.

PARTICULAR CASE

(a) Upon transforming the two monoclinic half-spaces, $\mathcal{M}$ and $\mathcal{M}'$, into transversely isotropic half-spaces, while aligning the axis of symmetry with the x-axis, we have

$$c_{12}=c_{13},\ \ c_{22}=c_{33},\ \ c_{55}=c_{66},\ \ c_{23}=c_{22}-2c_{44},$$
$$c_{14}=c_{24}=c_{34}=c_{56}=0,$$
$$c'_{12}=c'_{13},\ \ c'_{22}=c'_{33},\ \ c'_{55}=c'_{66},\ \ c'_{23}=c'_{22}-2c'_{44},$$
$$c'_{14}=c'_{24}=c'_{34}=c'_{56}=0$$

Using these values, the velocity equations can be expressed as follows:

$$v_1^2=\frac{\lambda+2\mu}{\rho},\ \ v_0^2=v_2^2=\frac{\mu}{\rho},\ \ v_3^2=\frac{\lambda'+2\mu'}{\rho'},\ \ v_4^2=\frac{\mu'}{\rho'}$$

These findings align with the principles of classical elasticity (Achenback 1973). Subsequently, the amplitude ratios are derived using the Eq. (27), incorporating the adjusted values provided in Appendix II. Similarly, the energy ratios associated with both regular and irregular waves are obtained using Eqs. (30) and (31), taking into account the modified values presented in Appendix III.

(b) When the interface corrugation is ignored, i.e., when $d = 0$, the problem simplifies to the interaction of elastic waves at a plane interface between two monoclinic elastic half-spaces. The energy ratios in this case correspond to the regularly reflected and transmitted waves and are described by Eq. (30).

(c) In the absence of the half-space $\mathcal{M}'$, the problem reduces only to the reflection of *qSV* and *qP* waves when an incident *qSV*-wave is considered. The energy ratios can be determined using Eq. (30), where the values are adjusted as follows

$$\wedge = y_1 z_2 - y_2 z_1,\ \wedge_{B_1} = y_2 z_0 - y_0 z_2,\ \wedge_{B_2} = y_0 z_1 - y_1 z_0$$

GEOMETRICAL INTERPRETATION

In the following section, we will analyse numerically the derived expressions for phase velocity and energy ratio, as discussed in the previous section. We take the following values of elastic constants and density for monoclinic medium (Singh and Lalvohbika 2018)

Table 1

For Half-space, $\mathcal{M}$ Lithium Tantalate			For Half-space, $\mathcal{M}'$ Lithium Tantalate		
c_{22}	2.33×10^{11}	Nm^{-2}	c'_{22}	2.03×10^{11}	Nm^{-2}
c_{23}	0.81×10^{11}	Nm^{-2}	c'_{23}	0.75×10^{11}	Nm^{-2}
c_{24}	0.11×10^{11}	Nm^{-2}	c'_{24}	-0.09×10^{11}	Nm^{-2}
c_{33}	2.75×10^{11}	Nm^{-2}	c'_{33}	2.45×10^{11}	Nm^{-2}
c_{34}	0	Nm^{-2}	c'_{34}	0	Nm^{-2}
c_{44}	0.94×10^{11}	Nm^{-2}	c'_{44}	1.06×10^{11}	Nm^{-2}
ρ	7400	Kgm^{-2}	ρ'	4700	Kgm^{-2}

To examine the effect of frequency parameters (ω/pv_0) and corrugated parameters (pd), we convert the parameters in dimensionless form by dividing with c_{44}. We consider a series of these parameters, (ω/pv_0) and (pd), to compare the variations of phase velocity and energy ratio with angle of incidence for the following series

ω/pv_0	80	90	100
pd	0.0001	0.0002	0.0003

Figure 1 represents the variation of velocities (v_1, v_2) and (v_3, v_4) for regularly reflected and transmitted waves respectively with respect to the angle of incidentce (θ_0). The findings reveal that the velocities of the transmitted waves are higher than those of the reflected waves at the same angle of incidence (θ_0). Furthermore, it is observed that the velocity of the *qP*-wave (v_1, v_3) exceeds those of the *qSV*-wave (v_2, v_4) for both reflection and transmission of wave propagation.

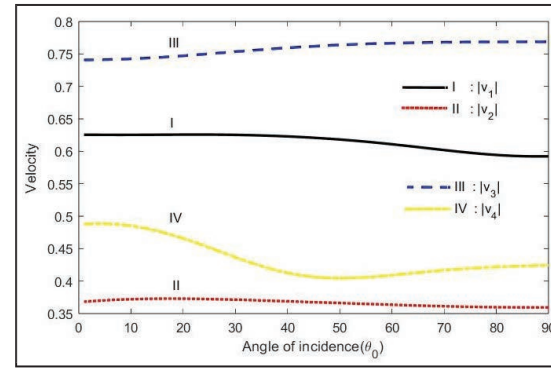

Fig. 1: Variation of Velocities with Respect to Angle of Incidence (θ_0).

Figure 2 depicts the variation of energy ratios ($|E_1|$, $|E_2|$), ($|E_3|$, $|E_4|$). for regularly reflected and transmitted *qSV* and *qP*-waves with respect to the angle of incidence (θ_0). The graph shows that initially, the values of $|E_1|$ and $|E_2|$ are nearly zero during the early stages of propagation. However, as θ_0 increases, they form parabolic curves. In the case of

transmitted waves, the energy ratio $|E_3|$ gradually decreases and reaches its minimum value around θ_0 = 85°. On the other hand, the energy ratio $|E_4|$ attains its minimum value at the grazing angle of incidence and approximately at 58°, and then rapidly increases as θ_0 continues to increase.

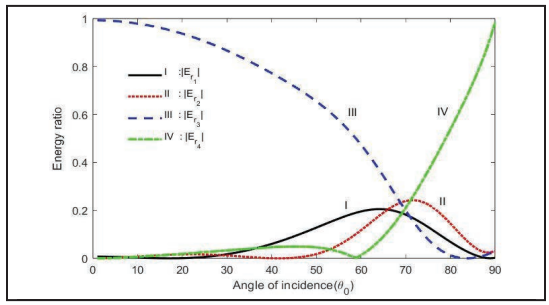

Fig. 2: Variation of Energy Ratios with Respect to Angle of Incidence (θ_0).

Effect of Frequency ω/pv_0 and Corrugation *pd* Parameters

By analysing Figs. 3 and 4, it can be observed that the energy ratios of irregularly reflected *qSV*-waves, namely $|E_1^+|$ and $|E_1^-|$, exhibit similar variations. These ratios increase as both the parameters ω/pv_0 and *pd* increase, with the influence of *pd* being more significant than ω/pv_0. In Figs. 3a and 3b, the energy ratio $|E_1^+|$ reaches its minimum value at the angles of incidence 15° and 84°, respectively. Similarly, in Figs. 4a and 4b, the energy ratio $|E_1^-|$ attains its minimum value at of 18° and 88°, respectively. The maximum effect of both parameters, ω/pv_0 and *pd*, occurs at 54° for $|E_1^+|$ and 58° for $|E_1^-|$, as illustrated in the figures.

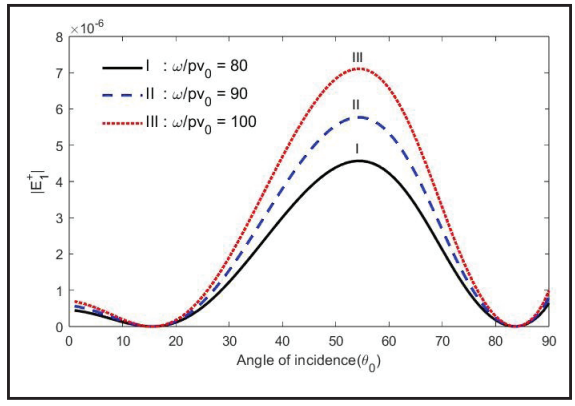

(a) Effect of ω/pv_0.

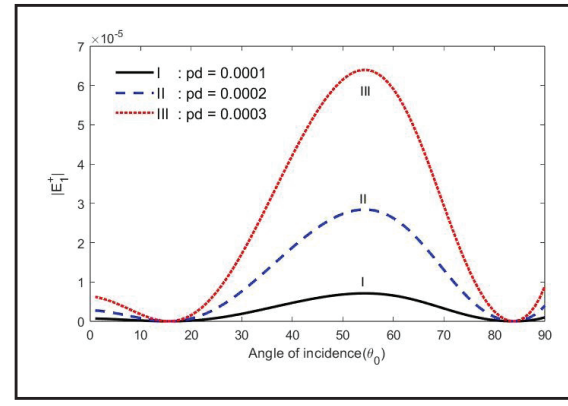

(b) Effect of *pd*.

Fig. 3: Variation of $|E_1^+|$ for Different Values of Parameters with (θ_0).

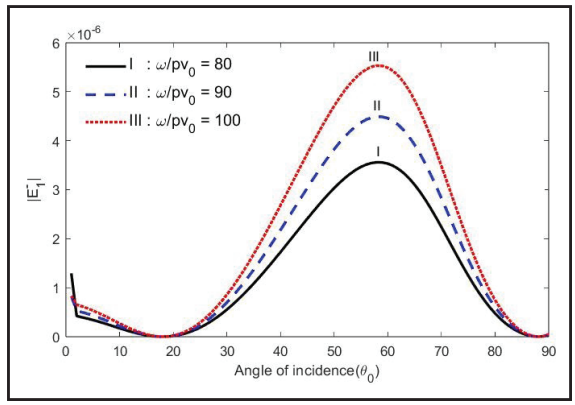

(a) Effect of ω/pv_0.

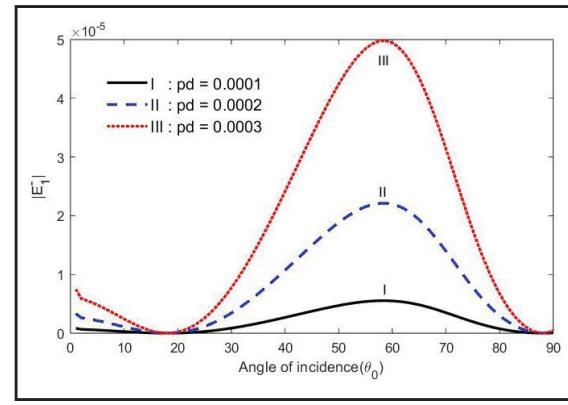

(b) Effect of *pd*.

Fig. 4: Variation of $|E_1^-|$ for Different Values of Parameters with (θ_0).

The analysis of Figs. 5 and 6 reveals an interesting pattern in the energy ratios of the irregularly reflected *qP*-waves, characterized by a corrugated nature. In Figs. 5a and 5b, the variation of $|E_2^+|$ exhibits a parabolic shape within the range of $0° < \theta_0 < 40°$ and $40° < \theta_0 < 90°$, while $|E_2^-|$ follows a similar pattern within the range of $2° < \theta_0 < 46°$ as shown in the Figs. 6a and 6b. The energy ratios increase as both ω/pv_0 and *pd* increase. Notably, $|E_2^+|$ reaches its minimum values at 0°, 40°, and 90°, while $|E_2^-|$ achieves its minimum values at 2° and 46°. In this variation, the parameter *pd* has a greater impact compared to ω/pv_0, and the maximum influence of both ω/pv_0 and *pd* occurs at 68° and 73° for $|E_2^+|$ and $|E_2^-|$ respectively.

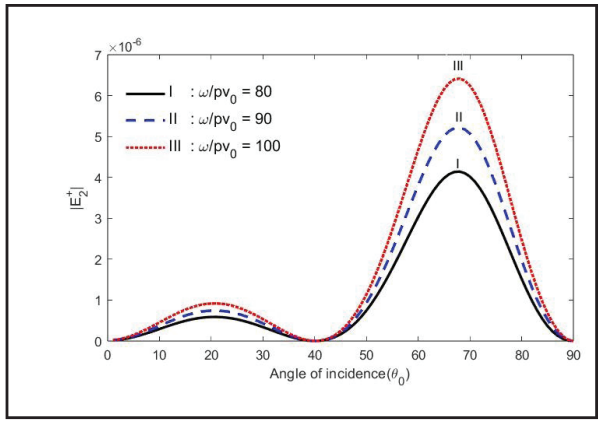

(a) Effect of ω/pv_0.

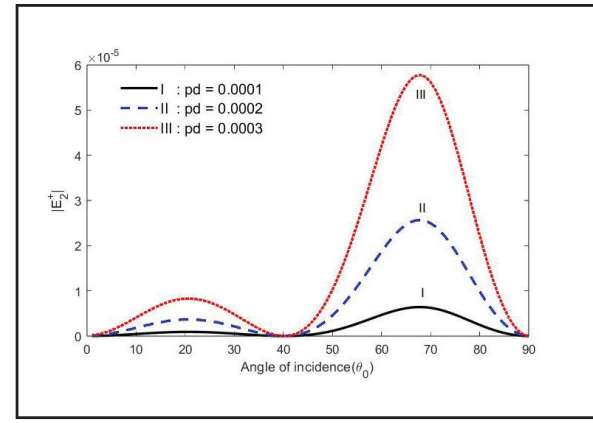

(b) Effect of *pd*.

Fig. 5: Variation of $|E_2^+|$ for Different Values of Parameters with (θ_0).

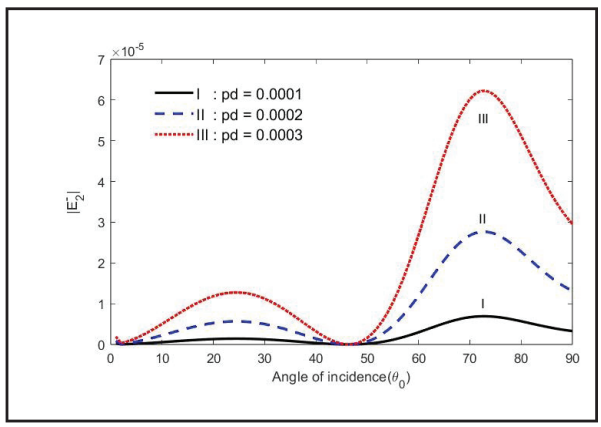

(a) Effect of ω/pv_0.

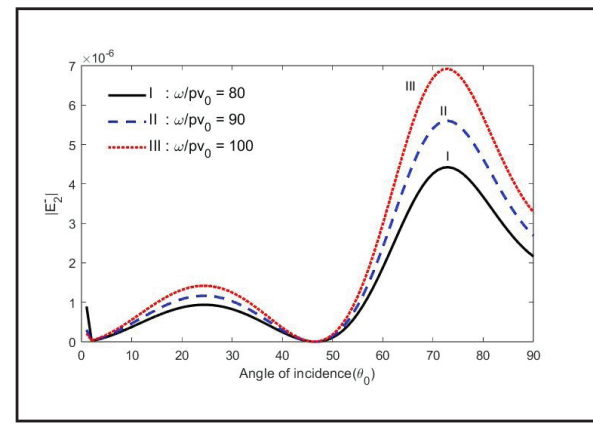

(b) Effect of *pd*.

Fig. 6: Variation of $|E_2^-|$ for Different Values of Parameters with (θ_0).

Figures 7 and 8 illustrate the variations in the energy ratios of the irregularly transmitted *qSV*-waves with respect to the angle of incidence. In Figs. 7a and 7b, the values of $|E_3^+|$ decrease beyond a certain point as θ_0 increases. A parabolic curve is formed within the range of $43° < \theta_0 < 73°$, and the minimum value of $|E_3^+|$ is observed at 43° and 73°. Subsequently, the curve increases as θ_0 increases, reaching its maximum value at the normal angle of incidence. In Figs. 8a and 8b, the curve of $|E_3^-|$ exhibits a sharp decrease within the range of $1° < \theta_0 < 3°$ and a gradual decrease in the range of $12° < \theta_0 < 55°$ and $67° < \theta_0 < 77°$. After these decrements, the curve increases for the rest of the interval of θ_0. Two peaks are observed at 12° and 67°, while two troughs are observed at 55° and 77°. From a comparative analysis of the curves represented by $|E_3^+|$ and $|E_3^-|$, it can be concluded that *pd* has a more significant effect than ω/pv_0, and the variation of these parameters is particularly influential at the initial stages of propagation.

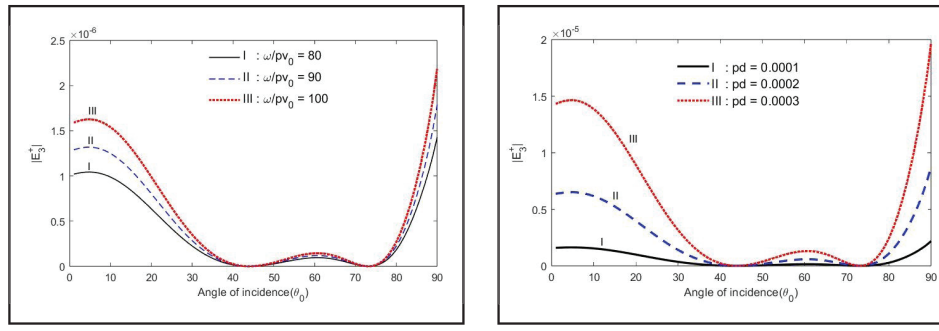

(a) Effect of ω/pv_0. **(b) Effect of *pd*.**

Fig. 7: Variation of $|E_3^+|$ for Different Values of Parameters with (θ_0).

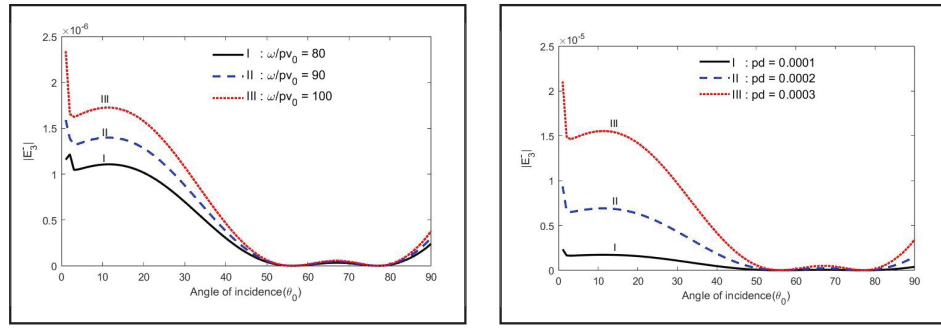

(a) Effect of ω/pv_0. **(b) Effect of *pd*.**

Fig. 8: Variation of $|E_3^-|$ for Different Values of Parameters with (θ_0).

The energy ratios, $|E_4^+|$ and $|E_4^-|$, of the corrugated transmitted *qP*-waves show interesting variations with respect to the incident angle, θ_0, as depicted in Figs. 9 and 10. Notably, both ratios exhibit similar patterns, which are influenced by the parameters ω/pv_0 and *pd.* Analysing the behaviour of the ratio $|E_4^+|$ which was shown in Figs. 9a and 9b, it gradually increases as both ω/pv_0 and *pd* change, then forming a parabolic curve within the range of $15°<\theta_0<70°$. However, beyond this range, the ratio experiences a sudden increase as θ_0 further increases. Examining the values of $|E_4^-|$ in Figs. 10a and 10b, it is observed that these values rapidly decrease within a narrow interval of $1°<\theta_0<3°$. However, in the broader range of $3°<\theta_0<70°$, the curves of $|E_4^-|$ form a parabolic shape with changes in both ω/pv_0 and *pd*. Subsequently, there is a sharp increase in the ratio as θ_0 approaches the grazing angle of incidence. The above analysis reveals that the effect of *pd* is more significant than that of ω/pv_0, and both parameters have minimal influence at the initial stages of wave propagation.

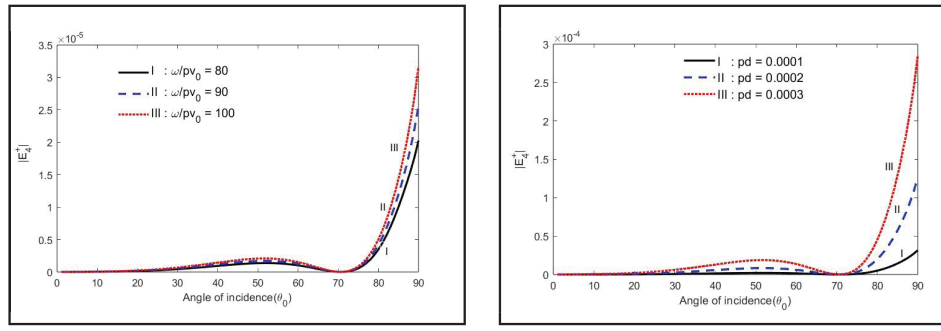

(a) Effect of ω/pv_0. **t(b) Effect of *pd*.**

Fig. 9: Variation of $|E_4^+|$ for Different Values of Parameters with (θ_0).

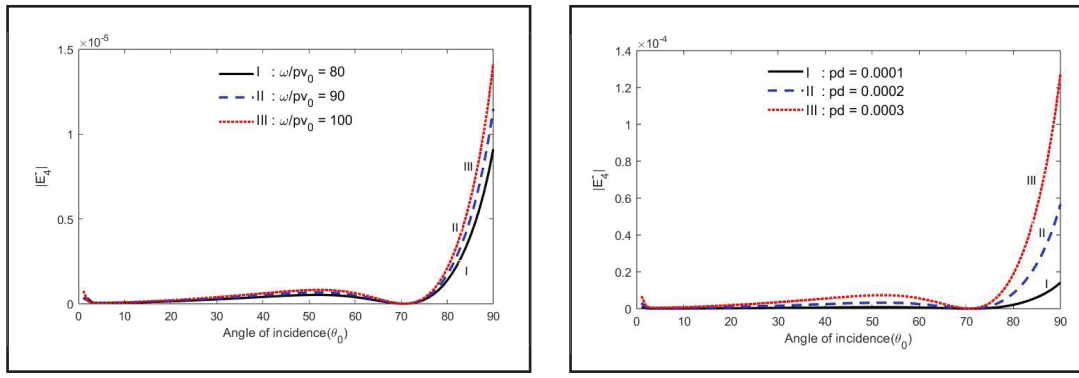

(a) Effect of ω/pv_0. **(b) Effect of *pd*.**

Fig. 10: Variation of $|E_4^-|$ for Different Values of Parameters with (θ_0).

In Fig. 11, the energy ratios corresponding to the regularly reflected and transmitted waves remain unaffected by changes in ω/pv_0 and *pd*. However, the energy ratios corresponding to the irregularly reflected and transmitted waves exhibit a nonlinear growth as ω/pv_0 and *pd* increase at different rates, as visually represented in Figs. 12 and 13.

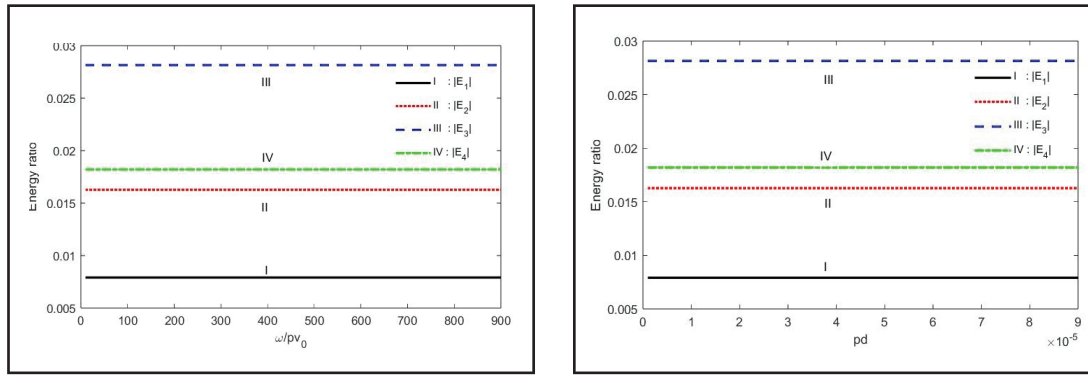

(a) **(b)**

Fig. 11: Variation of Energy Ratios of Regularly Reflected and Transmitted Waves with Respect to ω/pv_0 and *pd*.

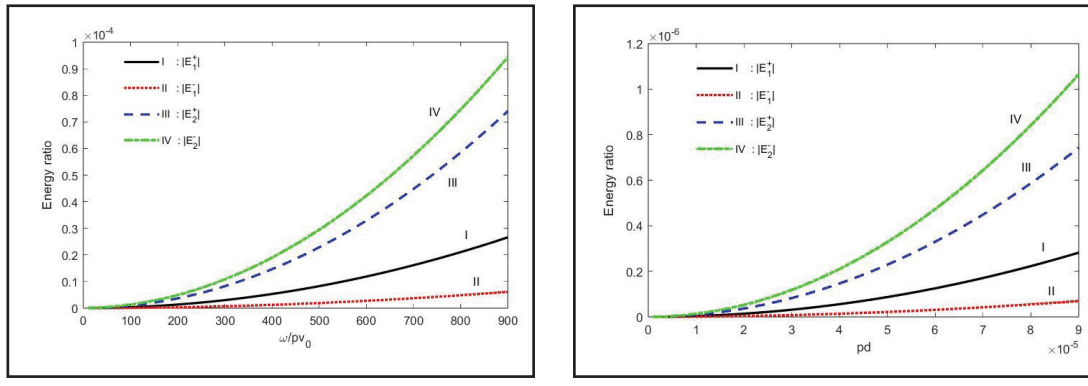

(a) **(b)**

Fig. 12: Variation of Energy Ratios of Irregularly Reflected Waves with Respect to ω/pv_0 and *pd*.

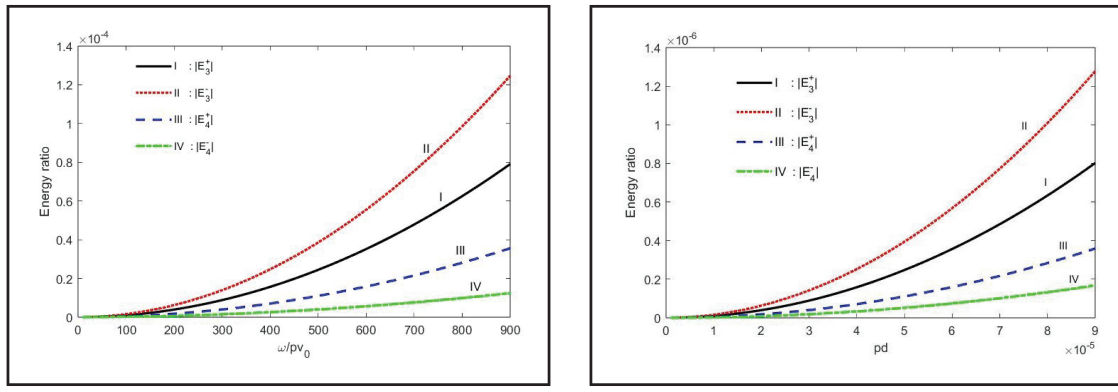

(a) (b)

Fig. 13: Variation of Energy Ratios of Irregularly Transmitted Waves with Respect to ω/pv_0 and *pd*.

CONCLUSION

The behaviour of elastic waves when a plane *qSV*-wave is incident upon a corrugated interface between two dissimilar monoclinic elastic half-spaces, each with different phase velocity are investigated. Rayleigh's method of approximation is employed to obtain the velocities and energy ratios for the regular and irregular reflection and transmission of *qSV*/*qP*-waves respectively. Numerical computations are performed for a specific model, enabling the examination of how the velocities and energy ratios change with variations in the frequency and corrugation parameters. The study discusses how these parameters affect the behaviour of elastic waves concerning reflection and transmission. The following conclusions can be drawn:

(i) The velocity and energy ratios are functions of several parameters, including the angle of incidence, elastic constants, corrugation, and frequency parameters.

(ii) Both theoretically and numerically, the velocities and energy ratios of regularly reflected and transmitted waves are independent of ω/pv and *pd*.

(iii) The energy ratios for irregularly reflected and transmitted waves increase with rising values of both ω/pv and *pd*.

(iv) The influence of pd on the irregularly reflected and transmitted waves is more significant than that of ω/pv.

(v) The energy ratios for irregular waves are observed to be relatively small.

APPENDIX I

$$y_0 = (\Pi_0 c_{24} + c_{44})P_0, \quad z_0 = (\Pi_0 c_{23} + c_{34})P_0,$$

$$\zeta_1^{\mp} = \iota\xi_{\mp 1}\sum_{i=1}^{4} K_i \frac{\mathcal{B}_i}{\mathcal{B}_0}, \quad \zeta_2^{\mp} = \iota\xi_{\mp 1}\sum_{i=1}^{4} \Pi_i K_i \frac{\mathcal{B}_i}{\mathcal{B}_0},$$

$$\zeta_3^{\mp} = \iota\left[\kappa_0^{\mp} + \kappa_1^{\mp}\frac{\mathcal{B}_1}{\mathcal{B}_0} + \kappa_2^{\mp}\frac{\mathcal{B}_2}{\mathcal{B}_0} - \kappa_3^{\mp}\frac{\mathcal{B}_3}{\mathcal{B}_0} - \kappa_4^{\mp}\frac{\mathcal{B}_4}{\mathcal{B}_0}\right],$$

$$\kappa_0^{\mp} = [\mp(c_{23} - c_{22})pP_0\Pi_0 \mp (c_{34} - c_{24})pP_0]\xi_{\mp 1},$$

$$\Phi_0^{\mp} = [\pm 2c_{24}pP_0\Pi_0 \pm 2c_{44}pP_0]\xi_{\mp 1}.$$

APPENDIX II

$$y_0 = c_{44}(P_0 - \Pi_0 K_0), \quad y_i = \begin{cases} c_{44}(P_0 + \Pi_i K_i), & i = 1,2 \\ c'_{44}(P_0 - \Pi_i K_i), & i = 3,4 \end{cases},$$

$$z_0 = c_{22}(\Pi_0 P_0 - K_0) - 2c_{44}\Pi_0 P_0,$$

$$z_i = \begin{cases} c_{22}(\Pi_i P_0 + K_i) - 2c_{44}\Pi_i P_0, & i = 1,2 \\ c'_{22}(\Pi_i P_0 - K_i) - 2c'_{44}\Pi_i P_0, & i = 3,4 \end{cases},$$

$$\zeta_1^{\mp} = \iota\xi_{\mp n}\left[-K_0 + \sum_{i=1}^{4} K_i \frac{\mathcal{B}_i}{\mathcal{B}_0}\right],$$

$$\zeta_2^{\mp} = \iota\xi_{\mp n}\left[-\Pi_0 K_0 + \sum_{i=1}^{4} \Pi_i K_i \frac{\mathcal{B}_i}{\mathcal{B}_0}\right],$$

$$\zeta_3^{\mp} = \iota\left[\kappa_0^{\mp} + \kappa_1^{\mp}\frac{\mathcal{B}_1}{\mathcal{B}_0} + \kappa_2^{\mp}\frac{\mathcal{B}_2}{\mathcal{B}_0} - \kappa_3^{\mp}\frac{\mathcal{B}_3}{\mathcal{B}_0} - \kappa_4^{\mp}\frac{\mathcal{B}_4}{\mathcal{B}_0}\right],$$

$$\zeta_4^{\mp} = \iota\left[\Phi_0^{\mp} + \Phi_1^{\mp}\frac{\mathcal{B}_1}{\mathcal{B}_0} + \Phi_2^{\mp}\frac{\mathcal{B}_2}{\mathcal{B}_0} - \Phi_3^{\mp}\frac{\mathcal{B}_3}{\mathcal{B}_0} - \Phi_4^{\mp}\frac{\mathcal{B}_4}{\mathcal{B}_0}\right],$$

$$\kappa_0^{\mp} = [\{\pm 2c_{44} npP_0 - c_{44}K_0^2\}\Pi_0 \pm 2c_{44} npK_0 + c_{44}P_0K_0]\xi_{\mp n},$$

$$\kappa_i^{\mp} = \begin{cases} \left(\{\pm 2c_{44} npP_0 - c_{44}K_i^2\}\Pi_i \mp 2c_{44} npK_i - c_{44}P_0K_i\right)\xi_{\mp n}, & i = 1,2 \\ \left(\{\pm 2c'_{44} npP_0 - c'_{44}K_i^2\}\Pi_i \pm 2c'_{44} npK_i + c'_{44}P_0K_i\right)\xi_{\mp n}, & i = 3,4 \end{cases},$$

$$\kappa_j^{\mp} = \begin{cases} -c_{44}\left\{K_{in}^{\pm}\Pi_{in}^{\pm} + P_0 \pm np\right\}, & j = 5,6, i = 1,2 \\ c'_{44}\left\{K_{in}^{\pm}\Pi_{in}^{\pm} - P_0 \mp np\right\}, & j = 7,8, i = 3,4 \end{cases},$$

$$\Phi_0^{\mp} = [\{(c_{22} - 2c_{44})P_0K_0 - 2c_{44} npK_0\}\Pi_0 - c_{22}K_0^2 \pm 2c_{44} npP_0]\xi_{\mp n},$$

$$\Phi_i^{\mp} = \begin{cases} \left(\{(2c_{44} - c_{22})P_0K_i \pm 2c_{44} npK\}\Pi_i - c_{22}K_i^2 \pm 2c_{44} npP_0\right)\xi_{\mp n}, i = 1,2 \\ \left(\{(c'_{22} - 2c'_{44})P_0K_i \mp 2c'_{44} npK_i\}\Pi_i - c'_{22}K_i^2 \pm 2c'_{44} npP_0\right)\xi_{\mp n}, i = 3,4 \end{cases},$$

$$\Phi_j^{\mp} = \begin{cases} -[c_{22} - 2c_{44})(P_0 \pm np)\Pi_{in}^{\pm} + c_{22}K_{in}^{\pm}], & j = 5,6, i = 1,2 \\ (2c'_{44} - c'_{22})(P_0 \pm np)\Pi_{in}^{\pm} + c'_{22}K_{in}^{\pm}, & j = 7,8, i = 3,4 \end{cases}$$

Appendix III

$$l_0 = (c_{22} - c_{44})P_0\Pi_0 - c_{44}K_0\Pi_0^2 - c_{22}K_0,$$

$$l_i = \begin{cases} (c_{22} - c_{44})P_0\Pi_i + c_{44}K_i\Pi_i^2 + c_{22}K_i, & i = 1,2 \\ (c'_{22} - c'_{44})P_0\Pi_i - c'_{44}K_i\Pi_i^2 - c'_{22}K_i, & i = 3,4 \end{cases},$$

$$l_i^{\pm} = \begin{cases} (c_{22} - c_{44})(P_0 \pm np)\Pi_{in}^{\pm} + c_{44}K_{in}^{\pm}(\Pi_{in}^{\pm})^2 + c_{22}K_{in}^{\pm}, & i = 1,2 \\ (c'_{22} - c'_{44})(P_0 \pm np)\Pi_{in}^{\pm} - c'_{44}K_{in}^{\pm}(\Pi_{in}^{\pm})^2 - c'_{22}K_{in}^{\pm}, & i = 3,4 \end{cases}.$$

ACKNOWLEDGEMENTS

The authors J. Lalvohbika and R. Lianngenga acknowledged the Science and Engineering Research Board (SERB) for the financial assistance through Grant No. CRG/2021/000083 and No. EEQ/2021/000011 to complete this research work.

REFERENCES

Abubakar I (1962) Scattering of plane elastic waves at rough surfaces-I. Math Proc Camb Philos Soc 58:136-157.

Abubakar I (1963) Scattering of plane elastic waves at rough surfaces-II. Math Proc Camb Philos Soc 59:231-248.

Achenback JD (1973) Wave propagation in elastic solids. North-Holland Ser Appl Math Mech

Asano S (1960) Reflection and refraction of elastic waves at a corrugated boundary interface Part-I. The case of incidence of SH-wave. Bull Earthqu Res Inst 38:177-197.

Asano S (1961) Reflection and refraction of elastic waves at a corrugated boundary interface. Part-II. Bull Earthqu Res Inst 39:367-466.

Chattopadhyay A, Choudhury S (1995) The reflection phenomena of P-waves in a medium of monoclinic type. Int J Eng Sci 33:195-207.

Chattopadhyay A, Saha S (1996) Reflection and refraction of P waves at the interface of two monoclinic media. Int J Eng Sci 34:1271-1284.

Chattopadhyay A, Saha S, Chakraborty M (1996) The reflection of SV-waves in a monoclinic medium. Indian J Pure Appl Math 27:1029-1042.

Gupta S, Das SK, Pramanik S (2022) Reflection and transmission phenomena of SH waves in fluid saturated porous medium with corrugated interface. Mech Adv Mater Struct 29:5122-5141.

Hermans AJ (2003) Interaction of free-surface waves with a floating dock. J Eng Math 45:9-53.

Kaur J, Tomar SK (2004) Reflection and refraction of SH-waves at a corrugated interface between two monoclinic elastic half-spaces. Int J Numer Anal Methods Geomech 28:1543-1575.

Lalvohbika J, Singh SS (2019) Effect of corrugation on incident qP/qSV-waves between two dissimilar nematic elastomers. Acta Mech 230:3317-3338.

Lalvohbika J, Singh SS (2022) Scattering of qSH-waves from a corrugated interface between two dissimilar nematic elastomers. Waves Rand Compl Med 32:19-42.

Lay T, Wallace TC (1995) Modern global seismology. Elsevier.

Levy A, Deresiewicz H (1967) Reflection and transmission of elastic waves in a system of corrugated layers.BSSA 57:393-419.

Mandal BN, Das P (1996) Oblique diffraction of surface waves by a submerged vertical plate. J Eng Math 30:459-470.

Mciver M, Urka U (1995)Wave scattering by circular are shaped plates. J Eng Math 29:575-589.

Nayfeh AH(1991) Elastic wave reflection from liquid-anisotropic substrate interfaces. Wave motion 14:55-67.

Paul A, Campillo M (1988) Diffraction and conversion of elastic waves at a corrugated interface. Geophysics 53:1415-1424.

Pandit DK, Kundu S, Gupta S (2017) Analysis of dispersion and absorption characteristics of shear waves in sinusoidally corrugated elastic medium with void pores. R Soc Open Sci 4:160511.

Prasad B, Pal PC, Kundu S (2017) Propagation of SH-waves through non planer interface between visco-elastic and fibre-reinforced solid half-spaces. J Mech 33:545-557.

Pujol J (2003) Elastic wave propagation and generation in seismology. Cambridge: Cambridge University Press 227.

Rayleigh L (1907) On the dynamical theory of gratings. Proc R soc Lond Series A 79:399-416.

Rice SO (1951) Reflection of electromagnetic waves from slightly rough surfaces. Commun Pure Appl Math 4:351-378.

Saha S, Singh AK, Chattopadhyay A (2020) Analysis of reflection and refraction of plane wave at the separating interface of two functionally graded incompressible monoclinic media under initial stress and gravity. Eur Phys J Plus 135:1-31.

Sato R (1955) The reflection of elastic waves on corrugated surfaces. J Seismol Soc Jpn 8:8-22.

Singh P, Singh AK, Chattopadhyay A (2020) Reflection and transmission of thermoelastic waves at the corrugated interface of crystalline structure. J Therm Stresses 44:469-512.

Singh SJ (1999) Comments on 'The reflection phenomena of P-waves in a medium of monoclinic type' by Chattopadhyay and Choudhury. Int J Eng Sci 37:407-410.

Singh SJ, Khurana S (2001) Reflection and transmission of P and SV waves at the interface between two monoclinic elastic half-spaces. PNAS 71:305-320.

Singh SS, Lalvohbika J (2018) Response of corrugated interface on incident qSV-wave in monoclinic elastic half-spaces. Int J Appl Mech 23:727-750.

Singh SS, Tomar SK (2007) Quasi-P-waves at a corrugated interface between two dissimilar monoclinic elastic half-spaces. Int J Solids Struct 44:197-228.

Singh SS, Tomar SK (2008) qP-wave at a corrugated interface between two dissimilar prestressed elastic half-spaces. J Sound Vib 317:687-708.

Tomar SK, Kaur J (2003) Reflection and transmission of SH-waves at a corrugated interface between two laterally and vertically heterogeneous anisotropic elastic solid half-spaces. EPS 55:531-547.

Tomar SK, Kaur J (2007) Shear waves at a corrugated interface between anisotropic elastic and visco-elastic solid half-spaces. J Seismol 11:235-258.

Yu CW, Dravinski M (2009) Scattering of plane harmonic P, SV or Rayleigh waves by a completely embedded corrugated cavity. Geophys J Int 178:479-487.

Science and Technology Journal Vol. 12 Issue: 2 June 2024 ISSN: 2321-3388

Functional Efficiency Quality of Indian Software Industry: A Computational Approach

Sajal Kanti Das[1]* and Jamal Hussain[2]
[1,2]Department of Mathematics and Computer Science
Mizoram University, Aizawl-796004, India
E-Mail: *[1]sajalhere@gmail.com, [2]jamal.mzu@gmail.com
*Corresponding Author

Abstract—Efficiency measures in the software industry are of huge importance as the software sector is a major contributor to the service sectors in India. This study applied a sensitivity function approach to assess the performance of a few selected software companies in India. A measure called Integrated Functional Efficiency Quality (IFEQ) is proposed. With the data from the CMIE database, the IFEQ is assessed and presented. The results revealed that the companies are performing at an average level. The trends of performance of companies are evaluated over a period from 1992 to 2021. The managerial decision-makers may be assisted with policy implementation to attain business efficiency.

Keywords: Performance analysis, Indian software industry, sensitivity function, functional efficiency, quality of efficiency.

INTRODUCTION

India's software industry began to shape in the 1980s and in the following years, the industry grew rapidly, driven by demand from global companies looking to outsource software development work to low-cost destinations. Today, India's software industry is estimated to be worth several billion dollars, with thousands of software development firms operating across the country. Some of India's biggest software firms, such as Tata Consultancy Services, Cognizant Technology Solutions, Infosys Technologies, Wipro, HCL Technologies etc. also have a global presence and are among the largest software companies in the world. Despite the COVID-19 pandemic-induced economic downturn, this sector achieved a real growth rate of 10.4 per cent in the financial year 2021 (Economic Survey 2023-24, Government of India). Hence the assessment of the performance of the software companies appeal its significance.

Efficiency is vital in the Indian software industry for many reasons. It is a must for gaining a competitive edge. Cost Optimization, Time-to-Market, Customer Satisfaction and Innovation are the other reasons. An efficient software development process helps organizations reduce their costs by streamlining workflows, automating tasks, and minimizing errors. The same also lead to higher customer satisfaction allowing organizations to focus more on innovation and exploring new ideas.

Bhattacharjee (2012) assessed the performance of technical efficiency of Kolkata's Software Technology Park (STP) for IT-ITeS firms considering the Variable Returns to Scale (VRS) assumption. Sahoo(2013) reported that the Mean Pure Technical Efficiency (PTE) score was about 0.6 specifying that companies have 40 per cent pure technical inefficiency. Infrastructure bottlenecks and frequent power cuts lead to unpunctual productivity loss in IT hub, Bengaluru. The percentage of efficient companies in the PTE score follow a cyclical pattern. Sahoo and Nauriyal (2014) applied the Malmquist productivity index to assess the determinants of Total Factor Productivity growth. The study compared the trends in technical efficiency of Indian software companies

 https://doi.org/10.22232/stj.2024.12.02.10

during 1999-2008. The efficiency of software firms were analyzed with an input-oriented DEA model under the VRS assumption. Many researchers assessed the performance of software and ITeS companies, i.e., Mathur (2007a, b), Sahoo D (2011), Das and Datta (2017), Das (2017), etc.

DEFINITIONS AND SOME THEORETICAL CONSTRUCTS

Functional Efficiency Quality (FEQ) and Quality Interval

To measure the overall quality of efficiency of the companies in the Indian software industry, we have considered the notion of functional efficiency quality. Functional efficiency is defined as the overall efficiency of the company to how it is performing from all aspects including financial, technical, production and employee growth, market share, etc. or in other sense the overall function considering all the variables available in the data set. Functional efficiency quality is a measure to assess the functional quality of the companies in an industry. The FEQ for all companies is computed for every financial year. This calculation will be data-oriented as all variables in the dataset will contribute to the FEQ. Every input parameter considered for the computation of functional efficiency quality has a recommended value **r**, or a recommended range ($\mathbf{r}_1 \le \mathbf{x} \le \mathbf{r}_2$) within which a minimum **l** and maximum **r** permissible limit is presumed. These (**l**) and (**r**) are generally referred to as the lower limit and upper limit respectively. The closed interval [**l, u**] in which the recommended value lies is termed the Quality Interval (QI). There lies an Excellent Quality Interval (EQI) or Excellent Quality Point (EQP) which is the region corresponding to the closed sub-interval [$\mathbf{r}_1$, $\mathbf{r}_2$]. The region on the left of EQI is a semi-closed sub-interval [**l**, $\mathbf{r}_1$] referred to as the Increasing Quality Interval (IQI) and right to the Excellent Quality Interval (EQI) there lies a semi-closed sub-interval [$\mathbf{r}_2$, **u**] known as Decreasing Quality Region (DQI). All these regions are described in Figure 1 below:

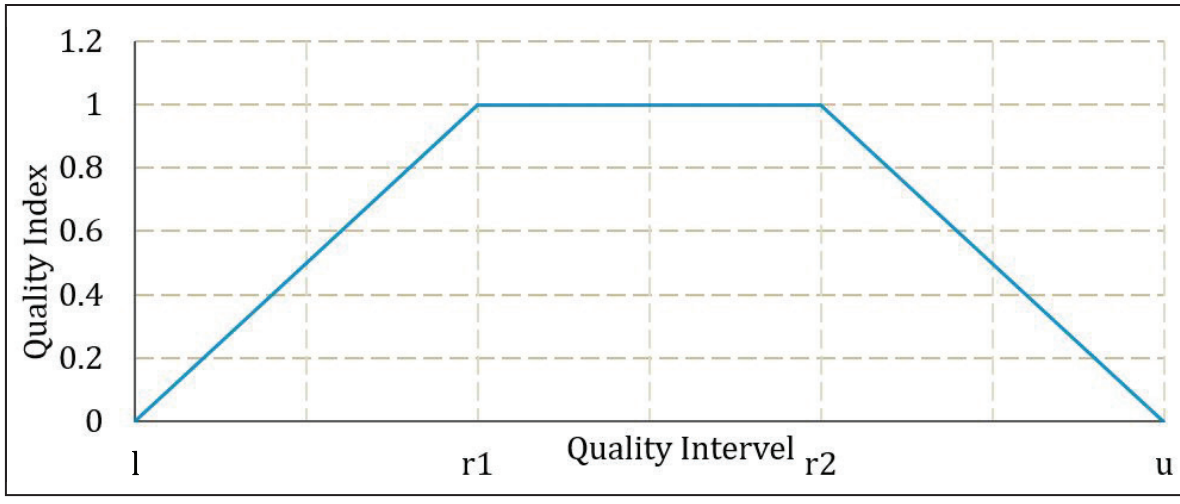

Fig. 1: Quality Map.

The values of the sensitivity function are termed sensitivity numbers which are obtained for all the chosen parameters of the company. These values of sensitivity number can be mapped to real domain *R* with a mapping *fp* : [–1, +1].

Sensitivity Function and Sensitivity Number

For accessing the quality index, the following sensitivity function is used (Sundararajan and Loveson, 2002):

$$f_p(x) = \begin{cases} -1 & if \quad x < l, \\ \dfrac{x - r_1}{r_1 - l} & if \quad l \le x < r_1 \\ 0 & if \ r_1 \le x \le r_2, \\ \dfrac{x - r_2}{u - r_2} & if \ r_2 < x \le u \\ 1 & if \ x > u, \end{cases}$$

where *l* and *u* are considered to be the lower limit and the upper limit respectively and *p* is referred to as the sensitivity number.

Integrated Functional Efficiency Quality (IFEQ)

The Integrated Functional Efficiency Quality (IFEQ) for a company is calculated year-wise for each of the companies considered from the dataset. IFEQ integrates the overall quality of efficiency or overall functioning for that company in a particular year. It is an aggregated value of the quality index of the parameters of a company for a particular selected year.

FUNCTIONAL EFFICIENCY ASSESSMENT

The data of the Indian software industry were collected from the CMIE PROWESS database. The datasets are usually unprocessed panel data unbalanced in nature, collected over a long period from 1990 to 2021. The data has a total of thirty variables. For computing the sensitivity number using the sensitivity function, we access the quality index and aggregating the quality index and compute the IFEQ. Twelve companies from the dataset are selected which are namely, Capricorn Systems Global Solutions Ltd., Digispice Technologies Ltd., EIT Services India Pvt. Ltd., Infosys Ltd., Mastek Ltd., NIIT Ltd., R S Software (India) Ltd., Silverline Technologies Ltd., Tata Elxsi Ltd., Tech Mahindra Ltd., Wipro Ltd. and Zensar Technologies Ltd. We used 21 parameters for measuring IFEQ. The input parameters are classified as favourable parameters and non-favourable based on their parameter value. If the value of a particular input variable goes high and the increasing trend of that variable is good for the company, then that variable is marked as favourable. For instance, *Pat* (profit_after_tax), for this variable if the value is increasing, we can conclude it is good for the company, hence *Pat* is marked as a favourable parameter for the company. Similarly, for a variable whose values if it goes high and from simple observation, it can be said that values of that variable if it goes high, is a loss for the company, then that variable is categorized as a non-favourable variable. Like if we consider the *total_liabilities,* and we see that the value of *total_liabilities* goes high that means the company need to pay more compensation to the employees. Such a scenario is not desirable for the company, hence *total_liabilities* is considered a non-favourable variable. To compute the quality index numbers two different formulae are employed for the favourable and non-favourable parameters. The sensitivity number is then calculated using the sensitivity function defined for the parameter in the interval index. The quality index of each parameter for every company for each year is then estimated from the respective sensitivity number. Finally, the quality index of each parameter is integrated to obtain IFEQ. The algorithm below is formulated to calculate the value of Integrated Functional Efficiency Quality (IFEQ).

Input: A dataset *D* consist of parameters P_i, *and l, u.*

Output: IFEQ(Integrated Functional Efficiency Quality)

IFEQ_Compute (D, P_i)
Step 1: Start
Step 2: For each, P_i *for a company* C_i *from dataset* D
when P_i*_class =favourable*
$f_p(x) = (P_i - l)/(u - l)$
P_i*_class =*non-*favourable*
$f_p(x) = (u - P_i)/(u - l)$

Step 3: Calculate quality index, $q_i = 1 - |f_p(x)|$
Step 4: Repeat steps 2 through 3,
$\forall C_i$ in D, *until* D = Null
Step 5: $QI_a = \left(\frac{1}{n}\sum_{i=1}^{n} q_i\right)$
Step 6: Stop

RESULT AND DISCUSSION

The IFEQ of all selected companies from the period of study is assessed and presented here. In the plotted graph the horizontal axis (x-axis) and vertical axis (y-axis) represent the years and IFEQ respectively. To capture the performance trend of the company the trend line is shown in the graph. The trend equation for every concerned company is shown in the graph. The R^2 values are also obtained for a better understanding of the performance. The slope *m*, from the plotted equation of the trend line, can be considered to understand the performance.

A positive increasing value of *m* (towards 1) represents the progress of the company whereas a decreasing value (towards -1) represents the regress (declining trends) of performance for the company for the considered period. The companies can be clustered into different clusters (or classes) based on the observed value of *m*. The following class may be adopted to classify the companies with some suggested remarks that may be used for better managerial decision-making for enhancing efficiency for the companies.

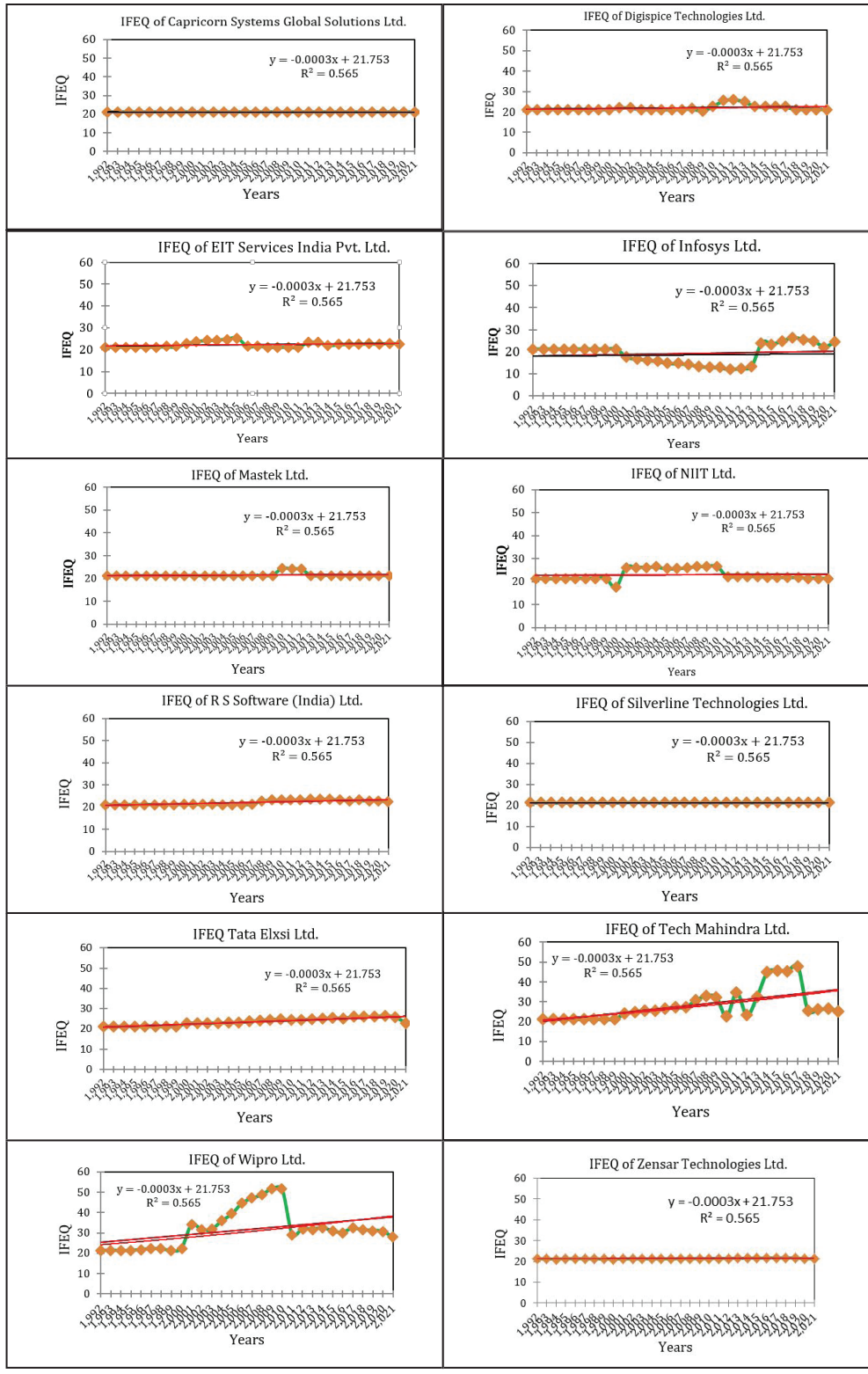
IFEQ of Capricorn Systems Global Solutions Ltd.
IFEQ of Digispice Technologies Ltd.
IFEQ of EIT Services India Pvt. Ltd.
IFEQ of Infosys Ltd.
IFEQ of Mastek Ltd.
IFEQ of NIIT Ltd.
IFEQ of R S Software (India) Ltd.
IFEQ of Silverline Technologies Ltd.
IFEQ Tata Elxsi Ltd.
IFEQ of Tech Mahindra Ltd.
IFEQ of Wipro Ltd.
IFEQ of Zensar Technologies Ltd.
y = -0.0003x + 21.753
R² = 0.565
IFEQ
Years

Fig. 2: IFEQ of Companies.

Table 3: Class and Remarks for the Companies.

Class	*m* (Slope)	Remarks	Class	*m* (Slope)	Remarks
C1	0.9 – 1	Outstandingly Progressive	C6	0.4 < 0.5	Satisfactory in Progress
C2	0.8 < 0.9	Excellently Progressive	C7	0.1 < 0.4	Poorly Progressive
C3	0.7 < 0.8	Very good in Progress	C8	0.0	Constant
C4	0.6 < 0.7	Good in Progress	C9	< 0.0	Regress
C5	0.5 < 0.6	Fair in Progress			

CONCLUSION

The IFEQ for the Wipro Ltd. is seen to be performing best, while Infosys Ltd. came out to be the least performing company. An almost similar pattern is depicted from the trend equation in the graph. Most of the companies fall into the Poorly Progressive class. For the considered period of study based on mean IFEQ Wipro Ltd., Tech Mahindra Ltd. and NIIT Ltd. came up as the top three companies among the 12 companies. Infosys Ltd., Zensar Technologies Ltd. and Mastek Ltd. are the bottom three companies respectively. R S Software (India) Ltd., Digispice Technologies Ltd. and Capricorn Systems Global Solutions Ltd. are the average-performing companies. From the performance trends analysis, it was observed that only Tech Mahindra Ltd. with a value of *m*=0. 5513 is in class C5 with the remark 'Fair in Progress' and Wipro Ltd. with a *m*= 0.4332 in class C6 with the remark of 'Satisfactory in Progress'.

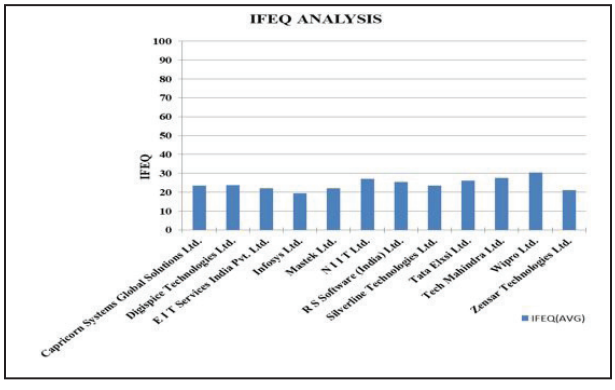

Fig. 3: Average IFEQ.

The rest of the companies are in class C7 with slope in the range of 0.1 to 0.4 and have remarks as Poorly Progressive. Capricorn Systems Global Solutions Ltd. is in the remark 'Regress' with a negative slope of its trend equation and it is classified as class C9. Only Silverline Technologies Ltd. is found to be with a remark 'constant' with its slope near zero. From this analysis, it is observed that the performances of the companies yet need to be more efficient. IFEQ can assist managerial decision-making with identifying the trends of performance. Better resource allocation and managerial effort may be needed to improve the overall IFEQ of the companies to gain efficiency.

REFERENCES

Sundararajan, M. and Loveson, V. J. (2002) An approach towards the development of an environmental quality index for evaluation and categorization of environmental impacts, Journal of Scientific & Industrial Research 61:219-223.

Mathur S.K.(2007a) Indian IT & ICT industry: A performance analysis using data envelopment analysis and Malquist index, Global Economy Journal,7(2)

Mathur S.K. (2007b) Indian IT industry: A Performance analysis and a model for possible adoption, MPRA 2368.

Sahoo D (2011) A Cross-Industry Efficiency Analysis and Contribution of the Information and Technology Sector to Indian Economic Growth. SSRN Electronic Journal, DOI: 10.2139/ssrn.1976083.

Bhattacharjee, S.(2012), Efficiency dynamics and sustainability of the Indian IT-ITeS industry: An empirical investigation using DEA. IIMB Management Review 24(4): 203-214.

Sahoo B.K. (2013), Total factor productivity of the software industry in India, Institute of Economic Growth, New Delhi.

Sahoo B.K., Nauriyal D.K. (2014), Trends in and determinants of technical efficiency of software companies in India, Journal of Policy Modeling 36:539-561.

Das P. (2017) An assessment of the performance of the Indian software industry during 2000-01 to 2014-15 using data envelopment analysis. 44(1):7-21.

Das P., Datta A. (2017) Performance evaluation of Indian information technology-enabled services (ITeS) industry. An Application of two-stage data envelopment analysis International Journal of Advances in Management and Economics. 6(2): 52-70.

Economic Survey 2023-24, July 2024, Government of India, https://www.indiabudget.gov.in/economicsurvey/doc/echapter.pdf.

Science and Technology Journal Vol. 12 Issue: 2 June 2024 ISSN: 2321-3388

Distance Estimation of Bok globule CB69

R.S. Paul[1*] and H.S. Das[2]
[1,*]Department of Physics, Karimganj College, Karimganj-788710, India
Associate Professor, Department of Physics, Karimganj College, Karimganj-788710, India
[1,2]Department of Physics, Assam University, Silchar-788011, India
E-Mail: *[1]subhra_rajat@yahoo.com, [2]hsdas13@gmail.com
*Corresponding Author

Abstract— Determining the distance of small, opaque dark clouds is particularly challenging due to their compact size. In this research, we have employed the near-infrared (NIR) photometric technique to compute the distance of Bok globule CB69. This method involves estimating the extinction (Av) of field stars using NIR data taken from the 2MASS catalogue, in conjunction with distance data obtained from Gaia. From the extinction (Av) versus distance (d) plot, the stars that exhibit an unexpected rise in extinction are considered the distance of the cloud. Consequently, we have estimated the distance to this CB69 cloud, as approximately 461±4 parsecs, respectively. This value aligns with previously published literature.

Keywords: dark clouds, extinction-ISM, distance-stars, formation-stars.

INTRODUCTION

For understanding the process of star formation, knowledge of the structure and physical conditions in molecular clouds is of great importance. The basic property of a molecular cloud is distance and is commonly a crucial part of molecular cloud catalogues (Miville-Deschênes *et al*. 2017; Colombo *et al*. 2019) The most simple and reliable way to estimate molecular cloud structure is to evaluate the dust extinction of background starlight. We have designed a new powerful approach for estimating and mapping the distribution of dust through a molecular cloud utilising data acquired in a near-infrared imaging survey. The estimation of the distance to an interstellar cloud is crucial for any celestial object. To calculate numerous significant physical properties, including masses, and densities (Clemens *et al*. 1991), distances to interstellar clouds are essential. The significant properties, like the luminosity of the star-forming cloud, cannot be determined without knowing the distance.

The accurate measurement of the distance of the molecular cloud is very tough, though it is not impossible. As an illustration, star counting is a technique of low accuracy (Wolf 1923) that experiences large systematic errors established by the assumed distribution of stars. Regardless of the difficulties, presently the NIR photometric technique appears to be of the utmost trustworthy for estimation of the distance. Previous research by Choudhury *et al*. (2019) utilised Gaia DR3 to estimate distances to faint stars near molecular clouds, a method useful for determining stellar extinction and absolute magnitudes—key parameters for near-infrared photometry. In this investigation, we refine this approach by the introduction of a near-infrared photometric technique and employing the Gaia database to evaluate the distance to Bok globule CB69 as 461±4 pc.

DETAILS OF THE GLOBULE CB69

It is an A-type cloud and is designated by another name, B49. In this cloud CB69, while the polarisation vectors exhibit good alignment, their collective orientation does not conform to the expected Galactic Plane alignment (120^0). Six *IRAS* sources are available in the CB69 cloud (16594 - 3315, 16595 - 3311, 16586 - 3304, 16589 - 3315, 16590 – 3313, and 16590 - 3305: Clemens and Barvainis 1988). The average location angle and polarisation values for CB69 field stars are θ_{av} = 155.8^0 and p_{av} = 2%, having standard deviations σ_θ = 13.06^0 and σ_p = 1.12%, respectively.

https://doi.org/10.22232/stj.2024.12.02.11

DISTANCE TO DARK MOLECULAR CLOUD

Bok globules or dark clouds are small, compact, and isolated neighbouring molecular clouds. Bok (Bok and Reilly 1947) was the first to recognise the significance of this globule in the star formation process. In general, the distance measurement of bok globules is very difficult due to their small size and opaqueness, which limits the application of star counts or photometric techniques as distance indicators. Addressing the challenge of determining distances to small Bok globules, (Das *et al*. 2015) applied the near-infrared photometric technique developed by (Maheswar *et al*. 2010) using extensive JHKs photometric data from the 2MASS catalog. Building upon this method, (Barman and Das 2015) estimated the distance to CB4 as 459±85 pc. More recently, Zuicker *et al*. (2019) utilised Gaia DR2 to create a catalogue of precise distances to molecular clouds according to extinction breakpoint. (Yan *et al*. 2019) determined distances to molecular clouds at high galactic latitudes using parallax (Lindegren *et al*. 2018) and G-band extinction estimates of stars along the clouds' sight lines from Gaia/DR2. Interstellar extinction gives a further approach to infer molecular cloud distances. Generally, the method of extinction was classified as a member of low accuracy, but because of the release of the Gaia DR3 catalogue (Gaia collaboration 2022), its precision has grown remarkably. The distance and visual extinction of molecular clouds is investigated (Sun *et al*. 2021) in the Milky Way (MBM) catalogue at |b| > 20°, combining accurate colour excess measurements with distance metrics from the third release of Gaia Early Data (Gaia/EDR3). A previous study employing a near-infrared photometric method and Gaia data (Choudhury *et al*. 2019) determined the distance to Bok globule CB17 as 253±43 pc. Launhardt and Henning (1997) estimated the distance to the CB69 cloud using the kinematic distance method, which was the best available technique at the time, as Gaia data was not yet available. Their estimate, approximately 500 pc, was based on the motion of the cloud relative to the local standard of rest. With the release of the Gaia data by the (Gaia collaboration 2022), more accurate and precise stellar distances became accessible. To determine the distance of Bok globule CB69, we employed a near-infrared (NIR) photometric technique. This method involves estimating the extinction (Av) of field stars using NIR data taken from the Two Micron All-Sky Survey (2MASS) catalogue, combined with the precise distance data from Gaia. In this research, we build upon this approach by utilising the near-infrared photometric technique and Gaia DR3 to estimate the distance to the dark cloud CB69. The key selection criteria for the sources analysed in this research are outlined in Table 1.

Table 1: Observational Log of Dark Cloud CB69 within 25×25 arcmin² Star Field Area.

Sl No.	ID(25′×25′)	RA(2000) (hms)	DEC(2000) (° ′ ″)	l(^{0})	b(^{0})	Distance, d (ref.) (pc)
1.	CB69	17:02:42	-33:17:00	351.23	5.14	500(1)

Distance References: (1) Launhardt & Henning (1997)

ESTIMATION OF EXTINCTION (AV)

Near-Infrared Photometric Study

The near-infrared photometric approach relies on determining absolute magnitude (M_{K_s}), distance (d), and extinction (Av) using information from the Two Micron All-Sky Survey (2MASS) catalogue, intrinsic colours of main-sequence stars, and the reddening law of (Rieke and Lebofsky 1985). This method validated by (Maheswar *et al*. 2010), has been extensively embraced for estimating stellar distances. While it's been successfully applied to evaluate the distances of some small Bok globules by (Das *et al*. 2015), its accuracy is limited by the existence of three unknown variables within the model.

By combining Gaia DR3 parallax measurements with stellar photometry, we can infer the distances to faint stars in the vicinity of a molecular cloud, which enables us to approximate the extinction in the region and absolute magnitudes of stars (for three filters, J, H, and K_s) precisely by applying the NIR approach. The technttique evolved in this instance by (Choudhury *et al*. 2019) is explained below.

The photometric distance of a star can be evaluated utilising the subsequent equation

$$X - M_X = 5(\log d - 1) + A_X \quad (1)$$

where X, A_X, and M_X are the apparent magnitudes, extinctions, and absolute magnitudes of stars in the three filters J, H, and Ks, respectively.

Simplifying equation (1), we get

$$A_V = \frac{1}{\left(A_X/A_V\right)}[(X - M_X) + 5(1 - \log d)] \quad (2)$$

Observationally, visual extinction (Av) is associated with A_J, A_H, and A_{Ks}. As stated by the law of extinction (Rieke and Lebofsky 1985), $A_J/A_V = 0.282$, $A_H/A_V = 0.175$, $A_{Ks}/A_V = 0.112$. Instead of 2MASS, the Galactic Centre in the Arizona-Johnson photometric system provided this extinction law. Since the values of MJ, MH, and MKs are unknown, the visual extinction (Av) is estimated using the iteration technique, which finds the collection of values for MJ, MH, and MKs that best fits the equations obtained for three filters using equation (2). Specifically, we have integrated the Gaia database into our method to estimate the parallax of stars within the dark cloud. With the use of parallax and parallax uncertainties, the individual star distances connected to the dark cloud are quantified in addition to their uncertainty.

Determination of Av

Near-infrared photometric data for field stars within $30' \times 30'$ field of view centred on CB69 were extracted from 2MASS All-Sky Catalogue (Cutri *et al.* 2003). Data selection criteria included:

(i) The photometric uncertainty ≤ 0.045 magnitudes in all J, H & K_S bands.

(ii) High quality photometric flag 'AAA' in all three bands that exhibits a SNR > 10.

(iii) The difference in magnitudes (J-K_s) ≤ 0.75 to exclude M-type stars from the study.

We have assessed the parallax of stars whose J, H, and Ks magnitudes are first acquired from the two MASS catalogues using the Gaia DR3 database (Gaia collaboration 2016, 2022). Table 2's second column displays data for 62 CB69 field stars in addition to their 2MASS identification numbers. In the same way, we have categorised all the parallax information that would have been used to estimate the uncertainty in the distance and the distance of individual stars, provided that the uncertainty in the distance is less than 2500 pc and the parallax of a single star is greater than zero.

Table 2: Identified Stars of Field in CB69. Columns 1, 2, 3, and 4 Represent the Star Serial Number, 2MASS Identification Number, Distance (in pc), and Visual Extinction (in mag).

Star	2MASS	d(pc)	Av(mag)	Star	2MASS	d(pc)	Av(mag)
1	17014317-3309016	1901.502	0	32	17023251-3322039	462.3209	1.02937
2	17014342-3314353	586.3727	0.84089	33	17023308-3305259	1002.506	0.95235
3	17014346-3321593	490.148	0	34	17023765-3313184	193.6333	0.00035
4	17014412-3317253	802.1176	0.17663	35	17024339-3318002	461.2121	0.68261
5	17014784-3308558	423.4776	0.60585	36	17024501-3324185	1835.199	0.8886
6	17014846-3312338	565.6109	1.31706	37	17024569-3326096	415.0928	0.02934
7	17014858-3323172	1557.39	0.77664	38	17024661-3307354	1152.472	1.60584
8	17014877-3316280	1418.239	0.28813	39	17024868-3321172	1635.858	1.06479
9	17014975-3322592	1015.125	0	40	17025090-3325049	868.7343	0.8708
10	17015174-3311414	1827.485	0	41	17025100-3308426	1245.795	0.14101
11	17015232-3328588	1155.001	0	42	17025518-3322361	1141.683	0.63572
12	17015385-3315034	1186.662	0.04739	43	17025838-3325516	890.8686	0.77636
13	17020259-3315269	283.1337	0.00015	44	17025930-3304563	1258.495	0.14093
14	17020408-3309232	1010.816	0.31787	45	17030252-3324122	1508.751	0
15	17020519-3323350	1373.815	0.02964	46	17030664-3311351	850.1955	0.04753
16	17020779-3311355	309.8757	1.61724	47	17031058-3310232	1995.211	0
17	17021052-3328473	1841.621	0	48	17031348-3328133	1635.59	0
18	17021120-3305314	553.5872	0.00025	49	17031456-3308454	377.3727	0.00052

(Table 2 Contd....)

(...Contd. Table 2)

19	17021145-3321030	554.0166	0.04747	50	17031677-3307210	1211.681	1.41156
20	17021353-3319306	1507.386	0.57049	51	17031828-3321263	1763.047	0
21	17021475-3318182	876.0403	1.11127	52	17031895-3310435	682.2213	0.88785
22	17021846-3318154	1037.129	0.01715	53	17031901-3305435	1362.398	0.0939
23	17021894-3310219	169.0674	0.09468	54	17031958-3327413	398.8354	0.00011
24	17021908-3318380	757.6332	0.74718	55	17032325-3315357	1805.38	0
25	17022078-3329073	945.1796	0	56	17032335-3307260	720.0461	1.0468
26	17022124-3327059	1617.338	0.57091	57	17032379-3324455	1007.151	0.47705
27	17022423-3309219	348.5171	0.15915	58	17032546-3307211	1301.236	0.04688
28	17022455-3323578	843.4548	0	59	17032688-3311385	738.607	0.98203
29	17022676-3316383	1323.627	0.00061	60	17032833-3305173	1452.855	0
30	17023048-3315108	239.3432	0.3826	61	17033111-3319297	570.4181	0.77685
31	17023196-3324140	1951.22	0.09386	62	17033308-3321107	966.4637	0.77685

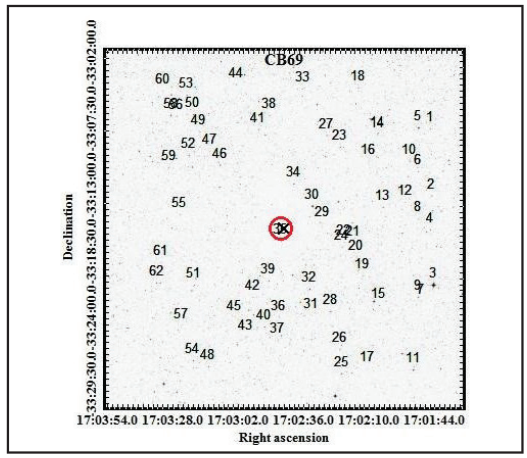

Fig 1: Designated Field Stars in the Neighbourhood of the CB69 Cloud with 30×30 Arcmin². The × Mark Indicates the Centre of the Cloud. A Circle Around Star Number 35 Denotes the Cloud's Distance from us and Shows an Abrupt Increase in Visual Extinction.

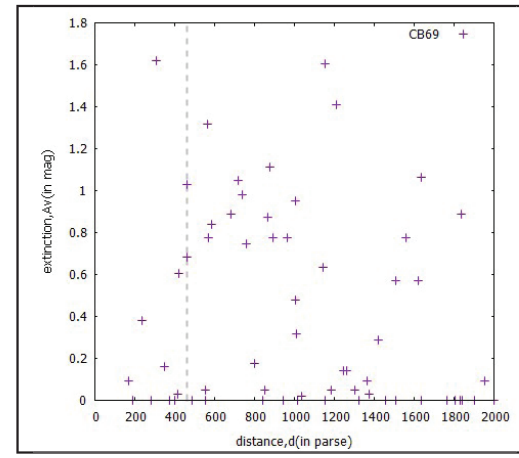

Fig 2: Distance, d Versus Visual Extinction, Av be Designed for Stars Projected Towards the CB69 Cloud. The Upright Dotted Dash is Represented at a Distance of 461±4 pc (Star 35; Table 2), where an Abrupt Rise in Av Occurs.

Thus, the values of visual extinction (Av) of individual stars are obtained by utilising the Gaia data and the near-infrared photometric technique. Plotting each star's distance (d) against visual extinction (Av) yields the distance indicator for that specific dark cloud. The vertically dotted line denotes an unexpected increase in extinction. As illustrated in Fig. 1, 62 field stars of the dark cloud CB69 are estimated in the current study. Furthermore, based on the results of this work shown in Table 2, we have created a distance versus extinction plot for each and every field star in this dark cloud, which is displayed in Fig 2. For the CB69, this plot shows a rapid surge in the value of extinction at a distance of 461±4 pc. As a result, we estimated the CB69 cloud's distance to be 461±4 pc, which is in good accord with (Launhardt and Henning 1997). In that investigation, Gaia DR3 is presented to determine the first accurate distance to the cloud CB69 for the first time. Table 3 highlights the literature distance together with the distance acquired from our present study.

Table 3: Details of Distance of the CB69 Dark Cloud.

S. No.	Cloud	d (Literature) (pc)	d (Our Study) (pc)
1	CB69	500	461±4

CONCLUSIONS

We have evaluated the distance to dark cloud CB69 utilising the technique of near-infrared photometry and Gaia data. Our new estimate for the distance to CB69 is 461±4 pc which is almost comparable with previously published work suggested by (Launhardt and Henning 1997). The difference between our distance estimate of 461±4 pc and the previously reported 500 pc can be attributed to the superior precision of Gaia data, which offers direct measurements of stellar distances. Furthermore, the variation of distance and visual extinction for 62 field stars of the CB69 cloud is designed, where a sharp rise in the extinction value represents the first real distance indicator for this dark cloud.

ACKNOWLEDGEMENTS

The VizieR database from the 2MASS,i.e., Two Micron All Sky Survey, has been used in this study. Additionally, the Gaia Data Processing and Analysis Consortium (DPAC,https://www.cosmos.esa.int/web/Gaia/dpac/consortium) processed data from the European Space Agency (ESA) project Gaia (https://www.cosmos.esa.int/gaia) for this article.

REFERENCES

Barman A, Das H S (2015) Study of grain alignment efficiency and a distance estimate for small globule CB4. Research in Astronomy and Astrophysics 15: 953-962

Bok B J, Reilly E F (1947) Small Dark Nebulae The Astronomical journal 105:255-257

Choudhury G B, Das H S, Barman A, Medhi B J (2019) Bok globule CB 17: polarisation, extinction, and distance. Monthly Notices of the Royal Astronomical Society 487: 475–485

Clemens D P, Barvainis R (1988) The Astrophysical Journal Supplement Series 68, 257

Clemens D P, Yun J L, Heyer M H (1991) Bok Globules and Small Molecular Clouds: Deep IRAS Photometry and ^{12}CO Spectroscopy. The Astrophysical Journal Supplement Series 75: 877-904

Colombo D, Rosolowsky E, Duarte-Cabral A, Ginsburg A, Glenn J, Zetterlund E, Hernandez A K, Dempsey J, Currie M J (2019) The integrated properties of the molecular clouds from the JCMT CO(3–2) High-Resolution Survey. Monthly Notices of the Royal Astronomical Society 483: 4291–4340

Cutri R M, Skrutskie M F, Dyk S van, Beichman C A, Carpenter J M, Chester T, Cambresy L, Evans T, Fowler J, Gizis J, Howard E, Huchra J, Jarrett T, Kopan E L, Kirkpatrick J D, Light R M, Marsh K A, McCallon H, Schneider S, Stiening R, Sykes M, Weinberg M, Wheaton W A, Wheelock S, Zacarias N (2003) Vizier Online Data Catalogue, 2246 : 0

Das A, Das H S, Senorita Devi A (2015) Distance estimation of some selected small Bok globules. Monthly Notices of the Royal Astronomical Society 452: 389–396

Launhardt R, Henning T (1997) Millimetre dust emission from northern Bok globules. Astronomy and Astrophysics 326: 329-346

Lindegren L, Hernandez J, Bomburn A (2018) Gaia Data Release 2. Astronomy and Astrophysics 616: A2

Maheswar G, Lee C W, Bhatt H C, Mallik S V, Dib S (2010) A method to determine distances to molecular clouds using near-IR photometry. Astronomy and Astrophysics 509: A44

Miville-Deschênes M A, Murray N, Lee Eve J (2017) Physical Properties of Molecular Clouds for the Entire Milky Way Disk. The Astrophysical Journal, 834:57-87

Gaia collaboration (2016) Astronomy and Astrophysics 595, A1

Gaia collaboration (2022) Astronomy and Astrophysics 667: A148

Rieke G H, Lebofsky M J (1985) The Interstellar Extinction Law From 1 To 13 Microns. The Astrophysical Journal, 288:618-621

Sun M, Jiang B, Yuan H, Li J (2021) The Ultraviolet Extinction Map and Dust Properties at High Galactic Latitude. The Astrophysical Journal Supplement Series, 254:38-49

Wolf M (1923), Astronomische Nachrichten 219: 109-116

Yan Qing-Zeng, Zhang Bo, Xu Ye, Guo Sufen, Macquart Jean-Pierre, Tang Zheng-Hong, Walsh Andrew John (2019), Distances to molecular clouds at high galactic latitudes based on Gaia DR2. Astronomy and Astrophysics, 624: A6

Zuicker Catherine, Speagle Joshua S, Schlafly Edward F, Green Gregory M, Finkbeiner Douglas P, Goodman Alyssa A, Alves João (2019) A Large Catalogue of Accurate Distances to Local Molecular Clouds: The Gaia DR2 Edition. The Astrophysical Journal, 879:125-144

Science and Technology Journal Vol. 12 Issue: 2 June 2024 ISSN: 2321-3388

Ab initio Study of Halide Double Perovskite Cs_2NaAlX_6(X=Br,I) for Optoelectronics and Thermoelectric Materials

Teda H. Lalrinmawii[1*], Laihnuna[2], Z. Pachuau[3], Joel Lalbiakkima[4], and G.C. Lalremruata[5]

[1,2,3,4,5]Department of Physics, Mizoram University, Aizawl-796004, India

*E-Mail: zaiapach14@gmail.com

[*]Corresponding Author

Abstract—Halide double perovskites represent a diverse class of materials, allowing researchers to explore a wide range of properties and functionalities. This diversity opens up opportunities for innovation in various technological applications. They can exhibit tunable bandgaps by adjusting the composition of halide ions. We present a broad theoretical exploration of $Cs_2NaAl(Br/I)_6$, focusing on its prospect for advanced optoelectronic applications and thermoelectric devices. Utilizing computational simulations, we analyze the band structure, optical properties, and thermoelectric performance of this compound to determine its effectiveness in energy conversion. Cs_2NaAlI_6, exhibits a bandgap of 2.4 eV. Moreover, our calculations reveal a promising thermoelectric efficiency of 1.006 and 1.32 at room temperature for $Cs_2NaAl(Br/I)_6$, suggesting its viability for waste heat recovery and power generation.

Keywords: Dielectric function, Seebeck coefficient, Absorption coefficient, Grüneisen parameter

INTRODUCTION

Recent advances in material science have accelerated the search for novel materials with outstanding properties, particularly in optoelectronics and thermoelectrics. Halide double perovskites have garnered significant interest due to their exceptional structural flexibility, tunable electronic properties, and potential for high-performance applications (Jain *et al*. 2018). These materials, with the general formula $A_2BB'X_6$—where A is a monovalent cation, B and B′ are distinct metal cations, and X is a halide anion—offer a rich compositional space that facilitates precise property tuning (Jain *et al*. 2018). Specifically, Cs_2NaAlX_6 (X = Br, I) have emerged as promising candidates for both optoelectronic and thermoelectric applications, thanks to their favourable band gaps, high stability, and the ability to achieve high carrier mobility and low thermal conductivity (NREL, 2020; Zhao *et al*. 2016). The substitution of halide anions (Br, I) in these compounds provides additional flexibility to fine-tune their electronic and thermal properties, making them versatile for next-generation technologies (Zhao *et al.* 2016).

In this study, we employ ab initio methods to investigate the structural, electronic, optical, and thermoelectric properties of Cs_2NaAlX_6 (X = Br, I). Utilizing first-principles calculations, we aim to develop a thorough understanding of these materials' fundamental characteristics and explore their potential for use in optoelectronic devices, such as light-emitting diodes (LEDs) and solar cells, as well as in thermoelectric applications where efficient waste heat conversion is crucial. The insights gained from this research will contribute to the ongoing development of halide double perovskites as versatile and high-performance materials for modern technology (Blancon *et al*. 2020).

https://doi.org/10.22232/stj.2024.12.02.12

Halide double perovskites represent a diverse class of materials, allowing researchers to explore a wide range of properties and functionalities (Cai *et al*. 2019). This diversity opens up opportunities for innovation in various technological applications. Halide double perovskites offer several advantages in various technological applications, making them promising candidates for diverse fields. They can exhibit tunable bandgaps by adjusting the composition of halide ions. They can be employed in electronic devices, including transistors and integrated circuits, contributing to advancements in electronics. Halide double perovskites often have high absorption coefficients and tunable bandgap which makes them suitable for applications in optoelectronics, like photodetectors, solar cells and LEDs (Charef *et al*. 2024). Kong *et al*. effectively synthesized Cs_2TiCl_6 and Cs_2TiBr_6 at room temperature utilizing solution-based methods.The study finds that cesium titanium halide perovskites (Cs_2TiX_6) exhibit tunable band gaps (1.7-2.5 eV), stable photoluminescence (535-670 nm), and high thermal stability up to 500°C. These lead-free perovskites, synthesized via a scalable room-temperature process, are promising for eco-friendly optoelectronic applications (Kong *et al*. 2020). Ghrib *et al.* found that $K_2Ti(Cl/Br)_6$ double perovskites are stable with direct band gaps of 2.80 eV (K_2TiCl_6) and 2.1 eV (K_2TiBr_6). Their strong absorption in the visible to ultraviolet range (2.5-4 eV) makes them suitable for solar cell applications with static dielectric constants of 3.16 and 3.62 (Ghrib *et al*. 2021). Slavney *et al.* study explores $Cs_2AgBiBr_6$, a lead-free double perovskite incorporating nontoxic Bi^{3+}, as a potential solar cell material. It demonstrates a long photoluminescence lifetime of ~660 ns and an indirect bandgap of 1.95 eV, making it suitable for tandem solar cells (Slavney *et al*. 2016). Volonakis *et al*. introduces Cs_2InAgX_6(X = Cl, Br, I) as a new class of lead-free halide double perovskites with potential for photovoltaics. First-principles calculations predict these compounds have direct band gaps, with $Cs_2InAgCl_6$ exhibiting 3.3 eV band gap and reversible color change under UV light (Volonakis *et al*. 2017). Recent investigations on $Rb_2AgIn(Cl/Br/I)_6$, reveal their potential as lead-free alternatives in photovoltaics and thermoelectric devices. The study found direct band gaps of 2.62 eV ($Rb_2AgInCl_6$), 1.74 eV ($Rb_2AgInBr_6$), and 0.56 eV (Rb_2AgInI_6) at the Γ-point, with absorption edges at 2.48 eV, 1.67 eV, and 0.45 eV, respectively (Hnuna *et al*. 2023). Huma *et al*. finds that lead-free double perovskites A_2SnI_6 (A = Cs, Rb) are mechanically stable and ductile, with direct band gaps of 1.147 eV and 1.197 eV, respectively. They exhibit visible spectrum absorption and p-type semiconducting behavior, with stable thermoelectric performance across 200–800 K (Huma *et al*. 2021). Ali *et al*. evaluates the thermoelectric properties of Tl_2(Se,Te) Cl_6 vacancy-ordered double perovskites using BoltzTraP and Wien2k codes. Both compounds exhibit indirect band gaps (2.976 eV for Tl_2SeCl_6 and 3.037 eV for Tl_2TeCl_6), with high Seebeck coefficients (183.50 μVK^{-1} and 185.49 μVK^{-1}, respectively), indicating p-type conductivity (Ali *et al*. 2021). Murtaza *et al.* investigates $X_2AgTlCl_6$ (X = Rb,Cs) double perovskites, revealing their suitability for optoelectronic applications with band gaps of 0.78 eV ($Rb_2TlAgCl_6$) and 0.74 eV ($Cs_2TlAgCl_6$). Both compounds exhibit high figures of merit (0.72 and 0.68) at elevated temperatures, making them promising for thermoelectric (Murtaza *et al* 2021). Recent research has increasingly focused on lead-free double halide perovskites for energy applications, owing to their tunable properties achievable through the substitution of various halide ions and metal cations (Karim *et al*. 2019; Saeed *et al*. 2020; Kale *et al* 2021; Mahmood *et al*. 2021; Nabi *et al*. 2021; Kangsabanik *et al*. 2018; Chakraborty *et al*. 2017). $Cs_2NaAl(Br/I)_6$ belongs to HDP family, which exhibit intriguing electronic and optical properties emerging due to the combination of two distinct cations inhabiting the A-site. Furthermore, the substitution of halide ions provides additional degrees of freedom to tailor the bandgap and optoelectronic attribute of $Cs_2NaAl(Br/I)_6$. We provide a comprehensive overview study of $Cs_2NaAl(Br/I)_6$ and its feasibility for optoelectronic and thermoelectric device applications of this material.

In summary, our investigation into $Cs_2NaAl(Br/I)_6$ compounds has revealed key insights into their structural stability, electronic properties, and potential applications. The negative enthalpy of formation confirms their thermodynamic stability, making them viable for synthesis. Stability trends among the halides highlight the influence of halogen size and electronegativity on formation energy. Goldschmidt and Bartel tolerance factors further validate the stability of these compounds in the cubic phase. Band structure analysis shows direct bandgaps, with halogen substitution impacting electronic transitions and absorption spectra. The computed elastic constants indicate strong mechanical stability, meeting Born stability criteria, with some anisotropy. Dielectric function analysis ($\varepsilon_1(\omega)$ and $\varepsilon_2(\omega)$) reveals capacitive behaviour, polarization variations, and shifts in resonance due to halide changes. Refractive index data suggest a high ionic bond concentration and semiconductor-like transparency, with significant visible light absorption. Importantly, thermoelectric efficiencies of 1.006 and 1.32 at room temperature suggest $Cs_2NaAl(Br/I)_6$

as promising candidates for waste heat recovery and power generation. The study also shows that transitioning from $Cs_2NaAlBr_6$ to Cs_2NaAlI_6 increases specific heat, enhancing vibrational modes and anharmonicity. The negative ΔG indicates a spontaneous tendency toward a lower energy state, and a nearly constant Debye temperature highlights the materials' thermal conductivity and hardness.

COMPUTATIONAL DETAILS

The calculations were performed using Density Functional Theory (DFT) with the FP-LAPW method in the WIEN2k software (Blaha *et al*. 2001). For analyzing band gaps and optical properties, the modified Becke-Johnson (mBJ) exchange-correlation potential was employed (Tran *et al*. 2009). The basis set was optimized with a product of R_{MT} and *k*max set to 8, and *l*max to 10, where *k*max is the maximum wave vector and R_{MT} is the smallest muffin-tin radius. The Fourier charge density was set to 12 Ry, with an energy threshold of −6.0 Ry, and 5000 k-points were utilized. Convergence criteria were set at 0.0001 Ry for energy and 0.001 e for charge (Hnuna *et al*. 2023). Thermoelectric properties were evaluated using semi-classical Boltzmann transport theory with a constant relaxation time approximation, as implemented in BoltzTraP2 (Madsen *et al*. 2018). Thermodynamic properties were obtained through the quasi-harmonic Debye model using the GIBBS2 code (de-la-Roza *et al*. 2011). Elastic constants were computed using the IRelast package, integrated with WIEN2k and specifically customized for cubic systems (Jamal *et al*. 2018).

RESULTS AND DISCUSSION

Structural and Electronic Properties

The image shows the optimized crystal structures of two halide double perovskites: $Cs_2NaAlBr_6$ on the left and Cs_2NaAlI_6 on the right. Both structures are depicted in a cubic phase, which is typical for this class of materials. The computed ground state properties of $Cs_2NaAl(Br/I)_6$ is shown in Table 1. Thermodynamics stability can be tested on the exothermic nature of the synthesis reaction, which can be calculated by the enthalpy of formation (ΔH_f). A negative ΔH_f indicates an exothermic reaction, signifying material stability. The formation enthalpy for $Cs_2NaAl(Br/I)_6$ was determined by (Hnuna *et al*. 2023);

$$\Delta H_f = E_{tot} - \left[mE_K + E_{In} + E_{Ag} + nE_x\right] \quad (1)$$

Here, E_{tot} represents the total energy of $Cs_2NaAl(Br/I)_6$, while E_{Cs}, E_{Na}, E_{Al}, and E_x denote the energies of Cs, Na, Al, and Br/I, respectively. The determined ΔH_f is provided in Table 1. The negative ΔH_f indicates the thermodynamic stability of $Cs_2NaAl(Br/I)_6$ (Zelai *et al*. 2024). The decrease in electronegativity from chlorine to iodine contributes to the increase in enthalpy of formation. To assess the cubic phase stability of $Cs_2NaAl(Br/I)_6$, we computed the Goldschmidt tolerance factor (t_G) and the octahedral factor (μ) using the provided equation (Hnuna *et al*. 2023; Goldschmidt 1926)

$$t_G = \frac{r_A + r_X}{\sqrt{2}\,(\bar{r}_B + r_X)} \quad (2)$$

$$\mu = \frac{\bar{r}_B}{r_X} \quad (3)$$

Here, r_A represents the ionic radius of Cs, $\bar{r}_B$ is the average of the ionic radii of Na and Al, and r_X denotes the ionic radius of the halides Br, and I. Nevertheless, current research indicates that the precision of the Goldschmidt tolerance (t_G) is frequently inadequate (Bartel *et al*. 2019). Using the newly introduced model by Bartel *et al*. (Hnuna *et al*. 2023), we calculated the tolerance factor to prevail over the drawbacks of the Goldschmidt tolerance factor (τ_B) (Bartel *et al*. 2019). The updated tolerance factor, τ_B is given as:

$$\tau_B = \frac{r_X}{\bar{r}_B} - n_A\left[n_A - \frac{r_A/\bar{r}_B}{\ln(r_A/\bar{r}_B)}\right] \quad (4)$$

For a stable cubic phase, τ_B needs to be less than 4.18 (Bartel *et al*. 2019), and the values of t_G should lie in the ranges of 0.9 to 1.02 and μ should fall within the ranges of 0.41 to 0.73 (Li *et al*. 2008). The calculated values of t_G, μ, and τ_B for $Cs_2NaAl(Br/I)_6$ are shown in Table 1, indicating their stability in the cubic phase.

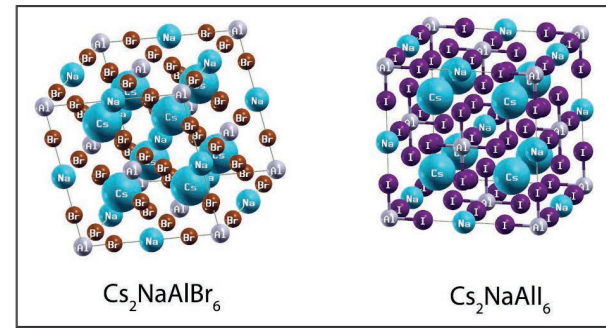

Fig. 1: Crystal Structure of $Cs_2NaAl(Br/I)_6$.

We utilized high-symmetry points within the BZ to compute the energy band of $Cs_2NaAl(Br/I)_6$. Fixing E_F at zero, we identified the maximum valence band (VB) and minimal conduction band (CB) at the Γ-points in the BZ, indicating direct bandgaps for $Cs_2NaAl(Br/I)_6$. Larger halogen atoms

with more diffuse atomic orbitals were produced when halogen ions were switched from Br to I. Consequently, increased overlap between the atomic orbitals of cations and anions weakened bonding and extended the electron cloud, leading to smaller energy gaps. The bandgap serves as the lower threshold for absorption, with $Cs_2NaAlBr_6$ and Cs_2NaAlI_6 exhibiting absorption within the ultraviolet spectrum. This suggests plausible applications of $Cs_2NaAl(Br/I)_6$ in optoelectronic devices operating within these spectral range. Table 1 displays the band gap values that were computed.

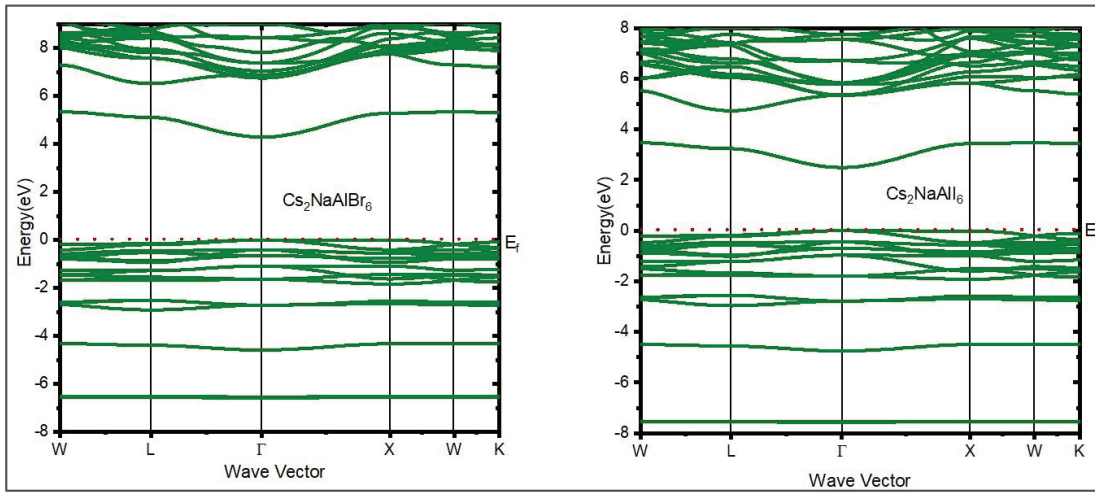

Fig. 2: Calculated Band Structures of $Cs_2NaAl(Br/I)_6$.

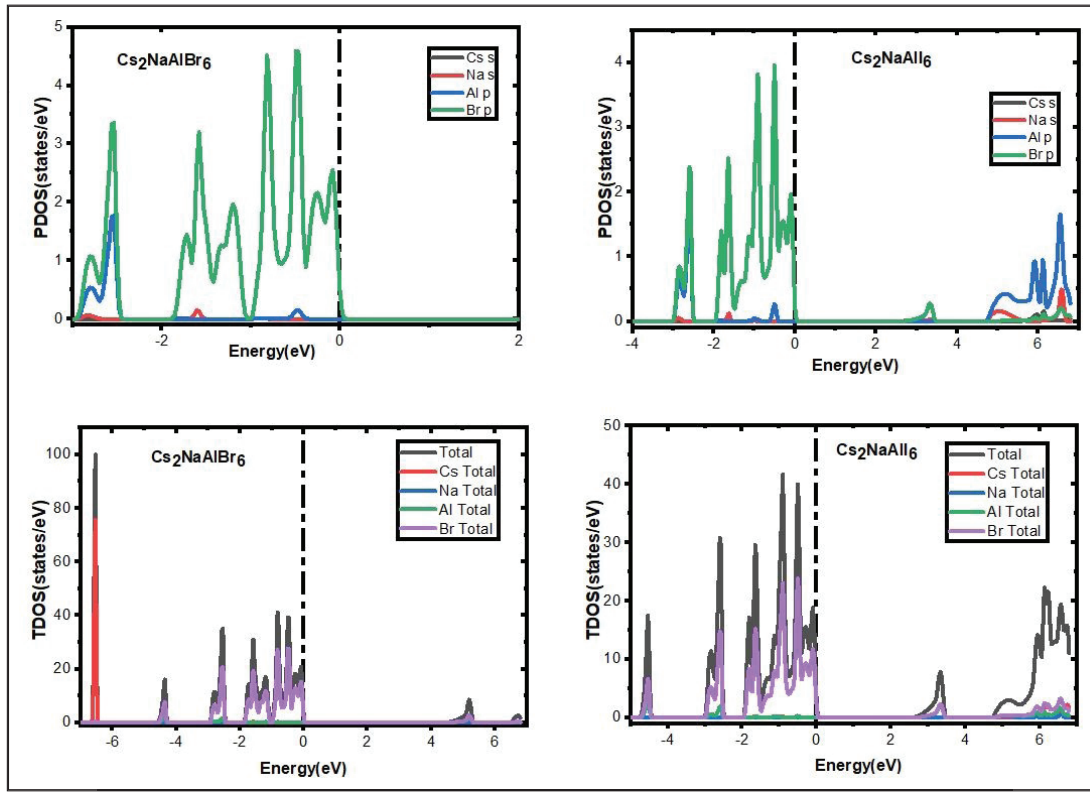

Fig. 3: Calculated Partial and Total Density of States of $Cs_2NaAl(Br/I)_6$.

Table 1: Computed Ground State Properties of $Cs_2NaAlBr_6$ and $Cs_2NaAlBr_6$.

Parameters	$Cs_2NaAlBr_6$	Cs_2NaAlI_6
a(Å)	11.1595	12.1766
V_o(Bohr^3)	2344.6043	3045.8909
E_o(Ry)	-63252.509176	-117401.213800
B(GPa)	21.7419	15.9015
B'	3.4210	3.9728
E_g(eV)	4.290	2.493
$\triangle H_f(eV)$	-1.969	-1.408
τ_G	0.90	0.96
μ	0.5659	0.4381
τ_B	3.884	4.07

To enhance our understanding of the energy band structure, we computed the partial density of states (PDOS) and the total density of states (TDOS), as shown in Figure 3. The TDOS offers a detailed overview of the material's energy band, illustrating how the energy levels are distributed. Peaks and variations in the TDOS correspond to specific electronic transitions. Notably, the energy band derived from energy-dispersed states align with the TDOS, confirming their consistency. Additionally, the energy band structure obtained from the energy-dispersed states aligns with the TDOS, confirming their consistency. The PDOS provides a more detailed analysis, revealing the contributions of individual orbitals to the electronic states (Nabi *et al*. 2021).

Mechanical Properties

Table 2 displays the calculated elastic constants and their corresponding mechanical properties, offering important insights into the material's mechanical behavior (Ziane *et al* 2014).

Table 2: Calculated Elastic Constant and Derived Mechanical Parameters.

Parameters	$Cs_2NaAlBr_6$	Cs_2NaAlI_6
C_{11} (GPa)	39.783	23.957
C_{12} (GPa)	14.192	13.177
C_{44} (GPa)	13.441	9.523
G_V (GPa)	13.183	7.870
G_R (GPa)	13.175	7.288
G (GPa)	13.179	7.579
B (GPa)	22.723	16.770
B/G	1.724	2.213
Y (GPa)	33.140	20.416
υ	0.257	0.297
A	1.0205	1.319
C′	12.796	5.39
C′′	0.751	3.654
A^G	0.0304	3.840
A^U	0.00304	0.39928
θ_D (K)	188.806	129.305
V_l (m/s)	3257.504	2609.127
V_t (m/s)	1862.957	1385.540
V_m (m/s)	2069.937	1548.330

For mechanical stability, the Born stability conditions must be fulfilled [30], i.e.,

$$(C_{11} + 2C_{12}) > 0; C_{11} - C_{12} > 0; C_{44} > 0 \quad (5)$$

Based on the calculated elastic constants, $Cs_2NaAl(Br/I)_6$ demonstrates mechanical stability as it satisfies the Born mechanical stability conditions outlined in Equation 5. B/G ratio was employed for assessing the ductility or brittleness, revealing values of 1.724, signifying brittle behavior for $Cs_2NaAlBr_6$ and 2.213 for Cs_2NaAlI_6 which shows ductile behaviour . The Poisson's ratio (ν), falls within the range of $0 < \nu < 0.5$ (Draxl *et al* 2006), suggesting limited plasticity in these halide double perovskites compounds. Different levels of anisotropy were found across the series by computing the elastic anisotropy percentages (A^G) and the universal elastic anisotropy index (A^U).

This analysis, summarized in Table 2. Using the ELATE software (Gaillac *et al*. 2016), we generated three-dimensional (3D) representations depicting the directional dependence of Young's modulus (Y), linear compressibility (β), shear modulus (G), and Poisson's ratio (υ) for $Cs_2NaAl(Br/I)_6$. The level of anisotropy is visually represented by deviations from spherical shapes in the figures, reflecting variations in physical attributes across different orientations (Aravindan *et al*. 2022). Table 3 summarizes the maximum and minimum values for these properties obtained for $Cs_2NaAl(Br/I)_6$.

Table 3: The Values of Young's Modulus (Y), Linear Compressibility (β), Shear Modulus (G), and Poisson's Ratio (υ) (Hnuna *et al*. 2023), at their Maximum and Minimum are.

Compound	Y (GPa)		β (TPa-1)		G (GPa)		υ	
	Y_{Min}	Y_{Max}	β_{Min}	β_{Max}	G_{Min}	G_{Max}	υ_{Min}	υ_{Max}
$Cs_2NaAlBr_6$	32.32	33.682	14.67	14.67	12.796	13.441	0.23989	0.27116
Cs_2NaAlI_6	14.605	24.022	19.876	19.876	5.39	9.523	0.086185	0.50262

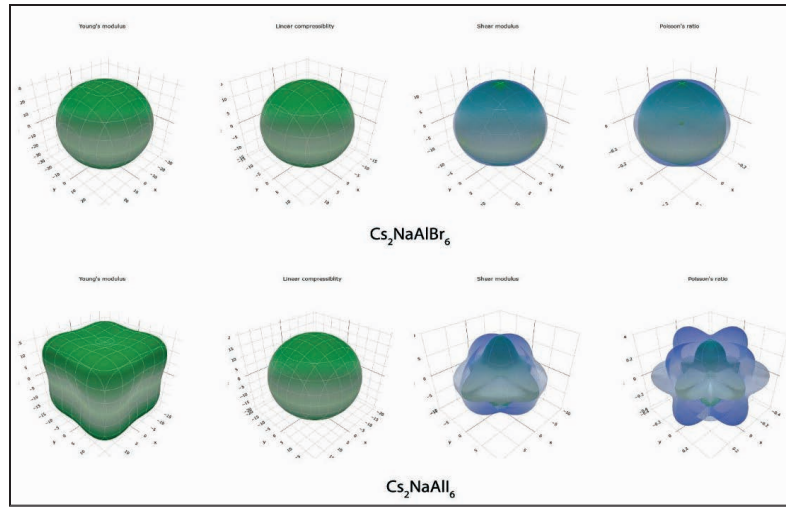

Fig. 4: Three-dimensional Graphical Representation of Young's Modulus, Linear Compressibility, Shear Modulus, and Poisson's Ratio of $Cs_2NaAl(Br/I)_6$.

Optical Properties

The linear response of a solid's macroscopic optical properties is generally characterized by the complex dielectric function, which can be computed by the following equation (Kramers, 1927, Kronig 1926):

$$\varepsilon(\omega) = \varepsilon_1(\omega) + i\varepsilon_2(\omega) \quad (6)$$

The extent of a material's polarization under incident light at the plasmonic resonance frequency is represented by $\varepsilon_1(\omega)$ while $\varepsilon_2(\omega)$ describes the level of light absorption by the material (Draxl, 2006). The imaginary component of the dielectric function, $\varepsilon_1(\omega)$, can be determined using the relevant momentum matrix, as shown below (Penn, 1962):

$$\varepsilon_2(\omega) = \frac{e\hbar}{\pi m^2\omega^2}\sum_{\upsilon,c}\int |M_{c\upsilon}(k)|^2\,\delta\,[\omega_{c\upsilon}(k)-\omega]d^3k \quad (7)$$

The Kramer-Kronig transformation can be used to get $\varepsilon_1(\omega)$ from $\varepsilon_2(\omega)$ (Khandy *et al*. 2016) as,

$$\varepsilon_1(\omega) = 1 + \frac{2}{\pi}P\int_0^\infty \frac{\omega'\varepsilon_2(\omega')}{\omega'^2-\omega^2}d\omega' \quad (8)$$

The following equations can be employed to determine distinct optical properties, including reflectivity (Ziane *et al*. 2014), refractive index, extinction coefficient (Cheddadi *et al*. 2017), and absorption coefficient (α) (Ziane *et al*. 2014).

$$R(\omega) = \left|\frac{\varepsilon^{\frac{1}{2}}(\omega)-1}{\varepsilon^{\frac{1}{2}}(\omega)+1}\right| \quad (9)$$

$$\alpha(\omega) = \sqrt{2}\omega\left[\left(\sqrt{\varepsilon_1^2(\omega)+\varepsilon_2^2(\omega)}\right)-\varepsilon_1(\omega)\right]^{\frac{1}{2}} \quad (10)$$

$$n(\omega) = \left[\frac{\varepsilon_1}{2}+\frac{\sqrt{\varepsilon_1^2(\omega)+\varepsilon_2^2(\omega)}}{2}\right]^{\frac{1}{2}} \quad (11)$$

$$k(\omega) = \left[\frac{\sqrt{\varepsilon_1^2(\omega)+\varepsilon_2^2(\omega)}}{2}-\frac{\varepsilon_1}{2}\right]^{\frac{1}{2}} \quad (12)$$

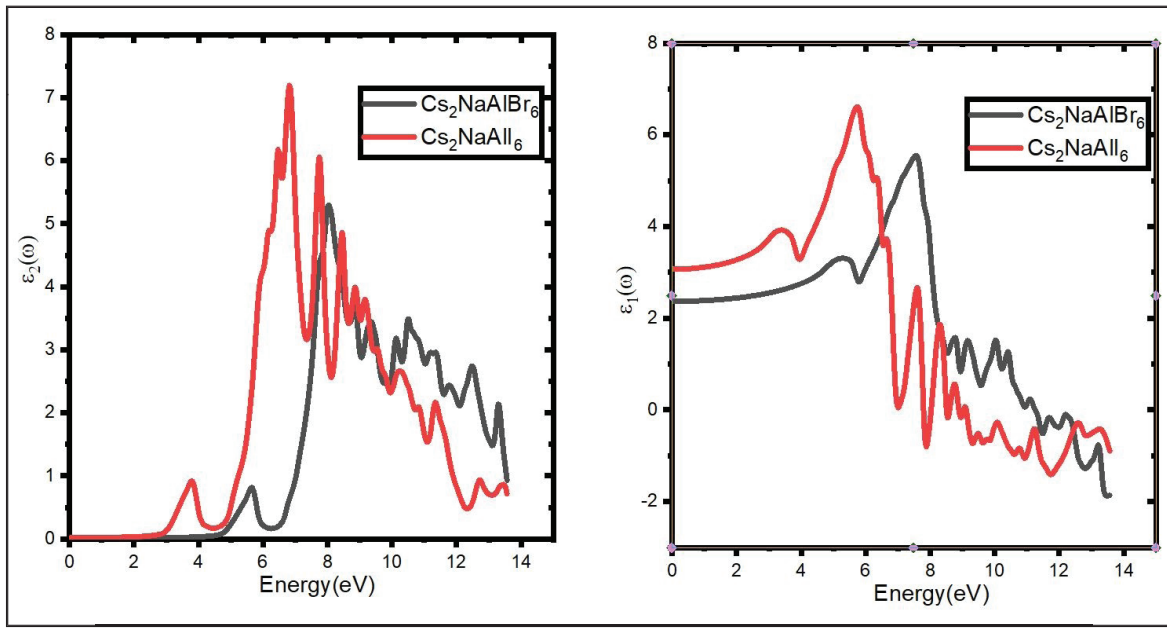

Fig. 5: Calculated (a) Imaginary and (b) Real Parts of Dielectric Function of $Cs_2NaAl(Br/I)_6$.

Figure 5 (b) illustrates the computed $\varepsilon_1(\omega)$ for $Cs_2NaAl(Br/I)_6$. $\varepsilon_1(\omega)$ signifies the material's capacity to retain and release electrical energy through polarization in response to an external electric field, indicating its capacitive behavior. Notably, the peak polarization occurs at 7.55 eV for $Cs_2NaAlBr_6$ and at 5.75 eV for Cs_2NaAlI_6. The change in resonance point towards lower energies with changing halides from Br to I is credited to the lowering of the energy gap (Kramers, 1927). Larger halogen ions possess increased polarizability due to their higher electron count, contributing to a higher real part of the dielectric constant. Consequently, heavier halogen ions exhibit stronger ionic polarization, resulting in enhanced capacitive behavior. The negative $\varepsilon_1(\omega)$ in the UV region indicates high absorption and polarization disappearance. The inverse correlation between the static dielectric constant and the band gap focus on the defect-tolerance capabilities of the compounds (Penn, 1962). Higher dielectric constants imply stronger Coulombic screening, reducing defect carrier-capture cross-sections and suppressing non-radiative recombination rates. Table 4 lists the calculated $\varepsilon(0)$ values of $Cs_2NaAl(Br/I)_6$. Figure 5 (a) showcases the calculated $\varepsilon_2(\omega)$ for $Cs_2NaAl(Br/I)_6$, revealing the frequency at which the material experiences maximum absorption of electromagnetic energy. The peak position in $\varepsilon_2(\omega)$ is indicative of loss mechanisms within the material, including absorption and dissipation of energy. Notably, as we transition from Bromine to Iodine, the size of the halogen atoms increases. Larger atoms exhibit lower-frequency vibrations, contributing to a downward shift in the peak value position. The fundamental edge of absorption, occurring at 4.86 eV, and 2.97 eV for $Cs_2NaAl(Br/I)_6$ corresponds to direct transitions between the lowest conduction band and highest valence band. As the size of the halogen atoms increases, ionization energies decrease, leading to lower-energy electronic transitions. Consequently, the fundamental edge of absorption tends to decrease with larger halogen atoms. The maximum intensity of these peaks, occurring at 7.83 eV, and 6.47 eV for $Cs_2NaAl(Br/I)_6$ respectively, highlights the zone of highest absorption within the ultraviolet spectrum. Notably, the magnitude of $\varepsilon_2(\omega)$ peaks increases and shifts towards decreased energies with alterations in halides from Bromine to Iodine, attributed to the expansion of the electron cloud from Bromine to Iodine.

Table 4: Computed Static Dielectric Constant $\varepsilon(0)$, Static Refractive Index $n(0)$ and Static Reflectivity $R(0)$.

Compound	$\varepsilon(0)$	$n(0)$	$R(0)$
$Cs_2NaAlBr_6$	2.37	1.54	0.0450
Cs_2NaAlI_6	3.07	1.75	0.0746

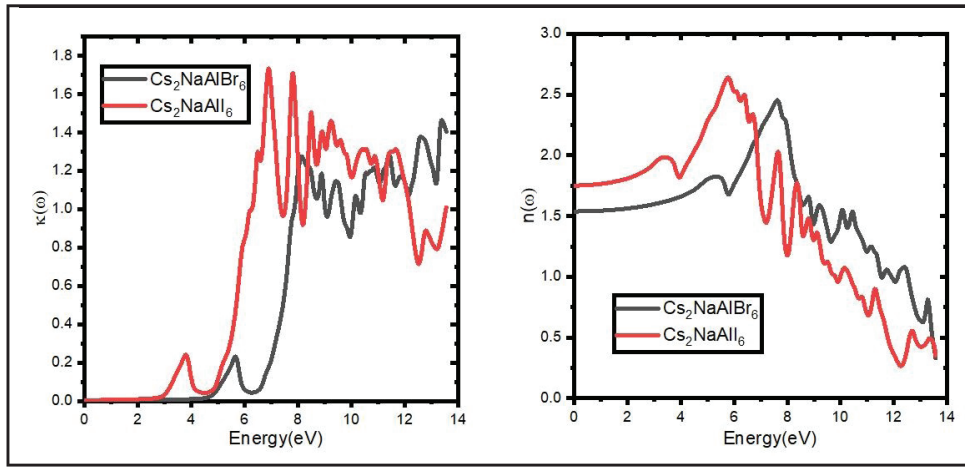

Fig. 6: Calculated (a) Extinction Coefficient and (b) Refractive Index of $Cs_2NaAl(Br/I)_6$.

Figure 6 (b) presents the calculated refractive index for $Cs_2NaAl(Br/I)_6$, offering insights into the type of interactions occurring when a photon interacts with the lattice. The refractive index reveals the nature of bonding in materials (Khandy *et al*. 2016). Covalently bonded materials generally exhibit higher n(ω) values compared to ionic compounds. This is because the stronger interactions between their shared electrons and incoming photons lead to a reduction in photon energy (Volonakis *et al*. 2017). Hence, materials with higher refractive indices typically feature more prominent covalent bonds, whereas those with lower refractive indices are characterized by predominant ionic bonds (Huma *et al*. 2021). The low refractive index observed in $Cs_2NaAl(Br/I)_6$ indicates the prevalence of ionic bonds within the compound. The transparency of a material is correlated with its refractive index, with semiconductors typically exhibiting values between 2–3 (Noor *et al*. 2018). The refractive index n(ω) rises in the IR and visible regions, reaching peaks at 7.86 eV and 5.93 eV in the UV region, before rapidly decreasing at elevated energies.At higher energies, the refractive index becomes fractional, transitioning the material's response towards a more metal-like behaviour, where group velocity exceeds phase velocity (Zai *et al*. 2003, Zhang *et al*. 2015). In Figure 6 (a), the calculated k(ω) for $Cs_2NaAl(Br/I)_6$ is depicted. The threshold energies of k(ω) begin at 4.72 eV, and 2.91 eV for $Cs_2NaAl(Br/I)_6$, closely aligned with the calculated bandgap. With energy in the visible range, these k(ω) values show a rising trend that peaks in the UV region. The computed $n(0)$ are summarized in Table 4.

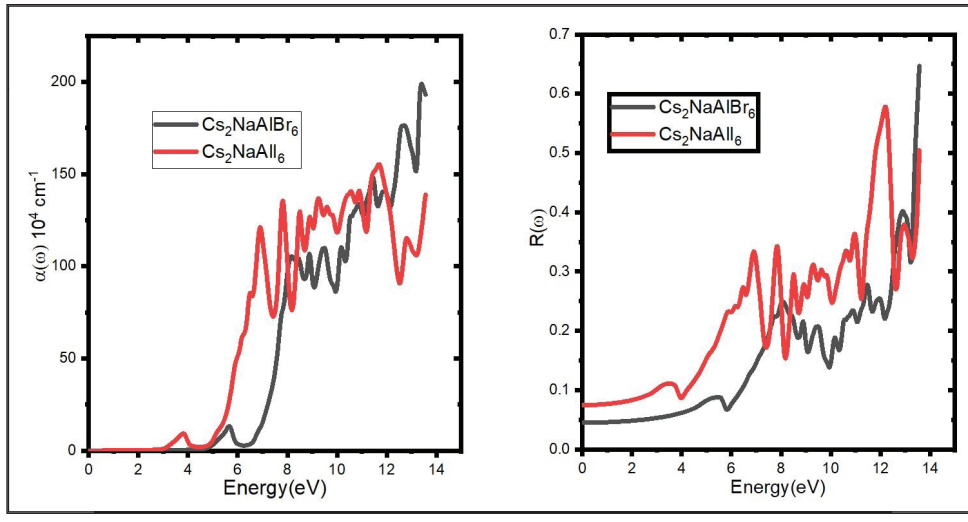

Fig. 7: Calculated (a) Absorption Coefficient and (b) Reflectivity of $Cs_2NaAl(Br/I)_6$.

In Figure 7 (a), the calculated α(ω) for $Cs_2NaAl(Br/I)_6$ are depicted. α(ω) displays two discernible categories of peaks: a shoulder peak ascribed to sub-bands and a noticeable peak coming from VB and CB transitions. Interestingly, the visible spectrum shows significant absorption in the first band of α(ω), with the UV area showing the highest absorption. R(ω) exhibit pronounced peaks in the ultraviolet spectrum, ranging from 7 to 14 eV, as displayed in Figure 7 (b). This suggests the promising potential of $Cs_2NaAl(Br/I)_6$, for applications in UV detectors, Bragg reflectors etc. Figure 7(b) illustrates a notable decrease in optical reflectivity within the low-energy range up to 6 eV, followed by a sharp increase in reflectivity at higher energy levels, with peaks observed beyond 11 eV for these compounds. The static reflectivity values that were computed are presented in Table 4. For $Cs_2NaAlBr_6$ and Cs_2NaAlI_6, the maximum reflectivity is 0.57 and 0.65, respectively, underscoring their effectiveness in the low-energy range. The low reflectivity scores, particularly evident in the visible and infrared regions, suggest transparency in these spectral regions, making these compounds suitable candidates for anti-reflective coatings.

Thermoelectric Properties

The thermoelectric properties of $Cs_2NaAl(Br/I)_6$ were calculated using semi-classical Boltzmann transport theory within the constant relaxation time approximation (RTA), as implemented in BoltzTraP2 (Madsen *et al*. 2018).

Figure 8(b) illustrates the computed electrical conductivity of the studied compounds. As temperature rises, the conductivity (σ) also increases, due to the enhanced ease with which carriers transition from the valence band to the conduction band at elevated temperatures. This observed rise in σ affirms the semiconducting behaviour of these materials. Notably, a decrease in σ is noted as Bromine is substituted with iodine. This decrease might be attributed to the growth of atoms, which leads to electron Coulomb repulsion and, as a result, limits carrier mobility. Additionally, the higher σ indicates a decrease in electrical resistivity (ρ = 1/σ) for the HDP.

Figure 8(a) presents the Seebeck coefficient (S), which quantifies the voltage shift caused by temperature variations (S = ΔV/ΔT) (Noor *et al*. 2018). The Seebeck coefficient is influenced by the carrier concentration and the effective mass associated with the density of states (DOS) (Yousuf *et al*. 2017), as shown below

$$S = \left[\left(\frac{8\pi^2}{3e}\right)\left(\frac{k_b^2}{h^2}\right)\left(\frac{3n}{\pi}\right)^{-2/3} m^*_{DOS}\, T\right] \quad (13)$$

Near the fermi level, materials with flat bands have a high effective mass and make good thermoelectric technology prospects. A positive Seebeck coefficient (S) indicates the presence of p-type carriers (Tang *et al*. 2011). The Seebeck coefficient exhibits an increasing trend with rising temperature. Additionally, Figure 8(a) highlights that Cs_2NaAlI_6 exhibits a higher Seebeck coefficient, which decreases when Iodine is replaced with Bromine. The decrease in the Seebeck coefficient is due to thermal agitation, which hinders carrier mobility and elevates the potential difference (Hnuna *et al*. 2023). The remarkable Seebeck coefficients observed in these HDPs can be attributed to the nearly flat conduction bands between the L and Γ directions, as shown in Figure 2. Table 5 lists the thermoelectric coefficients at room temperature.

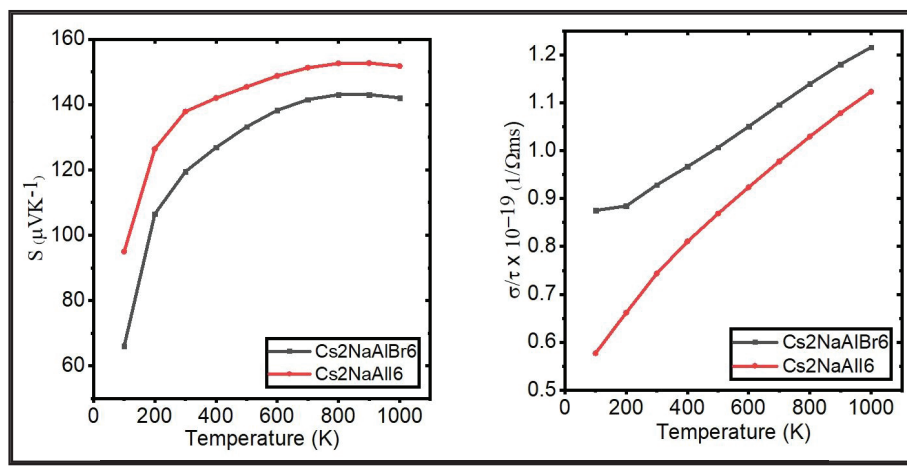

Fig. 8. Calculated (a) Seebeck Coefficient and (b) Electrical Conductivity of $Cs_2NaAl(Br/I)_6$.

Table 5: Computed Thermoelectric Coefficient at Room Temperature.

Compound	S (μVK^{-1})	σ (Ωm)$^{-1}$	κ_e (Wm^{-1}K^{-1})	*ZT*
$Cs_2NaAlBr_6$	119.503	9.29 x 10^{18}	3.95 x 10^{13}	1.006
Cs_2NaAlI_6	137.847	7.44 x 10^{18}	3.20 x 10^{13}	1.32

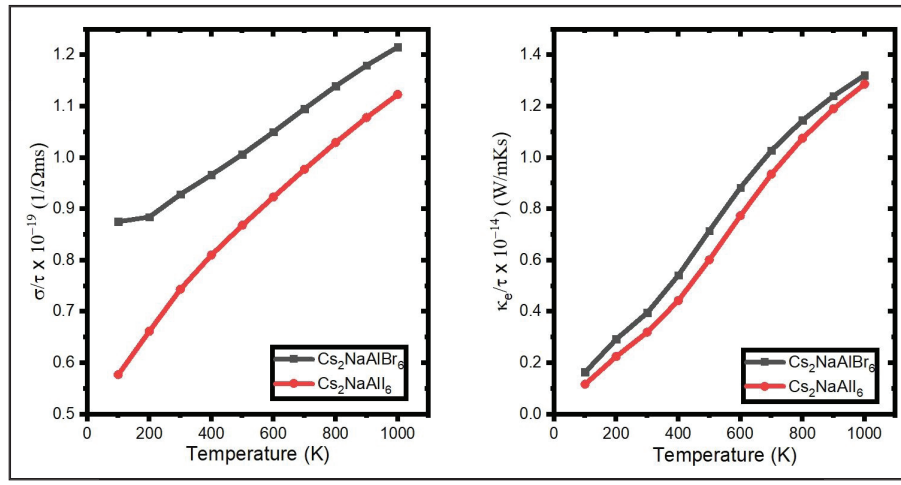

Fig. 9: Calculated Electrical and Thermal Conductivity of $Cs_2NaAl(Br/I)_6$.

Thermal conductivity arises from both electronic and lattice vibrations, which together constitute the overall thermal (Hnuna *et al.* 2023). Figure 9 illustrates the calculated electrical and thermal conductivities. The Wiedemann-Franz law, which relates electrical conductivity to thermal conductivity, is expressed as LT = κ/σ (Takeuchi, 2009). For ideal thermoelectric materials, maintaining a low ratio is crucial. $Cs_2NaAl(Br/I)_6$ exhibited exceptionally low κ/σ ratios, approximately on the order of 10^{-5}, making them highly suitable for thermoelectric applications.

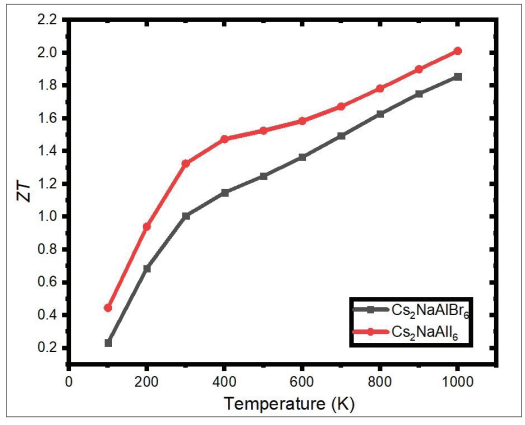

Fig. 10: Calculated Figure of Merit of $Cs_2NaAl(Br/I)_6$.

The efficiency of the thermoelectric material was estimated using the dimensionless figure of merit $ZT = S^2\sigma T/\kappa$ (Hnuna *et al.* 2023, Tritt *et al.* 2005). Figure 10 shows the temperature-dependent variation of *ZT*, with *ZT* increasing as the temperature rises.The combination of modest κ and large Seebeck S and σ is responsible for this increase in ZT. The efficiency of the materials elevated on substitution of halides from, Bromine to Iodine, owing to the augmented potential gradient.

Thermodynamic Properties

The thermodynamic properties were calculated using the GIBBS2 code in conjunction with the quasiharmonic Debye model (de-la-Roza *et al.* 2011). Figure 11 shows the specific heat values at constant pressure and constant volume obtained from these calculations. Specific heat at constant pressure and volume is a key thermodynamic property that indicates the amount of energy required to increase the temperature of a substance by one degree Celsius or Kelvin while keeping pressure or volume constant, respectively (Pan *et al.* 2016). Transitioning from $Cs_2NaAlBr_6$ to Cs_2NaAlI_6 involves a larger halogen atom size (Br, I), leading to reduced vibrational frequencies within the crystal lattice. This

augmented vibrational motion translates to higher heat capacity, as more energy is required to stimulate these modes. Under 400 K, the C_V values exhibit temperature sensitivity, increasing quickly and having a somewhat steep slope in accordance with Debye's T^3 law. This is mainly due to the exponential rise in the number of excited phonon modes (Pan *et al*. 2016), with long-wavelength lattice vibrations being the primary contributors to the heat capacity at constant volume.The values of C_V approach a constant at temperatures above 400 K, in accordance with the Dulong-Petit law (Hadi *et al*. 2017).

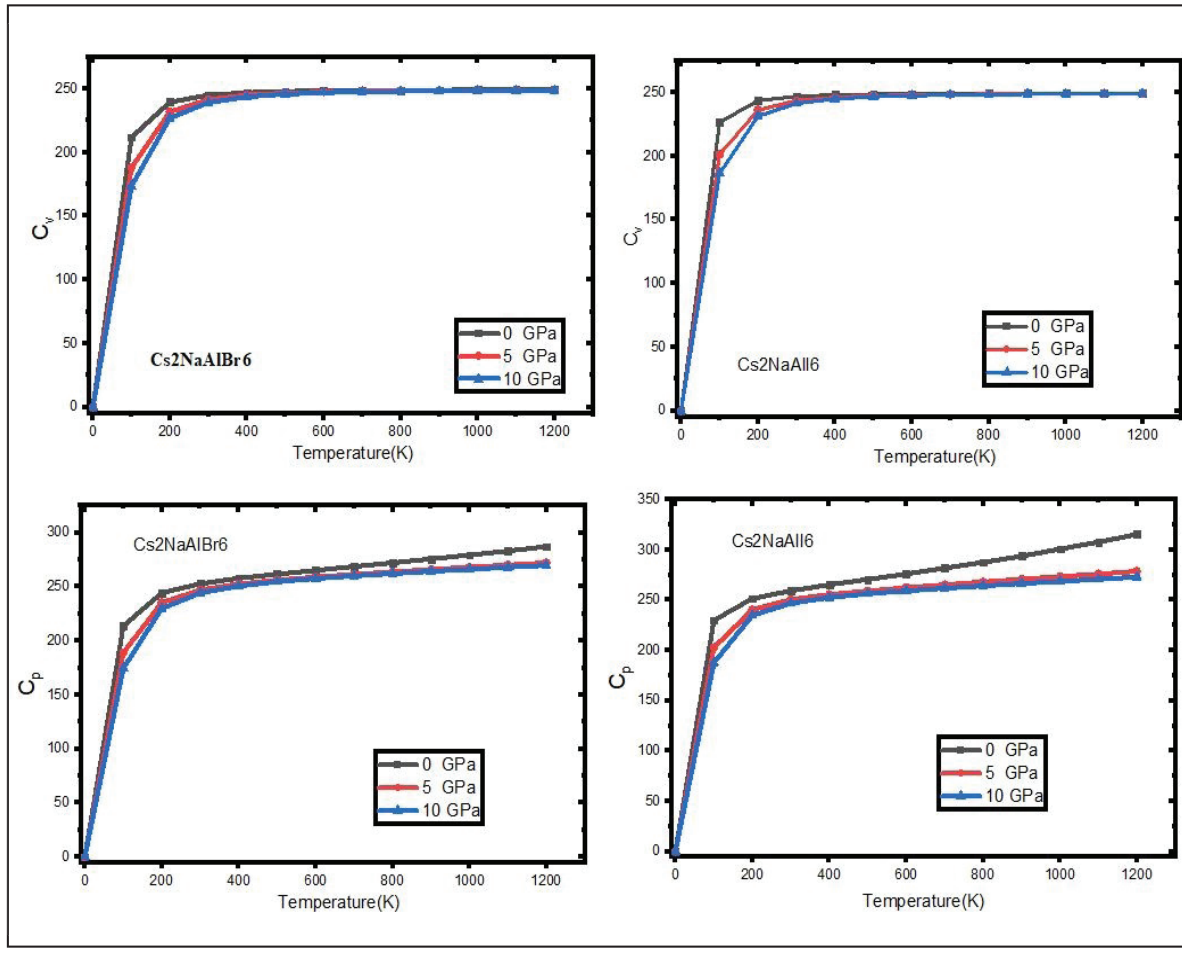

Fig. 11: Calculated Specific Heat at Constant Volume and Pressure of $Cs_2NaAl(Br/I)_6$.

The calculated Gibbs free energy (G) and entropy (S) are illustrated in Figure 12. G, a thermodynamic potential, amalgamates enthalpy and entropy, offering insights into the spontaneity and thermodynamic favourability of a process. It acts as an indicator of the maximum work that can be extracted from a system under constant temperature and pressure conditions (Hadi *et al*. 2017). A negative ΔG denotes a spontaneous process, indicating the system's tendency towards a lower energy state. Conversely, a positive ΔG suggests a non-spontaneous process necessitating input work. Entropy (S), in contrast, represents the level of disorder or randomness within a system, which is crucial for understanding the physical properties of materials. The entropy change (ΔS) delineates the system's disorder, with a positive ΔS favouring spontaneity by indicating an increase in system disorder. As the size of halogen atoms progresses from Bromine to iodine, larger atoms exhibit lower vibrational frequencies, intensifying vibrational modes and augmenting entropy. Larger atoms offer increased options for atomic arrangement, resulting in a greater number of microstates and consequently higher entropy.

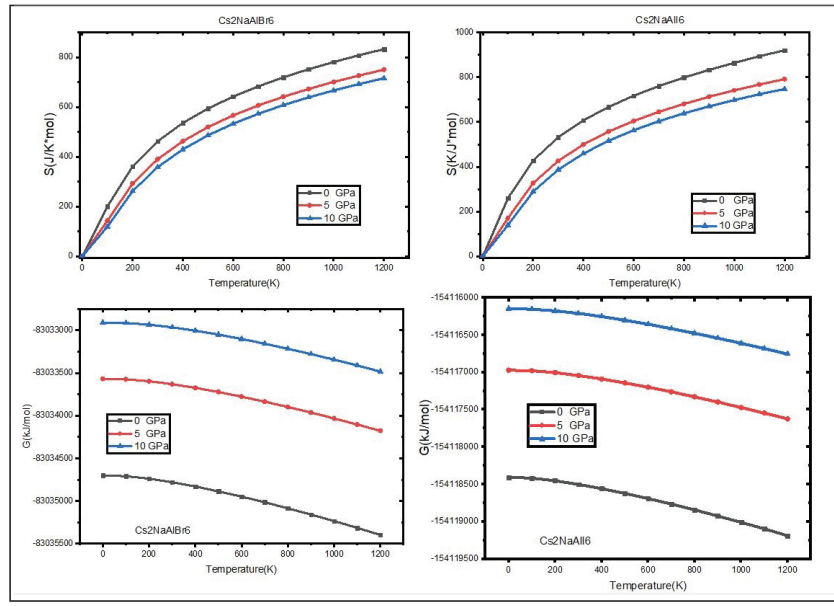

Fig. 12: Calculated Entropy and Gibb's Free Energy of $Cs_2NaAl(Br/I)_6$.

Figure 13 (b) illustrates the computed thermal expansion coefficient (α). This coefficient quantifies the fractional change in size for each Kelvin rise in temperature, offering insights into a material's expansion or contraction behaviour. A positive α denotes expansion, while a negative value signifies contraction, shedding light on the material's thermal responsiveness. The positive thermal expansion coefficients observed across the entire temperature spectrum for $Cs_2NaAl(Br/I)_6$ indicate their propensity to expand with increasing temperature. A higher thermal coefficient implies greater sensitivity to temperature variations, where even minor temperature fluctuations can induce notable dimensional changes. Understanding thermal expansion coefficients is crucial in engineering applications, particularly in structural design, where maintaining dimensional stability is paramount.

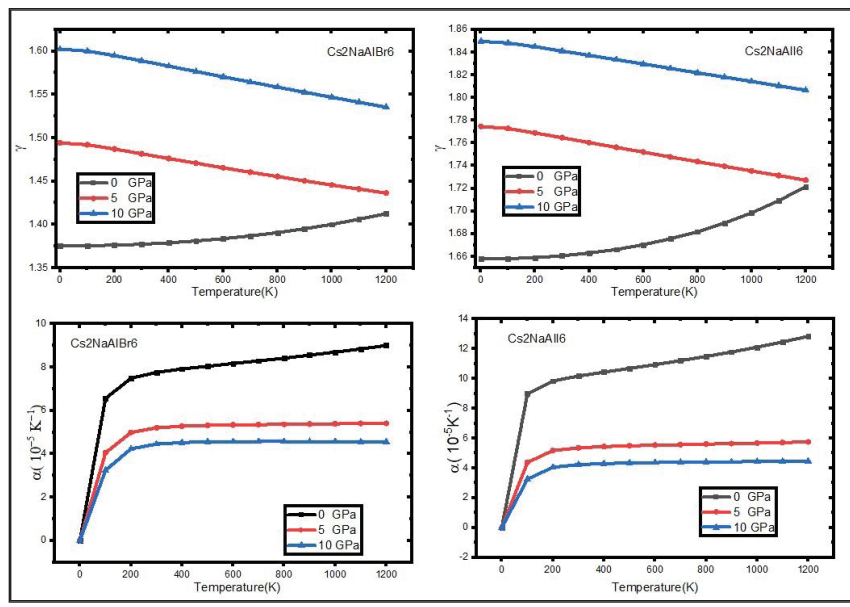

Fig. 13: Calculated Grüneisen Parameter and Thermal Expansion Coefficient of $Cs_2NaAl(Br/I)_6$.

In Figure 13 (a), the computed Grüneisen parameter (γ) is presented. While a harmonic crystal exhibits solely harmonic oscillations, real materials feature notable anharmonic effects, quantified by the Grüneisen parameter. The observed trend in γ for $Cs_2NaAl(Br/I)_6$ reveals a decrease as Bromine is replaced with Iodine. This variation correlates with the increasing size of halogen atoms within the group. Larger atoms possess greater degrees of freedom and tend to exhibit softer vibrational modes, influencing the overall anharmonicity of lattice vibrations.

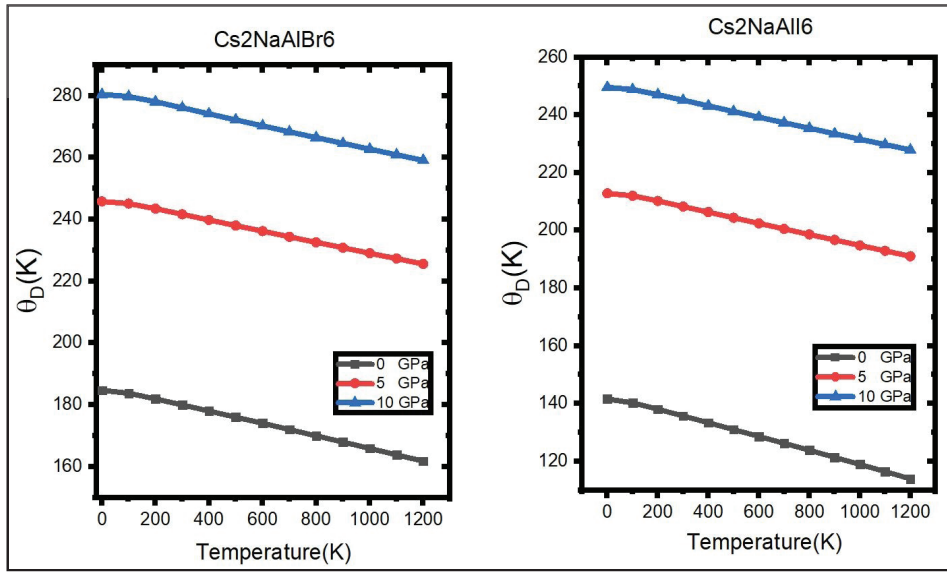

Fig. 14: Calculated Debye's Temperature of $Cs_2NaAl(Br/I)_6$.

Figure 14 illustrates our computed Debye temperature, a characteristic parameter delineating the average thermal vibrations of atoms or molecules within a crystal lattice. For $Cs_2NaAl(Br/I)_6$, the Debye temperature remains relatively constant within the range of 0 K to 100 K. This constancy arises from low anharmonicity and minimal expansion of the crystal structure with increasing temperature, leading to a nearly consistent Debye temperature. θ_D exhibits a gradual and nearly linear decrease as temperature rises, indicating alterations in the vibrational spectrum of atoms with changing temperature. Moreover, the Debye temperature can be used as a stand-in for measuring the hardness and strength of chemical bonds in a material; a higher Debye temperature corresponds to both stronger and harder bonds (Zelai *et al*. 2024). Accordingly, Figure 14 illustrates that the bond strength and hardness.

CONCLUSION

The novelty of this work lies in the comprehensive exploration of $Cs_2NaAl(Br/I)_6$ compounds, which are relatively uncharted in scientific research. By systematically investigating their structural, electronic, optical, and thermoelectric properties, this study provides the first detailed insights into their potential for advanced technological applications. These materials exhibit a unique combination of properties—thermodynamic stability, direct bandgaps, and high thermoelectric efficiency—that positions them as strong candidates for next-generation energy solutions. The ability to tune their electronic and optical behaviour through halogen substitution offers a versatile platform for optimizing performance in specific applications. For technological advancements, $Cs_2NaAl(Br/I)_6$ compounds could be implemented in efficient waste heat recovery systems, converting thermal energy into electricity with high efficiency. Their transparency and semiconductor-like properties make them suitable for optoelectronic devices, such as transparent conductors and photovoltaic cells, potentially leading to more efficient solar panels and energy-saving windows. Additionally, their stable cubic phase and mechanical robustness ensure durability in practical applications, making them reliable materials for long-term use in harsh environments.

Overall, the findings from this study not only introduce new materials with promising characteristics but also pave the way for their application in emerging technologies, contributing to the advancement of sustainable energy solutions and efficient electronic devices.

REFERENCES

Ali, M. A., Dar, S. A., AlObaid, A. A., Al-Muhimeed, T. I., Hegazy, H. H., Nazir, G., & Murtaza, G. (2021). Appealing perspectives of structural, electronic, mechanical, and thermoelectric properties of Tl2 (Se, Te) Cl6 vacancy-ordered double perovskites. *Journal of Physics and Chemistry of Solids*, *159*, 110258.

Ambrosch-Draxl, C., & Sofo, J. O. (2006). Linear optical properties of solids within the full-potential linearized augmented planewave method. *Computer physics communications*, *175*(1), 1-14.

Aravindan, V., Rajarajan, A. K., Vijayanarayanan, V., & Mahendran, M. (2022). First-principles calculations on novel Co-based equiatomic quaternary heusler alloys for spintronics. *Materials Science in Semiconductor Processing*, *150*, 106909.

Bartel, C. J., Sutton, C., Goldsmith, B. R., Ouyang, R., Musgrave, C. B., Ghiringhelli, L. M., & Scheffler, M. (2019). New tolerance factor to predict the stability of perovskite oxides and halides. *Science advances*, *5*(2), eaav0693.

Blaha, P., Schwarz, K., Madsen, G. K., Kvasnicka, D., & Luitz, J. (2001). wien2k. *An augmented plane wave+ local orbitals program for calculating crystal properties*, *60*(1).

Blancon, J. C., *et al*. (2020). First-Principles Calculations of Halide Perovskites: Methods, Accuracy, and Applications. *ACS Energy Letters*, 5(7), 1987-1996.

Cai, M. Q., Yin, Z., & Zhang, M. S. (2003). First-principles study of optical properties of barium titanate. *Applied physics letters*, *83*(14), 2805-2807.

Cai, Y., Xie, W., Teng, Y. T., Harikesh, P. C., Ghosh, B., Huck, P., ... & Asta, M. (2019). High-throughput computational study of halide double perovskite inorganic compounds. *Chemistry of Materials*, *31*(15), 5392-5401.

Chakraborty, S., Xie, W., Mathews, N., Sherburne, M., Ahuja, R., Asta, M., & Mhaisalkar, S. G. (2017). Rational design: A high-throughput computational screening and experimental validation methodology for lead-free and emergent hybrid perovskites. *ACS Energy Letters*, *2*(4), 837-845.

Charef, S., Assali, A., & Boukortt, A. (2024). Optoelectronic and thermoelectric properties of novel double halide perovskites Na2AgAsX6 (X= Cl, Br) for efficient green solar cells. *Materials Today Communications*, *38*, 108065.

Cheddadi, S., Boubendira, K., Meradji, H., Ghemid, S., Hassan, F. E. H., Lakel, S., & Khenata, R. (2017). First-principle calculations of structural, electronic, optical, elastic and thermal properties of MgXAs _ 2 MgXAs 2 (X= Si, Ge X= Si, Ge) compounds. *Pramana*, *89*, 1-10.

Gaillac, R., Pullumbi, P., & Coudert, F. X. (2016). ELATE: an open-source online application for analysis and visualization of elastic tensors. *Journal of Physics: Condensed Matter*, *28*(27), 275201.

Ghrib, T., Rached, A., Algrafy, E., Al-nauim, I. A., Albalawi, H., Ashiq, M. G. B., ... & Mahmood, Q. J. M. C. (2021). A new lead free double perovskites K2Ti (Cl/Br) 6; a promising materials for optoelectronic and transport properties; probed by DFT. *Materials Chemistry and Physics*, *264*, 124435.

Goldschmidt, V. M. (1926). Die gesetze der krystallochemie. *Naturwissenschaften*, *14*(21), 477-485.

Hnuna, L., & Pachuau, Z. (2023). Electronic, optical and thermoelectric properties of halide double perovskites Rb2AgInX6 (X= Cl, Br, I). *Physica Scripta*, *98*(3), 035814.

Huma, M., Rashid, M., Mahmood, Q., Algrafy, E., Kattan, N. A., Laref, A., & Bhatti, A. S. (2021). Physical properties of lead-free double perovskites A2SnI6 (A= Cs, Rb) using ab-initio calculations for solar cell applications. *Materials Science in Semiconductor Processing*, *121*, 105313.

Jain, A., Voznyy, O., Sargent, E. H., *et al*. (2018). Halide Perovskites and Their Emerging Applications. *Chemical Society Reviews*, 47(11), 3657-3672.

Jamal, M., Bilal, M., Ahmad, I., & Jalali-Asadabadi, S. (2018). IRelast package. *Journal of Alloys and Compounds*, *735*, 569-579.

Kale, A. J., Chaurasiya, R., & Dixit, A. (2021). Inorganic lead-Free Cs2AuBiCl6 perovskite absorber and Cu2O hole transport material based single-junction solar cells with 22.18% power conversion efficiency. *Advanced Theory and Simulations*, *4*(3), 2000224.

Kangsabanik, J., Sugathan, V., Yadav, A., Yella, A., & Alam, A. (2018). Double perovskites overtaking the single perovskites: A set of new solar harvesting materials with much higher stability and efficiency. *Physical Review Materials*, *2*(5), 055401.

Karim, M. M., Ganose, A. M., Pieters, L., Winnie Leung, W. W., Wade, J., Zhang, L., ... & Palgrave, R. G. (2019). Anion distribution, structural distortion, and symmetry-driven optical band gap bowing in mixed halide Cs2SnX6 vacancy ordered double perovskites. *Chemistry of materials*, *31*(22), 9430-9444.

Karki, B. B., Ackland, G. J., & Crain, J. (1997). Elastic instabilities in crystals from ab initio stress-strain relations. *Journal of Physics: Condensed Matter*, *9*(41), 8579.

Khandy, S. A., & Gupta, D. C. (2016). Structural, elastic and thermo-electronic properties of paramagnetic perovskite PbTaO 3. *RSC advances*, *6*(53), 48009-48015.

Kong, D., Cheng, D., Wang, X., Zhang, K., Wang, H., Liu, K., & Yin, L. (2020). Solution processed lead-free cesium titanium halide perovskites and their structural, thermal and optical characteristics. *Journal of Materials Chemistry C*, *8*(5), 1591-1597.

Kramers, H. A. (1927). The scattering of light by atoms Atti Cong. Intern. *Fisica (Transactions of Volta Centenary Congress) Como,* 2, 545–57.

Kronig, R. D. L. (1926). On the theory of dispersion of x-rays. *Josa*, *12*(6), 547-557.

Li, C., Lu, X., Ding, W., Feng, L., Gao, Y., & Guo, Z. (2008). Formability of abx3 (x= f, cl, br, i) halide perovskites. *Acta Crystallographica Section B: Structural Science*, *64*(6), 702-707.

M.A. Hadi, M. Roknuzzaman, A. Chroneos, A.K.M.A. Islam, R.V. Vovk, K. Ostrikov, S.H. Naqib, Elastic and thermodynamic properties of new $(Zr_{3-x}Ti_x)AlC2$ MAX-phase solid solutions, Comput. Mater. Sci. 137 (2017) 318e326.

Madsen, G. K., Carrete, J., & Verstraete, M. J. (2018). BoltzTraP2, a program for interpolating band structures and calculating semi-classical transport coefficients. *Computer Physics Communications*, *231*, 140-145.

Mahmood, Q., Younas, M., Ashiq, M. G. B., Ramay, S. M., Mahmood, A., & Ghaithan, H. M. (2021). First principle study of lead-free double perovskites halides Rb2Pd (Cl/Br) 6 for solar cells and renewable energy devices: a quantum DFT. *International Journal of Energy Research*, *45*(10), 14995-15004.

Murtaza, G., Alshahrani, T., Khalil, R. A., Mahmood, Q., Flemban, T. H., Althib, H., & Laref, A. (2021). Lead free double perovsites halides X2AgTlCl6 (X= Rb, Cs) for solar cells and renewable energy applications. *Journal of Solid State Chemistry*, *297*, 121988.

Nabi, M., & Gupta, D. C. (2021). Potential lead-free small band gap halide double perovskites Cs2CuMCl6 (M= Sb, Bi) for green technology. *Scientific reports*, *11*(1), 12945.

Noor, N. A., Mahmood, Q., Rashid, M., Haq, B. U., Laref, A., & Ahmad, S. A. (2018). Ab-initio study of thermodynamic stability, thermoelectric and optical properties of perovskites ATiO3 (A= Pb, Sn). *Journal of Solid State Chemistry*, *263*, 115-122.

Noor, N. A., Saddique, M. B., Haq, B. U., Laref, A., & Rashid, M. (2018). Investigations of half-metallic ferromagnetism and thermoelectric properties of cubic $XCrO_3$ (X= Ca, Sr, Ba) compounds via first-principles approaches. *Physics Letters A*, *382*(42-43), 3095-3102.

NREL (2020). A Comprehensive Review of Double Perovskites for Optoelectronic Applications. *Journal of Physical Chemistry Letters*, 11(15), 5963-5971.

Otero-de-la-Roza, A., Abbasi-Pérez, D., & Luaña, V. (2011). Gibbs2: A new version of the quasiharmonic model code. II. Models for solid-state thermodynamics, features and implementation. *Computer Physics Communications*, *182*(10), 2232-2248.

Pan, R. K., Wang, H. C., Shi, T. T., Tian, X., & Tang, B. Y. (2016). Thermal properties and thermoelasticity of L12 ordered Al_3RE (RE= Er, Tm, Yb, Lu) phases: a first-principles study. *Materials & Design*, *102*, 100-105.

Penn, D. R. (1962).Wave number dependent dielectric function of semiconductors. *Physical Review*, *128*(5), 2093

Reshak, A. H., Fedorchuk, A. O., Lakshminarayana, G., Alahmed, Z. A., Kamarudin, H., & Auluck, S. (2013). Influence of different exchange correlation potentials on band structure and optical constant calculations of ZrGa2 and ZrGe2 single crystals. *Computational materials science*, *78*, 134-139.

Saeed, Y., Amin, B., Khalil, H., Rehman, F., Ali, H., Khan, M. I., ... & Shafiq, M. (2020). Cs 2 NaGaBr 6: a new lead-free and direct band gap halide double perovskite. *RSC advances*, *10*(30), 17444-17451.

Slavney, A. H., Hu, T., Lindenberg, A. M., & Karunadasa, H. I. (2016). A bismuth-halide double perovskite with long carrier recombination lifetime for photovoltaic applications. *Journal of the American chemical society*, *138*(7), 2138-2141.

Takeuchi, T. (2009). Conditions of electronic structure to obtain large dimensionless figure of merit for developing practical thermoelectric materials. *Materials transactions*, *50*(10), 2359-2365.

Tran, F., & Blaha, P. (2009). Accurate band gaps of semiconductors and insulators with a semilocal exchange-correlation potential. *Physical review letters*, *102*(22), 226401.

Tritt, T. M., & Rowe, D. (2005). Thermoelectrics handbook: macro to nano. *Thermoelectrics Handbook: Macro to Nano*.

Volonakis, G., Haghighirad, A. A., Milot, R. L., Sio, W. H., Filip, M. R., Wenger, B., ... & Giustino, F. (2017). Cs2InAgCl6: a new lead-free halide double perovskite with direct band gap. *The journal of physical chemistry letters*, *8*(4), 772-778.

Yang, J., Qiu, P., Liu, R., Xi, L., Zheng, S., Zhang, W., & Yang, J. (2011). Trends in electrical transport of p-type skutterudites R Fe_4 Sb_{12} (R= Na, K, Ca, Sr, Ba, La, Ce, Pr, Yb) from first-principles calculations and Boltzmann transport theory. *Physical Review B*, *84*(23), 235205.

Yousuf, S., & Gupta, D. C. (2017). Investigation of electronic, magnetic and thermoelectric properties of Zr_2NiZ (Z= Al, Ga) ferromagnets. *Materials Chemistry and Physics*, *192*, 33-40.

Zelai, T., Mustafa, G. M., Alotaibi, S., Younas, B., Alhajri, F., Saba, S., ... & Mahmood, Q. (2024). Study of electronic, mechanical, thermoelectric, and optical aspects of K2AlAg (Br/I) 6 for solar cells, and energy storage applications. *Inorganic Chemistry Communications*, *163*, 112344.

Zhang, Y., Li, L., Bai, W., Shen, B., Zhai, J., & Li, B. (2015). Effect of CaZrO 3 on phase structure and electrical properties of KNN-based lead-free ceramics. *RSC Advances*, *5*(25), 19647-19651.

Zhao, L. D., Tan, G., & Kanatzidis, M. G. (2016). Thermoelectric Performance of Halide Perovskites. *Nature Reviews Materials*, 1(10), 16075.

Ziane, M. I., Bensaad, Z., Labdelli, B., & Bennacer, H. (2014). First-principles study of structural, electronic and optical properties of III-arsenide binary GaAs and InAs, and III-nitrides binary GaN and InN: Improved density-functional-theory Study. *Sensors & transducers, 27*(5), 374.

Science and Technology Journal Vol. 12 Issue: 2 June 2024 ISSN: 2321-3388

Topological Fermi Arcs in Weyl Semimetal $MoTe_2$

Md. Tanwir Alam[1] and Dr. Devendra Prasad Singh[2]
[1,2]University Department of Physics,
Bhupendra Narayan Mandal University, Madhepura, Bihar, India

Abstract—Topological Fermi arcs in Weyl semimetals, such as $MoTe_2$, represent a fascinating manifestation of non-trivial electronic surface states arising from the material's unique bulk topology. These surface states connect the projections of Weyl nodes on the surface Brillouin zone, providing a direct signature of the material's topological properties. Observing these Fermi arcs requires a synergy of advanced experimental and theoretical methods. Experimental techniques, including Angle-Resolved Photoemission Spectroscopy (ARPES), Scanning Tunneling Microscopy (STM), and various magneto transport measurements, are employed to visualize and characterize the surface states and Fermi arcs. These techniques allow for detailed mapping of the electronic structure and spatial distribution of the arcs. Theoretical support comes from Density Functional Theory (DFT) and low-energy effective Hamiltonians, which predict the electronic band structure and surface state features, while calculations of topological invariants confirm the topological nature of the material. Together, these approaches provide a comprehensive understanding of the topological characteristics of Weyl semimetals and offer insights into their potential applications in next-generation electronic and spintronic devices.

Keywords: Topological Fermi Arcs, Weyl Semimetal, $MoTe_2$, Angle-Resolved Photoemission Spectroscopy (ARPES), Scanning Tunneling Microscopy (STM), Density Functional Theory (DFT), Electronic Band Structure

INTRODUCTION

In Weyl semimetals like $MoTe_2$, topological Fermi arcs represent intriguing surface states that arise due to the unique electronic structure characterized by Weyl nodes. These nodes are points in momentum space where the conduction and valence bands touch, and their projections on the surface of the material lead to Fermi arcs—arcs of electronic states that connect these projected nodes. $MoTe_2$, a member of the transition metal dichalcogenide family, showcases these phenomena under certain conditions. The study of these Fermi arcs in $MoTe_2$ not only deepens our understanding of topological states of matter but also offers insights into the fundamental properties of Weyl semimetals, bridging theoretical predictions with experimental observations.

The topic of topological Fermi arcs in the Weyl semimetal $MoTe_2$ is an exciting area of research in condensed matter physics. $MoTe_2$ is a type of transition metal dichalcogenide (TMD) that has attracted significant attention due to its Weyl semimetal properties and the associated topological phenomena.

Overview

Weyl Semimetals: Weyl semimetals are materials that host Weyl fermions as low-energy excitations. These materials exhibit non-trivial topological properties, such as Fermi arcs on their surfaces. These Fermi arcs are surface states that connect the projections of Weyl nodes (points in momentum space where the conduction and valence bands touch) on the surface of the material.

$MoTe_2$: $MoTe_2$ is a TMD (Transition metal dichalcogenide) that can exhibit a Weyl semimetal phase under certain conditions. It has a layered structure and can transition between different phases (such as semimetallic and topologically trivial phases) depending on factors like temperature and pressure.

https://doi.org/10.22232/stj.2024.12.02.13

Key Points in Research Articles Observation of Fermi Arcs

Research on $MoTe_2$ often involves angle-resolved photoemission spectroscopy (ARPES) to directly observe the Fermi arcs on the surface of the material. Experiments have shown that $MoTe_2$ exhibits distinct Fermi arc structures, which are evidence of its Weyl semimetal state.

Topological Features

$MoTe_2$ hosts Weyl points that are protected by time-reversal symmetry, and these Weyl points lead to the formation of Fermi arcs on the surface. The nature of these Fermi arcs can provide insights into the topology of the electronic structure and the interplay between different Weyl points.

Phase Transitions

Studies often investigate how external factors like pressure, temperature, or chemical composition can induce phase transitions in $MoTe_2$, affecting its Weyl semimetal characteristics. For instance, $MoTe_2$ can exhibit transitions between different Weyl semimetal phases or even to a topologically trivial phase, which impacts the Fermi arc structure.

Theoretical Models

Theoretical work complements experimental findings by modeling the electronic structure of $MoTe_2$ and predicting the behavior of Fermi arcs.

Models help in understanding how different Weyl nodes and their interactions give rise to observed surface states.

Applications and Implications

The unique electronic properties of Weyl semimetals like $MoTe_2$ have implications for potential applications in electronics and spintronics. Understanding Fermi arcs can contribute to advancements in topological materials and their use in novel electronic devices.

Exploring Topological Fermi Arcs in Weyl Semimetal $MoTe_2$

Exploring topological Fermi arcs in Weyl semimetal $MoTe_2$ involves investigating how these surface states manifest due to the material's unique electronic structure. $MoTe_2$ features Weyl nodes—singular points in momentum space where conduction and valence bands meet—leading to Fermi arcs on its surface. These arcs are crucial for understanding the topological nature of $MoTe_2$ and are typically observed using angle-resolved photoemission spectroscopy (ARPES). Studying these arcs helps uncover the material's Weyl semimetal phase, its electronic properties, and the effects of external factors like pressure or temperature on its topological features.

Unveiling $MoTe_2$: A Weyl Semimetal

Unveiling $MoTe_2$ as a Weyl semimetal involves revealing its distinctive electronic properties and topological features. $MoTe_2$, a member of the transition metal dichalcogenides, exhibits Weyl semimetal behavior when its crystal structure and external conditions, such as temperature or pressure, induce the Weyl phase. This phase is characterized by the presence of Weyl nodes—points in momentum space where the conduction and valence bands touch—and is associated with the appearance of topological Fermi arcs on the surface. These surface states are direct manifestations of the material's non-trivial topological nature and are crucial for understanding the fundamental physics of Weyl semimetals.

The Role of Topological Fermi Arcs

Topological Fermi arcs play a critical role in understanding the electronic structure and topological properties of Weyl semimetals. Here's an overview of their significance:

1. Surface States and Topology

Surface Connection: Topological Fermi arcs are surface states that connect the projections of Weyl nodes on the surface of a Weyl semimetal. They serve as a direct manifestation of the bulk topology of the material.

Surface vs. Bulk: These arcs are not confined to the bulk of the material but are observed on its surface. They provide a tangible way to probe the underlying topological characteristics of the material that arise from the bulk Weyl nodes.

2. Weyl Nodes and Fermi Arcs

Weyl Nodes: Weyl semimetals feature Weyl nodes—points where the conduction and valence bands touch. These nodes act as sources or sinks of Berry curvature in momentum space.

Fermi Arcs: On the surface of a Weyl semimetal, the projections of these Weyl nodes manifest as Fermi arcs.

The arcs connect the projections of the Weyl nodes with opposite chirality and reflect the material's chiral nature.

3. Experimental Significance

Direct Observation: Fermi arcs can be directly observed using angle-resolved photoemission spectroscopy (ARPES). Their observation provides direct evidence of the Weyl semimetal phase and the presence of Weyl nodes.

Surface vs. Bulk: The study of Fermi arcs allows researchers to probe the topological properties of the bulk material through surface measurements. This can be especially useful for materials where bulk measurements are challenging.

4. Topological Protection

Robustness: Fermi arcs are protected by the topological nature of the Weyl nodes. They are robust against perturbations like impurities or surface defects, as long as these do not break theprotecting symmetries (such as time-reversal symmetry).

Edge States: Similar to the edge states in topological insulators, Fermi arcs are a consequence of the topological nature of the Weyl semimetal and are sensitive to changes in the system's symmetry and dimensionality.

5. Implications for Electronics

Conductance: The unique surface states represented by Fermi arcs can influence the electronic properties of the material, potentially leading to unusual transport phenomena.

Applications: Understanding Fermi arcs can impact the development of electronic and spintronic devices, as Weyl semimetals are promising candidates for new types of electronic applications due to their exotic electronic properties.

Experimental Observations Topological Fermi arcs in Weyl Semimetal $MoTe_2$

Experimental observations of topological Fermi arcs in the Weyl semimetal $MoTe_2$ involve several key techniques:

1. Angle-Resolved Photoemission Spectroscopy (ARPES)

Observation: ARPES experiments have directly visualized Fermi arcs on the surface of $MoTe_2$. These experiments reveal the surface state connectivity and the distinctive arc-like shapes connecting the projections of Weyl nodes.

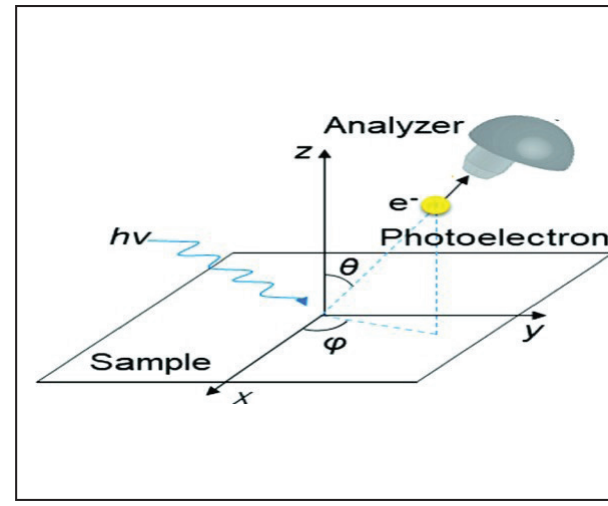

Fig. 1

Significance: Provides direct evidence of the topological surface states and confirms the Weyl semimetal phase.

Technique: ARPES is the most common method for observing Fermi arcs. It involves shining photons onto the surface of the material and measuring the emitted electrons to map out the electronic structure and surface states.

Findings: ARPES experiments on $MoTe_2$ have successfully detected Fermi arcs, revealing their distinctive curved shapes connecting the projections of Weyl nodes. These observations confirm the Weyl semimetal phase and provide insights into the surface state topology.

2. Scanning Tunneling Microscopy (STM)

Observation: STM studies have been used to examine the local electronic structure of $MoTe_2$. STM can confirm the spatial distribution of surface states and their relationship with theoretical predictions.

Significance: Helps visualize the local density of states and the surface features associated with Fermi arcs.

Technique: STM can be used to probe the local density of states at Fermi surface and support ARPES findings by visualizing the distribution and connectivity of surface states the surface of a material. By scanning a sharp tip across the surface, STM provides high-resolution images of surface states.

Findings: STM studies can reveal spatial variations in the Fermi surface and support ARPES findings by visualizing the distribution and connectivity of surface states

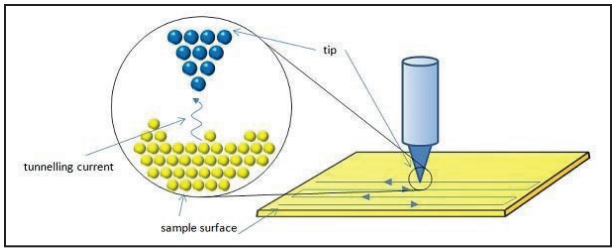

Fig. 2

3. Quantum Oscillations

Observation: Quantum oscillations, such as Shubnikov-de Haas oscillations, observed in transport measurements provide indirect evidence of Weyl nodes and their associated Fermi arcs.

Significance: Supports the presence of topologically protected states by revealing the Landau levels and their connection to the Weyl nodes.

Technique: Quantum oscillations, such as Shubnikov-de Haas oscillations, arise from the Landau quantization of electrons in a magnetic field. These oscillations can provide indirect evidence of Fermi arcs by revealing information about the electronic structure.

Findings: Observations of quantum oscillations can confirm the presence of Weyl nodes and their associated Fermi arcs by analyzing oscillatory patterns and electronic transport properties.

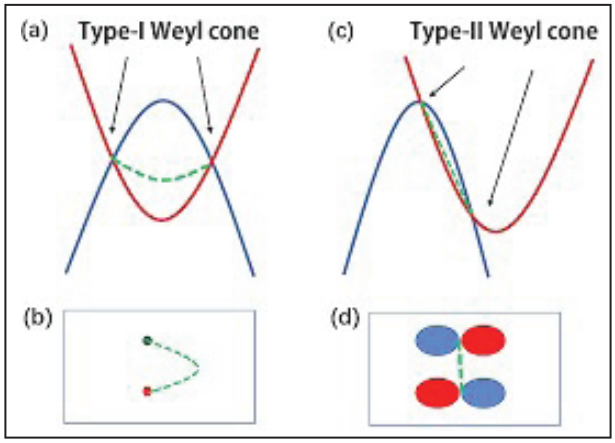

Fig. 3: Type-i and type-ii Weyl Semimetals.

4. Tranport Measurements

Observation: Hall effect and magnetoresistance measurements have shown anomalies consistent with the presence of topological surface states in $MoTe_2$.

Significance: Provides indirect evidence of Fermi arcs by examining the impact of these surface states on the material's electronic transport properties.

Technique: Electrical transport measurements, including Hall effect and magnetoresistance studies, can provide indirect evidence of Fermi arcs by examining how the electronic states contribute to conductivity and other transport properties.

Findings: These measurements often show signatures consistent with the presence of topologically protected surface states, corroborating the existence of Fermi arcs.

Magnetoresistance: By applying a magnetic field and measuring the change in resistance, researchers can probe the bulk and surface states. In Weyl semimetals, this can highlight unique features such as the chiral anomaly and contribute to understanding the Fermi arcs' role.

Quantum Oscillations: Techniques like Shubnikov-de Haas (SdH) and de Haas-van Alphen (dHvA) oscillations provide information about the Fermi surface and can indirectly reveal Fermi arcs through their impact on the electronic structure.

5. Surface State Characterization

Low-Energy Electron Diffraction (LEED): Used to determine the surface structure and periodicity, which can affect the observation of Fermi arcs.

Photoemission Spectroscopy (PES): Besides ARPES, PES can provide complementary information about the electronic states and their binding energies.

Technique: Combining different surface-sensitive techniques, such as ARPES and STM, can offer a comprehensive picture of the surface states and their relationship to the bulk Weyl nodes.

Findings: This approach helps map the connectivity and dispersion of Fermi arcs, providing a clearer understanding of their role in the material's topological properties.

6. **X-ray Photoelectron Spectroscopy (XPS):** Determines the surface composition and electronicstates.
7. **Sample Quality:** High-quality single crystals of $MoTe_2$ are essential for clear observation ofFermi arcs.
8. **Temperature Control:** Experiments are often conducted at low temperatures to reduce thermal broadening and enhance the resolution of surface states.

Theoretical Support

Theoretical support for studying topological Fermi arcs in Weyl semimetals like $MoTe_2$ typically involves:

First-Principles Calculations: Density Functional Theory (DFT) and its extensions help predict the electronic band structure and the location of Weyl nodes.

Density Functional Theory (DFT): Provides a detailed calculation of the electronic band structure, identifying Weyl nodes and their surface projections. This helps predict the presenceand characteristics of Fermi arcs.

Weyl Semimetal Models: Theoretical models, such as the low-energy effective Hamiltonians, describe the bulk Weyl nodes and the surface states, offering insight into the topological natureof Fermi arcs.

Topological Invariants: Calculations of topological invariants, like the Chern numbers or the Berry curvature, are used to characterize the topological phases and confirm the existence of Fermi arcs.

Surface State Theory: Models that predict the surface states and their dispersion help interpret experimental observations and connect them to the bulk topology.

CONCLUSION

The above theoretical and experimental approaches provide an ultimate framework for understanding the electronic properties and topological aspects of Fermi arcs in Weyl semimetals.

Together, these approaches help elucidate the unique properties of Weyl semimetals and contribute to the broader understanding of topological materials. The study of topological Fermi arcs not only advances fundamental physics but also paves the way for potential applications in electronic and spintronic devices

REFERENCES

M. N. Ali, J. Xiong, S. Flynn, J. Tao, Q. D. Gib-son, L. M. Schoop, T. Liang, N. Haldolaarachchige, M. Hirschberger, N. P. Ong, and R. J. Cava, Nature 514, 205 (2014).

X.-C. Pan, X. Chen, H. Liu, Y. Feng, Z. Wei, Y. Zhou, Z. Chi, L. Pi, F. Yen, F. Song, X. Wan, Z. Yang, B. Wang,G. Wang, and Y. Zhang, Nat. Commun. 6, 7805 (2015).

D. Kang, Y. Zhou, W. Yi, C. Yang, J. Guo, Y. Shi, S. Zhang, Z. Wang, C. Zhang, S.Jiang, A. Li, K. Yang, Q. Wu, G. Zhang, L. Sun, and Z. Zhao, Nat. Commun. 6, 7804 (2015).

Y. Qi, P. G. Naumov, M. N. Ali, C. R. Rajamathi, O. Barkalov, Y. Sun, C. Shekhar,S.-C. Wu, V. S¨uß, M. Schmidt, E. Pippel, P. Werner, R. Hillebrand, T. F¨orster, E. Kampertt, W. Schnelle, S. Parkin, R. J. Cava, C. Felser, B. Yan, and S. A. Medvedev,Nat. Com- mun. 7, 11038 (2016).

A. A. Soluyanov, D. Gresch, Z. Wang, Q. Wu, M. Troyer, X. Dai, and B. A. Bernevig,Nature 527, 495 (2015).

Y. Sun, S.-C. Wu, M. N. Ali, C. Felser, and B. Yan, Phys. Rev. B 92, 161107 (2015).

Z. Wang, D. Gresch, A. A. Soluyanov, W. Xie, X. Dai, M. Troyer, R. J. Cava, and B.A. Bernevig, arXiv:1511.07440 (2015).

T.-R. Chang, S.-Y. Xu, G. Chang, C.-C. Lee, S.-M. Huang, B. Wang, G. Bian, H. Zheng, D. S. Sanchez, I. Belopolski, N. Alidoust, M. Neupane, A. Bansil, H.- T. Jeng, H. Lin, and M. Z. Hasan, Nat. Commun. , 1(2016).

X. Wan, A. M. Turner, A. Vishwanath, and S. Y. Savrasov, Phys. Rev. B 83, 205101(2011).

H. Weng, C. Fang, Z. Fang, B. A. Bernevig, and X. Dai, Phys. Rev. X 5, 011029(2015).

H. B. Nielsen and M. Ninomiya, Phys. Lett. B 130, 389 (1983).

Science and Technology Journal Vol. 12 Issue: 2 June 2024 ISSN: 2321-3388

Celestial Harmony: Exploring the Analogy of Greek, Indian, South East Asian and Mizo Astronomy

T. Malsawmtluanga
Dept. of Physics, Lunglei Govt. College, Lunglei-796701, Mizoram, India
E-Mail: tochhawng1981@gmail.com

Abstract—This brief research explores the historical accounts and traditions of astronomy in Greece, India, Southeast Asia, and the Mizo people. We search to discover the common intellectual fabric that these civilisations share across space and time by examining their astronomical works. This research investigates the impact of Indian mathematical expertise on astronomical computations, from the discovery of zero to the development of trigonometric functions. As we shift our focus to Southeast Asia, we learn about the lesser-known but no less fascinating astrological traditions that were common in this area. Through the combination of Buddhism, Hinduism, and indigenous belief systems, a unique system emerged. The sky temples of Angkor and the ancient observatories are two instances of how Southeast Asian astronomy merges religious and scientific constituents.

Most importantly, this research includes the perception of the Mizo people, an indigenous group with a rich cultural history. Following Mizo's historical astrological customs, we find interesting similarities and divergences with the larger Greek, Indian, and Southeast Asian traditions. The way that the stars are connected throughout Mizo rites, agriculture, and folklore provides an insight into the relationship between cosmic and everyday life. The investigation goes past listing commonalities to investigate how the Mizo people have modified and customised astronomical knowledge. The Mizo contribution offers a lively notion of humanity's relationship with the skies, whether through cosmic narratives, celestial navigation methods, or traditional star lore.

INTRODUCTION

The study of stars and their movements has fascinated human civilisations across the globe for millennia. From the ancient Greeks to the cultures of India, Southeast Asia, and the Mizo people, the observation and exposition of the night sky have played a pivotal role in shaping worldviews, religious practices, and social structure. (Kak, 2009)

The foundation of Western astronomy in ancient Greece was built upon the accomplishments of earlier civilisations like the Babylonians and Egyptians. However, other cultures, such as those in India and Southeast Asia, developed revolutionary astronomical traditions. Ancient Indian astronomy, rooted in Vedic texts contains references to the heavenly bodies and their movements which suggests Indians were already at work in observation and documentation as early as 1500. (Kak, 2009)

A Brief History of Mizoram

Mizoram, one of the seven states in northeastern India, has a rich history and cultural heritage shaped by its unique geography and restilient people. The Mizo people believed to have migrated from China in the mid-1600s, have fiercely preserved their traditions. After periods of British rule (1858-1947) and political unrest, Mizoram attained statehood in 1986. Before the arrival of British Christian missionaries in the late 19th century, the Mizo people were head-hunters. Despite facing challenges, the state continues

https://doi.org/10.22232/stj.2024.12.02.14

to develop, driven by the enduring spirit of the Mizo people. (Lalthansanga, 2018; Joshi, 2005).

Greek Astronomy: From Mythical to Mathematical Understanding

Early Greek literature, including Homer's epics and Hesiod's "Works and Days" (Frank, 2014) highlights awareness of constellations and their practical use in agriculture and navigation. While initially less advanced than Egyptian and Babylonian astronomy, Greek understanding evolved with the application of geometry. Aristotle argued for Earth's spherical shape, Eratosthenes calculated its circumference, and Aristarchus pioneered methods to determine celestial distances. (Aaboe, 1974) Eudoxus developed an early model of planetary motion. This shift from mythical to mathematical interpretations marked a crucial development in scientific thought. (Qi *et al*., 2022)

Astronomy Connection with Mythology, Religion

The Greek's understanding of the celestial realm was deeply intertwined with various aspects of their cultural and intellectual landscape, from mythology and religion to time-keeping and agricultural practices. The ancient Greek worldview was profoundly shaped by their rich mythological traditions, which personified the celestial bodies and phenomena. The gods and goddesses of the Greek pantheon were believed to inhabit the heavens, and their movements and interactions were seen as influencing the lives of mortals on Earth. (Qi *et al*., 2022) This belief in the interconnectedness of the divine and the earthly realms was a driving force behind the Greeks' desire to comprehend the workings of the universe.

One example is Orion, who is a prominent figure in Greek mythology, renowned for his hunting prowess and tragic fate. According to Hesiod's *Astronomy*, as summarized by Eratosthenes, Orion was the son of Poseidon and Euryale. Known for his extraordinary hunting skills, Orion boasted that he could kill every beast on Earth. This angered Gaia, the Earth goddess, who sent a giant scorpion to kill him. After a fierce battle, the scorpion fatally stung Orion. As a tribute to his might, Zeus placed Orion among the stars as a constellation. (Most, 2006)

Astronomy and Agriculture

In Hesiod's Works and Days, he provided an agricultural calendar based on the appearance and disappearance of constellations. The Pleiades signal the time for harvest when rising and for ploughing when setting. Grape pruning should commence when Arcturus is visible all night, and grapes should be harvested when Arcturus is visible at dawn alongside Orion and Sirius. The setting of Orion, the Pleiades, and the Hyades marks the time for ploughing. Storms are expected when the Pleiades are hidden below the horizon. Fifty days after the solstice is suitable for sailing. Finally, the appearance of Orion signals the time for threshing. (Most, 2006)

VEDIC ORIGINS AND EVOLUTION OF INDIAN ASTRONOMY

The earliest foundations of Indian astronomy are ingrained in the Vedic tradition. The *Rigveda*, one of the earliest religious texts in the world, contains hymns with references to the cosmos, celestial bodies, and the passage of time. For example, the Sun (Surya), Moon (Chandra), and stars are regularly mentioned in Vedic hymns, reflecting their significance in ceremonial practices and agricultural cycles. The Vedic calendar system, which divides the year into 12 months of 30 days each, indicates an advanced comprehension of the solar year and the need to introduce months to keep the lunar calendar aligned with the solar cycle. (Kak, 2009) The Jyotisa Vedanga, the first Vedic written work to mention astronomical data, has records of events as early as 4000 BCE, making Indian astronomy one of the oldest known systems of its kind. (Srinivas, 2019).

As Indian astronomy evolved, it began to absorb ideas from neighbouring cultures. The exchange of astronomical knowledge with the Babylonians, Persians, and Greeks became particularly pronounced after the conquests of Alexander the Great in the 4th century BCE. (Springer, 1999; Mak, 2014) Greeks and Indians shared common methods for dividing the sky into constellations and assigning symbolic meanings to celestial bodies. The Greek zodiac system, which divided the sky into 12 equal parts, mirrors the Indian concept of nakshatras or lunar mansions. (Harness, 2004) This similarity has led scholars to believe there was significant cross-cultural interaction between Greek and Indian astronomers, with both civilizations influencing one another's astronomical frameworks. (Subrahmanya, 2020) The concept of epicycles (used to explain retrograde planetary motion) and the heliocentric model, though not initially developed in India, found their way into Indian astronomical texts as a result of this cross-cultural exchange. (Rao, 2017)

Mughal astronomy represents a crucial period in India's scientific history, characterized by the fusion of Persian, Islamic, and Hindu astronomical traditions that motioned innovations during the 16th to 18th centuries. For example, Maharaja Sawai Jai Singh II of Jaipur built one of the grandest astronomical observatories in India, the Jantar Mantar, in the early 18th century, showcasing the lasting legacy of Mughal influence on astronomy. This period fostered a collaborative environment that integrated diverse knowledge systems, leading to significant developments in astronomical practices. (Rudra, 2009; Singhania, 2009).

Origins and Solar Calendar: Ancient Indian Astronomy and Mythology and Similarities with the Greeks

Ancient Indian and Greek astronomy are deeply intertwined with their respective mythologies and cultural practices. As mentioned before Indian astronomy has its origins in the Vedic period (2000-1000 BCE), where celestial movements were crucial for religious rituals and agricultural cycles. Deities like Surya (the Sun) and Chandra (the Moon) were central to both mythology and astronomy, with concepts like nakshatras (lunar mansions) playing a key role in tracking the Moon's movement and determining auspicious times for rituals. (Thompson, 2007; Pingree, 1963) Similarly, in Greek mythology, celestial bodies like Orion and Aquila were associated with gods and heroes, reflecting divine will through the movements of the stars. (Schwab, 2011) The zodiac in Greek astronomy also had mythological significance, with each sign corresponding to a mythological figure, demonstrating a connection between celestial patterns and human destiny.(Springer, 1999; Nashkar, 1996)

Both cultures demonstrated remarkable astronomical accuracy within their mythological frameworks. Indian texts like the Surya Siddhanta and Aryabhatiya revealed a sophisticated understanding of planetary positions and celestial mechanics, including the Earth's rotation, long before these concepts were embraced in Europe. (Thompson, 1997; Clark, 1930) Likewise, Greek astronomers like Hipparchus and Ptolemy contributed to astronomy by calculating the precession of the equinoxes and developing planetary models. (Toomer, 1996; Goldstein, 1997). This cross-cultural influence enriched both astronomical traditions, highlighting their shared view of the cosmos as a scientific and spiritual domain.

Hinduism uses both solar and lunar calendars, with the solar calendar (Sauramana) playing a key role in festivals, agriculture, and astrology. The solar year is divided into 12 months, each aligned with a zodiac sign. (Gansten, 2018) Similarly, the Greek solar calendar divides the year into 12 months based on zodiac signs, linking celestial patterns to mythology. Each Greek zodiac sign was associated with specific deities or myths, like Capricorn, linked to Pan, symbolizing winter, and Leo, associated with the Sun and celebrated during summer with feasts and games honouring the gods. (Reingold *et al*., 2008)

The twelve solar months are given in Table 1.

Table 1: The Solar Months in Greek, Indian and Gregorian Months. (Gansten, 2018; Reingold *et al*., 2008).

Sl No.	Greek Name	Sanskrit	Sanskit meaning	Gregorian Months
1	Aries	Meṣa	ram	Mid-April to Mid-May
2	Taurus	Vṛṣabha	bull	Mid-May to Mid-June
3	Gemini	Mithuna	twins	Mid-June to Mid-July
4	Cancer	Karkaṭa	crab	Mid-July to Mid-August
5	Leo	Siṁha	lion	Mid-August to Mid-September
6	Virgo	Kanyā	girl	Mid-September to Mid-October
7	Libra	Tulā	scales	Mid-October to Mid-November
8	Scorpio	Vṛścika	scorpion	Mid-November to Mid-December
9	Sagittarius	Dhanus	archery bow	Mid-December to Mid-January
10	Capricorn	Makara	sea monster	Mid-January to Mid-February
11	Aquarius	Kumbha	water pot	Mid-February to Mid-March
12	Pisces	Mīna	fish	Mid-March to Mid-April

Agriculture and Festivals: The Significance of the Lunar Cycle in Time-Keeping in India and Greece

The lunar cycle has played a crucial role in timekeeping in various ancient civilizations, including India and Greece. In both cultures, the phases of the moon were closely observed and utilized for agricultural practices and the timing of festivals.

Indian farming practices have long been synchronized with lunar cycles, each lunar month is divided into two fortnights: Shukla Paksha (waxing phase) and Krishna Paksha (waning phase). Farmers use these bright and dark fortnights as a guide for various agricultural tasks. Shukla Paksha, with its increasing moonlight, is often associated with growth and prosperity, making it ideal for sowing and transplanting. Conversely, Krishna Paksha, with its diminishing light, is considered a time for activities like pest control and pruning, as the waning moon is thought to have a calming effect on nature. (Sivasankar and Thimmaiah 2021) . The full moon and new moon (Purnima and Amavasya) are seen as important markers for these activities allowing farmers to work in harmony with nature's rhythms, optimizing their yields. (Fuller, 2004)

Similarly, in ancient Greece, farmers also relied on the lunar cycle for planting and harvesting crops. The lunar calendar helped them determine the best times for sowing seeds and tending to their fields, ensuring a bountiful harvest. They believed the moon's gravitational pull had an effect on the Earth and the growth of crops. (Mayoral *et al*., 2020) During the new moon, it was common for farmers to rest and prepare for the next cycle of work. Root crops were often planted during this time, as the waning phase of the moon was believed to promote downward growth in the soil. The first quarter moon was associated with the planting of crops that grow above the ground, such as grains and vegetables, as the increasing moonlight was thought to promote upward growth. (Philips, 2012) The full moon was considered a time of abundance, ideal for harvesting, as it was believed to increase moisture content in plants Lastly, the waning moon was focused on land management activities like pruning and weeding. (Prentice, 2012)

In addition to agriculture, the lunar cycle also played a significant role in the timing of festivals in both India and Greece. Many religious and cultural festivals were by the phases of the moon. For example, in India, the festival of Diwali, also known as the Festival of Lights, is celebrated on the new moon day of the Hindu lunar month of Kartika (Singh, 2018; Sivananda and Sahajananda 1983). The festivals of Krishna Paksha like Amavasya, were associated with rest or preparatory activities, while Shukla Paksha festivals, such as Purnima, were favourable times for commencing new tasks. (Rinehart, 2004)

Many Greek festivals were originally timed to coincide with specific phases of the moon. For example, the Eleusinian Mysteries, one of the most important religious festivals in ancient Greece, was held during the full moon in the month of Boedromion (September/October). This timing was believed to enhance the spiritual significance of the rituals and ceremonies performed during the festival. (Parker, 2005) Furthermore, the full moon was often associated with fertility and abundance, while the new moon was seen as a time of renewal and purification. (Papadopoulos, 2017)

Southeast Asian Astronomy

The dissemination of Hindu and Buddhist beliefs throughout East and Southeast Asia served as a conduit for the introduction of Indian astronomical concepts. This cultural exchange had a profound impact on the development of astronomy in these regions. (Ôhashi, 2017) The subsequent sections will delve into the multifaceted aspects of this influence.

Zodiac: from Mesopotamia to Asia

Originating in Mesopotamia, the 12-sign zodiac spread throughout the Hellenistic world, eventually reaching India around the 3rd century CE. From India, it was further disseminated to East and Southeast Asia.

While some Southeast Asian regions adopted Arabic names for the zodiac signs due to Islamic influence, others retained Sanskrit names, reflecting the Indian transmission route.

Around the latter half of the 6th century CE, India fixed the zodiacal signs to their sidereal positions. This Indianized system influenced Southeast Asian calendars, such as the Thai "Songkran" festival, which celebrates the Sun's entry into Aries (vernal equinox). Due to precession, this event now falls on the 13th-15th of April, differing from the Western tropical vernal equinox.

The enduring legacy of the zodiac is evident in modern Thailand, where Sanskrit names for the signs are used to represent the 12 months of the Gregorian calendar. This cultural blend is further illustrated by the presence of zodiac signs on contemporary Burmese calendars (Fig. 1) and

Vietnamese postage stamps representing a 12-year animal cycle (Fig.12). (Ôhashi and Orchiston, 2021)

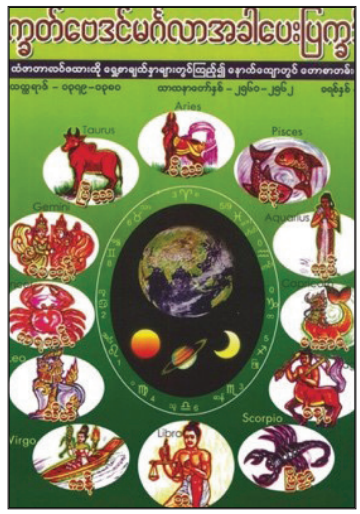

Fig. 1: Figures of Zodiac Signs from the Front Page of Modern Burmese Calendar.
Copyright @ 2021, Springer, Cham.

Fig. 2: Figures of the 12-year Animal Cycle used Modern Vietnamese Postage Stamps.
Copyright @ 2021, Springer, Cham.

The 7-Day Week: A Journey Across Cultures

The 7-day week, like the 12-sign zodiac, embarked on a journey from its origins in the Hellenistic world to India around the 3rd century CE and spread further eastward into Southeast and East Asia. The 7-day week's adoption into both the Islamic and Sanskrit traditions resulted in a fascinating linguistic blend across Asia. Some regions adopted Arabic names for the days of the week, while others retained names derived from Sanskrit.

In Thailand and Myanmar, the day of the week on which one is born carries significant weight. Thailand associates each day with a specific colour: Sunday (red), Monday (yellow), Tuesday (pink), Wednesday (green), Thursday (orange), Friday (blue), and Saturday (purple). (Saibejra, 2012; Segaller, 2005) Interestingly, Wednesday is divided into daytime and nighttime periods, with the latter associated with Rahu and sometimes represented by the colour black.

Myanmar connects each day with an animal symbol: Sunday, Monday (tiger), Tuesday (lion), Wednesday (forenoon - elephant with tusks, afternoon - elephant without tusks), Thursday (rat), Friday (guinea pig), and Saturday (dragon). These days also generally correspond to celestial bodies, with Wednesday afternoon linked to Rahu. The first letter of one's name is often associated with their birthday. (Shway, 1910)

Astronomical Practices of the Dayak People in Borneo

Hose and McDougall (1912) documented the astronomical knowledge of various Dayak groups in Borneo, including the Ibans, Kayans, Kenyahs, Klemantans, Maryts, and Punans. The Kenyahs, for instance, determined the appropriate season for agriculture by measuring the midday shadow cast by a vertical gnomon using a marked stick. Similarly, some Kayans observed the midday sun's position through a specially designed hole in their roofs.

The Klemantans employed a unique method of using a water-filled bamboo cylinder directed at a specific star to determine planting seasons. They also possessed a rich cosmology, viewing the Great Square of Pegasus as a storehouse, the Pleiades as a well, a constellation containing Aldebaran as a pig's jaw, and Orion as a human figure.

The Sea Dayaks relied on the Pleiades' position to guide their understanding of the seasons. Beyond the Dayak people, Ammarell and Tsin highlight the astronomical practices of people in South Kalimantan, who utilise the three stars of Orion's Belt to determine the direction of Qibla.

Vietnam's Champa Kingdom's Calendrical System

The Champa Kingdom (2nd century CE - 1832) in Vietnam utilised an Indianized calendar based on the Saka Era.

This legacy continues with the modern Cham people, who employ a unique dual calendar system: the 'Ahier' (a lunisolar calendar incorporating Indian and Chinese influences) and the 'Awal' (an Islamic lunar calendar). This blend of traditions exemplifies multiplex astronomy, highlighting the diverse cultural influences on astronomical practices. (Ôhashi and Orchiston 2021)

Indian Influence on Cambodian Calendars: A Historical Perspective

Historical records demonstrate a strong Indian influence on Cambodian timekeeping practices. Inscriptions using the Indian Saka Era, including one from 683 CE featuring an early use of the zero symbol, highlight this connection. Chinese accounts from the Angkor period further reveal the use of a Cambodian calendar with Sanskrit-derived terminology, indicating a blend of cultural influences. (Aczel, 2015; Cœdès, 1931) The Cambodian court even employed specialised astrologers for calendar creation and astrological predictions. (Porée and Maspero, 1938)

MIZO ASTRONOMY

While the Mizo people likely possessed knowledge of the stars as early as the late 1600s, the sole written record available is "Arsi Chanchin" by Rev. Liangkhaia, published in 1975. This discussion will focus on notable aspects of Mizo astronomy, drawing comparisons with Greek and Indian astronomical traditions.

Mizo Folklore and the Stars

Mizo astronomical folklore, much like that of the Greeks and Indians, is rich with stories woven around constellations. While numerous stars and constellations are recognised and named based on their position and movement in the sky, eight stand out with particularly popular narratives attached to them. These include Orion, Taurus, Pleiades, Castor and Pollux, Vega, Capella, Ursa Major, and a fascinating tale linked to the interaction of Venus, Jupiter, and Saturn.

For example, Canopus, known as "Sikawlhrut" in Mizo, literally translates to "the star that moves along the horizon," aptly describing its celestial path. The intriguing love story of "Hrangchhuana and Chawngmawii" is intricately connected to the movements of Venus, Jupiter, and Saturn, a tale so complex it warrants a dedicated study.

Let us delve into the captivating story of Ursa Major, known as "Zangkua" in Mizo tradition. The constellation is believed to be the transformed spirit of Kawlawia, a man from the present-day village of Sihphir. One day, Kawlawia was deeply troubled by a vivid dream, a premonition of his death. Seeking to avert this fate, he journeyed to his grandfather's village, Sairum, to request an animal sacrifice for protection.

The ritual completed, Kawlawia began his journey home, passing through "Berhvakawn," a crossroads known for its abundance of Tlaiberh birds. Tragically, he was ambushed and murdered by head-hunters from a neighbouring village.

Days turned into a worrisome period of absence. Then, a lone Tlaiberh bird arrived at Kawlawia's grandfather's house, perching on the porch and singing a haunting song: "Kawlawia has died at Berhvakawn." Initially dismissed as a strange melody, the bird's persistent return and sorrowful song convinced the family that something was amiss. Their worst fears were confirmed when they discovered Kawlawia's mutilated body at Berhvakawn. His head, arms, and one leg had been severed at the knee, the remaining limb already swarming with Khuaidang, a local wasp. As darkness enveloped the gruesome scene, a miraculous transformation occurred. Kawlawia's broken body vanished, ascending into the night sky to become the constellation Zangkua.

Unlike Greek and Indian mythology, where constellations are related to gods and heroes, Mizo star lore focuses on ordinary people's earthly lives and deaths. Upon death, village men, warriors, and animals are believed to ascend to the heavens and become stars, their chronicles inscribed in the sky as celestial objects.

Celestial Guides: Stars in Agriculture and Time

To the Mizo people the appearance of the Pleiades cluster, known locally as "Siruk" or "Six Stars" is deeply intertwined with the rhythms of daily life and the natural world. Most observers can only perceive six prominent stars within the cluster, hence the name. A poignant legend recounts the story of six individuals who met an untimely end while digging for clay. Their pit collapsed, burying them alive, but their spirits ascended to the heavens, transforming into the radiant stars of Siruk.

Siruk served as a celestial guide for the Mizo people, dictating their daily rhythms and agricultural practices. During winter months, when village elders gathered under the starlit sky, Siruk's position determined their schedule. Its zenith marked the time to seek the warmth of home, while its fading with the approaching dawn signalled the start of "Jhum cultivation." This traditional farming method,

timed for the end of February when the earth awakened from its winter sleep, involved burning vegetation to create fertile fields, the ashes serving as a natural fertiliser.

When May arrived, Siruk's setting at dusk heralded another crucial period: the time for sowing rice. This period often coincided with the arrival of powerful winds, sometimes even cyclones, which would temporarily obscure Siruk from view. These winds, known as "Siruk la" or "Siruk thief," were both feared and respected, a testament to the star cluster's perceived power over even the mightiest forces of nature.

Table 2: Summary of Names of Some Stars, Constellations, Planets and Zodiac Names in Greek/Common Name, Indian and Mizo.

Greek/Common Name	Indian	Mizo
Altair	Mesha	Sikawikap
Arcturus	Swati or Svati	Mazzaroth
Betelguese	Thiruvathirai	Sisakei
Canopus	Agastya	Sikawlhrut
Capella	Mithun	Dingdi puan tah
Cassiopeia	Sharmishtha	Darngawnraphak
Comet	dhumaketu	Simeikhu
Crux	Trishanku	Arsi Kraw
Mars	Mangala	Siaia/Sikeisen
Milky Way	Akasaganga	Thlasik kawng
Orion	Nataraja	Chhohhreivung
Pleiades	Kṛttikā	Siruk
Sun	Surya	Ni
Taurus	Vrsabha	Khiangte zawng zim
Ursa Major	Saptarshi	Zangkhua
Ursa Minor	Laghu Saptharishi	Zangkhawte
North Star(Kynosoura/Polaris)	Dhruv Tara	Hmar Arsi/Sisil
Solar Eclipse	Surya Grahan	Ni awk lem
Lunar Eclipse	Chandra Grahan	Thla awk lem

CONCLUSION

The ancient Greeks substantiated by the works of Homer's epics, initially perceived celestial phenomena through a mythical lens. Over time, this understanding matured into a more systematic approach, incorporating mathematical principles and evolving into the foundations of scientific astronomy.

Drawing from Vedic texts and precise architectural alignments, ancient Indian astronomy reflects a deep comprehension of the cosmos. This knowledge developed through a synthesis of influences, incorporating insights from Indian, Babylonian, Greek, and Persian traditions.

While Greek and Indian myths often revolve around deities and their actions, Mizo folklore connects the stars to the practical aspects of village life. Despite these differing perspectives, all three cultures—Greek, Indian, and Mizo—utilised celestial observations for essential timekeeping practices, including agricultural planning.

Astronomy in Southeast Asia predominantly developed under the influence of Hinduism and Buddhism. The observation of stars was crucial for establishing accurate calendar systems and astrology. For instance, the Malay people of Borneo relied on celestial navigation and used the stars to guide their agricultural practices.

REFERENCES

Blake, John F. "Astronomical Myths: Based on Flammarion's History of the Heavens." London Macmillan, 1877.

Cœdès, Georges. "À propos de l'origine des chiffres arabes." *Bulletin of the School of Oriental and African Studies* 6, no. 2 (1931): 323-328.

Fuller, Christopher John. *The camphor flame: Popular Hinduism and society in India*. Princeton University Press, 2004.

Gansten, Martin. "Astrology and astronomy (Jyotiṣa)." In *Brill's Encyclopedia of Hinduism*. Brill, 2010.

Goldstein, Bernard R. "Saving the phenomena: the background to Ptolemy's planetary theory." *Journal for the History of Astronomy* 28, no. 1 (1997): 1-12.

Harness, Dennis M. *Nakshastras: The Lunar Mansions of Vedic Astrology*. Motilal Banarsidass Publ., 2004.

Hose, Charles, and William McDougall. "The pagan tribes of Borneo." *London* 1 (1912): 912.

Joshi, Hargovind. *Mizoram: Past and Present*. Mittal Publications, 2005.

Kak, Subhash. "Time, space and structure in ancient India." arXiv preprint arXiv:0903.3252 (2009).

Vivekananda, K.R. "Ancient Indian Astronomy: Discoveries, Instruments, And Celestial Insights", Indian Streams Research Journal, Vol - I , ISSUE - X , November 2011

Lalthansanga, Chawngthu. "Mizo Values In Agricultural Sustenance: Lessons From Mizoram." In *2018 Annual Conference of Asian Association for Public Administration:" Reinventing Public Administration in a Globalized World: A Non-Western Perspective"(AAPA 2018)*, pp. 188-196. Atlantis Press, 2018.

Mak, Bill M. "The" Oldest Indo-Greek Text in Sanskrit" Revisited: Additional Readings from the Newly Discovered Manuscript of the Yavanajataka." Journal of Indian and Buddhist Studies (Indogaku Bukkyogaku kenkyu) 62, no. 3 (2014): 1101-1105.

Mayoral, Olga, Jordi Solbes, José Cantó, and Tatiana Pina. "What has been thought and taught on the lunar influence on plants in agriculture? Perspective from physics and biology." Agronomy 10, no. 7 (2020): 955.

Mohan, Chander. "Astronomy In India." 2015

Most, Glenn W., ed. Hesiod: Theogony, Works and Days, Testimonia. Vol. 1. Harvard University Press, 2006.

Reingold, Edward M., Nachum Dershowitz. (2008). Calendrical Calculations. Cambridge University Press. pp. 123–133, 275–311. ISBN 978-0-521-88540-9.

Ôhashi, Y. "Indianized astronomy in Asia." 2017): 145-152.

Ôhashi, Yukio, and Orchiston, Wayne. "The evolution of local Southeast Asian astronomy and the influence of China, India, the Islamic world and the West." Exploring the History of Southeast Asian Astronomy: A Review of Current Projects and Future Prospects and Possibilities (2021): 673-767.

Orchiston, Wayne, and Mayank N. Vahia, eds. "Exploring the History of Southeast Asian Astronomy: A Review of Current Projects and Future Prospects and Possibilities." (2021).

Papadopoulos, K. (2017). Lunar Timekeeping in Ancient Greece. Journal of Hellenic Studies, 20(2), 112-125.

Parker, R. (2005). Polytheism and society at Athens. Oxford University Press.

Phillips, Stuart. An Encyclopaedia of Plants in Myth, Legend, Magic and Lore. Robert Hale, 2012.

Pingree, David. "Astronomy and astrology in India and Iran." Isis 54, no. 2 (1963): 229-246.

Prentice, Jessica. Full moon feast: Food and the hunger for connection. Chelsea Green Publishing, 2012.

Qi, Yanling, Hang Wang, and Bohui Zhang. "Long live Hermes! Mercury retrograde and equity prices." In Long Live Hermes! Mercury Retrograde and Equity Prices: Qi, Yanling| uWang, Hang| uZhang, Bohui. [Sl]: SSRN, 2022.

Rao, S. (2017). "Cross-Cultural Influences in Ancient Indian Astronomy." Journal of South Asian Studies.

Rudra, P. "A Short History of Hindu Astronomy & Ephemeris." *arXiv preprint arXiv:0903.1778* (2009)

Rudra, A. (2009). Astronomy in Mughal India. Cambridge: Cambridge University Press.

Ruggles, Clive LN. Ancient astronomy: An encyclopedia of cosmologies and myth. Bloomsbury Publishing USA, 2005.

Saibejra, N., Mahatsacan manut kap duang-dāw (Amazing Story of Men and Stars). Bangkok, Chulalongkorn University Press (in Thai). (2012).

Rinehart, Robin (2004-07-21). Contemporary Hinduism: Ritual, Culture, and Practice. Bloomsbury Publishing USA. p. 125. ISBN 978-1-57607-906-5.

Schwab, Gustav. Gods and heroes of ancient Greece. Pantheon, 2011.

Segaller, Denis. *Thai ways*. Silkworm Books, 2005.

Shway, Yoe. *Burman: His Life and Notions*. Forgotten Books., 1901.

Singh, A. (2018). The Importance of the Lunar Cycle in Indian Agriculture. Journal of Agricultural Science, 12(3), 45-58.

Singhania, Kanta. "Abul Fazl's Vision of Astronomy in Historical Perspective." Annals of the Bhandarkar Oriental Research Institute 90 (2009): 81-97.

Sivasankar, J., and Thimmaiah, A. "Lunar rhythms in agriculture-review on scientific perspectives." *Int. J. Complement. Altern. Med* 14 (2021): 81-85

Sivananda, Swami, and Sahajananda ,Swami. Hindu fasts and festivals. Vol. 5. Divine Life Society, 1983.

Srinivas, Mandyam D. "The untapped wealth of manuscripts on Indian astronomy and mathematics." *Indian Journal of History of Science* 54, no. 3 (2019): 243-268.

Subrahmanya, B. (2020). "The Greek-Indian Astronomical Connection." Indian Journal of Science.

Thompson, Richard. "Planetary Diameters in the Surya-siddhanta." Journal of Scientific Exploration 11, no. 2 (1997): 193-200.

Thompson Richard L. (2007). The Cosmology of the Bhagavata Purana. Motilal Banarsidass.

Toomer, Gerald J. (1996). "Ptolemy and his Greek Predecessors". In Walker, Christopher B. F. (ed.). Astronomy before the Telescope. London: The British Museum Press.

Science and Technology Journal Vol. 12 Issue: 2 June 2024 ISSN: 2321-3388

Patient Satisfaction with Nursing Care: A Comparative Study on Communication and Psychological Support given by the Nurse in Medical and Orthopedic Ward

M. Lalhlimpuii[1*], A.K. Trivedi[2], and G. Konwar[3]
[1,2]Department of Zoology, Mizoram University, Aizawl-796001, Mizoram, India
[3]The Assam Royal Global University, Royal School of Nursing, Guwahati, Assam, India
*E-Mail: marytatea@gmail.com
*Corresponding Author

Abstract—The present study aimed to compare patient satisfaction with nursing care in the areas of communication and psychological support given by the nurse during the patient admitted in the medical ward and Orthopedic ward. The study was conducted at a civil hospital in Aizawl, Mizoram, India, from August 2023 to September 2023. A questionnaire regarding patient satisfaction in line with nursing theory by Virginia Henderson's basic nursing care model was administered. Out of 17 areas of nursing care, communication and psychological support given by the nurse on patient satisfaction were compared in the Medicine and Orthopedic wards. A total of 66 patients admitted to the medical and orthopedic ward were interviewed. Out of these, 40 (60.6%) participants were from the medicine ward, and 26 (39.3%) participants were from the orthopedic ward. The comparison of the mean scores of the two groups indicates that patients admitted to the Orthopedic ward are more satisfied than patients admitted to the Medical ward.

Keywords: Nurse, Patient, Satisfaction, Communication, Psychological support

INTRODUCTION

The practice and system of medicine has evolved over centuries. In order to fulfill patient demand, the healthcare delivery system has undergone a significant transformation thanks to new infrastructure, cutting-edge technology, creative tactics, and competition. As a result, the quality of healthcare becomes a promised goal of any healthcare organization (Xesfingi and Vozikis 2016). The positive advantage of competition among health service providers is to provide quality health services (Alsaqri 2016; Reck 2013). The need for increased quality of healthcare services has been identified via health-related information and advances in technology, changes in expectations and opinions about healthcare, an increase in individual involvement in their healthcare, and increased cost and competitiveness in the health sector (Freitas *et al.* 2014). Healthcare is changing rapidly, and the need to improve quality in its delivery is increasing. Patient satisfaction is a central indicator of health care quality and reflects the ability of the provider to meet the patient's needs (Morris 2013). Health care is considered to be a competitive market in which the patient is a customer and consumer. Although numerous indicators are used in the evaluation of quality health care, patient satisfaction remains a significant indicator (Johansson *et al*. 2002). Research on the quality of nursing care is becoming more and more important in the field of health care. The consumer's appraisal of services is being considered in assessments of quality. Thus, evaluating the quality of nursing care involves the measurement of its benefits to patients

 https://doi.org/10.22232/stj.2024.12.02.15

and society at large (Delbanco 2006). Patient satisfaction is defined as the extent of the resemblance between the expected quality of care and the actual received care. Patient satisfaction with nursing care is of great importance to any healthcare agency because nurses comprise most healthcare providers, and they provide care for patients 24 hours a day (Aiken *et al*., 2013). Patient satisfaction with nursing care is considered to be an important factor or predictor of the quality of the care patients receive (Jackson *et al*. 2001). As an example, good nursing care encompasses the following: adequate skills, correct staff members, appropriate nursing attitudes, effective communication, efficient administration systems, and good community participation (Loan *et al*. 2003). Positive health outcomes have been associated with effective communication as it has been connected to increased patient satisfaction, care compliance, and quality of care. It was determined that effective communication is a multifaceted notion that is defined as a mutual understanding between nurses and patients. This influenced the nursing process, clinical reasoning, and decision-making. Consequently, it promotes high-quality nursing care, positive patient outcomes, and patients' and nurses' satisfaction with care (Kelton and Davis, 2013). For safe, high-quality, patient-centered care to be delivered, strong communication is necessary. Every day, nurses establish therapeutic relationships with patients and their families in order to meet their needs and resolve any concerns about health care. Nurses optimize communication channels with patients and families by establishing trust and active listening to health care concerns. The quality of communication between nurse and patient is recognized as an influential factor in improving patient care (Fakhr-Movahedi *et al*. 2011). Effective patient care is achieved through effective communication. Also, effective communication can improve patients' independence and satisfaction and protect them from adverse health consequences caused by ineffective communication (Luker *et al*., 2000).

How patient satisfaction with nursing care is largely unknown for patients admitted to the hospitals of Mizoram, India. Therefore, the present study was conducted in a government hospital in Aizawl, Mizoram, India. The Civil Hospital is the first hospital established in Aizawl, Mizoram, and the biggest in bed strength, with a significant number of nurses and physicians. Among the different departments, the Department of Medicine and Orthopedics is known to have the highest percentage of bed occupancy. The study aimed to understand gender-based patient satisfaction with nursing care in the areas of communication and psychological support.

MATERIALS AND METHODS

A descriptive cross-sectional survey approach was adopted for the study. The study was conducted in a Civil Hospital Aizawl, Mizoram, from August-September 2023. In the present study, patients admitted to the Medicine ward and Orthopedic ward were included. For participants who did not complete the survey, data is not included. Data from 66 patients (40 patients from the Medical ward and 26 patients from the Orthopedic ward) was included for analysis. Virginia Henderson's guiding principles—which aim to explain, describe, predict, or prescribe nursing care—were used as the conceptual foundation for a qualitative, exploratory, and descriptive social study (George 2000). Out of 17 areas of nursing care, the areas of communication and psychological support given by the nurse on patient satisfaction were used in order to compare patients admitted to Medicine and Orthopedic wards. A structured interview scheduled for collecting information on patient satisfaction with nursing care was divided into two sections; section one consisted of items related to the demographic data such as gender, age, frequency of hospital admission, and days of hospitalization, and section two consisted of two areas, i.e., communication and psychological support. The area of communication comprises seven items related to patient satisfaction, and the area of psychological support has six items related to patient satisfaction. The structured questionnaire was translated into the Mizo language before being sent to the patient.

RESULTS

Both in the medical (57.5%) and orthopedic wards, the majority of the patients were male, in the medicine ward and 65.3 % in the orthopedic ward. The majority of the patients in both medicine and orthopedic wards were in the age group of 41 years and above, 62.5% in medicine and 65.3% in orthopedic wards. In the medicine ward, 70% were repeated admission, whereas 57.6% were admitted for the first time. In the medicine ward, 50% were hospitalized for more than 15 days, whereas in the orthopedic, 27.5% were hospitalized within 5 – 9 days.

Table 1: Frequency and Percentage of Medical and Orthopedic Wards According to Demographic Characteristics.

	Sample Characteristics	Medicine Ward		Orthopedic Ward	
		Frequency	%	Frequency	%
1	**Gender**				
	Male	23	57.5	17	65.3
	Female	17	42.5	9	22.5
2	**Age in years**				
	Below 20	1	2.5		
	21 – 30	6	16	7	26.9
	31-40	8	20	2	7.6
	41 and above	25	62.5	17	65.3
3	**Frequency of hospital admission**				
	New admission	12	30	15	57.6
	Repeated admission	28	70	11	27.5
4	**Days of hospitalize**				
	5-9	13	32.5	11	27.5
	10 -15	7	17.5	9	22.5
	More than 15 days	20	50	6	23

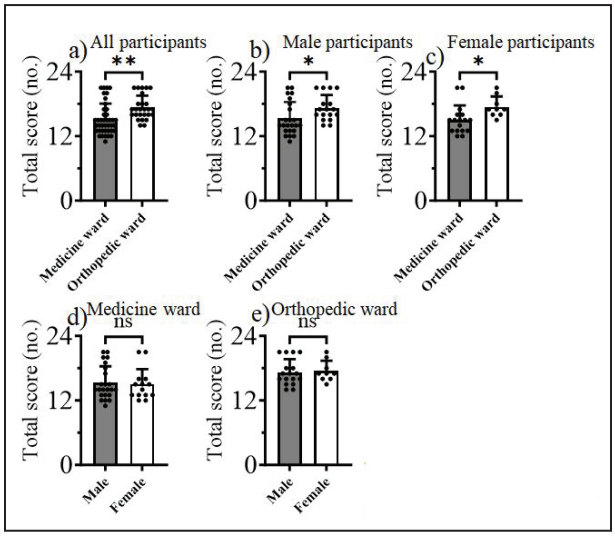

Fig. 1: Figure 1 Represents Communication Score among the Patients. A Significant difference was Observed in Communication Score between Medicine Ward and Orthopedic Ward Patients (a), Male Participants of Medicine Ward and Orthopedic Ward Patients (b), Female Participants of Medicine Ward and Orthopedic Ward (c). However, No Significant Difference was Observed in Communication Score between Male and Female of Medicine Ward (d) and Orthopedic Ward (e). * Signifies Significant Difference (P<0.05) between Two Groups.

There was a significant difference (P< 0.0005: Student t-test; Fig. 1) in the communication score of all participants between the medicine ward and orthopedic ward (Fig. 1a). Communication score was significantly higher in patients admitted to orthopedic ward than medicine ward (Fig. 1a). Gender wise differences were also observed in communication score of medicine and orthopedic ward patients (Fig. 1b,c). Among male participants, the communication score was higher in patients in the orthopedic ward (P< 0.0005: Student t-test; Fig. 1b). Female participants of the orthopedic ward reported similar responses and communication score was higher in patients of the orthopedic ward than in medicine ward patients (P< 0.0005: Student t-test; Fig. 1c). However, no difference in communication score between male and female participants was observed within medicine ward (Among male participants, communication score was higher in patients of orthopedic ward (P> 0.0005: Student t-test; Fig. 1d) or orthopedic ward (P > 0.0005: Student t-test; Fig. 1e).

There was no difference in the psychological score of patients between the medicine ward and orthopedic ward patients (P > 0.0005: Student t-test; Fig. 2). Further, we do not see gender-based differences in psychological scores between the wards (P > 0.0005: Student t-test; Fig. 2a,b) or within the wards (P > 0.0005: Student t-test; Fig. 2d,e).

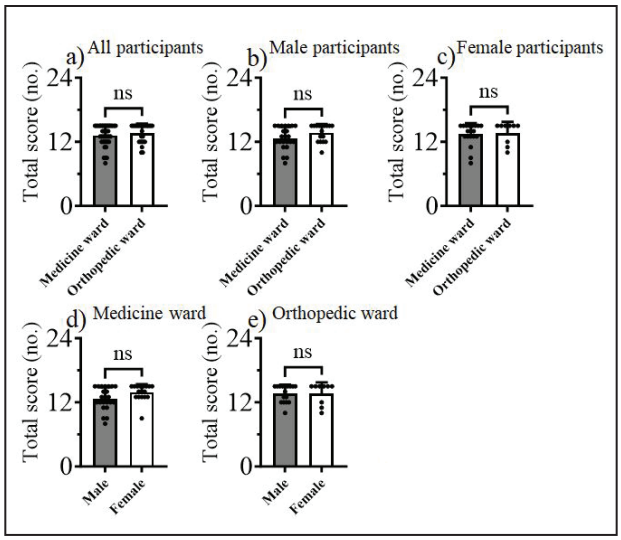

Fig. 2: Figure 2 Represents Psychological Support Score among the Patients. No Significant Difference was Observed in Psychological Support Score between Medicine Ward and Orthopedic Ward Patients (a), Male Participants of Medicine Ward and Orthopedic Ward Patients (b), Female Participants of Medicine Ward and Orthopedic Ward (c). However, No Significant Difference was Observed in Psychological Support Score between Male and Female of Medicine Ward (d) and Orthopedic Ward (e).

DISCUSSION

Although there has been a lot of improvement and development in Nursing education and Nursing administration, very little is known about the quality of nursing care and the level of patient satisfaction in the hospitals of Mizoram. This has been the first time that studies have been conducted on assessing patient satisfaction in nursing care. The study can be utilized by nursing administrators and staff nurses to recognize the strengths and weaknesses of nursing care quality and adopt necessary measures to enhance the quality of nursing care in order to increase patient satisfaction.

Our results show that there is a significant difference in the communication in nursing care between the medicine ward and the orthopedic ward. The finding on the comparison of the level of patient satisfaction on communication was that patients admitted to the Orthopedic ward were more satisfied than patients who were admitted to the Medicine ward. These differences can be due to the characteristics of providing care, the unit, patient, or family support. The cause of the differences and the contribution of each cause in the reduction of a patient's satisfaction should be considered in future studies. The higher satisfaction levels among the patients of the orthopedic ward were irrespective of gender (Fig. 1). However, we did not see the difference between male and female satisfaction levels within the ward.

Our pilot study suggests that there is no significant difference between patient from medical and orthopedic ward on the level of patient satisfaction on psychological support given by the nurse in either ward. Even though there is no difference on psychological support given by the nurse, it is important that nurses should continue and improve further in supporting the patient and their family during the hospitalization.

The study highlights the need for a study to assess the quality of nursing care and the level of satisfaction in more areas. Nurses are the frontline people that the patients most likely meet, spend time with, and rely upon for recovery during their hospitalization. Nursing care plays a crucial role in terms of the overall satisfaction of patients during the hospitalization experience. Insufficient communication results in patients feeling dissatisfied. Patients require nurses to accurately and understandably convey information to them about their health issues, illness state, course of treatment, prescription drugs, and pain management. The nurse-patient relationship has a significant influence on patient satisfaction and sets the tone for the treatment experience.

CONCLUSION

The result of this study showed that the nursing care provided between the two wards and communication care was higher in the orthopedic ward. However, no such differences were observed in psychological care. Although satisfaction with nursing care is a relatively desirable level, it is still far from complete satisfaction. Increasing the technical and professional capabilities of nurses promotes awareness in terms of nurse-patient communication and increases patients' trust in the medical staff, improving satisfaction with health care. Our study has limitations. Our pilot study included patients only from two wards, i.e., Medicine and Orthopedic wards. Future studies need to incorporate patients from all wards to understand the nursing care provided by the hospitals. Further, study timing and sample size should be increased to understand the long-term satisfaction levels. The scenario is similar in government and private hospitals and also needs to be addressed in future studies to improve health care for patients.

ACKNOWLEDGEMENTS

We sincerely thank our volunteers who took part in our study. We are also thankful to the hospital authorities to allow us to conduct this study in the Civil hospital, Aizawl.

REFERENCES

Aiken L, Clarke S, Sloane D (2013) Hospital nurse staffing and patient mortality, nurse burnout and job satisfaction. JAMA 288:1987-1993.

Alsaqri S (2016) Patient satisfaction with quality of nursing care at governmental hospitals, Ha'il City, Saudi Arabia. J Biol Agri and Healthcare 6(10): 128–142.

Ara BN, Somibala T, Urmila B (2015) Quality of Nursing Care rendered by Staff Nurse and Patients satisfaction: a comparative study. Int J Nurs educ 7(2):87-92.

Celik P, Mollaoglu (2016) Evaluation of emergency department nursing services and patient satisfaction of services. J Clin Nurs 25 (19-20): 2778-2785.

Delbanco T (2006) Quality of care through the patient's eyes satisfaction surveys are just the start of an emerging science. British Med J 313:832-833.

Fakhr-Movahedi A, Salsali M, Negharandeh R, Rahnavard Z (2011) Exploring contextual factors of the nurse-patient relationship: a qualitative study. Koomesh 13 (13): 23-34.

Freitas JS, Silva AEBC, Minamisava R, Bezerra ALQ, Sousa MRG (2014) Quality of nursing care and satisfaction of patients attended at a teaching hospital. Rev Lat-Am De Enferm 22(3):454-460.

Hartley S, Raphael J, Lovell K, Berry K (2020) Effective nurse patient relationship in mental health care : A systematic review of intervention to improve the therapeutic alliance. Int Nurs J Stud 102: 103490.

Jackson JL, Chamberlin J, Kronke K (2001) Predictors of patient satisfaction. Soc Sci Med 52(4),609-620.

Johansson P, Oleni M, Fridlund B (2002) Patient satisfaction with nursing care in the context of health care: A literature study. Scand J caring Sci 16 (4): 337-344.

Karaca A, Durna Z (2019) Patient satisfaction with the quality of Nursing care. Nurs Open 00:1-11.

Kelton D, Dacis C (2013) The art of effective communication. Nurs Made Incred Easy 11(1):55-56.

Loan LA, Jennings BM, Brosch LR, Depaul D, Hildreth P (2003) Indicators of nursing care quality. Findings from a pilot study. Outcomes Manag 7(2)51-58.

Lofti M, Zamanzadeh V, Valizadeh L, Mohammad K (2019) Assessment of nurse-patient communication and patient satisfaction from nursing care. Nurs Open 6:1189-1196.

Luker KA, Austin L, Caress A, Hallett CE (2000) The importance of 'knowing the patient: community nurses'constructions of quality in providing palliative care. J Adv Nurs 31(4): 775-82.

Morris J, Jahangir A, Sethi K (2013) Patient satisfaction: an emerging health policy issue. Am Acad Ortho Surg Now 7(6).

Motaghed Z, Mahboobi P, Mohammad M (2016) Comparative study of patients satisfaction with nursing services in Major Units of selected training hospitals in Tehran. Hosp Pract Res 1(1):33-36.

Noor S, Muhammad H, Muhammad A, Amir S (2019) Quality of Nurse patient therapeutic communication and Overall Patient Satisfaction during their hospitalization stay. Euro Acad Res 7 (3):1970 – 2011.

Reck DL (2013) Can and should nurses be aware of patients' expectations for their nursing care? Nurs Admin Quarterly 37(2): 109–115.

Shanmugapriya K, Seethalakshmi A, Manjula A (2020) Patients satisfaction with nursing care quality in Medical wards at selected Hospital in Chennai, South India. Iran J Nurs Midwifery Res 25(6):471-475.

Xesfingi S, Vozikis A (2016) Patient satisfaction with the healthcare system: Assessing the impact of socio-economic and health care provision factors. BMC Health Serv Res 15:16;94.

Science and Technology Journal Vol. 12 Issue: 2 June 2024 ISSN: 2321-3388

Shadowed and Redundant Rules Removal in the Cloud Firewall Policy: A Modified Tree Rule Firewall Approach

Dhwani Hakani[1] and Palvinder Singh Mann[2]
[1]Research Scholar, Gujarat Technological University, Ahmedabad, Gujarat, India
[2]Professor, Department of Computer Science & IT, Central University of Jammu, J&K-181143
E-Mail: [1]Adf_dhwani@gtu.edu.in, [2]palvinder.csit@cujammu.ac.in

Abstract—Firewalls are essential for security and are used to secure the majority of private networks. A firewall's goal is to examine every incoming and outgoing data before granting permission. One common type of conventional firewall is the rule-based firewall. But when it pertains to task performance, traditional listed-rule firewalls are limited, and they don't operate well on some networks with extremely big firewall rule sets. This study proposes a model firewall architecture called "Tree-Rule Firewall," which has benefits and functions well on large-scale networks like "cloud." In order to improve cloud network security, this study suggests an improved tree firewall that eliminates shadowing and redundant rules. Initially, this effort creates a tree rule. The proposed revised tree rule firewall effectively locates the shadow rules while avoiding the creation of redundant rules. Next, a cloud-based test was conducted on an altered Tree-Rule firewall that controls firewall rules. It is demonstrated that increased network security and quicker processing are offered by the modified Tree-Rule firewall. Large networks, such as cloud networks, are easier to build using a modified Tree-Rule firewall since it effectively eliminates shadow and redundant rules.

Keywords: Security, Tree rules, Firewall, redundant, shadowed rule

INTRODUCTION

Firewalls are currently commonly used on the Internet to protect network devices from hostile or undesired traffic [1], which could jeopardize the services' security, integrity, and accessibility. Security policies are implemented by firewalls as a series of rules, each of which consists of an action plus a condition that are defined across a few network header fields. Firewalls use the first matched approach to compare incoming packets to rule conditions gradually until an appropriate rule is found [2]. At this juncture, the packet is either allowed or denied based on the proper action. Firewall rules are defined by network parameters, destination Internet Protocol (IP) addresses and corresponding port numbers [3]. A firewall serves as a barrier between a trusted internal network and untrusted external networks, like the internet. Its primary function is to monitor and control incoming and outgoing network traffic based on predetermined security rules. Firewalls can be hardware, software, or a combination of both.

Here's a breakdown of how firewalls work:

Packet Filtering: Firewalls inspect packets of data as they pass through. They compare information like source and destination addresses, ports, and packet types against a set of rules. If a packet matches a rule (such as being from a trusted IP address or using a permitted protocol), it's allowed through. Otherwise, it's blocked.

 https://doi.org/10.22232/stj.2024.12.02.16

Stateful Inspection: This type of firewall not only examines individual packets but also tracks the state of active connections. It makes decisions based on the context of the traffic, allowing it to better distinguish legitimate packets from potential threats.

Proxy Service: Some firewalls act as intermediaries between clients and servers. Instead of allowing direct connections, they intercept requests from clients and make the requests on their behalf. This adds an extra layer of security by hiding internal network details from external sources.

Application Layer Inspection: Also known as deep packet inspection, this technique involves analyzing the contents of packets at the application layer. Firewalls can identify and block specific application protocols or even specific content within packets, providing granular control over network traffic.

Virtual Private Network (VPN) Support: Firewalls often include VPN capabilities, allowing remote users to securely access the internal network over the internet. VPNs encrypt traffic between the user's device and the firewall, protecting it from eavesdropping and tampering.

Firewalls play a crucial role in network security by enforcing security policies, preventing unauthorized access, and minimizing the risk of cyber attacks. They're a fundamental component of any organization's cyber security infrastructure. If the traffic satisfies the requirements of the filtering rule, the rule takes effect; if not, the subsequent rule in the order sequence takes effect, and so on. The sample rules for firewalls are shown in Table 1.

Table 1: Firewall Rules Sample.

Rule Id	Protocol	SrcIP	SrcPort	Dest IP	Dest Port	Action
R0	TCP	172.168.1.2	Any	123.45.12.36	25	Allow
R1	TCP	10.15.3.42	Any	192.108.1.16	80	Allow
R2	UDP	9.4.5.62	Any	192.108.1.17	25	Deny
R3	TCP	10.15.3.41	Any	3.7.12.78	25	Allow
R4	TCP	178.16.45.12	Any	3.4.12.4	80	Deny
R5	TCP	3.5.12.48	Any	3.5.7.56	25	Allow

Cloud computing is one technology that is incredibly available, private, and versatile. It provides cutting-edge online information exchange services. Adopting cloud computing requires careful consideration of safety concerns [4]. In order to protect the data centre from various attacks, a cloud-based firewall is necessary. High security can be ensured by adhering to the pertinent policies that were developed by a qualified administrator. A cloud gate and a regular firewall are identical save for the fact that the latter is stored on a cloud platform. In essence, cloud-based firewalls are just regular firewalls with an online firewall installed to create a virtual barrier against undesirable network traffic.[5]When it comes to traffic filtering, a virtual router is an application that works similarly as a hardware firewall.In a cloud context, the firewall can be set up as a service or appliance. The cloud-based firewall approach is depicted in Figure 1.

Rule disagreements in the context of firewalls fall into two categories: those pertaining to security and speed. Firewall rule conflicts can occur when two or more rules contradict each other or when the order of rules leads to unintended consequences. Here are some common types of conflicts:

Rule Priority: Firewalls typically process rules in order, from top to bottom. If a packet matches multiple rules, the firewall applies the action of the first matching rule it encounters and ignores the rest. Therefore, the order of rules is crucial Conflicts arise when rules with broader criteria precede more specific rules, leading to unintended access or denial [6].

Allow vs. Deny: Conflicts can arise between rules that allow certain traffic and rules that deny similar traffic. For example, if there's a rule allowing traffic from a specific IP address range but another rule denying traffic from the same range, it creates ambiguity about whether the traffic should be permitted or blocked.

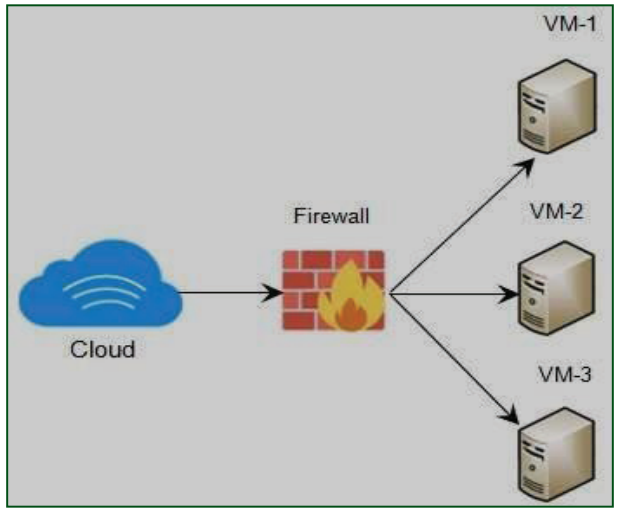

Fig. 1: Firewall Cloud Model.

Conflicting Port Rules: If there are conflicting rules regarding the same port or service, it can lead to confusion about whether the traffic should be allowed or blocked. For instance, one rule might permit traffic on a specific port while another rule denies traffic on the same port.

Inbound vs. Outbound Traffic: Firewalls often have separate rules for inbound and outbound traffic. Conflicts can arise when there are inconsistencies between inbound and outbound rules, leading to unexpected behavior.

Rule Overlaps: Sometimes, rules may overlap in their criteria, causing conflicts in how traffic is handled. For example, if there are two rules allowing traffic from overlapping IP address ranges, it's unclear which rule should take precedence.

To address firewall rule conflicts, it's essential to: Review and prioritize rules carefully to ensure they're logically ordered.

Regularly audit and update firewall rules to remove redundancies and conflicting rules.

Test firewall configurations thoroughly to identify and resolve conflicts before deploying them in production environments.

Document firewall rules and their intended purposes to provide clarity for administrators and troubleshooting purposes.

By proactively managing firewall rules and addressing conflicts, organizations can maintain effective network security and minimize the risk of misconfigurations leading to security breaches.

Moreover, having redundant rules slows down a firewall's processing speed. The reason for this is that they duplicate other rules and eat up processing time of the firewall. Shadowing and superfluous rules must therefore be eliminated from a rule list in order to speed up a firewall's performance.

The improved tree rule firewall suggested in this study would improve cloud network security by getting rid of unnecessary and shadowing rules. The relevant firewall policy's tree rule firewall is initially created by this effort. Next, the suggested improved tree rule firewall effectively locates the shadow rules without generating redundant rules. The main aim of this study's paper is:

- Tree rules firewall is initially built in this work. The initial firewall policy has been correspondingly simplified.
- A sizable number of firewall rules to identify and eliminate the shadowing and repetitive rules. Cloudsim is used to implement and assess the tree rule firewall.

Firewall Tree Rule

[7] He *et al.*'s A firewall tree rule, also known as a hierarchical rule or rule tree, is a concept used in firewall management to organize and structure firewall rules in a hierarchical manner. Instead of having a flat list of rules, where each rule is evaluated independently,[8,9] a firewall tree rule organizes rules into a tree-like structure, allowing for more granular control and efficient management of network traffic.

In a firewall tree rule setup, rules are grouped into categories or nodes, with each node representing a specific level of the hierarchy. Each node can contain sub-nodes or individual rules, further refining the criteria.[10]

For example, consider a firewall tree rule for controlling access to a web server:

At the root level, there might be a node for "Incoming Traffic."

Under "Incoming Traffic," there could be nodes for "HTTP Traffic" and "HTTPS Traffic."

Under "HTTP Traffic," there might be nodes for "Allowed IPs" and "Blocked IPs."

Under "Allowed IPs," there could be specific IP addresses or ranges allowed to access the web server.

By organizing firewall rules in this hierarchical manner, administrators can easily visualize and manage complex rule sets. It also allows for more efficient rule evaluation, as the firewall can quickly navigate the tree structure to determine the appropriate action for incoming or outgoing traffic.[11]

Firewall tree rules are particularly beneficial in large and complex network environments where there are numerous rules governing different aspects of network traffic.[12] They help streamline rule management, improve security posture, and facilitate troubleshooting and auditing processes.

Cloud Firewall

A virtual firewall, as proposed by Jekese *et al*. [13], allows for per-virtual machine network security maintenance, network traffic rule setting, and enhanced virtual environment safety. A private cloud is built using open-source software, and firewall rules are managed using the Tree-Rule approach. With this method, packets are tree-like filtered based on attributes such protocols and IP addresses. Furthermore, the rate that packets are screened and processed has significantly increased in order to keep the virtual firewalls from overloading in this specific scenario.

According to Dezhabad *et al*. [14], the firewall in the cloud should have adaptive auto-scalability. With software installed, this method divides incoming traffic among multiple virtualized firewalls located in a single pool. The goal is to determine, in many time steps, the total number of virtualized firewalls needed, taking into account the volume of traffic and the percentage of requests that reach each firewall.

Bagheri *et al*. [15] describe a method for moving rules from a central barrier to decentralized micro firewalls in a cloud/cloudlets architecture. Rearranging traffic channels during rule migration is required by the solution in order to preserve the network's overall defense policy.

An inspection-based method was developed by Praise *et al*. [16] to thwart malicious behavior by confirming the message signature for incoming communication. It combines the capabilities of reinforcement learning with rapid pattern recognition in parallel to arrive at the best answer as quickly as feasible. The message signature is processed concurrently by the RL approach while learning its environment.

DEFINITIONS

Examples are provided in this section to clarify the meanings of duplicate and shadowing firewall rules.

Redundant Rule

A redundant firewall rule is a rule within a firewall's configuration that duplicates the functionality of another rule or is rendered unnecessary due to the presence of other rules. Redundant rules can arise due to various reasons, such as oversight during rule creation, changes in network topology or policies, or the accumulation of rules over time without proper management.

Having redundant rules in a firewall configuration can lead to several issues:

Reduced Performance: Redundant rules increase the processing overhead on the firewall, as it needs to evaluate each packet against multiple rules unnecessarily. This can degradefirewallperformanceandpotentiallyimpact network throughput. Complexity: Redundant rules contribute to the complexity of the firewall configuration, making it more challenging to understand and manage. This complexity can increase the likelihood of misconfigurations or errors, which could compromise security.

Ambiguity: Redundant rules can introduce ambiguity into the firewall's behavior, leading to unexpected outcomes or conflicts between rules. This ambiguity makes it difficult to predict how the firewall will handle specific types of traffic.

Security Risks: Redundant rules may inadvertently create loopholes or bypasses in the firewall's security policies, leaving the network vulnerable to attacks or unauthorized access. To address redundant firewall rules, network administrators should regularly review and audit the firewall configuration to identify and remove any unnecessary or overlapping rules. This process involves analyzing the rule set, consolidating duplicate rules, and ensuring that each rule serves a specific purpose aligned with the organization's security requirements. Additionally, implementing proper change management processes can help prevent the proliferation of redundant rules in the future.

Shadowing Rule

The rules Ra and Rb only partially match if at least a single value in Ra is not comparable to the corresponding field in Rb.

$$\forall x: \quad R_a(x) \cap R_b(x) \neq \emptyset \; and \; R_a(action) \cap R_b(action) = \emptyset$$

$$Where\ x \in \{protocol, SrcIP, DestIP, SrcPort, DestIP\}$$

$$If\ R_a(proto) \cap R_b(proto) \neq \emptyset\ and\ R_a(IPaddr) \cap R_b(IPaddr) \neq \emptyset\ _a(port) \cap R_b(port) \neq \emptyset\ and\ R_a(action) \cap R_b(action) = \emptyset\ then\ R_a\ is\ shadowed\ by\ R_b$$

When the identical component of rules Ra is a part of rule Rb but their behaviors are different, this is known as shadowing. Since the rule forbids a shadow rule for always having repercussions, shadowing is a serious problem. Consequently, authorized traffic might be forbidden, and vice versa. Consequently, shadowv rules must be located in order for the administrator to move or remove the shadowing rule and fix the problem.

Modified Tree Rule Firewall

This section describes the suggested modified tree trule firewall. The MTRFcloud workflow is depicted in Figure 2.

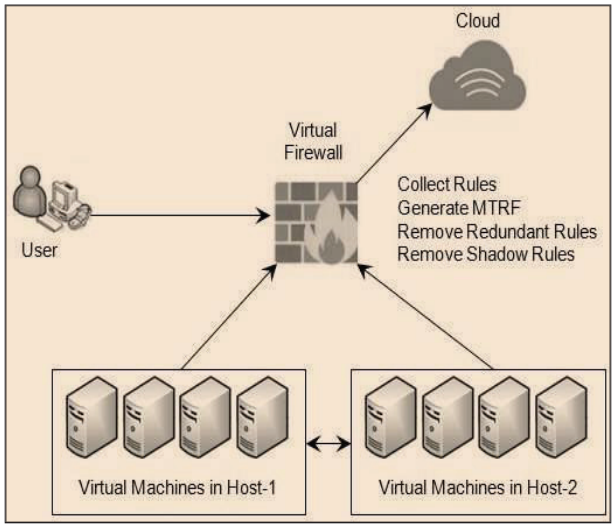

Fig. 2: Modified Tree Firewall Cloud Workflow.

Instead of presenting the rules statically or manually, a new virtualized firewall does it dynamically. The firewall is called a firewall with stateful inspection because it can monitor a flow's connection status in addition to filtering internet traffic utilizing IP addresses, communication protocols, and ports. This firewall will first read the attribute data from the packet then contrast it to the data stored in its root nodes. After then, the firewall will look at the packet's other attributes one after the other, narrowing its search to relevant nodes at the right levels. As a result, a specific action will be taken to quickly determine the traffic. The updated tree rule firewall is produced by means of algorithm-1. The algorithm creates tree rules based on a list of firewalls as input. The firewall branch rule initially has the first rule added to it. Based on the node's index, the remaining criteria are then inserted. The node in this instance indicates the fields (procedure type, destination and source IP, and port) in firewall rules.

Working example for tree rule generation

Consider the list of firewall rules

TCP	123.12.4.2 22	123.12.4.3 143	Allow
TCP	123.12.4.3 43	123.12.4.4 443	Allow
TCP	123.12.4.3 43	123.12.4.4 443	Deny
TCP	123.12.4.2 8443	123.12.4.3 8080	Allow
TCP	123.12.4.2 45	123.12.4.4 161	Allow
TCP	123.12.4.2 45	123.12.4.4 161	Allow
TCP	123.12.4.2 8443	123.12.4.3 143	Allow
TCP	123.12.4.2 8443	123.12.4.3 143	Allow

The first rule {TCP 123.12.4.222 123.12.4.3 143 Allow} is inserted into TR. Then, the for-loop is started for adding the remaining rule

Algorithm-1: Firewall Rule Tree Generation

```
currentNode = root
    for criterion in rule.criteria:
        if currentNode has child node matching criterion:
            currentNode = child node matching criterion
        else:
            newNode = create new node with criterion
            currentNode.add(newNode)
            currentNode = newNode
    currentNode.addRule(rule)
    optimizeTree(root)
return root
```

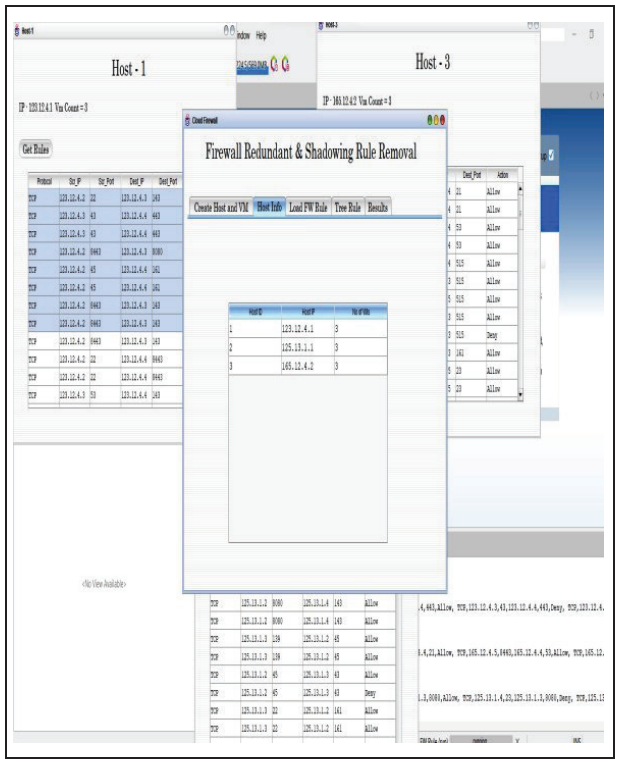

Fig. 3: Host Rule Information.

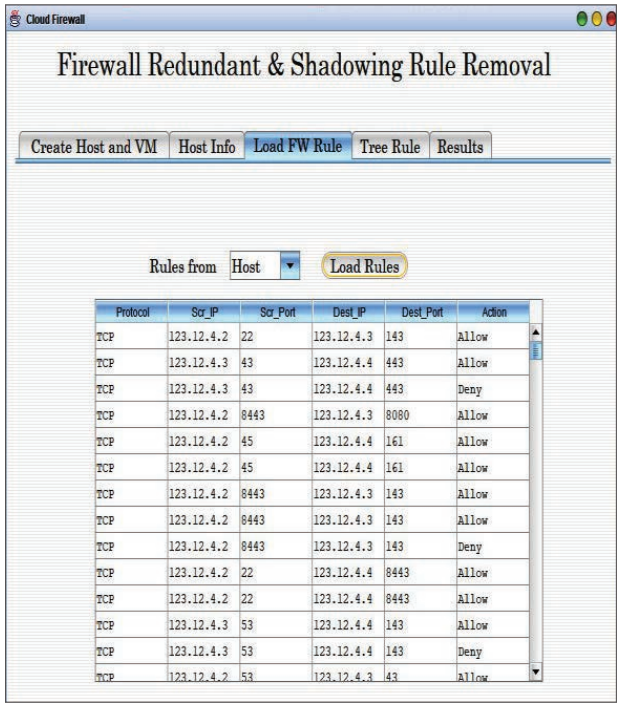

Fig. 4: Firewall Rules Loaded.

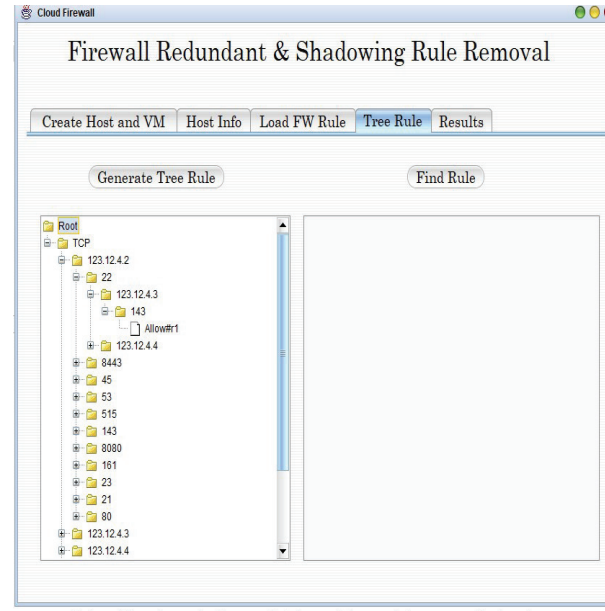

Fig. 5: Modified Tree Generation.

A firewall rule shouldn't change when a redundant rule is removed. Implementation and Results

Redundant Rules are removed

TCP,123.12.4.2,45,123.12.4.4,161,Allow

TCP,123.12.4.2,8443,123.12.4.3,143,Allow

TCP,123.12.4.2,22,123.12.4.4,8443,Allow

TCP,123.12.4.2,53,123.12.4.3,43,Allow

TCP,123.12.4.2,53,123.12.4.3,22,Allow

TCP,123.12.4.2,53,123.12.4.3,45,Allow

TCP,123.12.4.3,21,123.12.4.2,22,Allow

TCP,123.12.4.2,45,123.12.4.4,443,Allow

TCP,123.12.4.3,143,123.12.4.2,161,Allow

TCP,123.12.4.4,8080,123.12.4.2,43,Allow

Shadowed Rules

TCP,123.12.4.2,8443,123.12.4.3,143,Allow

TCP,123.12.4.2,8443,123.12.4.3,143,Deny

TCP,123.12.4.2,53,123.12.4.3,43,Allow

TCP,123.12.4.2,53,123.12.4.3,43,Deny

TCP,123.12.4.2,53,123.12.4.3,45,Allow

TCP,123.12.4.2,53,123.12.4.3,45,Deny

Table 2 shows the sample rules collected from VMs.

Table 2: Sample Rules From VMs.

Rule Id	Protocol	SrcIP	SrcPort	Dest IP	Dest Port	Action
R1	TCP	10.12.8.2	8080	10.12.8.1	43	Allow
R2	TCP	10.12.8.1	45	10.12.8.2	139	Allow
R3	TCP	10.12.8.2	43	10.12.8.1	45	Deny
R4	TCP	192.168.03	515	192.168.0.2	53	Deny
R5	TCP	192.168.0.4	45	192.168.0.5	8080	Allow
R6	TCP	192.168.0.4	45	192.168.0.5	8080	Allow
R7	TCP	105.34.89.3	8443	105.34.89.1	515	Allow
R8	TCP	105.34.89.2	8080	105.34.89.1	23	Allow
R9	TCP	105.34.89.1	143	105.34.89.2	21	Deny
R10	TCP	105.34.89.3	8443	105.34.89.1	515	Deny

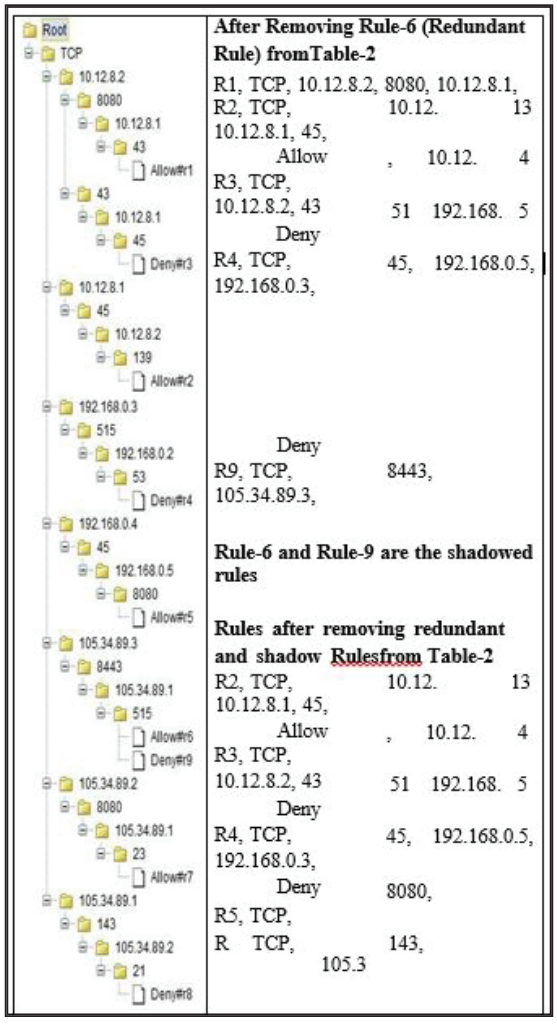

R6, TCP, 105.34.89.3, 8443, 105.34.89.1, 515, Allow
R7, TCP, 105.34.89.2, 8080, 105.34.89.1, 23, Allow
R8, TCP, 105.34.89.1, 143, 105.34.89.2, 21,

Fig. 6: Tree Rules and Results.

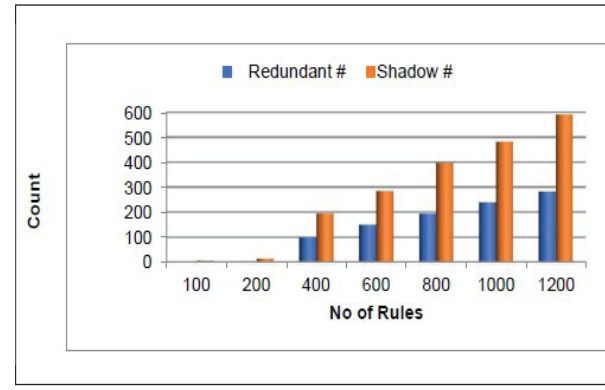

Fig. 7: No of Rules Vs Redundant and Shadow Rules.

Table 3: Number of Redundant and Shadow Rule.

Rules	Redundant	Shadowed
100	3	5
400	100	194
600	151	285
1000	241	485

Table 4 shows the time comparison for different numbers of rules.

Table 4: Time Comparison.

Rule	Tree time for Generation in ms	Processing in ms
100	113	181
400	404	550
600	616	751
1000	1258	3931

Figure 8 shows the execution time of tree generation and processing time.

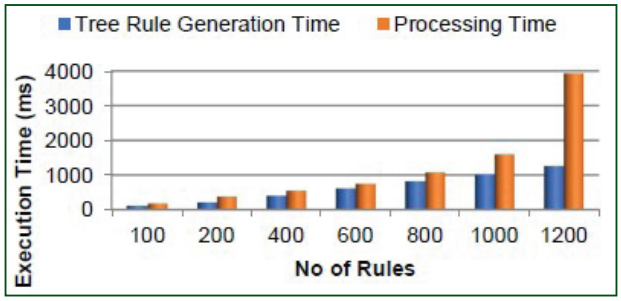

Fig. 8: Execution Time for Different Numbers of Rules.

The total processing time of MTRFcloud is compared with an adaptive cross-domain firewall (ACD) [17] and a double decision tree (DDT) [18]. Figure 9 shows the total processing time comparison of different rules. From that results, the time percentage between ACD and proposed is 32.78% and DDT and proposed is 14.75%.

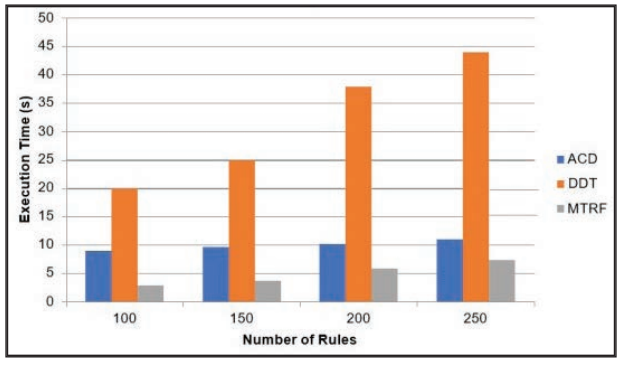

Fig. 9: Total Processing Time Comparison.

CONCLUSION AND FUTURE WORK

This study proposed a modified Tree-Rule firewall to remove shadow and unnecessary rules. The transmitting choice for incoming traffic based on tree policy will follow the tree formation before deciding on the traffic sooner in the MTRFcloud, which employs rules in a tree-based architecture. Since MTRFcloud was extensively tested in a cloud environment, it works best there. Additionally, it was seen to make decisions on packet forwarding quickly. However, the experiment results show that the processing times for generating tree rules and identifying shadowing and redundant rules in a firewall are reasonable in a real-world scenario. Based on those findings, the time percentage difference between the proposed and ACD is 32.78%, and the proposed and DDT is 14.75%.Future work describes removing intra and inter firewall anomalies

REFERENCES

Liu, A. X., Khakpour, A. R., Hulst, J. W., Ge, Z., Pei, D., & Wang, J. (2017). Firewall fingerprinting and denial of firewalling attacks. IEEE Transactions on information forensics and security, 12(7), 1699-1712.

Cheminod, M., Durante, L., Seno, L., & Valenzano, A. (2021). An Algorithm for Security Policy Migration in Multiple Firewall Networks. In ITASEC (pp. 344-359).

Jabal, A. A., Davari, M., Bertino, E., Makaya, C., Calo, S., Verma, D., *et al.* (2019). Methods and tools for policy analysis. ACM Computing Surveys (CSUR), 51(6), 1-35.

Ullrich, J., Cropper, J., Frühwirt, P., & Weippl, E. (2016). The role and security of firewalls in cyber-physical cloud computing. EURASIP Journal on Information Security, 2016(1), 1-20

Toumi, H., Fagroud, F. Z., Zakouni, A., & Talea, M. (2019). Implementing Hy-IDS, mobiles agents and virtual firewall to enhance the security in IaaS Cloud. Procedia Computer Science, 160, 819-824.

Voronkov, A., Iwaya, L. H., Martucci, L. A., & Lindskog, S. (2017). Systematic literature review on usability of firewall configuration. ACM Computing Surveys (CSUR), 50(6), 1-35.

He, X., Chomsiri, T., Nanda, P., & Tan, Z. (2014). Improving cloud network security using the Tree-Rule firewall. Future generation computer systems, 30, 116-126.

Chomsiri, T., He, X., Nanda, P., & Tan, Z.(2016). Hybrid tree-rule firewall for high speed data transmission. IEEE transactions on cloud computing, 8(4), 1237-1249.

Chomsiri, T., He, X., Nanda, P., & Tan, Z. (2014, September). A stateful mechanism for the tree-rule firewall. In 2014 IEEE 13th International Conference on Trust, Security and Privacy in Computing and Communications (pp. 122-129). IEEE.

Suresh, N., & Bai, B. M. (2016). Predictive Modelling of Tree Rule Firewall for the Efficient Packet Filtering. International Journal of Computer Science and Information Security, 14(10), 189.

Trabelsi, Z., Masud, M. M., & Ghoudi, K.(2015). Statistical dynamic splay tree filters towards multilevel firewall packet filtering enhancement. Computers & Security, 53, 109-131.

Trabelsi, Z., Zeidan, S., Shuaib, K., & Salah, K. (2018). Improved session table architecture for denial of stateful firewall attacks. IEEE Access, 6, 35528-35543.

Jekese, G., & Hwata, C., "Virtual Firewall Security on Virtual Machines in Cloud Environmen", International Journal of Scientific and Engineering Research, 6(2), 2015

Dezhabad, N., & Sharifian, S. (2018). Learning-based dynamic scalable load-balanced firewall as a service in network function-virtualized cloud computing environments. The Journal of Supercomputing, 74, 3329-3358.

Bagheri, S., & Shameli-Sendi, A. (2020). Dynamic firewall decomposition and composition in the cloud. IEEE Transactions on Information Forensics and Security, 15, 3526- 3539.

Praise, J. J., Raj, R. J. S., & Benifa, J. B. (2020). Development of Reinforcement Learning and Pattern Matching (RLPM) Based Firewall for Secured Cloud Infrastructure. Wireless Personal Communications, 115, 993-1018.

Kadam, P. R., & Bhusari, V. K. (2014) Redundancy removal of rules with reordering them to increase the firewall optimization. International Journal of Research in Engineering and Technology, 3(10), 317-321.

Lin, Z., & Yao, Z. (2022). Firewall Anomaly Detection Based on Double Decision Tree. Symmetry, 14(12), 2668.

Science and Technology Journal Vol. 12 Issue: 2 June 2024 ISSN: 2321-3388

Artificial Intelligence Techniques for Rainfall Prediction in Mizoram

Abul Kashim Md Fujail[1*] and Jarita Das[2]
[1]Department of Computer Science, MHCM Science College, Hailakandi, Assam, India
[2]Department of Statistics, MHCM Science College, Hailakandi, Assam, India
E-Mail: [1]abul_fujail@yahoo.com, [2]jaritadas@gmail.com
*Corresponding Author

Abstract—Rainfall prediction plays a vital role in managing hydrological events. An accurate predictive model can provide timely information to reduce the affects of extreme events such as, drought and flood. In Mizoram, agriculture is a key component of the economy. Accurate and early rainfall predictions are crucial to mitigate the adverse affects of prolonged dry periods or heavy rains on crop yield and the overall economy of the state. Artificial intelligence (AI) models can achieve precise rainfall predictions by uncovering concealed patterns within historical rainfall data. In the present study, AI models viz. extreme learning machine (ELM), artificial neural network (ANN) and support vector machine (SVM) have been used for predicting rainfall in Mizoram state of India. The meteorological data from 2002 to 2021 is used to train and test the predictive accuracies of the models. The study demonstrates reasonably accurate predictive capability of all the aforesaid AI models considered in the study. The performance of ELM was found superior, exhibiting smaller error and higher coefficient of determination than ANN and SVM.

Keywords: Artificial neural network, Extreme learning machine, Support vector machine, Rainfall prediction, Artificial intelligence

INTRODUCTION

Accurate rainfall prediction is crucial due to its significant impact on various activities including agriculture and transportation. In a state like Mizoram, India, where the economy relies heavily on agriculture and occurrences of landslides due to heavy rain is a common phenomenon that results in transportation difficulties and loss of lives and properties, the development of an accurate rainfall estimation model bears immense potential. Alterations in historical rainfall patterns lead to extreme weather events such as droughts and floods which causes change in cropping practices, and pose significant challenges for water resource management authorities. Rainfall prediction is an important research area given its significant impact on lives and property. Heavy rainfall affects various aspects of society and daily life, spanning from agriculture to disaster preparedness measures. Consequently, accurate rainfall estimation is essential for policymakers, water resource engineering, and farmers (Abebe & Endalie, 2023; Barman & Barman, 2021). The earlier studies on rainfall prediction in Mizoram has centered around traditional ecological knowledge such as, the behaviors of insects, birds, and mammals, as well as the traits of plants, cloud condition etc (Chinlampianga, 2011). There are limited number of statistical studies on rainfall forecasting in Mizoram (Saha *et al*., 2015; Saha *et al*., 2021).The existence of nonlinear and chaotic structures within historical rainfall data series disrupts the effectiveness of conventional statistical prediction models. The nonlinear patterns of rainfall makes it is crucial to develop data-driven models for enhancing the accuracy of rainfall prediction (Garai & Paul, 2024). Adopting an intelligent forecasting model would offer significant benefits in the field of water resources management.

 https://doi.org/10.22232/stj.2024.12.02.17

Machine learning models represent a recently developed approach to rainfall prediction that utilizes advanced algorithms and artificial intelligence techniques to analyze vast amounts of data and identify patterns and trends that can be used to predict rainfall patterns. Artificial intelligence (AI) methodologies excel in rainfall prediction because they have the capacity to discern intricate patterns, capture non-linear correlations (Waqas, *et al*., 2023). AI models shows capability in rainfall prediction with significant accuracy. In the last two decades, AI models have shown incredible accuracy in their performance in forecasting across various domains of science and engineering (Dash, *et al*., 2018a). By learning from existing historical data, AI models can make accurate and efficient rainfall prediction. Various AI models such as, artificial neural network (ANN), support vector machine (SVM), K-Nearest Neighbor (KNN), Echo State Networks, deep neural network and extreme learning machine (ELM) have been employed to predict rainfall with remarkable precision in different regions around the world (Barman & Barman, 2021; Waqas, *et al*., 2023; Weesakul, *et al*., 2018; Hussain & Zoremsanga, 2021; Lakshminarayana, *et al*., 2020). However, there is lack of studies using artificial intelligence methodologies for prediction of rainfall in Mizoram.

ANNs can identify and model functional relationships between data (Fujail & Das, 2023). It has been utilized for rainfall forecasting with satisfactory accuracy (Singh & Borah, 2013; Kala & Vaidyanathan, 2018; Dada, *et al*., 2021; Nandakumar, *et al*., 2021; Aïzansi, *et al*., 2024). ANN models and SVM have been employed for predicting rainfall in the Bolangir district, Odisha, India. SVM model has shown superior performance than ANN models in the field of rainfall forecasting (Samantaray, *et al*., 2019). Different studies have revealed efficiency of SVM in rainfall prediction (Dawoodi & Patil, 2021). SVM is also reported to predict more accurately than Random Forests (Dhamodaran, *et al*., 2020). Recently, ELM has been introduced in rainfall forecasting that provides reasonable accuracy, however multilayer perceptron (MLP) neural network outperformed ELM, and the researcher suggested for further investigation to improve the accuracy of ELM (Lazri, *et al*., 2022). The effectiveness of KNN, ANN and ELM in predicting rainfall was assessed in (Dash, *et al*., 2018a). Among these methods, the ELM model demonstrated superior accuracy compared to both KNN and ANN. This research seeks to evaluate the effectiveness of ANN, ELM and SVM models in predicting rainfall in Mizoram.

DEVELOPMENT OF RAINFALL PREDICTION MODEL

In this study, artificial neural network, extreme learning machine and support vector machine have been developed to predict rainfall in Mizoram. Brief descriptions about the models have been given in this section.

Artificial Neural Network

An artificial neural network (ANN) is a collection of interconnected neurons organized in layers, designed to map input patterns to corresponding output patterns. Neural networks achieve this by training neurons on specific patterns and then using this trained model to predict outputs for new inputs. The study utilized the backpropagation learning algorithm to train a feed-forward neural network comprising of an input layer, a hidden layer, and an output layer. The number of neurons in the input and output layers is determined by the number of input and output variables, respectively. However, figuring out the size of the hidden layer requires a trial-and-error approach. ANN is the most popular data-driven approach in hydrology. The backpropagation neural networks are commonly utilized in rainfall forecasting (Singh & Borah, 2013; Shukla, *et al*., 2011; Mislan, *et al*., 2015; Dash, *et al*., 2018b; Velasco, *et al*., 2019; Khan, *et al*., 2024). The ANN produces output (o) for each input pattern and adjusted weights to minimize the difference of network output from target (t) value. The error between target and predicted values is computed using Eq. (1).

$$Error = \frac{1}{n}\sum_{i=1}^{n}(t_i - o_i)^2 \quad (1)$$

In the present study, ANN with Levenberg-Marquardt algorithm using logistic sigmoid transfer function in the hidden layer and linear transfer function is employed for rainfall prediction.

EXTREME LEARNING MACHINE

An Extreme Learning Machine (ELM) is a type of single-hidden layer feedforward neural network. Unlike traditional neural networks, ELMs are characterized by their fast learning capabilities, primarily due to the random assignment of input weights and biases, which are not adjusted during the training process. Instead, only the weights connecting the hidden layer to the output layer are optimized. ELMs often exhibit good generalization performance, meaning they can effectively make predictions

on new, unseen data (Lazri, *et al*., 2022; Li, *et al*., 2019). This is partly due to their ability to capture complex patterns with fewer computational resources. ELM offers a fast and efficient alternative to traditional neural networks, with strong performance in many practical applications (Lazri, *et al*., 2022). Their unique training approach and ability to generalize well make them valuable tools in the sphere of machine learning. In this study, the ELM utilized radial basis activation function.

Support Vector Machine

Support Vector Machine (SVM) is a robust and adaptable supervised learning algorithm employed for both classification and regression tasks. Its primary objective is to identify the optimal hyperplane that separates data points into distinct classes while maximizing the margin, defined as the distance between the hyperplane and the closest data points from each class, known as support vectors. SVM excels at managing high-dimensional data and can find complex decision boundaries by employing kernel functions. These functions transform the input data into a higher-dimensional space, making the classes linearly separable (Yin, *et al*., 2022). This feature enables SVM to accurately identify complex patterns in the data and make accurate predictions even in cases of non-linear relationships. By leveraging its capability to find optimal decision boundaries, SVM can effectively classify different rainfall levels based on historical data (Mehr, *et al*., 2019). ANNs focus on minimizing training errors, while SVMs are designed to reduce generalization errors.

METHODOLOGY

The rainfall data for Mizoram is collected from Directorate of Economics & Statistics, Planning & Programme Implementation Department, Government of Mizoram (MDM, 2022), which compiled data from 45 rainfall collecting stations. The dataset comprises of monthly rainfall of the state for the period 2002 to 2021. Thus, the dataset contains 2 input parameters *viz*. month and year, and one output parameter i.e. rainfall in millimeter. For effective training of the machine learning models, the dataset is normalized using Eq. (2).

$$x_N = \frac{x - x_{min}}{x_{max} - x_{min}} \tag{2}$$

where, x represent the original value, and x_N denote the normalized value of x. The variables x_{max} and x_{min} denote the maximum and minimum actual values of each parameter. The formula normalizes data in the range 0 to 1.

The dataset was randomly divided into a training set, comprising 80% of the data, and a testing set with the remaining 20%. The training set is utilized for training the AI models, while the testing set is used to assess their performance.

The performance of the AI models is assessed based on root mean square error (RMSE), mean absolute error (MAE), and coefficient of determination (R^2).

$$RMSE = \sqrt{\frac{1}{n}\sum_{i=1}^{n}(t_i - o_i)^2} \tag{3}$$

$$MAE = \frac{1}{n}\sum_{i=1}^{n}|t_i - o_i| \tag{4}$$

$$R = \frac{\sum_{i=1}^{n}(t_i - \bar{t})(o_i - \overline{o})}{\sqrt{\sum_{i=1}^{n}(t_i - \bar{t})^2 \sum_{1}^{n}(o_i - \bar{o})^2}} \tag{5}$$

Here, o_i and t_i represent the predicted and measured outputs for the i^{th} input pattern, respectively. The symbols $\bar{o}$ and $\bar{t}$ denote the averages of the predicted and measured outputs, respectively, and n stands for the total number of patterns.

EXPERIMENTAL RESULTS

The ANN, ELM and SVM models are trained with the normalized rainfall data. The effetiveness of the AI models is assessed using statistical metrics, such as mean absolute error (MAE), root mean square error (RMSE) and coefficient of determination (R^2), comparing the AI models predicted values and target values. The best structures for all AI models were identified based on the lowest MAE and RMSE values, as well as the highest R^2 values observed during testing. A grid search strategy was employed to determine the optimal hyper-parameter values of the AI models. The ANN model provided better performance with 12 nodes in the hidden layer, whereas in the ELM model, optimal results are achieved with the hidden layer comprising of 25 nodes. In the present study, the SVM with radial basis kernel function provides superior accuracy compared to other kernel functions. The results obtained on testing dataset with ANN, ELM and SVM with optimal architecture is tabulated in Table 1.

Table 1: Performance Matrices of AI Models.

AI Model	MAE	RMSE	R^2
ANN	0.061092	0.087383	0.86479
ELM	**0.051456**	**0.068434**	**0.89202**
SVM	0.053572	0.068757	0.87476

Table 1 show that MAE for ANN, ELM and SVM are 0.061092, 0.051456 and 0.053572, respectively and the corresponding RMSE values are 0.087383, 0.068434 and 0.068757, respectively. Thus, ELM model gives lowest error between predicted and target values than the other models considered in the study. Moreover, ELM provided highest R^2 value i.e. 0.89202 compared to ANN and SVM with R^2 values 0.86479 and 0.87476, respectively. Figure 1 presents a comparison of the results from the AI models using the specified evaluation metrics. Thus, the study suggests that the ELM model outperforms the ANN as well as SVM models in predicting rainfall.

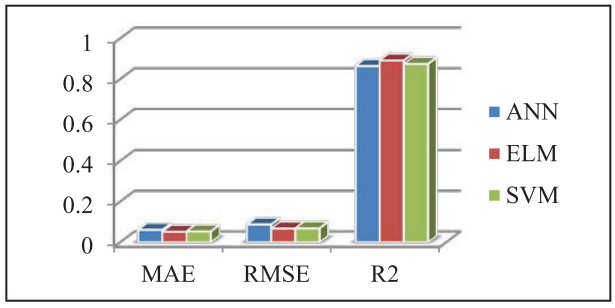

Fig. 1: AI Models with Different Performance Metrics.

Figures 2-4 visually depict the performance of the different models under consideration, highlighting the errors between the estimated and target values with testing dataset.

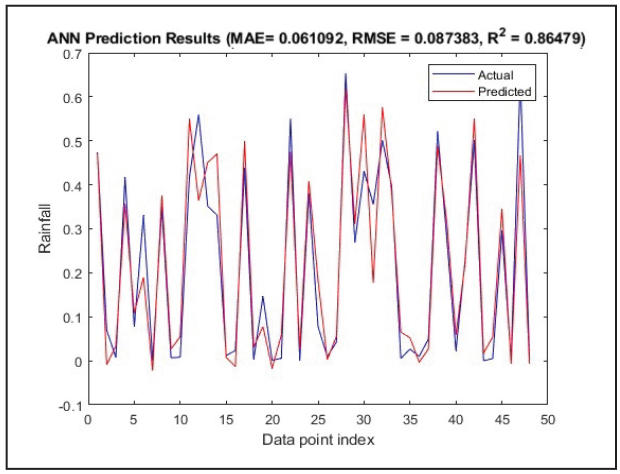

Fig. 2: Normalized Rainfall value Predicted by ANN and Measured Rainfall Value.

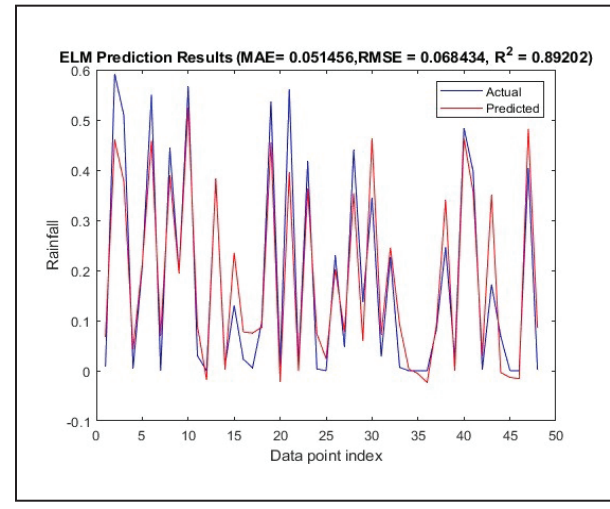

Fig. 3: Normalized Rainfall Value Predicted by ELM and Measured Rainfall Value.

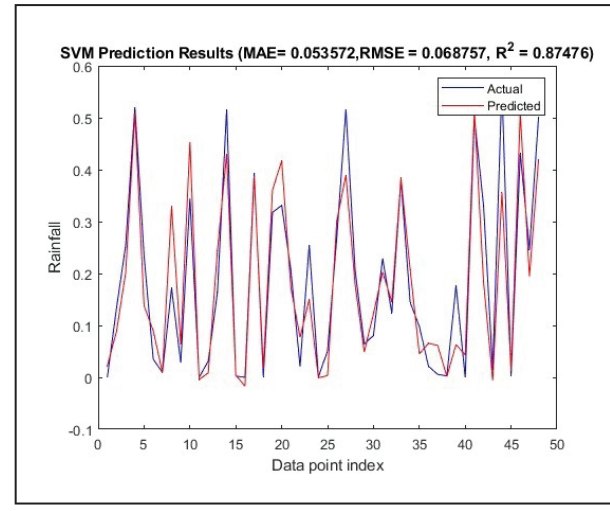

Fig. 4: Normalized Rainfall value Predicted by SVM and Measured Rainfall Value.

Figures 2-4 illustrate the correlation between the rainfall values forecasted by the AI models and the observed rainfall values, showing a remarkable similarity between the two. However, upon comparison, the ANN model demonstrates the lowest performance among the three models, while the ELM model outperforms both the ANN and SVM models in terms of error and coefficient of determination. The findings of the study highlight the effectiveness of AI models in accurately predicting rainfall. Furthermore, the ELM model demonstrates exceptional performance in precisely estimating rainfall. As a result, the ELM model emerges as a valuable tool for reliably predicting rainfall without climatic data.

CONCLUSION

The Performances of ANN, ELM and SVM models were evaluated for predicting monthly rainfall using data from meteorological stations in Mizoram. These models were trained with historical data and validated using unseen data, with predicted values closely matching actual measurements. The study shows that ANN, ELM and SVM models can accurately predict rainfall, achieving a high degree of accuracy. The experimental results indicate that the ELM model outperforms the ANN and SVM models. The AI technique can aid in planning effective countermeasures to minimize the impact of prolong dry season or heavy rainfall and thus help in development of overall economic condition of the state. Further study can be carried out to explore the effectiveness of other AI models along with examining the impacts of climate variables and environmental features.

REFERENCES

Abebe, W. T., & Endalie, D. (2023). Artificial intelligence models for prediction of monthly rainfall without climatic data for meteorological stations in Ethiopia. *Journal of Big Data*, *10*(1). https://doi.org/10.1186/s40537-022-00683-3

Aïzansi, A. N., Ogunjobi, K. O., & Ogou, F. K. (2024). Monthly rainfall prediction using artificial neural network (case study: Republic of Benin). *Environmental Data Science*, *3*. https://doi.org/10.1017/eds.2024.10

Barman, U., Sahu, D., & Barman, G. G. (2021). Comparison of LR, SVR, and DNN for the Rainfall Forecast of Guwahati, Assam. In *Lecture notes in networks and systems,* 170, 297–304. https://doi.org/10.1007/978-981-33-4084-8_28

Chinlampianga, M. (2011) Traditional knowledge, weather prediction and bioindicators: A case study in Mizoram, Northeastern India. *Indian Journal of Traditional knowledge*. 10(1), 207-211

Dada, E. G., Yakubu, H. J., & Oyewola, D. O. (2021). Artificial Neural Network Models for Rainfall Prediction. *European Journal of Electrical Engineering and Computer Science*, *5*(2), 30–35. https://doi.org/10.24018/ejece.2021.5.2.313

Dash, Y., Mishra, S. K., & Panigrahi, B. K. (2018a). Rainfall prediction for the Kerala state of India using artificial intelligence approaches. *Computers & Electrical Engineering*, *70*, 66–73. https://doi.org/10.1016/j.compeleceng.2018.06.004

Dash, Y., Mishra, S. K., Sahany, S., & Panigrahi, B. K. (2018b). Indian summer monsoon rainfall prediction: A comparison of iterative and non-iterative approaches. *Applied Soft Computing*, *70*, 1122–1134. https://doi.org/10.1016/j.asoc.2017.08.055

Dawoodi, H.H., Patil, M.P. (2021). Rainfall prediction in North Maharashtra region using support vector machine. *Turk J Comput Math Educ*. 12(7),1501-1505.

Dhamodaran, S., KipsonRoy, G., Kishor, A., Refonaa, J., & JanyShabu, S. L. (2020). A Comparative Analysis of Rainfall Prediction Using Support Vector Machine and Random Forest. *Journal of Computational and Theoretical Nanoscience*, *17*(8), 3539–3542. https://doi.org/10.1166/jctn.2020.9227

Fujail, A. K. M., & Das, J. (2023). Artificial Intelligence Modeling for Scour Depth Prediction Upstream of Bridge Piers. *SN Computer Science*, *4*(6). https://doi.org/10.1007/s42979-023-02336-5

Garai, S., Paul, R.K., Yeasin, M., Roy, H.S., Paul, A.K. (2024). Machine learning algorithms for predicting rainfall in India. Current Science. 163(3),360-367.

Hussain, J., Zoremsanga, C. (2021). A survey of rainfall prediction using deep learning. In: 3rd International Conference on Electrical, Control and Instrumentation Engineering (ICECIE); Kuala Lumpur, Malaysia. IEEE; 1-10. https://doi.org/10.1109/ICECIE52348.2021.9664730

Kala, A., Vaidyanathan, S.G. (2018). Prediction of rainfall using artificial neural network. In: International Conference on Inventive Research in Computing Applications (ICIRCA); Coimbatore, India. IEEE; 2018:339-342. https://doi.org/10.1109/ICIRCA.2018.8597421.

Khan, M. U. S., Saifullah, K. M., Hussain, A., & Azamathulla, H. M. (2024). Comparative analysis of different rainfall prediction models: A case study of Aligarh City, India. *Results in Engineering*, *22*, 102093. https://doi.org/10.1016/j.rineng.2024.102093

Lakshminarayana, S. (2020). Rainfall Forecasting using Artificial Neural Networks (ANNs): A Comprehensive Literature Review. *Indian Journal of Pure & Applied Biosciences*, *8*(4), 589–599. https://doi.org/10.18782/2582-2845.8250

Lazri, M., Ouallouche, F., Labadi, K., Ameur, S. (2022). Extreme learning machine versus multilayer perceptron for rainfall estimation from MSG data. E3S Web of Conferences. 353(01006).

Li, H., Chou, C., Chen, Y., Wang, S., & Wu, A. (2019). Robust and Lightweight Ensemble Extreme Learning Machine Engine Based on Eigenspace Domain for Compressed Learning. *IEEE Transactions on Circuits and Systems I Regular Papers*, *66*(12), 4699–4712. https://doi.org/10.1109/tcsi.2019.2940642

Mehr, A. D., Nourani, V., Khosrowshahi, V. K., & Ghorbani, M. A. (2019). A hybrid support vector regression–firefly model for monthly rainfall forecasting. *International Journal of Environmental Science and Technology*, *16*(1), 335–346. https://doi.org/10.1007/s13762-018-1674-2

Mislan, N., Haviluddin, N., Hardwinarto, S., Sumaryono, N., & Aipassa, M. (2015). Rainfall Monthly Prediction Based on Artificial Neural Network: A Case Study in Tenggarong Station, East Kalimantan - Indonesia. *Procedia Computer Science*, *59*, 142–151. https://doi.org/10.1016/j.procs.2015.07.528

Meteorological Data of Mizoram (MDM). (2022) Directorate of Economics & Statistics, Planning & Programme Implementation Department, Government of Mizoram. https://des.mizoram.gov.in/uploads/attachments/2022/09/

c7a320a0094f8d1f1de1714562d8788b/meteorological-data-of-mizoram-2021.pdf , Accessed on April 5, 2024

Nandakumar, S.D., Kumar, S.D., Menon, V.V., Radhakrishnan, K., Sivakumar, R. (2021) Artificial neural network for rainfall analysis using deep learning techniques. J Phys Conf Ser. 1964:042022.

Saha, S., Chakraborty, D., Choudhury, B.U., Singh, S.B., Chinza, N., Lalzarliana, C., Dutta, S.K., Chowdhury, S., Boopathi, T., Lungmuana, Singh, A.R., & Ngachan, S.V.. (2015). Spatial variability in temporal trends of precipitation and its impact on the agricultural scenario of Mizoram. *Current Science*. 109(12), 2278-2282.

Saha, S., Das, B., Chakraborty, D., Chawdhury, S., Shakuntala I., Mishra, V.K., Lalhmachhuana, P., Lungmuana, Lalliansanga, S., Saithantluanga, H. (2021). Quantitative Accuracy Assessment of District Level Rainfall Forecast in Mizoram. *Journal of Agricultural Physics*. 21(2),332-340.

Samantaray, S., Tripathy, O., Sahoo, A., & Ghose, D. K. (2019). Rainfall Forecasting Through ANN and SVM in Bolangir Watershed, India. In *Smart innovation, systems and technologies* (pp. 767–774). https://doi.org/10.1007/978-981-13-9282-5_74

Singh, P., & Borah, B. (2013). Indian summer monsoon rainfall prediction using artificial neural network. *Stochastic Environmental Research and Risk Assessment*, *27*(7), 1585–1599. https://doi.org/10.1007/s00477-013-0695-0

Shukla, R. P., Tripathi, K. C., Pandey, A. C., & Das, I. (2011). Prediction of Indian summer monsoon rainfall using Niño indices: A neural network approach. *Atmospheric Research*, *102*(1–2), 99–109. https://doi.org/10.1016/j.atmosres.2011.06.013

Velasco, L. C. P., Serquiña, R. P., Zamad, M. S. a. A., Juanico, B. F., & Lomocso, J. C. (2019). Week-ahead Rainfall Forecasting Using Multilayer Perceptron Neural Network. *Procedia Computer Science*, *161*, 386–397. https://doi.org/10.1016/j.procs.2019.11.137

Waqas, M., Humphries, U. W., Wangwongchai, A., Dechpichai, P., & Ahmad, S. (2023). Potential of Artificial Intelligence-Based Techniques for Rainfall Forecasting in Thailand: A Comprehensive Review. *Water*, *15*(16), 2979. https://doi.org/10.3390/w15162979

Weesakul, U., Kaewprapha, P., Boonyuen, K., Mark, O. (2018). Deep learning neural network: A machine learning approach for monthly rainfall forecast, case study in eastern region of Thailand. Engineering and Applied Science Research. 45(3):203-211.

Yin, G., Yoshikane, T., Yamamoto, K., Kubota, T., & Yoshimura, K. (2022). A support vector machine-based method for improving real-time hourly precipitation forecast in Japan. *Journal of Hydrology*, *612*, 128125. https://doi.org/10.1016/j.jhydrol.2022.128125

Science and Technology Journal Vol. 12 Issue: 2 June 2024 ISSN: 2321-3388

Refinements of Generalized Jacobi Method: A Higher-Order Approach

Urboshi Hazarika[1*] and Samira Behera[2]
[1]Research Scholar, Department of Mathematics, Assam University, Silchar, Assam 788011, India
[2]Professor, Department of Mathematics, Assam University, Silchar, Assam 788011, India
E-Mail: [1]hzurboshi1@gmail.com, [2]samirabehera@yahoo.in
[*]Corresponding Author

Abstract—This study presents a comparative analysis of the p^{th} Refinement of Generalized Jacobi method, focusing on its derivation, convergence properties, and numerical performance. We first derive the Third Refinement of Generalized Jacobi method and establish a general formula applicable to any p^{th} Refinement. The analysis rigorously proves convergence for various types of matrices, including Strictly Diagonally Dominant (SDD) and M-matrices. Additionally, we demonstrate that the convergence rate of the $(p + 1)^{th}$ Refinement surpasses that of the p^{th} Refinement, assuming the Generalized Jacobi method converges. Numerical examples are provided to support our theoretical findings, showcasing the improved convergence rates of the $(p + 1)^{th}$ Refinement compared to the p^{th} Refinement. These results underline the advantages of higher-order refinements in the Generalized Jacobi method.

Keywords: System of Linear Equations; Iterative methods; Jacobi; Generalized Jacobi; SDD matrix; M-matrix, Banded matrix.

MR(2020) Subject Classification: 65F10, 65F15, 65F50.

INTRODUCTION

The Jacobi method, introduced by Carl Gustav Jacob Jacobi in the 19th century, is a fundamental iterative approach for solving systems of linear equations. Despite its simplicity and effectiveness in solving such systems, it often suffers from slow rate of convergence, particularly for matrices that are diagonally dominant or possess closely clustered eigenvalues. To address these limitations, various refinement techniques have been developed over time.

Salkuyeh (2007) proposed an extension of the Jacobi method that incorporates the concept of a banded matrix, which significantly improves convergence for SDD and M-matrices (Salkuyeh 2007). Based on this work, Dafchahi (2008) introduced the Refinement of Jacobi (RJ) method, which accelerates convergence for systems with SDD matrices by employing a new iterative update scheme. This method has demonstrated convergence for Symmetric Positive Definite (SPD) and M-matrices (Dafchahi 2008).

Vatti and Gonfa (2011) further extended the method by combining generalization and refinement techniques to create the Refinement of Generalized Jacobi method. Their study demonstrated that this method is more efficient than the Refinement of Jacobi method, particularly in terms of performance, convergence speed, storage requirements, and accuracy (Vatti and Gonfa 2011).

Further advancements were made by Enyew *et al*. (2019), who introduced the Second Refinement of Jacobi (SRJ) method, enhancing convergence for SDD, SPD, and M-matrices. This method reduced the number of iterations required and lowered the spectral radius, thus improving the rate of convergence (Enyew *et al*. 2019). In 2020, Enyew *et al*. introduced the Second Refinement of Generalized Jacobi (SRGJ) method, which showed superior performance in terms of iteration count and spectral radius compared to traditional Jacobi and related methods, with guaranteed convergence for SDD, SPD, and M-matrices (Enyew *et al*. 2020).

 https://doi.org/10.22232/stj.2024.12.02.18

This paper presents the development of higher-order refinements of the Generalized Jacobi method and investigates their convergence properties across various types of matrices. Section 2, provides the necessary preliminary definitions, theorems, and a review of existing methods. In Section 3, we derive Third Refinement of Generalized Jacobi method and extend the approach to higher-order refinements. Additionally, we explore the convergence properties of these higher-order methods and provide numerical examples that illustrate their efficiency in comparison to other refinement techniques. Finally, Section 4 summatrizes the key findings and offers concluding remarks on the overall performance of the proposed methods.

MATERIALS AND METHODS

Let $A = (a_{ij})$ be an $n \times n$ matrix. Then $D_m = (d_{ij})$ is the banded matrix of bandwidth $2m + 1$, defined as follows:

$$d_{ij} = \begin{cases} a_{ij}, & |i-j| \le m, \\ 0, & \text{otherwise.} \end{cases}$$

Let us consider the splitting of matrix A as

$$A = D_m + L_m + U_m$$

where L_m and U_m are the strictly lower and strictly upper parts of the matrix $A - D_m$, respectively.

Thus, we have,

$$D_m = \begin{pmatrix} a_{1,1} & \cdots & a_{1,m+1} & & \\ \vdots & \ddots & & \ddots & \\ a_{m+1,1} & & \vdots & & \\ & & \vdots & & a_{n-m,n} \\ & \ddots & & \ddots & \vdots \\ & & a_{n,n-m} & \cdots & a_{n,n} \end{pmatrix}$$

$$L_m = \begin{pmatrix} & & & & \\ & & & & \\ & & & & \\ a_{m+2,1} & & & & \\ \vdots & \ddots & & & \\ a_{n,1} & \cdots & a_{n,n-m-1} & & \end{pmatrix},$$

$$U_m = \begin{pmatrix} & a_{1,m+2} & \cdots & a_{1,n} \\ & & \ddots & \vdots \\ & & & a_{n-m-1,n} \\ & & & \\ & & & \end{pmatrix}$$

Definition 2.1. Spectral Radius of a mattrix:(Butt, 2015) *The spectral radius of a matrix A is defined as the largest absolute value of its eigenvalues. That is*

$$\rho(A) = \max_{1 \le i \le n} |\lambda_i|,$$

where λ_i are the eigenvalues of A.

Definition 2.2. Strictly Diagonally Dominant (SDD) matrix: (Salkuyeh, 2007) *A square matrix $A = (a_{ij})$ is said to be Strictly Diagonally Dominant (SDD) if*

$$|a_{ii}| > \sum_{j \ne i} |a_{ij}|, \quad \text{for all } i = 1, 2, \ldots, n,$$

where a_{ij} represents the elements of the matrix.

Definition 2.3. Symmetric Positive Definite (SPD) matrix: (Salkuyeh, 2007) *An $n \times n$ matrix $A = (a_{ij})$ is said to be Symmetric Positive Definite if A is symmetric ($A = A^T$) and positive definite, that is, $x^T Ax > 0$ for all $x \ne 0$.*

Definition 2.4. M-matrix: (Enyew *et al.*, 2020) *A matrix is classified as an M-matrix if it adheres to the following criteria:*

- $a_{ii} > 0$ for $i = 1, 2, \ldots, n$.
- $a_{ij} \le 0$ for $i \ne j$ and $i, j = 1, 2, \ldots, n$.
- A is non-singular.
- $A^{-1} \ge 0$.

Lemma 2.1. (Enyew *et al.*, 2020) *The Spectral radius satisfies the following rule:*

$$\rho(A^k) = (\rho(A))^k \quad \text{for all} \quad k \in N \quad \text{and} \quad A \in C^{n \times n}.$$

Theorem 2.1. (Salkuyeh, 2007) *For any initial approximation $x^{(0)} \in \mathbb{R}$, the sequence $\{x^{(k)}\}_{k=0}^{\infty}$ of approximations defined by*

$$x^{(k+1)} = Tx^{(k)} + c,$$

for each $k \ge 0$, and $c \ne 0$, converges to the unique solution of $x = Tx + c$, if and only if $\rho(T) < 1$. Also, since $\rho(T) \le ||T||$ for any natural norm, $\rho(T) < 1$ is equivalent to $||T|| < 1$.

Now we will discuss the established Jacobi method and its refinement forms.

For the system of linear equations,

$$Ax = b \qquad (1)$$

where $A = (a_{ij})$ is a non-singular real matrix of order n, b is a real n-dimensional vector, and x is the vector to be determined.

Let us consider the splitting of matrix A as,

$$A = D_m + L_m + U_m$$

where D_m is the banded matrix of bandwidth $2m + 1$, and L_m and U_m are the strictly lower and strictly upper parts of the matrix $A - D_m$, respectively. Then,

- The Generalized Jacobi method is given by (Salkuyeh, 2007):

$$x^{(k+1)} = -D_m^{-1}(L_m + U_m)x^{(k)} + D_m^{-1}b, \quad (2)$$

where $k = 0, 1, 2, \ldots$, and $m = 0, 1, 2, \ldots$

- The Refinement (or First Refinement) of Generalized Jacobi method is given by (Dafchahi, 2008):

$$x^{(k+1)} = \left(-D_m^{-1}(L_m + U_m)\right)^2 x^{(k)} + \left(I - D_m^{-1}(L_m + U_m)\right) D_m^{-1}b, \quad (3)$$

where $k = 0, 1, 2, \ldots$, and $m = 0, 1, 2, \ldots$

- The Second Refinement of Generalized Jacobi method is given by (Enyew *et al*., 2019):

$$x^{(k+1)} = \left(-D_m^{-1}(L_m + U_m)\right)^3 x^{(k)} + \left(I - D_m^{-1}(L_m + U_m) + \left(-D_m^{-1}(L_m + U_m)\right)^2\right) D_m^{-1}b, \quad (4)$$

where $k = 0, 1, 2, \ldots$, and $m = 0, 1, 2, \ldots$

Theorem 2.2. (Salkuyeh, 2007) *Let A represent an SDD and M-matrix. Then, for any natural number m ≤ n, the Generalized Jacobi (GJ) method exhibits convergence with an initial guess* $x^{(0)}$.

Theorem 2.3. (Vatti and Gonfa, 2011; Enyew *et al*., 2019) *Let A represent an SDD and M-matrix. Then, for any natural number m ≤ n, the Refinement Generalized Jacobi (RGJ) method exhibits convergence with an initial guess* $x^{(0)}$.

Theorem 2.4. (Enyew *et al*., 2019) *Let A represent an SDD and M-matrix. Then, for any natural number m ≤ n, the Second Refinement Generalized Jacobi (SRGJ) method exhibits convergence with an initial guess* $x^{(0)}$.

RESULTS AND DISCUSSION

Consider the system (1)

$$\begin{aligned} & Ax = b \\ \Rightarrow & (D_m + L_m + U_m)x = b \\ \Rightarrow & D_m x = b - (L_m + U_m)x \\ \Rightarrow & D_m x = b + (D_m - A)x \\ \Rightarrow & x = x + D_m^{-1}(b - Ax) \end{aligned}$$

So, the Refinement iterative form will be,

$$x^{(k+1)} = \tilde{x}^{(k+1)} + D_m^{-1}(b - A\tilde{x}^{(k+1)}) \quad (5)$$

To find the desired Third Refinement of Generalized Jacobi, we put the value of

$\tilde{x}^{(k+1)} = (-D_m^{-1}(L_m + U_m))^3 x^{(k)} + (I - D_m^{-1}(L_m + U_m) + (-D_m^{-1}(L_m + U_m))^2) D_m^{-1}b$ taking from (4) in the equation (5). So, we get,

$$\begin{aligned} x^{(k+1)} =& (-D_m^{-1}(L_m + U_m))^4 x^{(k)} + (I + (-D_m^{-1}(L_m + U_m)) \\ & + (-D_m^{-1}(L_m + U_m))^2) D_m^{-1}b + \\ & D_m^{-1}(b - A((-D_m^{-1}(L_m + U_m))^3 x^{(k)} + (I - D_m^{-1}(L_m + U_m) \\ & + (-D_m^{-1}(L_m + U_m))^2) D_m^{-1}b)) \end{aligned}$$

After some simplification and arrangement, finally we get,

$$\begin{aligned} x^{(k+1)} =& (-D_m^{-1}(L_m + U_m))^4 x^{(k)} + (I + (-D_m^{-1}(L_m + U_m)) \\ & + (-D_m^{-1}(L_m + U_m))^2 + (-D_m^{-1}(L_m + U_m))^3) D_m^{-1}b \end{aligned}$$

where, $k = 0, 1, 2, \ldots$, and $m = 0, 1, 2, \ldots$

Which is the required Third Refinement of Generalized Jacobi method.

In the same way, we can also find the Fourth Refinement of Generalized Jacobi method and it is,

$$\begin{aligned} x^{(k+1)} =& (-D_m^{-1}(L_m + U_m))^5 x^{(k)} + (I + (-D_m^{-1}(L_m + U_m)) \\ & + (-D_m^{-1}(L_m + U_m))^2 + (-D_m^{-1}(L_m + U_m))^3 \\ & + (-D_m^{-1}(L_m + U_m))^4) D_m^{-1}b \end{aligned}$$

where, $k = 0, 1, 2, \ldots$,and $m = 0, 1, 2, \ldots$

By generalizing the above sequence we can talk about any p^{th} Refinement of Generalized Jacobi method, for $p = 0, 1, 2, \ldots$ and it will be of the form,

$$\begin{aligned} x^{(k+1)} =& (-D_m^{-1}(L_m + U_m))^{p+1} x^{(k)} + (I + (-D_m^{-1}(L_m + U_m)) \\ & + (-D_m^{-1}(L_m + U_m))^2 + (-D_m^{-1}(L_m + U_m))^3 + \ldots \\ & + (-D_m^{-1}(L_m + U_m))^p) D_m^{-1}b \end{aligned}$$

where, $k = 0, 1, 2, \ldots$, and $m = 0, 1, 2, \ldots$

If $p = 0$, then the scheme will be the Generalized Jacobi method.

Also, if $p = 0$ and $m = 0$, it is nothing but the original Jacobi method.

Now, we will discuss the convergence of the p^{th} Refinement of Generalized Jacobi method.

Theorem 4.1. *For an SDD matrix, any* p^{th} *Refinement of Generalized Jacobi method is convergent for any initial approximation* $x^{(0)}$.

Proof. From Theorem 2.2 Generalized Jacobi method is convergent.

So the spectral radius of the iteration matrix is less than 1. That is,

$$\rho(-D_m{}^{-1}(L_m + U_m)) < 1. \tag{6}$$

Since the Spectral radius of p^{th} Refinement of Generalized Jacobi method is,

$\rho((-D_m{}^{-1}(L_m + U_m))^{p+1})$, where $p = 1, 2, \ldots$

Now by using Lemma 2.1 and equation 6,

$\rho((-D_m{}^{-1}(L_m + U_m))^{p+1}) = (\rho(-D_m{}^{-1}(L_m + U_m)))^{p+1} < 1.$

So for the SDD matrix p^{th} Refinement of Generalized Jacobi Method is convergent for any initial guess.

Theorem 4.2. *If the coefficient matrix is an M-matrix, then any p^{th} Refinement of Generalized Jacobi method is convergent for any initial guess $x^{(0)}$.*

Proof. Similar to the above theorem, by using Theorem 2.2 and Lemma 2.1 we can prove it.

Theorem 4.3 *If the Generalized Jacobi method is convergent, then any p^{th} Refinement of the Generalized Jacobi method converges faster than the Generalized Jacobi method. Additionally, any $(p + 1)^{th}$ Refinement of the Generalized Jacobi method converges faster than any p^{th} Refinement of the Generalized Jacobi method for any initial guess $x^{(0)}$.*

Proof. We can write, GJ method as,

$$x^{(k+1)} = Gx^{(k)} + K_1.$$

RGJ (FRGJ) method as,

$$x^{(k+1)} = G^2x^{(k)} + K_2.$$

SRGJ method as,

$$x^{(k+1)} = G^3x^{(k)} + K_3.$$

TRGJ method as,

$$x^{(k+1)} = G^4x^{(k)} + K_4.$$

$\vdots$

Any p^{th} RGJ method as,

$$x^{(k+1)} = G^{(p+1)}x^{(k)} + K_{p+1}.$$

Where,

$$G = -D_m{}^{-1}(L_m + U_m).$$

$$K_1 = D_m{}^{-1}b.$$

$$K_2 = D_m{}^{-1}b(I + (-D_m{}^{-1}(L_m + U_m))).$$

$$K_3 = D_m{}^{-1}b(I + (-D_m{}^{-1}(L_m + U_m)) + (-D_m{}^{-1}(L_m + U_m))^2).$$

$$K_4 = D_m{}^{-1}b(I + (-D_m{}^{-1}(L_m + U_m)) + (-D_m{}^{-1}(L_m + U_m))^2 + (-D_m{}^{-1}(L_m + U_m))^3).$$

$$K_{p+1} = D_m{}^{-1}b(I + (-D_m{}^{-1}(L_m + U_m)) + (-D_m{}^{-1}(L_m + U_m))^2 + \ldots + (-D_m{}^{-1}(L_m + U_m))^p).$$

Given that, the GJ method is convergent.

So,

$$||G|| < 1 \tag{7}$$

Let x be the exact solution of $Ax = b$, then

$$x = Gx + K_1, \quad x = G^2x + K_2, \quad x = G^3x + K_3, \quad x = G^4x + K_4,$$

$$x = G^{p+1}x + K_{p+1}.$$

Now, consider the GJ method,

$$x^{(k+1)} = Gx^{(k)} + K_1$$

$$\Rightarrow x^{(k+1)} - x = Gx^{(k)} - x + K_1$$

$$\Rightarrow x^{(k+1)} - x = G(x^{(k)} - x) + Gx + K_1 - x$$

$$\Rightarrow x^{(k+1)} - x = G(x^{(k)} - x)$$

$$\Rightarrow ||x^{(k+1)} - x|| = ||G(x^{(k)} - x)||$$

$$\Rightarrow ||x^{(k+1)} - x|| \leq ||G||\ ||(x^{(k)} - x)||$$

$$\leq ||G^2||\ ||(x^{(k-1)} - x)||$$

$$\leq \ldots \leq ||G^{k+1}||\ ||(x^{(0)} - x)||$$

$$= \|G\|^{k+1}\ ||(x^{(0)} - x)||$$

Now, considering RGJ,

$$x^{(k+1)} = G^2x^{(k)} + K_2$$

$$\Rightarrow x^{(k+1)} - x = G^2x^{(k)} - x + K_2$$

$$\Rightarrow x^{(k+1)} - x = G^2(x^{(k)} - x) + G^2x + K_2 - x$$

$$\Rightarrow x^{(k+1)} - x = G^2(x^{(k)} - x)$$

$$\Rightarrow ||x^{(k+1)} - x|| = ||G^2(x^{(k)} - x)||$$

$$\Rightarrow ||x^{(k+1)} - x|| \leq ||G^2||\ ||(x^{(k)} - x)||$$

$$\leq ||G^4||\ ||(x^{(k-1)} - x)||$$

$$\leq \ldots \leq ||G^{2k+2}||\ ||(x^{(0)} - x)||$$

$$= \|G\|^{2k+2}\ ||(x^{(0)} - x)||$$

Again, considering any p^{th} RGJ,

$$x^{(k+1)} = G^{p+1}x^{(k)} + K_{p+1}$$

$$\Rightarrow x^{(k+1)} - x = G^{p+1}x^{(k)} - x + K_{p+1}$$

$$\Rightarrow x^{(k+1)} - x = G^{p+1}(x^{(k)} - x) + G^{p+1}x + K_{p+1} - x$$

$$\Rightarrow x^{(k+1)} - x = G^{p+1}(x^{(k)} - x)$$

$$\Rightarrow ||x^{(k+1)} - x|| = ||G^{p+1}(x^{(k)} - x)||$$
$$\Rightarrow ||x^{(k+1)} - x|| \leq ||G^{p+1}||\ ||(x^{(k)} - x)||$$
$$\leq ||G^{2(p+1)}||\ ||(x^{(k-1)} - x)||$$
$$\leq \ldots \leq ||G^{(p+1)(k+1)}||\ ||(x^{(0)} - x)||$$
$$= \|G\|^{(p+1)(k+1)}\ ||(x^{(0)} - x)||$$

According to the coefficient of the above inequalities,

We have,

$$||G||^{(p+1)(k+1)} \leq \ldots \leq ||G||^{2(k+1)} \leq ||G||^{k+1} \qquad \text{(From 7)}$$

The p^{th} Refinement of the Generalized Jacobi method achieves faster convergence than the original, with the $(p + 1)^{th}$ Refinement outperforming the p^{th} for any initial guess $x^{(0)}$.

Here, we present two illustrative numerical examples to validate the accuracy and effectiveness of our established theorems.

Example 4.1. (Audu *et al.*, 2023) Consider an example of a 9 × 9 matrix, where the matrix is SDD and with an error tolerance 10^{-4}.

$$4x_1 - x_2 = 20$$
$$-x_1 + 4x_2 - x_3 - x_5 = 20$$
$$-x_2 + 4x_3 - x_5 = 0$$
$$-x_2 + 4x_4 - x_5 - x_7 = 20$$
$$-x_3 - x_4 + 4x_5 - x_6 - x_8 = 0$$
$$-x_5 + 4x_6 - x_9 = 0$$
$$-x_4 + 4x_7 - x_8 = 30$$
$$-x_5 - x_7 + 4x_8 - x_9 = 10$$
$$-x_6 - x_8 + 4x_9 = 10$$

Now, solving this system in MATLAB for different iterative methods with the error tolerance 10^{-4} and $(0, 0, 0, 0, 0, 0, 0, 0, 0)^T$ as an initial approximation, we compare the number of iterations, their spectral radius, and solutions for different methods as shown in the tables below.

Table 1: Comparison with No. of Iterations and Spectral Radius.

Methods	No. of Iterations	Spectral Radius
GJ	14	0.5177
RGJ	9	0.2681
2^{nd} RGJ	6	0.1388
3^{rd} RGJ	5	0.0719
4^{th} RGJ	4	0.0372
5^{th} RGJ	4	0.0193
6^{th} RGJ	4	0.0100
7^{th} RGJ	3	0.0052
8^{th} RGJ	3	0.0027
9^{th} RGJ	3	0.0014
10^{th} RGJ	3	7.1653×10^{-4}
11^{th} RGJ	3	3.7098×10^{-4}
12^{th} RGJ	3	1.9207×10^{-4}
13^{th} RGJ	3	9.9442×10^{-5}
14^{th} RGJ	2	5.1485×10^{-5}
15^{th} RGJ	2	2.6656×10^{-5}

Table 2: Numerical Results for GJ, RGJ, SRGJ, TRGJ,. . . , 15^{th} RGJ with $m = 1$.

Method	n	$x_1^{(n)}$	$x_2^{(n)}$	$x_3^{(n)}$	$x_4^{(n)}$	$x_5^{(n)}$	$x_6^{(n)}$	$x_7^{(n)}$	$x_8^{(n)}$	$x_9^{(n)}$
GJ	0	0	0	0	0	0	0	0	0	0
	1	6.7857	7.1429	1.7857	5.3571	1.4286	0.3571	8.9286	5.7143	3.9286
	2	6.9133	7.6531	2.2704	10.2679	5.0000	2.2321	10.4719	6.5306	4.2219
	⋮	⋮	⋮	⋮	⋮	⋮	⋮	⋮	⋮	⋮
	14	7.4260	9.7042	4.2189	12.4255	7.1731	3.1712	12.8254	8.8772	5.5120
RGJ	0	0	0	0	0	0	0	0	0	0
	1	6.9133	7.6531	2.2704	10.2679	5.0000	2.2321	10.4719	6.5306	4.2219
	2	7.2803	9.1212	3.6651	11.8965	6.5816	2.9121	12.2918	8.2510	5.1728
	⋮	⋮	⋮	⋮	⋮	⋮	⋮	⋮	⋮	⋮
	9	7.4262	9.7049	4.2197	12.4262	7.1739	3.1716	12.8260	8.8780	5.5124
⋮	⋮	⋮	⋮	⋮	⋮	⋮	⋮	⋮	⋮	⋮

(Table 2 Contd...)

(...Contd. Table 2)

	0	0	0	0	0	0	0	0	0	0
15thRGJ	1	7.4262	9.7048	4.2195	12.4260	7.1737	3.1715	12.8259	8.8779	5.5123
	2	7.4262	9.7050	4.2197	12.4262	7.1739	3.1716	12.8261	8.8781	5.5124

Table 1 demonstrates the iteration counts for different methods. The Generalized Jacobi(GJ) method requires 14 iterations, the Refinement of Generalized Jacobi(RGJ) method needs 9 iterations, the Second Refinement of Generalized Jacobi(SRGJ) method takes 6 iterations, and so up to the 15th Refinement of Generalized Jacobi method which takes only 2 iterations. Table 2 shows the solutions obtained by these respective methods. This indicates that increasing the refinement levels in the Generalized Jacobi methods reduces both spectral radii and the number of iterations.

Example 4.2. (Meligy and Youssef, 2022) Consider an example of an 8 × 8 matrix, where the matrix is SDD and with an error tolerance 10^{-4}.

$$
\begin{aligned}
4.2x_1 - x_3 - x_4 - x_7 - x_8 &= 6.2\\
-x_1 + 4.2x_2 - x_4 - x_5 - x_8 &= 5.4\\
-x_1 - x_2 + 4.2x_3 - x_5 - x_6 &= -9.20\\
-x_2 - x_3 + 4.2x_4 - x_6 - x_7 &= 0.00\\
-x_3 - x_4 + 4.2x_5 - x_7 - x_8 &= 6.20\\
-x_1 - x_4 - x_5 + 4.2x_6 - x_8 &= 1.20\\
-x_1 - x_2 - x_5 - x_6 + 4.2x_7 &= -13.4\\
-x_2 - x_3 - x_6 - x_7 + 4.2x_8 &= 4.20
\end{aligned}
$$

Utilizing MATLAB, we approach solving this system through several iterative methods. Starting with an initial guess of $(0, 0, 0, 0, 0, 0, 0, 0)^T$ and setting an error tolerance of 10^{-4}, we analyze and compare the performance in terms of iteration counts and spectral radii, as depicted in the following tables.

Table 3: Comparison with No. of Iterations and Spectral Radius.

Methods	No. of Iterations	Spectral Radius
GJ	90	0.9398
RGJ	51	0.8833
2nd RGJ	37	0.8302
3rd RGJ	29	0.7802
4th RGJ	24	0.7333
5th RGJ	21	0.6892
6th RGJ	18	0.6477
7th RGJ	16	0.6088
8th RGJ	15	0.5721
9th RGJ	14	0.5377
10th RGJ	13	0.5054
11th RGJ	12	0.4750
12th RGJ	11	0.4464
13th RGJ	10	0.4195
14th RGJ	10	0.3943
15th RGJ	9	0.3706

Table 4: Numerical Results for GJ, RGJ, SRGJ, TRGJ,. . . , 15th RGJ with m = 1.

Method	n	$x_1^{(n)}$	$x_2^{(n)}$	$x_3^{(n)}$	$x_4^{(n)}$	$x_5^{(n)}$	$x_6^{(n)}$	$x_7^{(n)}$	$x_8^{(n)}$
GJ	0	0	0	0	0	0	0	0	0
	1	1.4762	1.6372	−1.8007	−0.4287	1.3741	0.6129	−3.0446	0.2751
	2	0.2860	1.6444	−0.9744	−0.4212	0.2878	0.6691	−1.9627	0.6397
	⋮	⋮	⋮	⋮	⋮	⋮	⋮	⋮	⋮
	90	0.9985	1.9985	−1.0015	−0.0015	0.9985	0.9985	−2.0015	0.9985
RGJ	0	0	0	0	0	0	0	0	0
	1	0.2860	1.6444	−0.9744	−0.4212	0.2878	0.6691	−1.9627	0.6397
	2	0.6223	1.7449	−1.2265	−0.3639	0.6015	0.7318	−2.2315	0.6359
	⋮	⋮	⋮	⋮	⋮	⋮	⋮	⋮	⋮
	51	0.9993	1.9993	−1.0007	−0.0007	0.9993	0.9993	−2.0007	0.9993
⋮	⋮	⋮	⋮	⋮	⋮	⋮	⋮	⋮	⋮

(Table 4 Contd...)

(...Contd. Table 4)

15^{th} *RGJ*	0	0	0	0	0	0	0	0	0
	1	0.8497	1.8516	−1.1486	−0.1481	0.8520	0.8515	−2.1486	0.8519
	2	0.9443	1.9450	−1.0550	−0.0549	0.9451	0.9450	−2.0550	0.9451
	⋮	⋮	⋮	⋮	⋮	⋮	⋮	⋮	⋮
	9	0.9999	1.9999	−1.0001	−0.00001	0.9999	0.9999	−2.0001	0.9999

Table 3 represents the number of iterations and the spectral radius of different refinement methods and it observes that GJ takes 90 iterations to converge, which decreases as the application of refinement and it took only 9 iterations in the case of 15^{th} RGJ method. So from both tables, it is clear that increasing the refinement level in the Generalized Jacobi methods leads to a reduction in both the spectral radii and the number of iterations required for convergence. So, any $(p + 1)^{th}$ Refinement is better than that of the p^{th} Refinement of Generalized Jacobi method.

We have demonstrated results up to the 15^{th} RGJ method in the above examples. However, the same approach can be extended to any higher-order RGJ methods, and the observed trends regarding convergence and spectral radii will remain true.

CONCLUSION

In summary, our study focused on the comparative analysis of the p^{th} Refinement of Generalized Jacobi method, covering derivation, convergence characteristics, and numerical performance assessment. Initially, we derived the Third Refinement of Generalized Jacobi method and formulated a comprehensive expression applicable to any p^{th} Refinement. Our investigation involved rigorous theoretical scrutiny, including proofs of convergence for the p^{th} Refinement method across various matrix types such as SDD and M-matrices. Our research revealed a significant insight: the convergence rate of the $(p + 1)^{th}$ Refinement exceeds that of the p^{th} Refinement once the Generalized Jacobi method achieves convergence. This observation underscores the accelerated convergence potential offered by higher-order Refinements within the Generalized Jacobi method. To support our theoretical assertions, we conducted numerical experiments, demonstrating the superior convergence rate of the $(p + 1)^{th}$ Refinement compared to its predecessor, the p^{th} Refinement.

Overall, our findings highlight the efficacy and theoretical advantages of higher-order Refinements in improving the convergence properties of the Generalized Jacobi method. These results contribute valuable insights to the field of iterative methods for solving linear systems of equations, with potential applications in enhancing computational efficiency and accuracy across various scientific and engineering domains.

REFERENCES

Audu KJ, Essien JN, Zahiri AB, Taiwo AR (2023) A third refinement of Jacobi method for solutions to system of linear equations. FUDMA J Sci 7(5): 234-239.

Butt R (2015) An Introduction to Applied Numerical Linear Algebra Using MATLAB. Alpha Science International Limited, Oxford.

Dafchahi FN (2008) A new refinement of Jacobi method for solution of linear system equations Ax = b. Int J Contemp Math Sci 3(17): 819-827.

Enyew TK, Awgichew G, Haile H, Abie GD (2019) Second refinement of Jacobi it- erative method for solving a linear system of equations. Int J Comput Sci Appl Math 5(2): 41-47.

Enyew TK, Awgichew G, Haile H, Abie GD (2020) Second refinement of Generalized Jacobi iterative method for solving linear system of equations. J Niger Math Soc 39(1): 117-133.

Meligy SA, Youssef IK (2022) Relaxation parameters and composite refinement tech- niques. Results Appl Math 15: 100282.

Salkuyeh DK (2007) Generalized Jacobi and Gauss-Seidel methods for solving linear systems of equations. Numer Math J Chin Univ (Engl Ser) 16(2): 164-170.

Vatti VK, Gonfa GG (2011) Refinement of Generalized Jacobi (RGJ) method for solving system of linear equations. Int J Contemp Math Sci 6(3): 109-116.

Science and Technology Journal Vol. 12 Issue: 2 June 2024 ISSN: 2321-3388

Empowering Mizoram State Museum Applying Virtual Reality on Linked Data and Smart Objects

V.D. Ambeth Kumar[1], Rajesh Ramasamy[2], Gurram Ramakrishna[3], and R. Ramesh Prabhakaran[4*]

[1,4]Department of Computer Engineering, Mizoram University, Aizawl-796004, India
[2]Department of Tourism and Hospitality Management, Mizoram University, Aizawl-796004, India
[3]Department of Commerce, Mizoram University, Aizawl-796004, India
E-Mail: [1]ambeth@mzu.edu.in, [2]rajeshrphd@gmail.com,
[3]mzut258@mzu.edu.in, [4]rkrrameshsamy5@gmail.com
*Corresponding Author

Abstract—Augmented Reality (AR) and Virtual Reality (VR) can be combined to create Mixed Reality (MR) experiences that significantly benefit India's tourism department. These technologies enhance higher-order cognitive learning by immersing users in realistic environments, making them invaluable complements to traditional museum techniques. This Full Research explores the implementation of various algorithms, including Rendering Algorithm, pathfinding navigation meshes Algorithm, convolutional neural networks Algorithm (CNNs) and Simultaneous Localization and Mapping Algorithm (SLAM), to develop a 3D model of Advanced Mizoram State Museum Environment in Unity Hub. This model was then converted into a VR experience for the Meta Quest 2. First, I go to Mizoram State Museum to Collect the information and take the picture for Creating Dataset and Converting the 3D Image to the Unity Hub Application for advanced Museum Environment Creating Purpose. This Paper Only Explain the two Algorithms only Rendering Algorithm and Convolutional Neural Network Algorithm (CNN). The rendering algorithm was employed to optimize the Animals, Birds, Insects and Leaf's to get the information and Create the Dataset to upload the code. The Unity Hub application wants to them Object Assets. I go to Download to the Various Assets stores Example Unity Hub Assets Store, Sketch Fab and Blender Assets Store Websites. The Convolutional Neural Network Algorithm (CNN) have explained the Object Detection, Object Recognition and Object Identification to the information for the Visitors peoples. The 3D model of Mizoram State Museum effectively showcases biological animals, plants, insects, and human features, offering users the convenience of exploring the museum anytime and anywhere.

Keywords: Augmented Reality, Virtual Reality, Rendering Algorithm, Conventional Neural Network, Museum, Object Detection, Environment Creation, 3D View.

INTRODUCTION

This paper presents a comprehensive exploration of the infrastructure and specifications required to implement Augmented Reality (AR) and Virtual Reality (VR) experiences within the 3D model environment of Mizoram State Museum. The objective is to enable remote visitors and tourists to experience the museum's offerings through these immersive technologies. To create the 3D model, the museum was initially captured through photographs and videos. These images were then converted into 3D models using specialized software and integrated into a Unity Hub-based AR/VR environment. Four key algorithms were employed in the development of this AR/VR museum:

 https://doi.org/10.22232/stj.2024.12.02.19

rendering, Visual Simultaneous Localization and Mapping (vSLAM), pathfinding and navigation meshes, and Convolutional Neural Networks (CNNs). In this Paper have Explained to the two algorithms only Rendering Algorithm and Convolutional Neural Networks Algorithm (CNN).

A Rendering Algorithm is a crucial component of computer graphics, transforming 3D scenes into 2D images or displays. It calculates how objects within a scene should appear from a specific camera perspective, considering factors like lighting, shading, texturing, and geometry. Rendering algorithms are widely used in video games, simulations, virtual reality (VR), and augmented reality (AR) to create realistic or stylized visual environments. The rendering process involves mesh generation, data loading, prefetching, and tile rendering. While rendering algorithms are fundamental to computer graphics, they can be complex and difficult to optimize. Techniques like global illumination, texture mapping, and normal mapping enhance the realism and detail of rendered images. The choice of rendering algorithm depends on the specific application's requirements. For instance, real-time games often prioritize speed and use rasterization, while photorealistic renderings for films or architectural visualizations may employ more computationally intensive methods like ray tracing or hybrid approaches.

In particular, experimentation consisted of two main stages: a preliminary and a parallel test. As concern the former, a group of domain experts was involved in this study in order to collect qualitative data and perform a preliminary selection of the most commonly used AR rendering techniques as evident from the existing literature. Second, the parallel test, carried out with the involvement of representative users, consisted in performing an inspection task on a physical prototype by adopting an AR application, implementing different visualization modalities according to the rendering techniques selected by the experts. Both quantitative and qualitative metrics were considered to evaluate the influence of the selected AR rendering techniques on user performance in detecting design discrepancies [1].

Convolutional Neural Networks (CNNs) are a powerful type of deep learning algorithm that have revolutionized various fields, including computer vision. In the context of AR/VR museums, CNNs can enhance the user experience by providing intelligent features such as object recognition, scene understanding, and interactive elements. For object recognition, CNNs can be trained on extensive datasets of museum artifacts to accurately identify and classify objects in real-time using camera input. Once an artifact is identified, AR/VR experiences can offer additional information, including historical context, related exhibits, or interactive elements. CNNs can also aid devices in understanding the surrounding environment, including the museum's layout, object positions, and the presence of other visitors. This information enables relevant and immersive experiences, such as placing virtual objects in appropriate locations or suggesting exhibits based on the user's current position. Furthermore, CNNs can recognize hand gestures and other body movements, allowing users to interact with virtual objects or trigger specific actions within the AR/VR experience. By enabling natural language or gesture-based interactions, CNNs make AR/VR experiences more accessible to a wider audience. CNNs open up new possibilities for educational and entertainment experiences, including interactive exhibits, personalized tours, and gamified learning.

Evolutionary algorithms are often applied for optimal parameters setting. However, to this end, a considerable part of the search space should be explored. Finding the optimal ensemble of CNNs using an evolutionary approach is out of the scope of this study since this task has an extremely high computational cost because not only a large number of different architectures must be evaluated, but also a plethora of combinations of CNNs to form the ensembles. Instead, authors propose the use of an evolutionary algorithm for efficiently searching near-optimal ensembles of CNNs by evolving an initial population with no additional cost besides the evolutionary process itself. The term efficient search used in this study refers to a search strategy that can be implemented in con venational hardware and leads to reasonably good solutions from engineering viewpoint in a short period of time [3].

RELATED WORKS

Santina Fortuna *et al*., 2024 (1) Augmented Reality (AR) is increasingly used in manufacturing to improve operators' performance in inspection and assembly tasks. This study evaluates the impact of different AR rendering techniques on user efficiency and accuracy during industrial inspections. Using a custom AR tool, qualitative and quantitative metrics were compared among selected rendering techniques. Results from 17 experts and 33 users showed that rendering methods significantly aid in identifying design discrepancies. A correlation was found between specific rendering techniques and the types of assembly errors detected, highlighting their potential in industrial applications.

Qing Gong *et al*., 2024 (2) Virtual Reality (VR) Cultural Heritage Exhibitions (VRCHEs) present unique challenges

and opportunities in user experience (UX) design due to differences in interaction methods compared to traditional interfaces. Existing UX models are insufficient, lacking comprehensive insights and design strategies. This study uses grounded theory with qualitative and quantitative methods to build a detailed UX model for VRCHEs. It also proposes practical design strategies based on three-level coding and theoretical analysis.

Yarens J. Cruz *et al*., 2021 (3) This paper introduces an ensemble-based image classification approach using five convolutional neural networks (CNNs) combined through a voting policy. An evolutionary algorithm was employed to optimize network parameters and voting strategies. The method was validated in a case study detecting metal sheet misalignments in submerged arc welding, outperforming seven other strategies across various metrics. It achieved superior performance while maintaining reasonable computational efficiency.

Wang Shu-Xi *et al*., 2012 (4) The shortest path problem is common in many fields, with Dijkstra's algorithm being a well-known solution. However, it faces issues in directed graphs, adjacent vertices, and simultaneous "p-label" assignment. By addressing these, we significantly improved the algorithm, with experimental results showing effective resolution of these issues.

Mateus Mendes *et al*., 2019 (5) This paper presents a model combining Augmented Reality (AR) and AI algorithms to enhance user experiences with a 3D map of Coimbra, using data from OpenStreetMap. The AR effect is achieved via video projection over a 3D printed map, allowing users to interact through smartphones and simulate optimized itineraries using genetic algorithms and A*. This model has applications for tourism, virtual reconstructions, and travel simulations.

Hassan Mohyuddin *et al*., 2023 (6) This paper introduces a methodology combining gesture recognition data from a Leap Motion Controller (LMC) with the Spotted Hyena-based Chimp Optimization Algorithm (SSC) for feature selection in deep neural networks (DNNs). A comparative analysis shows SSC outperforms other optimization techniques like PSO, GWO, and SCA, achieving 98% accuracy in gesture recognition. The proposed approach enhances both accuracy and versatility in various feature extraction applications.

S. Suganya *et al*., 2023 (7) The Virtual Museum Android App offers an immersive experience, allowing users to explore galleries, interact with exhibits, and learn about their history. It includes audio-visual guides and educational resources to enhance learning. The app uses graphical modeling and augmented reality to create a realistic and interactive environment.

Young Min Kim *et al*., 2021 (8) 3D indoor environment scanning often faces issues like occlusions and misalignments, leading to geometry holes and texture ghosting. This article explores using planes to both represent the environment geometrically and solve inverse rendering problems, simplifying shape inference and intrinsic imaging. The resulting 3D content provides realistic, visually compelling environments suitable for AR/VR Applications.

Chioma Udeozor *et al*., 2023 (9) Immersive learning technologies like VR, AR, and educational games offer significant benefits to teaching, but current assessment practices may not be sufficient for these environments. This paper develops a game-based assessment framework (GBAF) for evaluating learning in VR and AR, grounded in Constrictive Alignment and Evidence-Centered Design principles. It provides a stepwise design for assessments in immersive settings, including a case study on assessing engineering students' laboratory competencies.

Andreas Philipp Hassler *et al*., 2019 (10) As life expectancy increases, more elderly individuals face age-related diseases, with frailty being a key factor linked to falls, hospitalization, and mortality. Predictive data mining can identify risk factors, aiding clinical decision-making to prevent adverse outcomes. This study developed predictive models using medical data from 474 participants, with the support vector machine (SVM) achieving the best accuracy (78.31%), and highlighted the potential of using incomplete medical data to predict frailty.

Valerie Czok *et al*., 2023 (11) New technologies, such as augmented reality (AR), are transforming education by enhancing interactivity and understanding. This paper explores the positive learning effects of AR through a game-based environment, "Beat the Beast," focusing on microplastics within an interdisciplinary framework of biology, chemistry, and engineering. The approach aims to improve learning outcomes and motivation in science education.

Yuzhao Liu *et al*., 2020 (12) Online apparel shopping poses risks as consumers cannot physically see or try on products. To improve this, an AR- and VR-based try-on system allows users to view garments on a personalized virtual body. User studies show that AR-based try-ons offer a more realistic shopping experience than VR, though personalized motions don't significantly impact the experience.

Shilong Su *et al.*, 2023 (13) This study examines the effectiveness of extended reality (XR) in training for total hip arthroplasty (THA). A systematic review and meta-analysis of five studies with 106 participants showed XR training improved inclination accuracy and reduced surgical duration compared to conventional methods. However, the accuracy of anteversion was similar between both approaches.

Agariadne Dwinggo Samala *et al.*, 2023 (14) This study analyzed international publications on augmented reality (AR) and virtual reality (VR) for learning from 2001 to 2021, using bibliometric analysis and data from Scopus. The findings show that both technologies have seen rising trends, with Denmark, India, and prominent researchers like Y. Zhou and Archana M. making significant contributions. The research predicts continued development of AR/VR and mixed reality (MR) technologies, emphasizing the importance of pedagogical competence in enhancing learning experiences.

PROPOSED METHOD

This Research is presented to the Mizoram State Museum to explain the use of Augmented Reality (AR) and Virtual Reality (VR) to the Mixed Reality in creating an advanced museum environment. The virtual museum allows visitors to explore exhibits in a 3D virtual reality space. I employed four different algorithms, but this paper focuses on two: the Convolutional Neural Network (CNN) and the Rendering Algorithm. First, I Collect the Dataset for the image and Image to 3D convert Pictures to create the one Dataset in the All Type of Animals, Birds, Insects and leaf's after creation I upload the Dataset to the Convolutional Neural Network (CNN) Algorithm mainly YOLOv7 model code and execute the full code detect the object recognition, identification and all information in the output. The execute platform is Anaconda Jupyter Notebook in Python Kernal. The Rendering Algorithm is responsible for creating the museum's environment, handling data loading and per fetching, and developing the 3D view of the Mizoram State Museum. I open the Unity Hub Application and create the new terrain to put the one structural building in the application, next all Downloaded assets load and per fetching to the correct places into the terrain. The Advanced Mizoram State Museum Environment was Created after we Convert to the Augmented Reality to Virtual Reality (2D to 3D). The CNN, specifically the YOLOv7 model, is employed for object detection and recognition within the museum. It identifies animals, insects, and other items, providing detailed information about them, such as whether an animal or insect is poisonous or non-poisonous. The advanced museum environment was created using Unity Hub, offering an interactive space for tourists, visitors, and the general public. Wearing a VR headset, visitors can immerse themselves in the virtual museum. The CNN ensures accurate detection of objects, making it easy for visitors to explore and learn about the exhibits. This combination results in a seamless, immersive experience in the advanced museum environment.

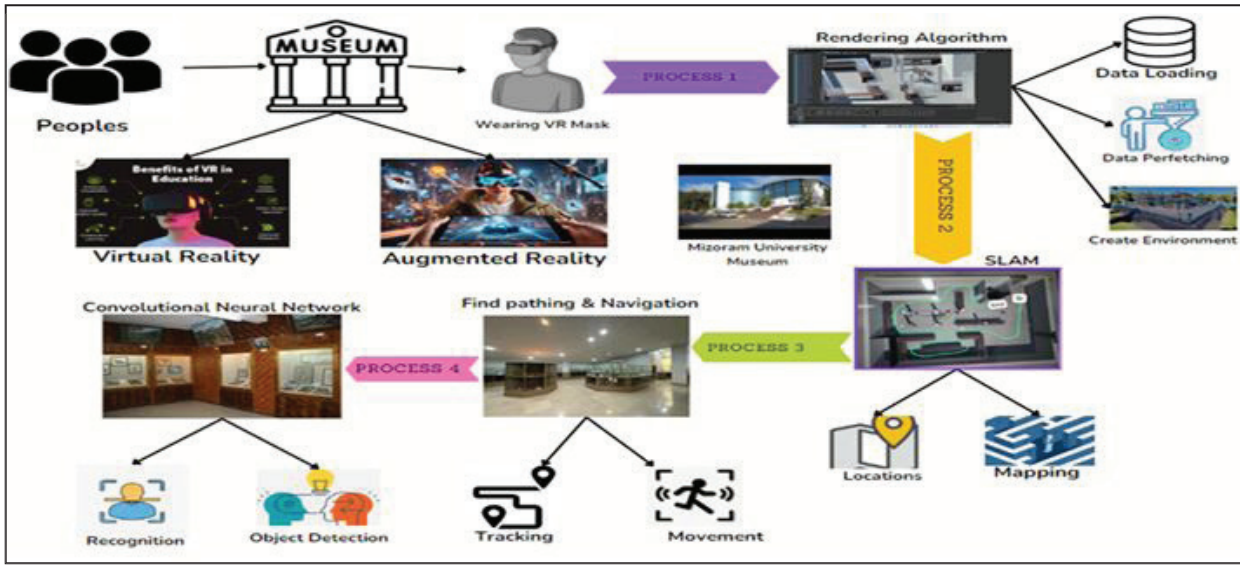

Fig. 1: Full Research Architecture in the Museum.

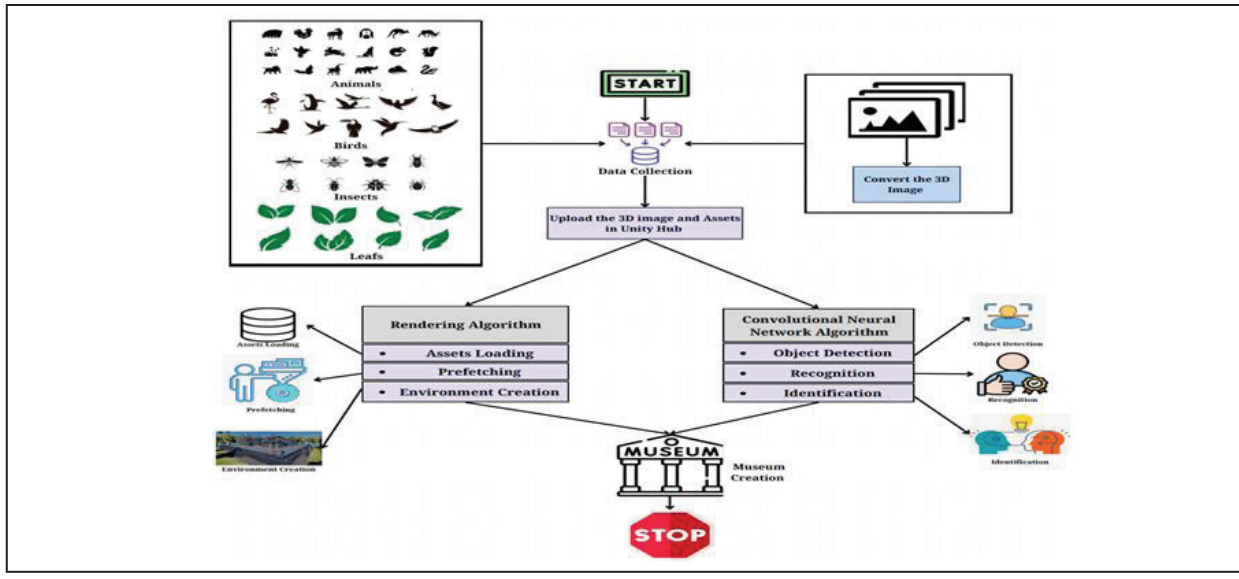

Fig. 2: This Paper Architecture.

DATASETS

Empowering the Mizoram State Museum with Virtual Reality through Linked Data and Smart Objects. This project focuses on enhancing the Mizoram State Museum experience by applying virtual reality (VR) integrated with linked data and smart objects. The Mizoram State Museum, located at PPQ8+68R, MacDonald Hill, Zarkawt, Aizawl, Mizoram 796001 (Coordinates: 23.73795610514955, 92.71507056537367), is a three-story facility showcasing six distinct galleries. These galleries represent the cultural heritage, history, and biodiversity of Mizoram, including the History Gallery, Leaders Gallery, Zoological Gallery, Anthropological Gallery, Ethnological Gallery, Archaeological Gallery and Textile Gallery. As part of this initiative, our team conducted a full-day visit to the museum, gathering comprehensive data to recreate the environment in a 3D VR format. This immersive experience aims to provide a modern, interactive way for visitors to explore and learn about Mizoram's rich cultural and historical legacy.

Fig. 3: History Gallery.

Fig. 4: Anthropological Gallery.

Fig. 5: Archaeological Gallery.

Fig. 6: Leaders Gallery.

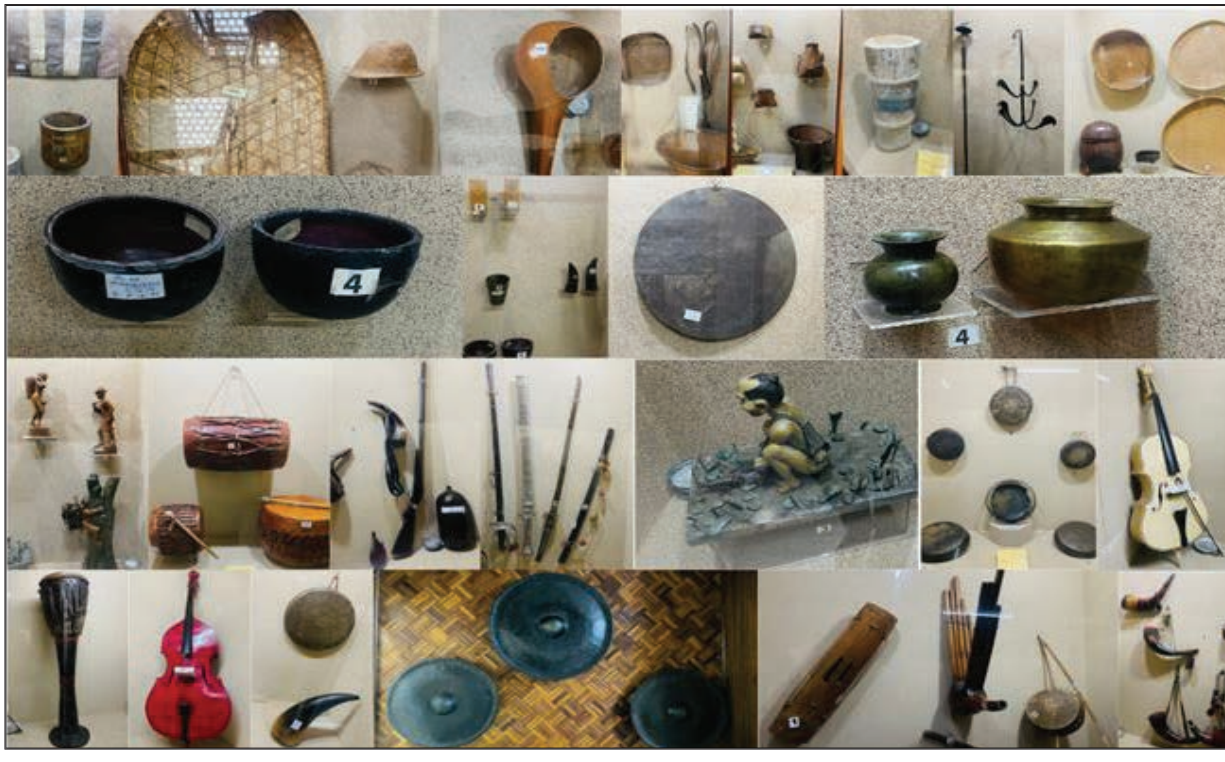

Fig. 7: Ethnological Gallery.

Fig. 8: Textile Gallery.

Fig. 9: Zoological Gallery.

ALGORITHMS

Rendering Algorithms are responsible for converting 3D models of exhibits and surroundings into 2D images that users see in their VR headsets or AR displays. These algorithms handle lighting, shading, textures, and visibility to produce realistic scenes. While the process is complex, we can break it down into key equations used in different stages of the rendering process.

Rasterization Equation: Rasterization is the process of converting 3D vertices of a model into 2D screen coordinates. For AR/VR, this is done to display exhibits or virtual objects in a museum. The basic equation for transforming 3D coordinates (x, y, z) (x, y, z) (x, y, z) into 2D screen coordinates (x′, y′) (x', y') (x′, y′) using a Perspective Projection Matrix is:

$$\begin{bmatrix} x' \\ y' \\ w \end{bmatrix} = \boldsymbol{P} \times \boldsymbol{M}_{view} \times \boldsymbol{M}_{model} \times \begin{bmatrix} x \\ y \\ z \\ 1 \end{bmatrix}$$

$\boldsymbol{M}_{model}$ The model transformation matrix (object's position in the world). $\boldsymbol{M}_{view}$ The view matrix (camera's position and orientation in the virtual museum). $\boldsymbol{P}$ The perspective projection matrix. (x, y, z). The object's 3D coordinates. (x', y') The object's 2D screen coordinates. Finally, you calculate the 2D coordinates.

$$x' = \frac{x}{w}, y' = \frac{y}{w}$$

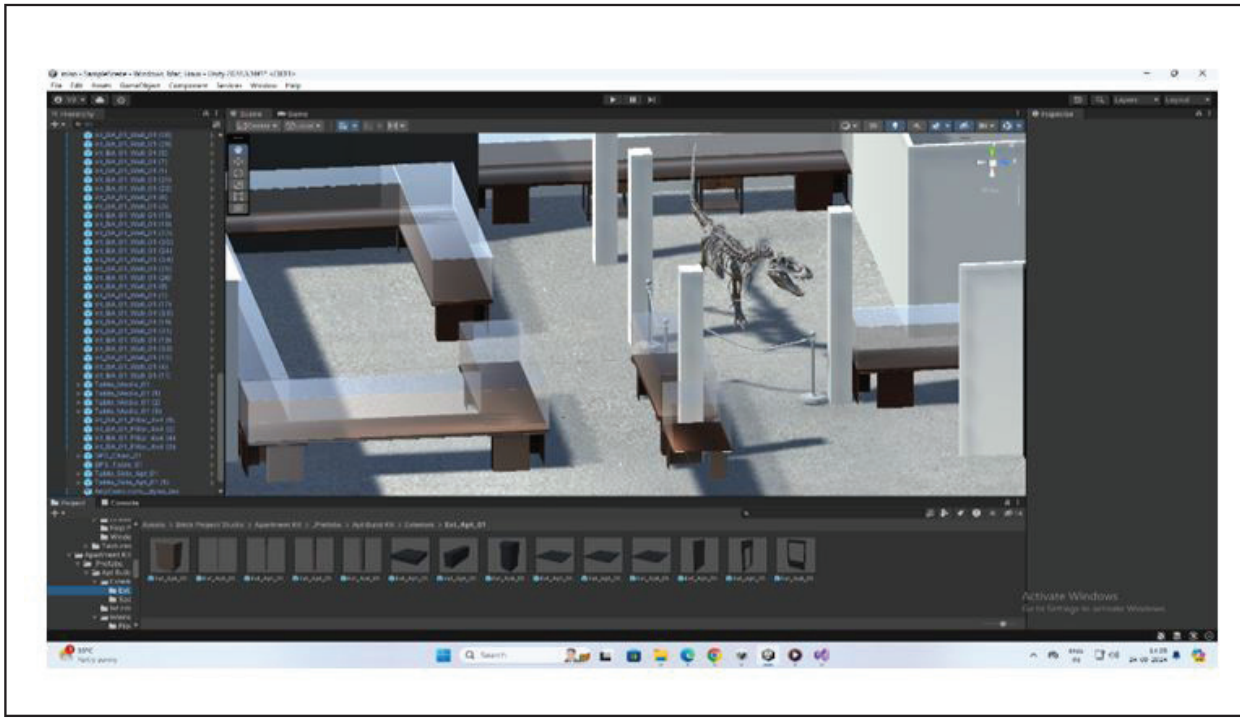

Fig. 10: Creating to Advanced Museum Environment.

Here, w is the depth component used to handle perspective. The Rendering Algorithm is used to download datasets and load them into the Unity Hub application to create the terrain for the museum environment. I downloaded the datasets from sources such as Unity Hub Assets Store, Sketch fab, Polygon Gap, and Blender Store, using the same username across these platforms for consistency. After downloading the assets, I imported them into Unity Hub and added them to the terrain. First, I created a new terrain and placed the building asset on it. Then, I added various assets like animals, insects, birds, and leaves to the terrain. I carefully arranged all these assets in their correct positions and orientations to accurately represent the Mizoram State Museum environment. In conclusion, the Rendering Algorithm handles data loading, asset prefetching, and ultimately, the creation of the advanced museum environment.

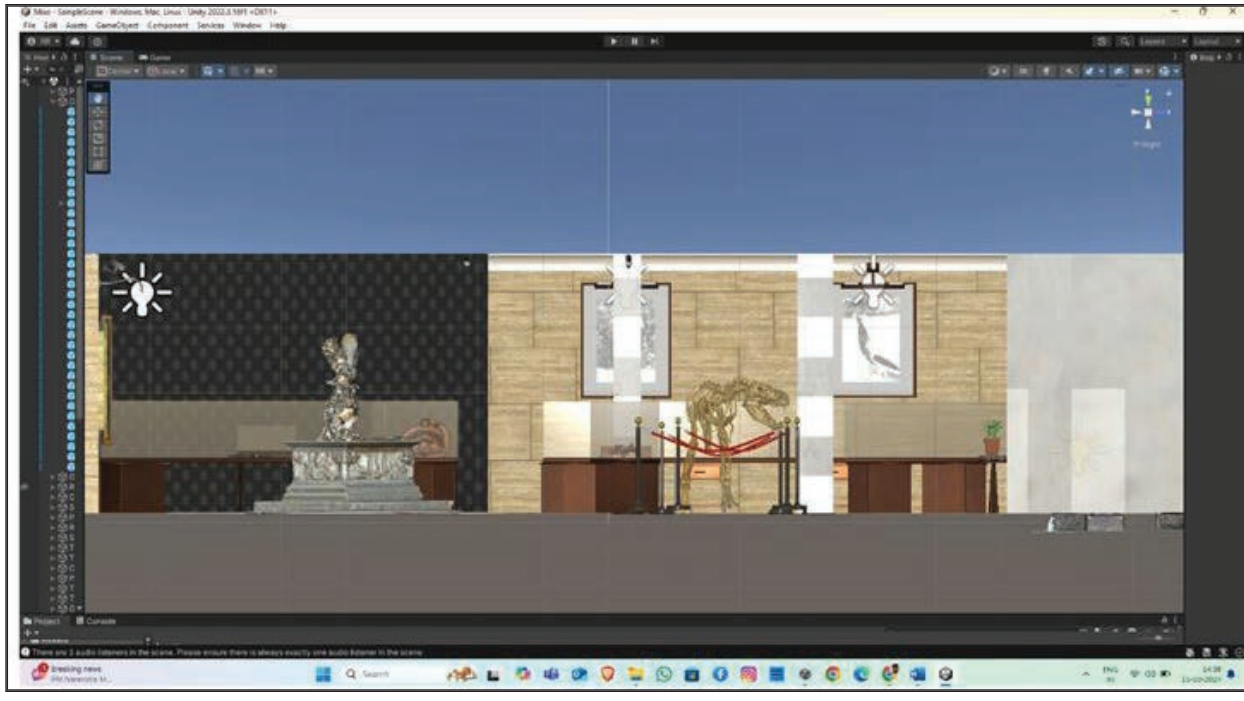

Fig. 11: Final Output for the Rendering Algorithm.

Fig. 12: Fitting the Animal in the Environment.

Figure 3 illustrates the top view of the museum, showing the arrangement of all structures and the placement of objects within the environment. The image highlights asset information on the right side, package names on the left side, and the layout of asset structures and storage locations at the bottom. Figure 3 provides a side view and

the final output of the advanced Mizoram State Museum environment. The final output includes the proper lighting and color adjustments on the walls, as well as detailed information about the animals, insects, birds, leaves, and butterflies within the museum.

Convolutional Neural Networks (CNNs) YOLO (You Only Look Once) Algorithm YOLO is a state-of-the-art object detection algorithm that has gained significant popularity due to its speed and accuracy. It differs from traditional object detection methods by dividing the input image into a grid and predicting bounding boxes and class probabilities for each cell.

YOLO Works Grid Division: The input image is divided into a grid of SxS cells. Bounding Box Prediction: Each cell predicts a fixed number of bounding boxes (B) and their corresponding confidence scores. Class Prediction: For each bounding box, the algorithm predicts the probability of belonging to each class. Non-Maximal Suppression (NMS): To avoid redundant detections, NMS is applied to suppress overlapping bounding boxes with lower confidence scores

Convolutional Neural Networks (CNNs) are highly effective for image recognition tasks, as they are adept at identifying patterns and features within large datasets. This makes them well-suited for applications such as object detection, image segmentation, and even natural language processing. CNNs work by applying filters to input images, extracting key features, and then combining this information to make classification decisions. In a museum setting, CNNs can significantly enhance the visitor experience through features like artifact recognition, personalized tours, and virtual reality interactions. For instance, visitors could use augmented reality (AR) devices to scan artifacts and receive real-time contextual information, or museums could leverage CNNs to analyze visitor behavior and optimize future exhibits accordingly.

While YOLO doesn't have a single, unified equation, its core concept can be expressed as:

$$y,i=\varphi(x,i)$$

y,i: Predicted output for cell i,(x, i): Input image (or feature map) for cell i, φ: Neural network function that predicts bounding boxes, confidence scores, and class probabilities. YOLO Architecture typically uses a deep convolutional neural network architecture. The network consists of several convolutional layers, followed by a fully connected layer. The final layer outputs the predicted bounding boxes, confidence scores, and class probabilities for each cell. Data Preparation: Gather and preprocess a diverse set of images, ensuring they are properly labeled and categorized. Model Building: Select an appropriate CNN architecture, construct the model using layers such as convolutional, pooling, and fully connected, then compile it with the chosen optimizer and loss function. Training: Train the model on the prepared dataset, adjusting hyperparameters and monitoring performance as necessary. Evaluation: Assess the model's accuracy and performance using a validation set. Deployment: Implement the trained model into the target application for recognition tasks.

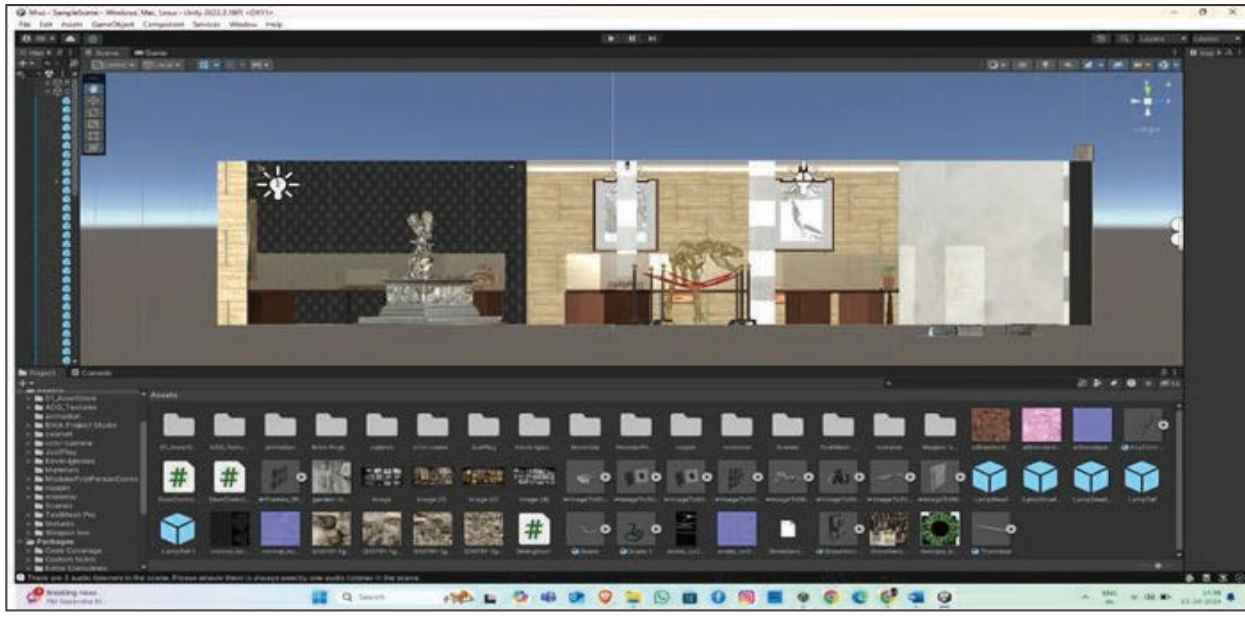

Fig. 13: Loading in the all Object in Environment.

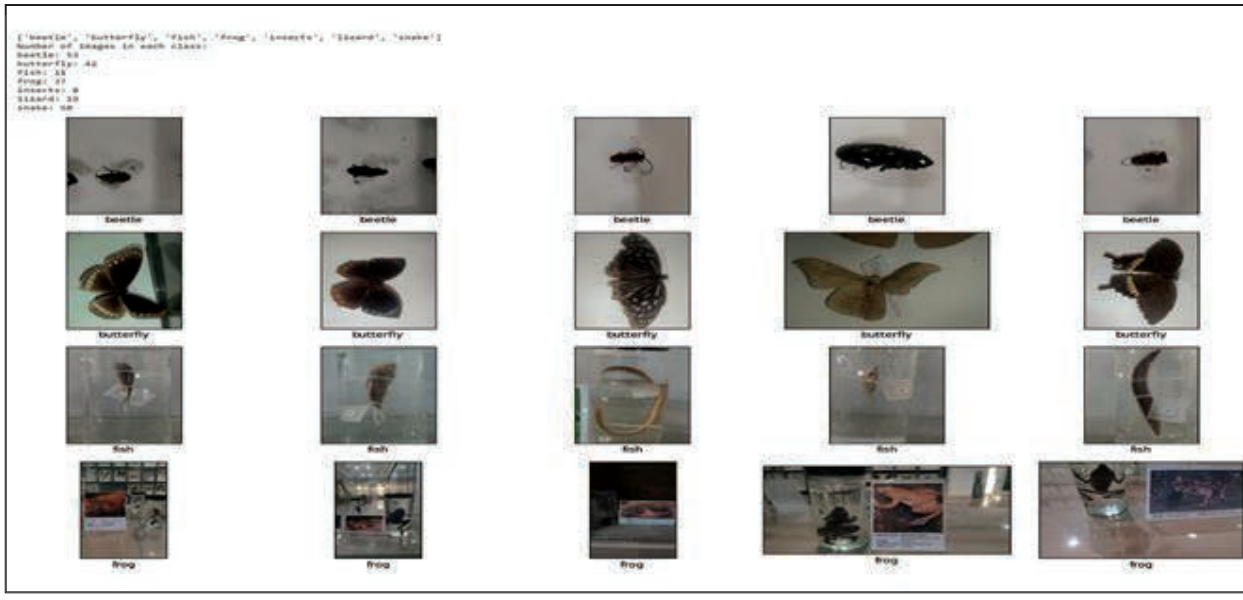

Fig. 14: Classification of Museum Objects.

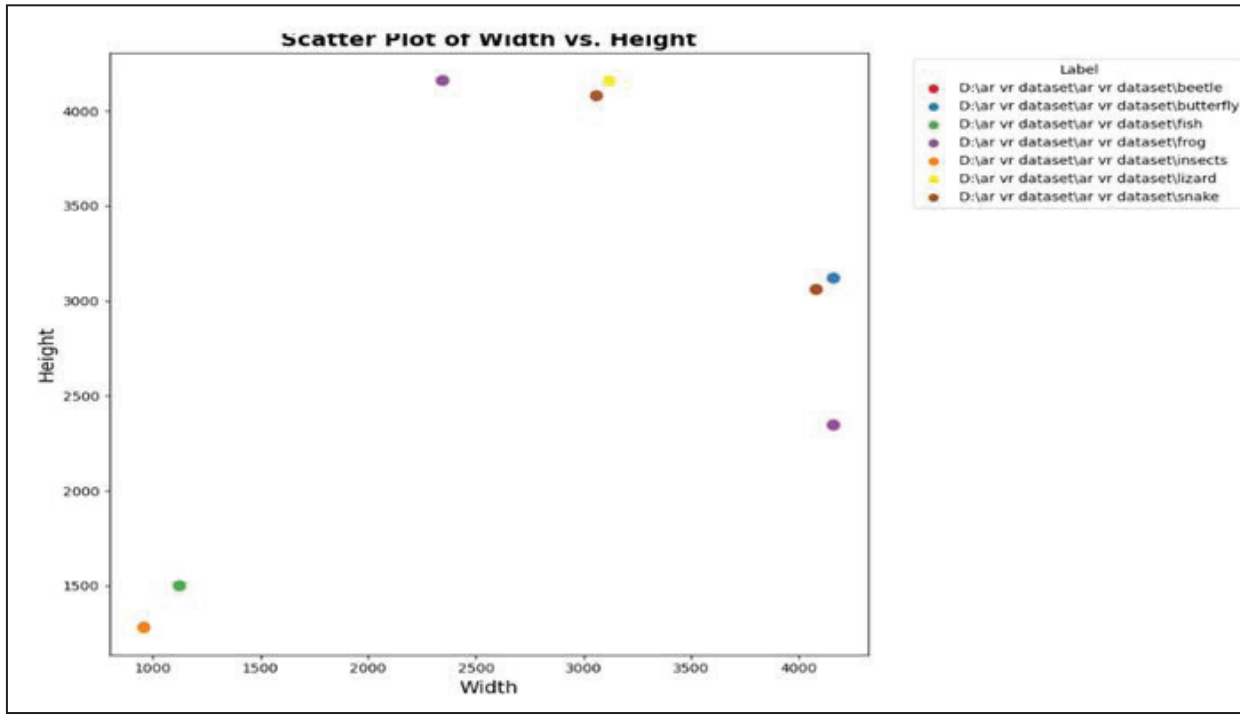

Fig. 15: Image Size Scatter Polt.

RESULT AND CONCULSION

Virtual Reality (VR) holds immense potential to transform the museum visitor experience by offering engaging and immersive storytelling. Through VR, visitors can be transported to historical events and gain a deeper understanding of the context surrounding artifacts. This technology can also facilitate personalized interactions; for

example, smart objects can trigger tailored VR content that aligns with individual preferences and interests, enhancing the overall engagement. In terms of educational value, VR enriches the learning experience by providing rich historical and cultural contexts. Interactive exhibits allow visitors to manipulate virtual objects and participate in simulations, which fosters a more profound comprehension of the museum's collections. This hands-on approach not only makes learning more enjoyable but also encourages critical thinking and exploration. Moreover, VR can attract a diverse range of audiences, drawing in new visitors while encouraging repeat visits through unique and memorable experiences. Additionally, the ability to share VR encounters on social media can further promote the museum, extending its reach and impact. However, there are challenges to consider, including technical limitations related to hardware requirements and user experience. Developing high-quality VR content is often time-consuming and resource-intensive. Additionally, integrating VR with existing museum systems and collections may require careful planning and significant investment. In summary, while VR presents exciting opportunities for museums to enhance visitor experiences, improve educational value, and increase engagement, addressing the associated challenges is essential to fully realize its potential in the cultural sector.

LIMITATIONS

While integrating Virtual Reality (VR) with linked data and smart objects at the Mizoram State Museum offers exciting opportunities, several challenges need to be overcome for effective implementation. A key issue is the technical requirements; high-quality VR experiences demand advanced hardware and software, which may not be available in all museum settings, potentially creating inconsistencies in visitor experiences depending on the museum's budget and infrastructure. Additionally, creating immersive VR content is both time-consuming and resource-intensive, requiring specialized skills in technology and cultural heritage expertise that may be limited among museum staff. Ensuring cultural accuracy and sensitivity in VR content is also critical, as any misrepresentation could diminish the authenticity of Mizo heritage. Technical glitches during VR sessions could disrupt the visitor experience and reduce the likelihood of return visits. Accessibility presents another challenge; while VR can offer greater inclusivity for some individuals with disabilities, others, such as those prone to motion sickness or with visual impairments, may find it difficult to engage with VR. Moreover, incorporating linked data requires careful planning and the development of strong data management systems, which may pose logistical hurdles. Staff training is essential to equip museum personnel with the skills to guide visitors and address technical issues effectively. While VR experiences can boost the museum's visibility through social sharing, there is a risk of oversimplifying or commodifying cultural stories. Lastly, maintaining long-term visitor interest in VR experiences can be challenging, as content will need regular updates and innovations to stay engaging. While VR holds significant potential to enhance visitor engagement at the Mizoram State Museum, addressing these challenges will be key to its successful and sustainable use.

Declaration of Competing Interest: The authors declare that they have no known competing financial interests or personal relationships that could have appeared to influence the work reported in this paper.

Data availability: The data that support the findings of this study are openly available at the Online Assets Store.

REFERENCES

Fortuna, Santina, *et al*. "A comparative study of Augmented Reality rendering techniques for industrial assembly inspection." *Computers in Industry* 155 (2024): 104057.

Gong, Qing, *et al*. "User experience model and design strategies for virtual reality-based cultural heritage exhibition." *Virtual Reality* 28.2 (2024): 69.

Cruz, Yarens J., *et al*. "Ensemble of convolutional neural networks based on an evolutionary algorithm applied to an industrial welding process." *Computers in Industry* 133 (2021): 103530.

Shu-Xi, Wang. "The improved dijkstra's shortest path algorithm and its application." *Procedia Engineering* 29 (2012): 1186-1190.

Mendes, Mateus, *et al*. "Projected augmented reality intelligent model of a city area with path optimization." *Algorithms* 12.7 (2019): 140.

Hassan Mohyuddin, ea al. "A comprehensive framework for hand gesture recognition using hybrid-metaheuristic algorithms and deep learning models" Array, Volume 19, 2023, 100317, ISSN 2590-0056, https://doi.org/10.1016/j.array.2023.100317.

Othman, Mohd Kamal, *et al*. "Usability evaluation of a virtual reality smartphone app for a living museum." *Universal Access in the Information Society* 21.4 (2022): 995-1012.

Kim, Young Min, Sangwoo Ryu, and Ig-Jae Kim. "Planar Abstraction and Inverse Rendering of 3D Indoor Environments." *IEEE transactions on visualization and computer graphics* 27.6 (2019): 2992-3006.

Hassler, Andreas Philipp, *et al*. "Importance of medical data preprocessing in predictive modeling and risk factor discovery for the frailty syndrome." *BMC medical informatics and decision making* 19 (2019): 1-17.

Czok, Valerie, *et al*. "Learning Effects of Augmented Reality and Game-Based Learning for Science Teaching in Higher Education in the Context of Education for Sustainable Development." *Sustainability* 15.21 (2023): 15313.

Liu, Yuzhao, *et al*. "Comparing VR-and AR-based try-on systems using personalized avatars." *Electronics* 9.11 (2020): 1814.

Hsu, Hsiao-Ping, Yin Hong Cheah, and Joan E. Hughes. "A Case Study of a Secondary Biology Teacher's Pedagogical Reasoning and Action with Augmented Reality Technology." *Education Sciences* 13.11 (2023): 1080.

Samala, Agariadne Dwinggo, *et al*. "Global Publication Trends in Augmented Reality and Virtual Reality for Learning: The Last Twenty-One Years." *International Journal of Engineering Pedagogy* 13.2 (2023).

Al-Ansi, Abdullah M., *et al*. "Analyzing augmented reality (AR) and virtual reality (VR) recent development in education." *Social Sciences & Humanities Open* 8.1 (2023): 100532.

Trunfio, Mariapina, Salvatore Campana, and Adele Magnelli. "Measuring the impact of functional and experiential mixed reality elements on a museum visit." *Current Issues in Tourism* 23.16 (2020): 1990-2008.

Hou, Weiting. "Augmented reality museum visiting application based on the Microsoft HoloLens." *Journal of Physics: Conference Series*. Vol. 1237. No. 5. IOP Publishing, 2019.

Pietroni, Eva. "Experience design, virtual reality and media hybridization for the digital communication inside museums." *Applied System Innovation* 2.4 (2019): 35.

Baradaran Rahimi, Farzan, *et al*. "Museum beyond physical walls: an exploration of virtual reality-enhanced experience in an exhibition-like space." *Virtual Reality* 26.4 (2022): 1471-1488.

Khan, Mudassar Ali, *et al*. "Using augmented reality and deep learning to enhance Taxila Museum experience." *Journal of Real-Time Image Processing* 18 (2021): 321-332.

Marques, Diana, and Robert Costello. "Concerns and challenges developing mobile augmented reality experiences for museum exhibitions." *Curator: The Museum Journal* 61.4 (2018): 541-558.

Wei, Wei. "Research progress on virtual reality (VR) and augmented reality (AR) in tourism and hospitality: A critical review of publications from 2000 to 2018." *Journal of Hospitality and Tourism Technology* 10.4 (2019): 539-570.

Panciroli, Chiara, Anita Macauda, and Veronica Russo. "Educating about art by augmented reality: new didactic mediation perspectives at school and in museums." *Proceedings*. Vol. 60. No. 1. MDPI, 2018.

Yung, Ryan, and Catheryn Khoo-Lattimore. "New realities: a systematic literature review on virtual reality and augmented reality in tourism research." *Current issues in tourism* 22.17 (2019): 2056-2081.

Shi, Zhun, and Zihan Zhao. "Research on the Interactive Effects of Augmented Reality (AR) Technology: A Case Study in Science Museum Applications." *Proceedings of the 3rd International Conference on New Media Development and Modernized Education, NMDME 2023, October 13–15, 2023, Xi'an, China*. 2024.

Lypak, Halyna, *et al*. "An information system project using augmented reality for a small local history museum." *2023 IEEE 18th International Conference on Computer Science and Information Technologies (CSIT)*. IEEE, 2023.

Li, Yue, Eugene Ch'ng, and Sue Cobb. "Factors influencing engagement in hybrid virtual and augmented reality." *ACM Transactions on Computer-Human Interaction* 30.4 (2023): 1-27.

Zhou, Yuting, Juanjuan Chen, and Minhong Wang. "A meta-analytic review on incorporating virtual and augmented reality in museum learning." *Educational Research Review* 36 (2022): 100454.

Trunfio, Mariapina, *et al*. "Innovating the cultural heritage museum service model through virtual reality and augmented reality: The effects on the overall visitor experience and satisfaction." *Journal of Heritage Tourism* 17.1 (2022): 1-19.

Teixeira, Natalia, *et al*. "Augmented reality on museums: the ecomuseu virtual guide." *Proceedings of the 23rd Symposium on Virtual and Augmented Reality*. 2021.

Giaconi, Catia, *et al*. "Virtual and Augmented Reality: A Pilot Study." *The International Journal of the inclusive museum* 14.1 (2021): 95.

TING SHENG, "Real-Time AR Technology Assisted High-Resolution Image Processing and Its Graphic Design Application," Digital Object Identifier 10.1109/ACCESS.2020.3014139. pp. 142916 – 142930, 04 August 2020.

MARIAPAOLA PUGGIONI," ScoolAR: An Educational Platform to Improve Students' Learning Through Virtual Reality," Digital Object Identifier 10.1109/ACCESS.2021.3051275, pp. 21059 – 21070, 13 January 2021.

S. Sylaiou, K. Mania, I. Paliokas, L. Pujol-Tost, V. Killintzis, and F. Liarokapis, ''Exploring the educational impact of diverse technologies in online virtual museums,'' Int. J. Arts Technol., vol. 10, no. 1, pp. 58–84, Apr. 2017.

Pochtoviuk, S., Vakaliuk, T., & Pikilnyak, A., 2020." Possibilities of application of augmented reality in different branches of education". Available at SSRN 3719845

Santina Fortuna," A comparative study of Augmented Reality rendering techniques forndustrial assembly inspection," Computers in Industry 155 (2024) 104057.